PALACKY UNIVERSITY, OLOMOUC
Faculty of Science
Department of Experimental Physics

SELECTED SYNTHESIS OF IRON AND IRON-OXIDES AND THEIR CHARACTERIZATION

Doctoral Dissertation

Claudia Jeannette Sarita APARICIO ORDOÑEZ

Study program: Applied Physics

Supervisor: prof. RNDr. Miroslav Mašláň, CSc.

Olomouc 2013

To the memory of my beloved grandfather Benedicto

Acknowledgements

First of all I would like to express my sincere gratitude to my supervisor prof. RNDr. Miroslav Miroslav Mašláň for giving me the opportunity to develop my thesis in the Center of Nanomaterials Research (now Regional Center of Advanced Technologies and Materials – RCPTM). Many thanks to my colleagues, who helped me in many ways during the developing of my thesis.

Special thanks to: Jan Filip, from whom I learned a lot of things about XRD and mineralogy; Libor Machala, who introduced me to the preparation of iron oxides by solid state method; Jiří Tuček, for the valuable discussions about magnetism and Mössbauer spectroscopy; Zdeněk Marušák, for his valuable help with the preparation of samples in the furnaces and TGA/DSC techniques; Jiří Pechoušek, for the always good quality measurements in the Mössbauer spectrometer; Klára Šafárová, for the microscopy photos (SEM and TEM); Oldřich Schneeweiss and Bohumil David from Institute of Physics of Materials in Brno (IPM), for low temperature Mössbauer and XRD in-situ measurements, respectively; Giorgio Zoppellaro, for his advices and comments of the thesis manuscript.

Big thanks to my family and friends, who gave me moral support when I needed it. Also I would like to thanks the Minister of education, youth and sports for the government scholarship that allowed me to study in the Czech Republic.

Overview of the author's publications

1. **Aparicio C.**, Machala L., and Zdenek M. (2012) "Thermal decomposition of Prussian blue under inert atmosphere". *Journal of Thermal Analysis and Calorimetry* **110**(2), 661-669.

2. **Aparicio C.**, Filip J., Skogby H., Marusak Z., Mashlan M., and Zboril R. (2012) "Thermal behavior of almandine at temperatures up to 1,200 °C in hydrogen". *Physics and Chemistry of Minerals* **39**(4), 311-318

3. **Aparicio C.**, Filip J., and Mashlan M. (2010) "High Temperature Decomposition of Almandine and Pyrope in Reducing Atmosphere". *AIP Conference Proceedings* **1258**, 47-54.

Declaration

I hereby declare that this thesis has been written by me independently, using the sources given in the list of references at the end of each chapter. I also declare that my role in the preparation of the publications (1 – 3) was as following: Interpretation of most of the experimental results, preparation of graphs and tables, and preparation of the manuscript.

In Olomouc,

……..……

Claudia J. S. Aparicio Ordoñez

As a co-author of the above mentioned publications (1 – 3), affirm that Claudia Aparicio has the major contribution in these publications.

……..…….....

prof. RNDr. Miroslav Mašláň, CSc.

……..…….....

doc. RNDr. Libor Machala, Ph.D.

……....……..……..

prof. RNDr. Radek Zbořil, Ph.D.

……..…….....

Mgr. Jan Filip, Ph.D.

Annotation

Nowadays, the nanoparticles have an extended use in many practical applications, where iron and iron oxides are not an exception. For example, zerovalent iron (ZVI) finds large application as an efficient tool for removal of heavy metal and microorganism from soils and water. The iron oxide hematite (α-Fe_2O_3) is the most widely used magnetic material in industry, because it allows tuning of physical properties by particle's morphology and size. Another very useful iron oxide is maghemite (γ-Fe_2O_3); in particular, the small nanoparticles (< 20 nm) are used in biomedical applications due to their superparamagnetism and biocompatibility. There are other two iron oxide polymorphs, β- and ε-Fe_2O_3, but their valorization potential has not been assessed yet.

There are many techniques that enable the synthesis of iron and iron oxide nanoparticles. One of those is the solid state synthesis being the main objective of this thesis. The method is based on thermal decomposition of powders or powder mixtures under controlled gas conditions. Therefore, both the minerals and salts in crystalline or in amorphous state are employed. The main advantages of this method are the simplicity of the synthesis and the possibility to scale-up the process. It is known that this is the only technique that allowed to synthesize the four iron(III) oxide polymorphs. To optimize the solid state synthesis, we studied the mechanism of thermal precursor decomposition, the influence of temperature, heating rate, atmosphere as well as the reaction time. Here, preferential use of thermogravimetric analysis (TGA) and differential scanning calorimetry (DSC) was chosen, along with X-ray diffraction (XRD) and Mössbauer spectroscopy (MS) measurements. In some cases MS was very useful to identify a Fe-bearing phase in amorphous state that was not possible to do by XRD.

This work was mainly devoted to the preparation of zerovalent iron (Fe^0) and ferric oxides (Fe_2O_3) from the thermal decomposition of selected materials. Two materials were used in this work: natural garnets (4 from almandine-pyrope series and 1 from spessartine series) and iron (III) hexacyanoferrate (Prussian blue). From iron-bearing garnets, metallic iron nanoparticles embedded in a mineral matrix were obtained as a result of the thermal decomposition in reducing atmosphere. On the other hand, Prussian blue thermally

decomposed in inert and reducing atmosphere gave metallic iron particles and iron carbides. On the contrary, when Prussian blue was heated in the air, two polymorphs of ferric oxide β-Fe_2O_3 and γ-Fe_2O_3 (maghemite) were formed under temperature conditions below 400 °C.

The detailed study of the formation of aforementioned iron compounds revealed a crucial role of the thermal decomposition regime and the precursor shape. Furthermore, it was proved that the morphology of the precursors, under certain conditions, is retained after the thermal decomposition.

A nice example of morphology retention is witnessed in the case of Prussian blue (PB) transformation into maghemite nanoparticles taking place in air at temperatures below 350 °C. We noted that the initially present spherical and cubic shape geometry retained after the transformation process. The resulting similarly shaped aggregates are composed of very small nanoparticles (~ 4 nm in size) exhibiting magnetic activity. The superparamagnetic behavior of these aggregates was observed in magnetization measurements, and additionally verified in room temperature MS measurements. From these results, a potential use of these nanostructures in cell separation processes might become possible, but appropriate surface modifications would be necessary.

As a final remark, it is to note that the combination of the characterization techniques employed in this PhD study allowed to deepen the knowledge concerning the thermal precursor behavior. Thus, to further advance in optimizing the conditions of solid state method yielding desired structure and properties of nanosized iron and iron(III) oxides.

Anotace

V současné době, nanočástice mají rozšířené použití v mnoha praktických aplikacích, kde železo a oxid železa nejsou výjimkou. Například nulamocné nanometrické železo našlo široké využití při extrakci těžkých kovů a mikroorganismů z kontaminovaných půd a vod. Oxid železa hematit (α-Fe_2O_3) je nejpoužívanější magnetický materiál v průmyslových aplikacích, s možností kontroly jeho morfologie a velikosti částic jakožto jejich výsledných fyzikálních vlastností. Další užitečný oxid železa je nanometrický maghemit (γ-Fe_2O_3) s velikostí částic pod 20 nm, které jsou používané v biomedicínských aplikacích díky jejich superamagnetismu a biokompatibilitě. Další dva polymorfy, β- a ε-Fe_2O_3 vyžadují více studií k posouzení jejich praktické použitelnosti.

Existuje mnoho metod přípravy nanočástic elementárního železa a jeho oxidů. Jednou z nich je syntéza v pevné fázi v různých atmosférách a teplotních režimech, což bylo hlavním cílem studií předložené dizertace. Tato metoda je založena na termickém rozkladu práškových sloučenin minerálů a solí či jejich směsí jak v krystalickém, tak i amorfním stavu. Strategie bez solventu je jednoduchá a umožnuje vyšší výstupy produkce. Je také známo, že se jedná pravděpodobně o jediný postup, jak připravit čtyři polymorfy oxidu železitého. Pro optimalizaci syntéz v pevné fázi bylo nezbytné studovat mechanismus tepelného rozkladu prekurzorů, vlivy jejich geometrie a morfologie, jakožto teplotní režimy a kinetiku transformací. Toto studium umožnilo použití moderních metod termické analýzy, strukturální rentgenová difrakce, Mössbauerovská spektroskopie a hmotnostní spektrometrie.

Absolvovaná práce byla nasměrována především k přípravě nulamocného železa (Fe^0) a oxidu železitého (Fe_2O_3) použitím dvou centrálních prekurzorů: (1) Přírodní granát (čtyři různé z almandin-pyropovské řady a jeden z almandin-spessartinovské řady); (2) Hexakyanoželeznatan železitý (Berlínská modř). Prekurzory granátů umožnily přípravu nanokompozitů, kde nanokovové částice železa se tvořily v nitru minerální matrice tepelným rozkladem v redukční atmosféře. V případě berlínské modři jsme pozorovali tvorbu nanočástic nulmocného železa a jeho karbidů v redukčních či inertních podmínkách. Zatímco v oxidační atmosféře (vzduch) a při teplotách pod 400°C byly získány dva polymorfy oxidu železitého β-Fe_2O_3 a γ-Fe_2O_3 (maghemite).

Nejkritičtějšími parametry syntéz se ukázaly teplotní režim a geometrie či morfologie použitých prekurzorů oxidu železa. Jedním z typických příkladů bylo pozorování morfologie nanoagregátů maghemitu vzniklých transformací berlínské modři (PB) na vzduchu a při teplotách pod 350 °C. Sférická a kubická geometrie výchozího materiálu zahřátého na 350 °C zůstala zachována i po proběhlé transformaci. Obdržené nanoagregáty maghemitu obsahovaly malé superparamagnetické nanočástice s velikostmi kolem 4 nm. Superparamagnetické chování nanoagregátů bylo verifikováno v rámci měření magnetizace a Mössbauerovských spektrálních profilů při pokojové teplotě. Tyto výsledky poukazují na možnost použití zmíněných nanoagregátů v biomedicínské separaci buněk, což ale bude požadovat další nutné chemické povrchové modifikace.

Závěrem lze konstatovat, že použitím zvolených prekurzorů a moderních analytických aparatur bylo možné získat další důležité poznatky ohledně termické reaktivity a průběhu transformačních procesů, a tím i nové možnosti příprav nanočástic železa a jeho oxidů metodou reakce v pevné fázi.

Contents

List of abbreviations

Characterization techniques

TGA	Thermogravimetric analysis
DSC	Differential scanning calorimetrie
XRD	X-ray diffraction
MS	Mössbauer spectroscopy
TEM	Transmission electron microscopy
SEM	Scanning electron microscopy
SQUID	Superconducting quantum interference device
EGA	Evolved gas analysis
EMPA	Electron microprobe analysis
EDS	Energy dispersive X-ray spectroscopy
SAED	Selected area electron diffraction
FTIR	Fourier transformed infrared spectroscopy

Approved abbreviations of mineral names (Whitney D. L. and Evans B. W. (2010) Abbreviations for names of rock-forming minerals. *American Mineralogist* **95**, 185-187)

Alm	almandine	Grt	garnet	Phl	phlogopite
An	anorthite	Grs	grossular	Pgt	pigeonite
Cen	clinoenstatite	Hem	hematite	Prp	pyrope
Cpx	clinopyroxene	Hc	hercynite	Qz	quartz
Crd	cordierite	Ilm	ilmenite	Rt	rutile
Crs	cristobalite	Jrs	jarosite	Sil	sillimanite
Di	diopside	Mgh	maghemite	Sps	spessartine
En	enstatite (ortho-)	Mfr	magnesioferrite	Spl	spinel
Fa	fayalite	Mag	magnetite	Tep	tephroite
Fs	ferrosilite	Ol	olivine	Uv	uravovite
Fo	forsterite	Opx	orthopyroxene	Wus	wüstite

1. Introduction

The chemical element iron is widespread in the earth crust, it is commonly found in minerals and forming iron oxides. Iron oxides, especially hematite and maghemite, have been used since ancient times as pigments, for example to give reddish coloration to pottery. In counterpart, iron and its allotropic forms are important for the steel industry. The magnetic properties like spontaneous magnetization or magnetic anisotropy are influenced by the size of the material. When iron and iron oxides have nanometric sizes (< 100 nm) they exhibit especial magnetic properties induced by surface and finite-size effects. Microscopically, the magnetic materials have many magnetic domains in their structure, each domain represent a region where the magnetic moments are oriented in one direction. In the case of nanoparticles, because of their reduced size, the number of magnetic domains is reduced to keep the minimum internal energy. When a critical size is reached the nanoparticle became monodomain, then the value of the coercivity is maximum; but with a more reduced particle's size the coercivity decreases till zero, and then the particles acquire a property called superparamagnetism. Because of the possibility to manipulate the magnetic properties of iron and iron oxides, they are useful in many practical applications, in the range from industry to medicine.

Currently, a lot of physical or chemical techniques make possible to synthesize iron and iron oxide nanoparticles. From them, up to now the solid state synthesis is the only technique known that allows the synthesis of the four iron(III) oxide polymorphs (α-, β-, γ-, and ε-Fe_2O_3). The method is based on thermal decomposition of powders or powder mixtures under controlled gas conditions, an advantage of this method is that different materials can be used as a precursor of nanoparticles.

The preparation of iron and iron oxide nanoparticles by solid state synthesis was the aim of this thesis. This method was chosen because of its simplicity and the possibility to scale-up the process. The materials used as precursors were natural garnets bearing iron, and the iron salt Prussian blue. To fulfill this aim, was studied the thermal decomposition of garnets and Prussian blue, and after carefully phase identification was elucidated the decomposition mechanism for each case, in order to get the best conditions for the synthesis of iron and iron oxides. In the case of Prussian blue, also it was studied the influence of the atmosphere and precursor morphology on phase composition after thermal decomposition.

The present thesis is divided into six chapters. The first chapter briefly describes previous works, motivation and the main goal of the present thesis. The second chapter contains the necessary background to understand the rest of the chapters, it includes the description of iron and iron oxides, thus as the synthesis methods (physical and chemical), characterization techniques (XRD, Mössbauer spectroscopy, TGA/DSC, SEM, magnetization measurements, etc), and their practical applications known up to date. Chapter three describes the thermal decomposition of natural garnets from almandine-pyrope and almandine-spessartine series, it was discussed the influence of iron on the garnet decomposition, and also the formation of small iron particles embedded in mineral matrices. Chapter four presents the results of the thermal decomposition of iron(III) hexacyanoferrate (Prussian blue) under inert atmosphere (argon and nitrogen) including XRD *in situ* measurements for a better understanding of the decomposition mechanism; it was discussed the influence of the heating rate and the layer thickness of the powder sample on the formation of decomposition products (mainly iron carbides and iron as a final product). Chapter five, describe the synthesis of Prussian blue with two morphologies (spherical and cubic), and their posterior thermal decomposition in air; is discussed the formation of basically two polymorphs of ferric oxide (β and γ), and two different decomposition mechanism of Prussian blue with and without potassium. Finally, chapter six summarizes the main conclusions of this thesis and presents an outlook for future work.

2. Iron and iron oxides: features, synthesis, characterization and applications

2.1 Iron

Iron is one of the most common chemical elements on the earth, it can be found in minerals and oxides. In pure form is a dense magnetic metal, it has a high melting point, a good thermal conductivity, and a low coefficient of linear expansion. Natural iron has four stable nuclides: ^{54}Fe (5.845%), ^{56}Fe (91.754%), ^{57}Fe (2.119%), and ^{58}Fe (0.282%). Pure iron is a chemically active metal, it oxidizes very fast when it is in contact with moist air forming rusts. The magnetic properties of iron are linked to its crystalline structure, and it is affected by the temperature and pressure. From room temperature to its melting point at 1808 K (T_m), iron exhibits allotropism (Fig. 2.1), which is the ability of some materials to change their crystallographic structure with the variation of temperature or pressure, these changes are reversible [1].

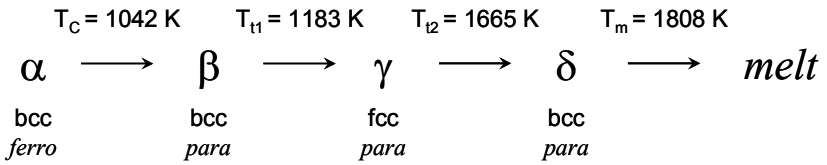

Figure 2.1 Scheme of thermal transformation of iron. The words *ferro* and *para* stand for ferromagnetism and paramagnetism. T_C: Curie temperature, T_{t1}, T_{t2}: transition temperatures, T_m: melting temperature.

Iron has a body centered cube (bcc) lattice from room temperature up to 1042 K, which is the Curie temperature (T_C), it is known as α-Fe and presents a ferromagnetic behaviour with a saturation magnetization at room temperature of 220 A.m^2/kg. Above the T_C, iron loses its ferromagnetism and becomes paramagnetic, but retains the bcc structure, this is known as β-Fe (nowadays, this name is not use anymore). When the temperature reaches a value around 1183 K, iron suffers another phase transformation to face centered cube (fcc) lattice, which involve an expansion of the unit cell, but this is a more compact atom arrange, it is the γ-Fe that remains paramagnetic at this temperature range, but below the Neel temperature (T_N = 67 K) it becomes antiferromagnetic. The last

transformation, before melting, occurs at 1665 K, when the fcc lattice reverts to bcc, it is still paramagnetic and it is know as δ-Fe. A resume of the magnetic properties of the different phases is shown in the figure 2.2 [1,2].

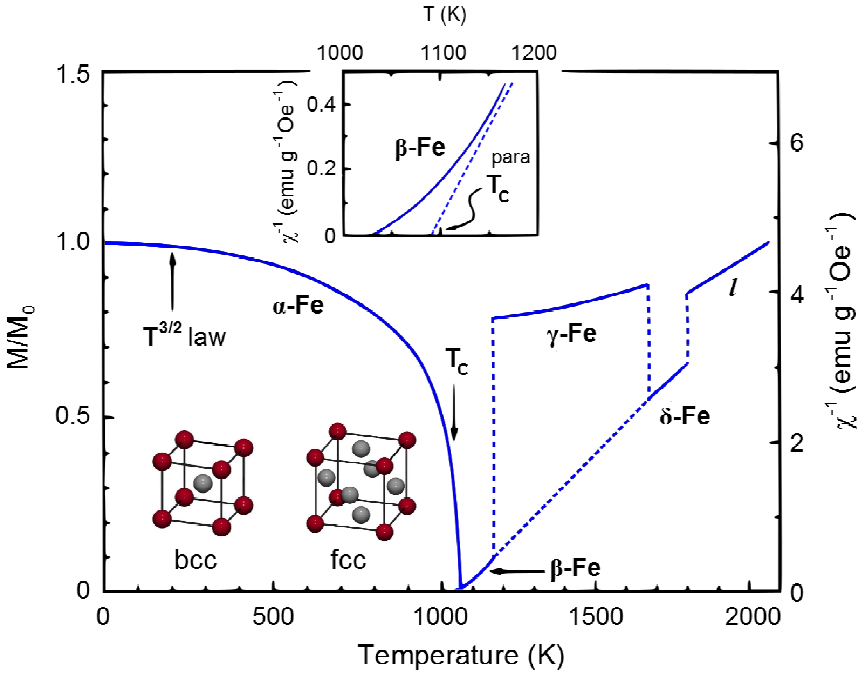

Figure 2.2 Temperature dependence of the spontaneous magnetization ($T < T_C$) and the inverse susceptibility ($T>T_C$) of iron. The dashed line connects χ^{-1} of the β- and δ- phases, which have the same crystalline array. The Curie-Weiss behavior near $T = T_C$ is represented by the dashed line in the inset, T_C^{para} is the paramagnetic Curie temperature (modified from [2]).

2.2 Iron(III) oxide

Iron (III) oxide or ferric iron is a versatile material with a wide range of applications in industry, medicine, biology, and environment, basically because of its polymorphic nature. Ferric iron has four polymorphs, and only two of them had been found in nature as minerals hematite (α-Fe_2O_3) and maghemite (γ-Fe_2O_3), but the others two (β-Fe_2O_3, ε-Fe_2O_3) can be found only as synthetic nanoparticles (Fig. 2.3). Each polymorph has unique magnetic properties, which make them suitable for specific applications, for example at room temperature α-, β-, γ-, and ε-Fe_2O_3 show weak ferromagnetism, paramagnetism, ferrimagnetism, and non-collinear ferrimagnetism or canted anti-ferromagnetism respectively [3,4].

At nanoscopic level hematite [5], maghemite [6–8], magnetite [6], and iron [9] present a special magnetic property known as *superparamagnetism*, that is only present in monodomain particles below a critical size. When the nanoparticles are too small or ultrafine, they have only one magnetic domain and their spins thermally fluctuate inside of the nanoparticles following several orientations corresponding to the minima of the anisotropy energy. The most important characteristic of the superparamagnetic nanoparticles is that they have a zero coercitvity. It means that after the application of an external magnetic field the particles returns to their fluctuant state without any remanent magnetization [7,10].

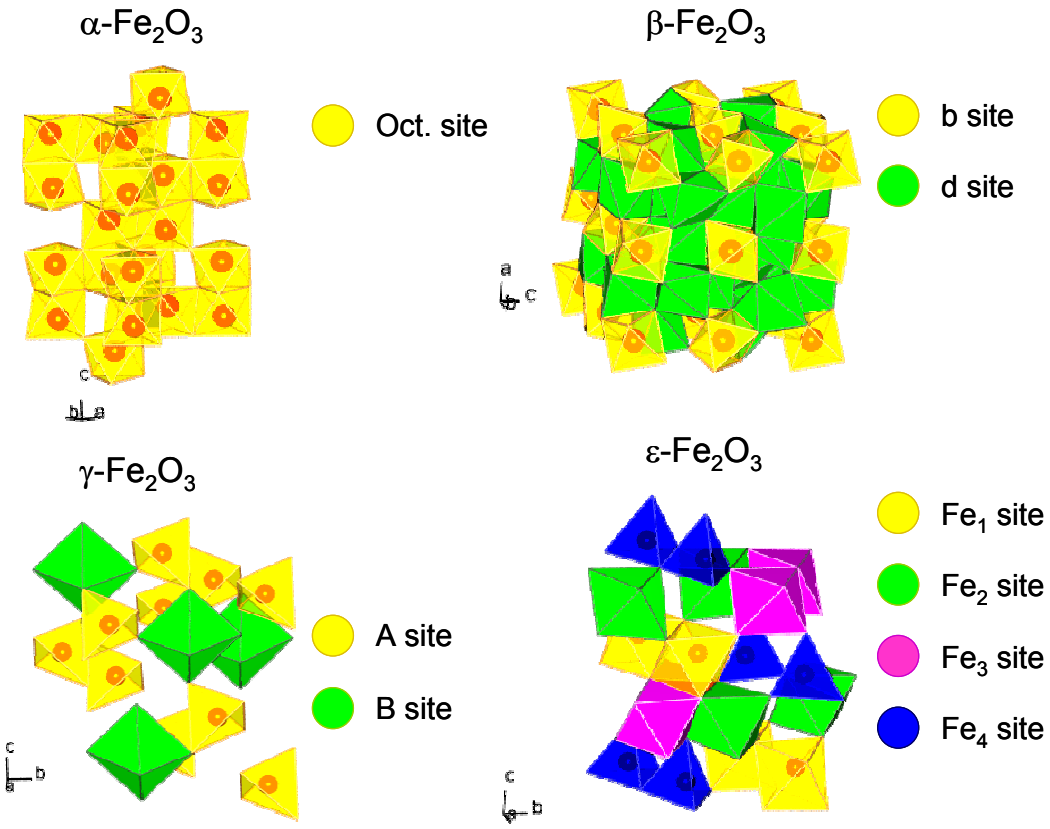

Figure 2.3 Polyhedral representation of iron(III) oxide polymorphs, showing the crystallographic sites of ferric ions for each polymorph.

2.2.1 α-Fe_2O_3 (Hematite)

This polymorph exists in nature as a mineral hematite. It has a rhombohedrally centered hexagonal structure (isostructural with corundum), where Fe^{3+} ions occupy the

two-thirds of the octahedral sites (Fig. 2.3a). The crystallization structure corresponds to the $R\bar{3}c$ space group, with lattice parameters a = 5.036 Å and c = 13.749 Å, and six formula units per unit cell. The sharing of three edges and one face between FeO_6 octahedra is responsible for the distortion of the cation sub-lattice from the ideal packing. The magnetic ordering of the hematite changes with the temperature, and it has two magnetic transition temperatures (Fig. 2.4): Morin temperature (T_M) and Néel temperature (T_N). The magnetic transition temperatures for bulk hematite have values of $T_M \sim 260$ K and $T_N \sim 950$ K [3,4,11].

The Morin temperature varies with the particles size, and rapidly decreases when the particles size is below 100 nm [12,13]. Below T_M hematite behaves as antiferromagnet (AF), where the spins lie along the electric field gradient and crystallographic c-axis. When the temperature increases above the T_M, the spins change their orientation to ~ 90° with respect to c-axis and the magnetic subtattices are aligned almost antiparallel, with a ~ 5° canting between spins, giving a weak ferromagnetism (WF) to hematite. The weak ferromagnetism remains up to 950 K (T_N), and above this temperature hematite behaves as paramagnet [3,4].

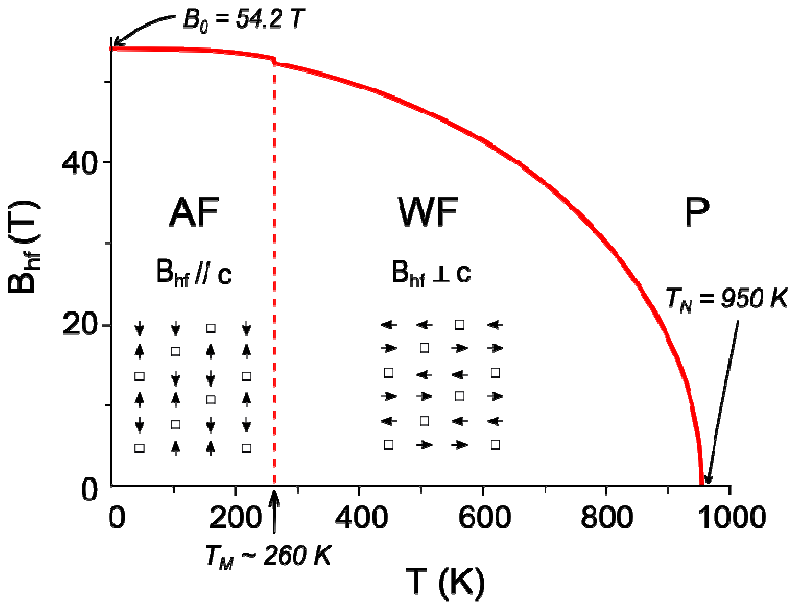

Figure 2.4 Temperature dependence of the magnetic properties of hematite. T_N: Néel temperature, T_M: Morin temperature, P: paramagnetism, WF: weak ferromagnetism, AF: antiferromagnetism, B_{hf}: magnetic hyperfine field, c: crystallographic c-axis of hematite. In the schema, the arrows represent the spin direction and the squares the vacancies in the hematite lattice (modified from [11]).

2.2.2 β-Fe_2O_3

This is a metastable polymorph of ferric oxide, it has never been found naturally, but prepared synthetically as powders [14–16] or thin films [17]. The β-Fe_2O_3 has a bcc "bixbyite" structure, where the Fe^{3+} ions occupy two non-equivalent octahedral sites (Fig. 2.3b). In the unit cell 32 ferric ions are distributed in b and d sites, which have a ratio d/b =3. It crystallize in the $Ia\bar{3}$ space group, with a lattice constant a = 9.393 Å, and 16 formula units per unit cell. At room temperature this polymorph is paramagnetic, but it has a magnetic transition at low temperature (T_N ~ 100-119 K). Below T_N, β-Fe_2O_3 has antiferromagnetic behavior [3,4].

2.2.3 γ-Fe_2O_3 (Maghemite)

Like hematite, this polymorph is found in nature as a mineral maghemite. It has an inverse spinel structure (isostructural with magnetite), where Fe^{3+} ions occupy tetrahedral (A) and octahedral (B) sites as is show in figure 2.3c. The crystalline structure of maghemite contains vacancies, represented by □, in octahedral sites to compensate the excess of positive charge. It can be expressed by the formula $Fe_A(Fe_{5/3}\square_{1/3})_BO_4$. Nevertheless, there have been found three different crystal symmetries for maghemite, each one depending on the vacancy ordering. Then, maghemite crystallizes in the space group: a) cubic $Fd\bar{3}m$ for randomly distributed vacancies (a = 8.339 Å); b) cubic $P4_332$ or $P4_132$ for partially ordered vacancies (a = 8.351 Å); and c) tetragonal $P4_32_12$ for well ordered vacancies (a = 8.349 Å, c = 24.996 Å) [3,4,7].

Maghemite, which has two magnetic sublattices, shows a ferrimagnetic behavior. It has a high magnetic response when is placed under an external magnetic field. From extrapolation it is possible to estimate the value of T_C ~ 790 – 980 K, but it is not possible to do its experimental measurement because of its thermal instability. Thus, above certain temperature (300 – 900 °C) maghemite irreversibly transforms to the most stable polymorph, *i.e.* hematite. The variation of transition temperature is affected by multiple factors such as: particle shape, size and crystallinity [7]. The size of the maghemite particles plays an important role in its magnetic properties, when particles are smaller than 10 nm they show superparamagnetic relaxation and make them useful for several applications.

2.2.4 ε-Fe_2O_3

This polymorph of ferric oxide has been found only at nanometric scale, and it is possible to synthesize, usually inside of a matrix, with different morphologies: nanoparticles [18–22], rods [23], and wires [24]. This polymorph, ε-Fe_2O_3, can be considered as an intermediate phase between maghemite and hematite. The crystalline structure of ε-Fe_2O_3 is orthorhombic, and it can be described with the space group $Pna2_1$, lattice parameters a = 5.095 Å, b = 8.789 Å, c = 9.437 Å, and eight formula units per unit cell. In the unit cell the ferric ions occupy three octahedral non-equivalent sites (Fe_1, Fe_2, and Fe_3) and one tetrahedral site (Fe_4), without any vacancies in its structure, as depicted in figure 2.3d [3,4,25].

There are known two magnetic transition for ε-Fe_2O_3, one at 495 K (T_C) and at 110 K. When the temperature is less than 110 K, ε-Fe_2O_3 behaves as a metamagnet, *i.e.* a material that increase considerably its magnetization with a small change of temperature [20]. At 110 K there are structural transformations and spin reorientation phenomena [25], but there is not an agreement about the kind of magnetism displayed, it is said to be non-collinear ferrimagnet [18] or canted antiferromagnet [20]. Finally, above T_C ε-Fe_2O_3 becomes paramagnetic. Another interesting characteristic of this polymorph is its giant coercive field (0.8 – 4.1 T) at room temperature, probably due to its disordered crystalline structure [25].

2.3 Iron and iron oxide nanocomposites

Nanocomposites are materials composed of small particles embedded in a matrix. In the case of magnetic nanoparticles, the matrix prevents interparticle interactions, and also acts as a coating to prevent oxidation of metallic particles [26]. The particles used commonly in magnetic nanocomposites are zerovalent iron (ZVI) and iron oxides (maghemite or magnetite). Several minerals are used as matrices: magnesium oxide [27], bentonite [28–31], mullite [32], laponite [33], montmorillonite [34–36], muscovite and vermiculite [36]. These nanocomposites can be useful as adsorbents of contaminants in water [29,30], removal of colorants [31], and MRI contrast agents [28,33].

2.4 Methods of synthesis

There are several methods of nanoparticles synthesis, which are also applicable for the synthesis of magnetic nanoparticles (*e.g.* iron and iron oxides). Gubin *et al.* [37] divide the preparation methods of nanoparticles in two categories: physical and chemical synthesis. The methods using gas or solid phase and high energy treatment are called physical, and the methods involving solutions and temperature are considered chemical. In the next sections will be described some of the synthesis methods for each category.

2.4.1 Physical methods

High energy ball-milling: in this method the powder materials (precursors) are finely ground using a planetary ball mill, after grinding for a determinate time the precursors react or its crystalline structure is changed, giving as a result a product with different characteristics. Strength of this method is the possibility of scaling-up, while the size polydispersity and shape irregularity are weaknesses [38]. Using this method Fe^0 [38], maghemite [39], and magnetite [39,40] nanoparticles had been prepared.

Spray pyrolysis: it is a droplet-to-particle conversion, where a starting precursor solution is atomized, then the resultant droplets are heated, provoking the solvent evaporation and the solute condensation, then the precipitation occurs with production of submicron particles. During the condensation the precursor can react with the surrounding atmosphere or be thermally decomposed [41,42]. Small nanoparticles of hematite [43] and maghemite [44] were prepared by spray pyrolysis, in both cases the particles sizes have a broad distribution.

Flow injection: in this technique the reagents are continuously or periodically injected into a carrier stream with laminar flow regime, the reagents react during travelling through a capillary reactor, and then the reaction products are stored in a collector, which is located at the end of the capillary reactor. The technique offers reproducibility, mixing homogeneity, and it is highly controllable [41,45]. Magnetite, with a size range of 2-7 nm, has been prepared using flow injection, with a reaction temperature of 80 °C [45].

2.4.2 Chemical methods

Co-precipitation: it is a very simple method for synthesize maghemite and magnetite, with the advantage of having a high yield and being easily scalable, but with limitations in the control of particles shape and size distribution. For preparing iron oxides by this method, an aqueous solution of iron salt (perchlorate, chloride, sulfate, nitrate) is prepared, then an alkali (base) is added to the solution, after that it is aged at ambient conditions. During the synthesis two stages are identified: nucleation and slow growth of nanoparticles. For reach a better control of the particles size distribution it must be avoided nucleation during particles growth. Other factors affecting the particles size, and also their shape are: type of salts used, reaction temperature (between 20 – 90 °C), PH value, and ionic strength of the solution [10,41,46,47].

Water-in-oil emulsions or reverse micelles: in this methods constrain environments are used as tiny reactors or "nanoreactors". Microemulsion is a stable system conformed by two immiscible liquids, where one of them (water) is isotropically dispersed into the other (oil). To stabilize the water droplets inside the oil, a surfactant is added to the emulsion creating a thin film on their surface [10,37,41,46,47]. Using this method were produced a well shaped nanoparticles of maghemite [41,48], magnetite [41], hematite [49,50], and zerovalent iron [51]. The advantages of this method are the possibility of control the composition and average size of the particle with a relatively narrow size distribution, but with a low yield and difficult to scale-up. The variables affecting the particles size are: synthesis temperature, reaction time, surfactant amount, and ratio of water to oil [41,49,50].

Hydrothermal synthesis: The reaction is carried in a sealed ambient, inside of a reactor or Teflon autoclave, where an aqueous solution of iron salts is heated up to temperatures higher than the water boiling temperature (200 – 220 °C), as a consequence the internal pressure increases above the atmospheric pressure allowing a better crystallization of the iron oxide nanoparticles [10,41,46,47]. Using this technique are obtained highly crystalline nanoparticles with good magnetic properties, other advantages of the technique are its simplicity, relatively narrow size distribution, shape control of nanoparticles, and medium yield. The requirement of special equipment, high pressure, and long reaction times is their principal disadvantages [10,46]. The reaction time and

temperature, even PH and concentration of solution have important effects on the size and shape of reaction products. It allows the production of hematite and magnetite with different sizes and shapes (rods, nanowires [47], hollow nanoclusters, nanorings, short nanotubes, nanostars, and needles [52]).

Sol-gel: it is a "wet" chemical process suitable for the synthesis of metal oxides at room temperature. The process has two steps: in the first step hydroxylation and condensation of molecular precursors in a solution forms a "sol" of nanoparticles; second, further condensation and polymerization creates a three-dimensional metal oxide network or wet "gel". To crystallize the nanoparticles it is necessary a thermal treatment of the gels. The principal advantage that this method offers is a good control of the material properties, such as composition, structure and particle size, by only varying the experimental conditions (precursor concentration, PH, temperature, stirring). The final product and its quality depend on the gelation process, where the surface-volume ratio (S/V) of the sol also has an important role [41,47,53]. Following this route it has been possible to synthesize not only magnetite [53], maghemite [54,55], and hematite [54], but also the rare iron oxide polymorph ε-Fe_2O_3 [21].

Sonochemical decomposition or sonolysis: it consists in the application of ultrasound to an iron-compound solution. The ultrasound provides localized heating by acoustic cavitation, which leads to the compound decomposition, but without control of the nanoparticles size. Using iron pentacarbonyl as precursor was prepared zerovalent iron [38], magnetite [41], and hollow hematite [56], while using iron acetylatonate was prepared amorphous Fe_2O_3 and maghemite [57].

Thermal decomposition or thermolysis: This method consists in chemically decompose a material using heat. Usually organometallic compounds (*e.g.* metal carboxylates, carbonyls, acetylacetonates) are decomposed in high boiling organic solvents containing stabilizing surfactants (fatty acids, oleic acid) to synthesize nanocrystals. Control of nanoparticles sizes and shapes is achieved varying the time and temperature reaction, concentration and ratio of the reactants. Advantages offered by this method are the nanoparticles crystallinity, good shape control, very narrow size distribution, possibility to scale-up because of its high yield, but on the other hand some of the precursor reagents are toxic and not easy to manipulate [10,41,46]. Monodisperse

nanocrystals of magnetite (6 – 30 nm) [58] and maghemite (4 – 16 nm) [59] had been obtained using this technique with a very high yield 80 – 95 %.

Precipitation by anhydrous solution: is the synthesis of metallic nanoparticles from aqueous solutions of metal salts, using strong reducing agents (*e.g.* $NaBH_4$) at room temperature [37]. Using this method were prepared zerovalent iron nanoparticles from ferric chloride, with particles size less than 100 nm [34,60–63].

Solid state synthesis: The method consists in thermally decompose powdered compounds (crystalline or amorphous) or a mix of them under a determinate atmosphere to obtain nanoparticles. Simplicity of the synthesis and possibility to scale-up the process are their advantages, while sometimes it is difficult to obtain a uniform size distribution, or homogeneous phases. In the case of the iron and iron oxides, they can be obtained not only through the precursor decomposition, but also through its reduction or oxidation. The composition and size of the nanoparticles can be controlled varying the reaction time, temperature, heating rate, atmosphere (inert, oxidant or reducing) or using different heating regimes (dynamic or isothermal). A very wide variety of precursors can be used to synthesize iron oxides by this technique: iron(III) compounds, iron(II) compounds, iron salts, iron complexes (carbonly, carboxylate) and iron bearing minerals (goethite, akaganeite, lepidocrocite, ilmentite, almandine) [3].

The four iron(III) oxide polymorphs can be synthesized using this technique, but the final product is always hematite, because it is the most stable polymorph, existing two routes of polymorph transformation: $\beta \rightarrow \alpha$, and $\gamma \rightarrow \varepsilon \rightarrow \alpha$ [3,4,14,64]. Maghemite has been synthesized from thermal decomposition in air of: iron(II) acetate at 400 °C [65], ferrous sulfate at 370 °C, ferric oxalate at 250 °C, almandine at 900 °C [64]. The metastable polymorph β-Fe_2O_3 could be obtain as a decomposition sub-product of ferric ferrocyanide [66] and ferric sulfate [14], being very difficult to synthesize from other compounds, the synthesis was optimized by mixing the ferric sulfate with sodium chloride (NaCl) [67], and recently by mixing $NaFe(SO_4)_2$ with NaCl [15]. The rare polymorph ε-Fe_2O_3 has been identified as a decomposition sub-product of almandine [64] and ferric sulfate [3].

2.5 Techniques of characterization

2.5.1 Structural: XRD, SAED

X-ray Diffraction (XRD) is a non-destructive technique, which allows the identification of the crystalline phases present in materials (monocrystalline or powder). The surface of a material is irradiated with X-ray, and then the coherently scattered (diffracted) X-ray are collected by a detector, the signals are then processed to give an X-ray pattern or diffractogram. The diffractogram, where the diffraction intensities are plotted vs. the 2θ Bragg angle, is the one-dimensional graphic representation of the three-dimensional reciprocal lattice of a material. From XRD patterns it is possible to identify the phases present in a sample and obtain information of its structural properties (cell parameters, lattice type, atomic parameters, crystallinity, particles size, strain, preferred orientation) analyzing the position, intensity and shape of the peaks [68,69]. The quantitative analysis of the identified phases on the X-ray pattern is done using the Rietveld Method. The Rietveld Method uses the least-square refinement to minimize the difference between the observed and calculated intensity profiles. It requires a reference structure file of the identified phase, and does not need any internal or external standard. During the refinement of the structures, the phase weight fraction can be calculated using the values of scale factors, number of formula units per unit cell, molecular mass of the formula unit, and the unit cell volume [69,70].

Selected-Area Electron Diffraction (SAED) permits to obtain an electron diffraction pattern of a material being analyzed under a TEM microscope. The image is formed using the detected signals from the elastic scattered electrons, which are product of the interaction of the electron bean passing through a small selected area (0.5 μm) of a thin specimen. The information obtained allows the identification of crystalline structure and lattice parameters of the material being observed; it also permits to recognize the polycrystalline and amorphous materials [68,71].

2.5.2 Thermal properties: TGA, DSC

Thermogravimetric analysis (TGA), in this technique the mass of a sample is measured as a function of temperature or time. When the sample is heated at a constant

heating rate it is a dynamic measurement, while when the temperature is held constant it is an isothermal measurement. The thermogravimetric curve is the plot of the mass (in percentage) versus the temperature or time. The analysis can be done under different atmospheres: reactive, oxidizing or inert. TGA registers the thermal changes involving mass change, the processes commonly monitored are: desorption or absorption, thermal decomposition with formation of gaseous products, oxidation, uptake or loss of water [72].

Differential scanning calorimetry (DSC), this technique measures the energy changes occurring during the heating or cooling of a sample. Similar to TGA, it has two measurement regimens (dynamic and isothermal), and it can be done under different atmospheres. Due to the similarity between both techniques, in modern equipments they are performed simultaneously. In the DSC graph is plotted the heat flux on the y-axis and the temperature on the x-axis. The DSC curve usually shows downward and/or upward peaks, which represent the endothermic and exothermic processes occurring in the sample. DSC records the transitions occurring during the sample heating, and allows the identification of melting of the sample, glass transition, thermal decomposition, phase transition, and crystallization [72].

2.5.3 Morphology: SEM, TEM

Scanning Electron Microscopy (SEM) provides the magnified image of the material's surface, in addition to the topographical information this technique allows us to know the elemental composition of the material. The image is formed as a result of the interaction of the electrons with a volumetric section of the material, around the electron beam, thus producing X-rays, secondary and backscattering electrons, which are collected by a scintillation detector coupled to a photomultiplier tube, then converted to digital signals, which construct the final image. The image is reconstructed from the digital signals, after transformed to pixels, which carried information of the spatial position and the brightness [68,73].

Transmission Electron Microscopy (TEM), it is a very useful technique for the visualization of the internal structure of materials, by the phase contrast imaging of a thin specimen. It allows distinguishing between highly crystalline materials, clusters, core-

shell structures, and hollow structures. The operation principle is similar to the SEM, with the difference that in TEM are used the direct forward-scattered electron passing through the thin specimen to form the image [71].

2.5.4 Magnetic properties: SQUID magnetometry, Mössbauer spectroscopy

SQUID (Superconducting Quantum Interference Device) based magnetometry. An uncoupled DC SQUID consists of two Josephson junction coupled with a superconducting loop arrangement and biased by an external DC source. In a typical measurement the sample is attached to a rod, the rod is moved in short steps through the detection coils, and a current is induced by the magnetic moment of the sample, then the voltage at each step is recorded as a function of the sample position, after the response curve is analyzed to obtain the corresponding magnetic moment of the sample. The measured magnetic moment is usually a function of the applied magnetic field or temperature [74,75]. Using this technique, the global magnetization of the material is measured, in function of the magnetic field intensity or the temperature. This device allows to record the Zero field-cooled (ZFC) and field-cooled (FC) magnetization curves, and also the hysteresis curve. ZFC and FC allow us to determinate the blocking temperature of the sample, while from the hysteresis curve we can determinate the type of magnetism in the sample, and obtain information about the coercivity, saturation and remanent magnetization [76].

Mössbauer spectroscopy (MS), the physical principle of this technique is the "recoilless emission and resonant absorption of gamma radiation by atomic nuclei in solids", which is better known as Mössbauer effect [77]. In the experiment a gamma source (usually ^{57}Co in a rhodium matrix) is moved forward and back to a thin absorber, where the emitted gamma radiation is modulated by the Doppler effect. After, the gamma rays passing through the sample are detected by a scintillation detector, then amplified and analyzed by a multichannel analyzer, and finally the Mössbauer spectrum is produced. The spectrum is essentially a graph of the count rate registered as a function of the source velocity in a multichannel analyzer. Two mirror spectra are recorded, folded and fitted in order to obtain the Mössbauer parameters: Isomer shift (IS), quadrupole splitting (QS), peak width-line (W), and hyperfine magnetic field (B_{hf}). From the values of the Mössbauer parameters it is possible to obtain information about the iron oxidation

state, nature of the chemical bond, electronic and crystallographic structure, symmetry of the iron site, and determinate the present or absence of magnetic ordering [77–79]. Using this technique at different conditions (room temperature, low and high temperature, and under magnetic field) we can study the magnetic behavior of nanoparticles: magnetic relaxation, superparamagnetism, collective magnetic excitation, inter-particles excitation, and spin canting.

2.5.5 Others: EDS, BET

Energy-Dispersive X-ray Spectroscopy (EDS) is a sensitive technique, which permit to determine the elemental composition of the analyzed material under a SEM microscopy. The X-ray spectrum is acquired from a small area of the specimen being focused with an electron beam. The characteristic X-ray, which is unique for each element, is produced when an electron from the one shell is ionized and its place is filled with an electron from an upper shell. These X-rays are detected by a solid state detector and converted to an electric signal, these signals are amplified and digitalized, and then the X-ray spectrum is collected. The advantages of this technique is the detection of elements with $Z \geq 4$, the speed of data collection, and high detector efficiency, but one inconvenience is the poor energy resolution of the peaks, which complicates the identification of elements in samples with multielemental composition [68,80].

Surface Areas by the BET (Brunauer, Emmett and Teller) method, it is a technique based in the adsorption (physical or chemical) of a gas over the surface of a thin layer or powder sample. In this method, the material is heated and outgassed to remove any adsorbed gases, then an inert gas is introduced and it is adsorbed by the sample surface forming a monolayer. After that the sample is placed in a vacuum chamber at constant low temperature, then the pressure is varied to obtain adsorption and desorption isotherms. The surface area is calculated from the monolayer volume, this value is calculated using the BET equation, which relates the gas pressure and the volume of gas adsorbed [68].

2.6 Applications

One of the first uses of iron oxides was the production of pigments for wall

painting, cosmetics, and artistic decoration [11]. Since then many other uses appear, especially after the developing of nanotechnology. A summary of these applications is done in the following sections.

2.6.1 Industry

The pigments made from iron oxide have the advantage of being stable, non-fading, resistant to acids and alkaline solutions, which make them very suitable for outdoor uses [11]. Controlling the shape and size of the iron oxides [47], and also the kind of polymorphs allows the production of different color tonalities [81]. Magnetic pigments are also used in electronic recording devices; they are made from maghemite [11] or metallic iron [38] with needle shape, and are used because of its high coercive field strength.

Iron and iron oxides are also used in several catalytic processes. Zerovalent iron (ZVI), hematite and maghemite are more commonly used in catalysis, but β-Fe_2O_3 nanoparticles in a carbon paste were also tested as an electro-catalyst for the reduction of hydrogen peroxide [82]. Iron oxides demonstrated its usefulness in the decomposition of H_2O_2 [83] used in the oxidation of contaminants, dehydrogenation of ethylbenzene to produce styrene, and the Fischer-Tropsch reaction for transport of fuels from biomass [44].

Gas sensing is another interesting application, based basically on changes of the material resistivity in the presence of a gas, where hematite of maghemite thin films are more often used. The gases detected are from ethanol, acetone, heptane, gasoline, formaldehyde, acetic acid [84–87]. The sensor efficiency vary with the morphology of the particles deposited on a substrate, examples of morphology are nanorods [84,85], flowerlike [86], and mesoporous structures [87].

Other applications include: a) Photo-electrochemical water splitting, using hematite as photoanode in a solar cell, for hydrogen production and storage of solar energy [44,88]; b) energy storage devices, where hollow maghemite nanoparticles [89], hematite nanorods [84], mesoporous hematite [87], and composites of reduced graphene oxide with hematite nanoparticles [90], are used as anodes for lithium ion batteries; c) and recently hollow β-Fe_2O_3 nanoparticles characteristics make it interesting for optoelectronic [91].

2.6.2 Biology and medicine

Iron oxide nanoparticles have a promising future in biological and medicine applications, especially in diagnostic (*in-vitro* and *in-vivo*) and also recently in in-vivo therapy [47]. The interest is focused mainly in four areas: labeling and cell separation (*in-vitro*), MRI contrast enhancement, drug delivery, and hyperthermia (*in-vivo*). The most used particles for these applications are the SPION (SuperParamagnetic Iron Oxide Nanoparticles), which are maghemite or magnetite nanoparticles displaying superparamagnetism. The advantages of these particles are: suitable magnetic properties, low citotoxicity, biodegradability, biocompatibility, chemical stability, reduced particle size, and large surface area [65]. In order to be used *in-vivo* bio-applications, the nanoparticles require to be functionalized, *i.e.* stabilize the particles by coating to prevent their agglomeration, chemical degradation, and enable the attachment of other compound on the particle surface [6,41,46,65]. Other requirement for usage of magnetic nanoparticles in *in-vivo* applications are: stability in aqueous ionic solutions at physiological PH (~7.4), non-toxicity, permanence in blood circulation for enough time, ability to attach functional groups on their surface, hydrophilicity, high zeta-potential to avoid particle precipitation and increase the cellular phagocytosis, preferably narrow size distribution, and avoid the particles uptake by reticuloendothelial system in the cells, and low protein adsorption [6,92,93].

Cell separation: it is an *in-vitro* application, which enables the separation of cell with intrinsic magnetic moment (red blood cells) or those tagged by a magnetic label. The separation process can be done by direct or indirect methods. In direct separation a ligand is coupled to a magnetic particle, then the cells are tagged, and finally they are removed using a magnet. In indirect separation, the targed cells are first sensitized with a primary affinity ligand, then the excess of ligand is removed by washing, after that the magnetic particles with a secondary affinity ligand are added to the solution containing the sensitized cells, where the magnetic particles and cells are bind thanks to the affinity ligands, finally the tagged cells are recovered using a magnetic separator. The size of the magnetic particles used for this particular application varies between 50-200 nm and 1-5 μm. The smaller particles are used as colloidal magnetic labels, are usually superamagnetic, and are coated with polysaccharides or synthetic polymers. The bigger particles are coated with a polymer shell; they are also superparamagnetic, because the

particle is actually a cluster of nanoparticles. These particles are available commercially as Dynabeads®. Cell separation is very useful in microbiology, where the inmunomagnetic separations are used for the detection of microorganism as: Salmonella, Listeria, Escherichia coli, and Helicobacter pylori among others. The same technique is useful for isolation of human cells as: B-lymphocytes, T-limphocytes, endothelial cells, leukocytes, etc. Good results were also obtained in the removal of parasites (*e.g.* Giardia lamblia, Toxoplasma gondii, Plasmodium faciparum) from water [94].

Contrast enhancement in magnetic resonance imaging (MRI): The principle of MRI is the production of an image from electrical signals, which are a result of the nuclear spins relaxation of protons, previously excited by a radio frequency pulse, under an external magnetic field (B_0). They are two kinds of relaxation mechanism: a) longitudinal (T_1) or recovery of magnetic moment along the direction of B_0; and b) transversal (T_2) or loss of signal in the plane perpendicular to B_0. T_1 and T_2 are given in ms, being $T_1 > T_2$. The contrast in MRI depends basically of the nuclear spin density, relaxation times T_1 and T_2 [10]. From them, T_2 can be modified using a contrast agent, one example are the SPION, which create local variations in the proton magnetic field and decreasing the T_2 time relaxation, thus producing a darkening of the produced image or negative contrast [6,10,41,44,65]. The efficiency of SPION depends on their size, charge and coating. To use the particles, they must be able to form magnetic colloids or ferrofluids, where the functionalized particles are immersed in a fluid that make possible their application intravenously of orally. Also it must consider other factors, which could affect their efficiency or bring problems in blood circulation. The SPION hydrodynamic size used in MRI varies between 20-3500 nm and 20-150 nm (including the coating) in the case of intravenous application. The most common coatings are dextran, carboxydextran, polyethyleneglycol, starch, albumina, citrate, and silica [6,41]; also SPION in bentonite matrix has been used as oral contrast agent [65].

Hyperthermia: it is a medical treatment; where a tumoral tissue is heated up to temperatures above 42 °C with the objective of destroy it. Three different types of hyperthermia are available: local (applied to a very small area as a tumor), regional (for large areas of tissue), and whole body. When magnetic nanoparticles are used, it is restricted only to local hyperthermia. In magnetic hyperthermia a magnetic fluid is used, for its delivery it can be used arterial injection, direct injection into the tumor, *in-situ*

implant formation, or active targeting [93]. Heat is generated because of delay in the relaxation of nanoparticles magnetic moment, when they are under an oscillating external magnetic field with reversal times shorter than the magnetic relaxation time (τ) of the nanoparticles, therefore they act as a localized heat sources and heating the surrounding tissue. Two mechanism of heat generation has been identified: a) Néel relaxation (τ_N), due to rotations of magnetic moment inside of the particle, when it is overcome the energy barrier that maintain the particle in its equilibrium position producing magnetic hysteresis loss; and b) Brown relaxation (τ_B), due to frictional losses when the particles rotate in a viscous fluid [6,10,41,92,93]. A measure of the absorbed heat by the surrounding tissue is given by the specific absorption rate (SAR [W/g]), for small particles with small anisotropy SAR proportional to the relaxation time, and broad size distribution causes a fast decrease of SAR, which make the particles less efficient for hyperthermia treatment. Typical SAR values are 100-800 W/g, for use with alive organisms there is a limit of $B_0 < 15$ kA/m and oscillation frequency $f < 1.2$ MHz [10,93]. The most used nanoparticles coatings in hyperthermia are: polyethylene glycol fumarate, polyvynil alcohol, acrylate based, polysaccharide based, alginate, chitosan, silica, gold [93].

Targeted drug delivery: this term apply to pharmaceutical agents attached or embedded to an organic matrix or inorganic particles, which increase the efficacy and improve its deliver to specific targets. Following this approach, drugs can be attached onto the surface of SPION or encapsulated inside of a hollow magnetic nanoparticles (acting as a nanocontainer), then the magnetic nanoparticles can be manipulated using an external magnetic field, and guided to a specific place where the drug is released [10,92]. There are specific requirements that particles have to fulfill: long circulation in blood (half-size), bioavailability and specific targeting, intracellular delivery, response to external stimuli (*e.g.* magnetic field), and biodegradability [92]. The behavior of nanoparticles inside of a living organism is variable, depending on their size. Particles having sizes greater than 200 nm, they are trapped by spleen and removed by phagocyte cells; when the particles have sizes between 10-100 nm they are ideal for use in intravenous application and they have a prolonged blood circulation time. In contrast, when the particles are too small (< 10 nm), they are removed fast by renal clearance [41]. Three possibilities of targeting are available: passive (through the drug and carrier properties), active (drugs or carriers are tagged to specific cells), and physical (through

external influences as magnetic field) [6]. To enable the targeting the particles have to be coated with organic compound that will be used as ligands for drugs, examples of coatings are: albumin, starch, dextran, chitosan, polyalkycyanoacrylate, polyethileneglycol, siloxane, and polyvinyl alcohol [6,92].

Other applications are: gene therapy [95], stem cell trackling [10], transplant monitoring [10], molecule immobilization [41,65], and biosensors [44].

2.6.3 Environment

The environmental applications are mainly focused in the removal of pollutants from water or soil [96]. To reach this goal many studies had been done using nano-ZVI [61,96–98], iron oxides [29,30,99], and composites of these particles with clays [29–31] or carbon [99]. The particle sizes used for this purpose vary between 26 – 150 nm for nZVI and 10 – 60 nm for iron oxides. The needed amount of nanoparticles or composites for spiked liquids vary from 0.01 – 1.30 g/L for ions removal, and rise up to 40 g/L for colorant removal.

The ions removal can be done following different mechanisms [96]: a) reduction of the ionic state of metallic cations in a compound to a smaller ionic state, b) precipitation, sorption by the nanoparticles surface or incorporation in the structure of formed oxohydroxides, and c) increment of the compound solubility and co-precipitation with formation of oxyhydroxides. To the present date, the experimental evidence proved the satisfactory removal, from 80% to 100% usually at laboratory scale, of the following ions: As(V) [98], As(III) [96], Ni(II) [29], Cu(II) [29,96], Cd(II) [29,96], Zn(II) [29,96], Co(II) [30], Cr(VI) [61,96,97,99] , U(VI) [96], and others.

2.7 Final remarks

Alpha iron has found a wide application in the environment removing metallic pollutants and microorganism from soils and water, which is important to keep the delicate environmental equilibrium. Concerning to iron(III) oxides, hematite and maghemite are the better known and most used polymorphs. Hematite is the last product in the thermal conversion of iron oxides, and also is the most widely used in industrial

applications, varying their physical properties by the modification of their morphology and particle size. The second most used polymorph is maghemite, principally in biomedical applications due to the superparamagnetism present in very small particles and biocompatibility. The other two polymorphs β- and ε-Fe_2O_3, still need to be deeply studied to find their practical applications. The combination of synthetic methods and the use of many of the available characterization techniques will be no only useful, but also expand the research in the fully understanding of iron oxide polymorphs and their control for practical uses.

Bibliography

1. F. Cardarelli, *Materials Handbook: A Concise Desktop Reference*, Second (Springer-Verlag London Limited, London, 2008), p. 1340.
2. W. Pepperhoff and M. Acet, *Constitution and Magnetism of Iron and its Alloys* (Springer-Verlag, Berlin, Heidelberg, 2001), p. 226.
3. R. Zboril, M. Mashlan, and D. Petridis, *Chem. Mater.* **14**, 969–982 (2002).
4. L. Machala, J. Tuček, and R. Zbořil, *Chem. Mater.* **23**, 3255–3272 (2011).
5. F. Bødker, M. Hansen, C. Koch, K. Lefmann, and S. Mørup, *Phys. Rev. B* **61**, 6826–6838 (2000).
6. T. Neuberger, B. Schöpf, H. Hofmann, M. Hofmann, and B. von Rechenberg, *J. Magn. Magn. Mater.* **293**, 483–496 (2005).
7. J. Tuček, R. Zboril, and D. Petridis, *J. Nanosci. Nanotechnol.* **6**, 926–947 (2006).
8. S. Mørup and E. Tronc, *Phys. Rev. Lett.* **72**, 3278–3281 (1994).
9. F. Bødker, S. Mørup, M.S. Pedersen, P. Svedlindh, G.T. Jonsson, J.L. Garcia-Palacios, and F.J. Lazaro, *J. Magn. Magn. Mater.* **177-181**, 925–927 (1998).
10. A. Figuerola, R. Di Corato, L. Manna, and T. Pellegrino, *Pharmacol. Res.* **62**, 126–143 (2010).
11. R.M. Cornell and U. Schwertmann, *The Iron Oxides: Structure, Properties, Reactions, Occurences and Uses*, Second (Willey-VCH, Heppenheim, 2003), p. 694.
12. R.E. Vandenberghe, E. Van San, and E. De Grave, *Czech. J. Phys.* **51**, 663–675 (2001).
13. Ö. Özdemir, D.J. Dunlop, and T.S. Berquó, *Geochem. Geophy. Geosy.* **9**, Q10Z01 (2008).
14. R. Zboril, M. Mashlan, D. Krausova, and P. Pikal, *Hyperfine Interact.* **120/121**, 497–501 (1999).
15. T. Danno, H. Asaoka, M. Nakanishi, T. Fujii, Y. Ikeda, Y. Kusano, and J. Takada, *J. Phys. Conf. Ser.* **200**, 082003 (2010).

16. C.-W. Lee, S.-S. Jung, and J.-S. Lee, *Mater. Lett.* **62**, 561–563 (2008).

17. E.R. Bauminger, L. Ben-Dor, I. Felner, E. Fischbein, I. Nowik, and S. Ofer, *Physica B* **86-88**, 910–912 (1977).

18. E. Tronc, C. Chanéac, and J.P. Jolivet, *J. Solid State Chem.* **139**, 93–104 (1998).

19. E. Taboada, M. Gich, and A. Roig, *ACS Nano* **3**, 3377–3382 (2009).

20. M. Kurmoo, J.-L. Rehspringer, A. Hutlova, C. D'Orléans, S. Vilminot, C. Estournès, and D. Niznansky, *Chem. Mater.* **17**, 1106–1114 (2005).

21. M. Popovici, M. Gich, D. Nižňanský, A. Roig, C. Savii, L. Casas, E. Molins, K. Zaveta, C. Enache, J. Sort, S. de Brion, G. Chouteau, and J. Nogués, *Chem. Mater.* **16**, 5542–5548 (2004).

22. M. Gich, C. Frontera, A. Roig, E. Taboada, E. Molins, H.R. Rechenberg, J.D. Ardisson, W.A.A. Macedo, C. Ritter, V. Hardy, J. Sort, V. Skumryev, and J. Nogués, *Chem. Mater.* **18**, 3889–3897 (2006).

23. K. Kelm and W. Mader, *Z. Anorg. Allg. Chem.* **631**, 2383–2389 (2005).

24. S. Sakurai, K. Tomita, K. Hashimoto, H. Yashiro, and S. Ohkoshi, *J. Phys. Chem. C* **112**, 20212–20216 (2008).

25. J. Tuček, R. Zbořil, A. Namai, and S. Ohkoshi, *Chem. Mater.* **22**, 6483–6505 (2010).

26. D.L. Leslie-Pelecky and R.D. Rieke, *Chem. Mater.* **8**, 1770–1783 (1996).

27. O. Schneeweiss, R. Zboril, N. Pizurova, M. Mashlan, E. Petrovsky, and J. Tucek, *Nanotechnology* **17**, 607–616 (2006).

28. H. Bartonkova, M. Mashlan, I. Medrik, D. Jancik, and R. Zboril, *Chem. Pap.* **61**, 413–416 (2007).

29. L.C.A. Oliveira, R.V.R.A. Rios, J.D. Fabris, K. Sapag, V.K. Garg, and R.M. Lago, *Appl. Clay Sci.* **22**, 169–177 (2003).

30. T. Shahwan, Ç. Üzüm, A.E. Eroğlu, and I. Lieberwirth, *Appl. Clay Sci.* **47**, 257–262 (2010).

31. Y. Xi, M. Megharaj, and R. Naidu, *Appl. Clay Sci.* **53**, 716–722 (2011).

32. H. Wang, T. Sekino, K. Niihara, and Z. Fu, *J. Mater. Sci.* **44**, 2489–2496 (2009).

33. V. Tzitzios, G. Basina, A. Bakandritsos, C.G. Hadjipanayis, H. Mao, D. Niarchos, G.C. Hadjipanayis, J. Tucek, and R. Zboril, *J. Mater. Chem.* **20**, 5418–5428 (2010).

34. M. Fan, P. Yuan, T. Chen, H. He, A. Yuan, K. Chen, J. Zhu, and D. Liu, *Chin. Sci. Bull.* **55**, 1092–1099 (2010).

35. S. Li, P. Wu, H. Li, N. Zhu, P. Li, J. Wu, X. Wang, and Z. Dang, *Appl. Clay Sci.* **50**, 330–336 (2010).

36. M. Mashlan, H. Bartonkova, D. Jancik, J. Tucek, and P. Martinec, *Hyperfine Interact.* **191**, 151–157 (2009).

37. S.P. Gubin, Y. a Koksharov, G.B. Khomutov, and G.Y. Yurkov, *Russ. Chem. Rev.* **74**, 489–520 (2005).

38. D.L. Huber, *Small* **1**, 482–501 (2005).

39. N. Randrianantoandro, A.. Mercier, M. Hervieu, and J.. Grenèche, *Mater. Lett.* **47**, 150–158 (2001).

40. J.D. Betancur, J. Restrepo, C.A. Palacio, A.L. Morales, J. Mazo-Zuluaga, J.J. Fernández, O. Pérez, J.F. Valderruten, and A. Bohórquez, *Hyperfine Interact.* **148/149**, 163–175 (2003).

41. S. Laurent, D. Forge, M. Port, A. Roch, C. Robic, L. Vander Elst, and R.N. Muller, *Chem. Rev.* **108**, 2064–2110 (2008).

42. K. Okuyama and I. Wuled Lenggoro, *Chem. Eng. Sci.* **58**, 537–547 (2003).

43. R.F.C. Marques, A.F.R. Rodriguez, J.A.H. Coaquira, J.G. Santos, V.K. Garg, M. Jafelicci, S.J.L. Ribeiro, M. Verelst, J. Dexpert-Ghys, and P.C. Morais, *Hyperfine Interact.* **189**, 159–166 (2009).

44. P. Tartaj, M.P. Morales, T. Gonzalez-Carreño, S. Veintemillas-Verdaguer, and C.J. Serna, *Adv. Mater.* **23**, 5243–5249 (2011).

45. G. Salazar-Alvarez, M. Muhammed, and A.A. Zagorodni, *Chem. Eng. Sci.* **61**, 4625–4633 (2006).

46. A.-H. Lu, E.L. Salabas, and F. Schüth, *Angew. Chem., Int. Ed.* **46**, 1222–1244 (2007).

47. M. Mohapatra and S. Anand, *Int. J. Eng. Sci. Tech.* **2**, 127–146 (2010).

48. M.J. Tueros, L.A. Baum, R.A. Borzi, S.J. Stewart, R.C. Mercader, S.G. Marchetti, J.F. Bengoa, and L.V. Mogni, *Hyperfine Interact.* **148/149**, 103–108 (2003).

49. K. Wongwailikhit and S. Horwongsakul, *Mater. Lett.* **65**, 2820–2822 (2011).

50. M.F.R. Fouda, M.B. El-Kholy, S.A. Moustafa, A.I. Hussien, M.A. Wahba, and M.F. El-Shahat, *Int. J. Inorg. Chem.* **2012**, 989281 (2012).

51. T. Li, S. Li, S. Wang, Y. An, and Z. Jin, *J. Water Resour. Protect.* **01**, 16–21 (2009).

52. W. Wu, X. Xiao, S. Zhang, J. Zhou, L. Fan, F. Ren, and C. Jiang, *J. Phys. Chem. C* **114**, 16092–16103 (2010).

53. J. Xu, H. Yang, W. Fu, K. Du, Y. Sui, J. Chen, Y. Zeng, M. Li, and G. Zou, *J. Magn. Magn. Mater.* **309**, 307–311 (2007).

54. L. Suber, P. Imperatori, G. Ausanio, F. Fabbri, and H. Hofmeister, *J. Phys. Chem. B* **109**, 7103–7109 (2005).

55. C. Cannas, G. Concas, F. Congiu, A. Musinu, G. Piccaluga, and G. Spano, *Z. Naturforsch. A* **57a**, 154–158 (2002).

56. J.H. Bang and K.S. Suslick, *J. Am. Chem. Soc.* **129**, 2242–2243 (2007).

57. J. Pinkas, V. Reichlova, R. Zboril, Z. Moravec, P. Bezdicka, and J. Matejkova, *Ultrason. Sonochem.* **15**, 257–264 (2008).

58. W.W. Yu, J.C. Falkner, C.T. Yavuz, and V.L. Colvin, *Chem. Commun.* 2306–2307 (2004).

59. T. Hyeon, S.S. Lee, J. Park, Y. Chung, and H.B. Na, *J. Am. Chem. Soc.* **123**, 12798–12801 (2001).

60. Y.-P. Sun, X. Li, J. Cao, W. Zhang, and H.P. Wang, *Adv. Colloid Interface Sci.* **120**, 47–56 (2006).

61. R. Singh, V. Misra, and R.P. Singh, *J. Nanopart. Res.* **13**, 4063–4073 (2011).

62. X. Li, D.W. Elliott, and W. Zhang, *Crit. Rev. Solid State Mater. Sci.* **31**, 111–122 (2006).

63. M.A.V. Ramos, W. Yan, X. Li, B.E. Koel, and W. Zhang, *J. Phys. Chem. C* **113**, 14591–14594 (2009).

64. R. Zboril, M. Mashlan, K. Barcova, and M. Vujtek, *Hyperfine Interact.* **139/140**, 597–606 (2002).

65. K. Kluchova, R. Zboril, J. Tucek, M. Pecova, L. Zajoncova, I. Safarik, M. Mashlan, I. Markova, D. Jancik, M. Sebela, H. Bartonkova, V. Bellesi, P. Novak, and D. Petridis, *Biomaterials* **30**, 2855–2863 (2009).

66. R. Zboril, L. Machala, M. Mashlan, and V. Sharma, *Cryst. Growth Des.* **4**, 1317–1325 (2004).

67. R. Zboril, M. Mashlan, and D. Krausova, in *Mössbauer Spectroscopy in Materials Science*, edited by M. Miglierini and D. Petridis (Kluwer Academic Publishers, 1999), pp. 49–56.

68. C.R. Brundle, C.A.J. Evans, and S. Wilson, editors, *Encyclopedia of Materials Characterization: Surfaces, Interfaces, Thin Films* (Manning Publications Co., Greenwich, 1992), p. 751.

69. V.K. Pecharsky and P.Y. Zavalij, *Fundamentals of Powder Diffraction and Structural Characterization of Materials*, Second (Springer, New York, 2009), p. 744.

70. R.A. Young, editor, *The Rietveld Method. IUCr Monographs on Crystallography 5* (Oxford University Press, New York, 1995), p. 308.

71. D.B. Williams and C.B. Carter, *Transmission Electron Microscopy: A Textbook for Materials Science* (Springer, New York, 2009), p. 729.

72. P. Gabbott, editor, *Principles and Applications of Thermal Analysis*, First (Blackwell Publishing, Singapore, 2008), p. 480.

73. R.F. Egerton, *Physical Principles of Electron Microscopy: An Introduction to TEM, SEM, and AEM* (Springer, 2005), p. 202.

74. R.C. Black and F.C. Wellstood, in *The SQUID Handbook, Vol. 2*, edited by J. Clarke and A.I. Braginski (Willey-VCH Verlag GmbH & Co. KGaA, Weinheim (Germany), 2004), pp. 391–440.

75. C.D. Graham, *J. Mater. Sci. Technol.* **16**, 97–101 (2000).

76. G.C. Papaefthymiou, *Nano Today* **4**, 438–447 (2009).

77. G. Amthauer, M. Grodzicki, W. Lottermoser, and G. Redhammer, in *EMU Notes in Mineralogy, Vol. 6: Spectroscopic Methods in Mineralogy*, edited by A. Beran and E. Libowitzky (Eötvös University Press, Budapest, 2004), pp. 345–367.

78. M.D. Dyar, D.G. Agresti, M.W. Schaefer, C. a. Grant, and E.C. Sklute, *Annu. Rev. Earth Planet. Sci.* **34**, 83–125 (2006).

79. P. Gütlich, E. Bill, and A.X. Trautwein, *Mössbauer Spectroscopy and Transition Metal Chemistry: Fundamentals and Applications* (Springer-Verlag, Berlin, Heidelberg, 2011), p. 620.

80. B. Fultz and J. Howe, *Transmission Electron Microscopy and Diffractometry of Materials*, Third (Springer, Berlin, Heidelberg, New York, 2008), p. 758.

81. R. Zboril, M. Mashlan, D. Petridis, D. Krausova, and P. Pikal, *Hyperfine Interact.* **139/140**, 437–445 (2002).

82. J. Hrbac, V. Halouzka, R. Zboril, K. Papadopoulos, and T. Triantis, *Electroanalysis* **19**, 1850–1854 (2007).

83. M. Hermanek, R. Zboril, I. Medrik, J. Pechousek, and C. Gregor, *J. Am. Chem. Soc.* **129**, 10929–10936 (2007).

84. C. Wu, P. Yin, X. Zhu, C. OuYang, and Y. Xie, *J. Phys. Chem. B* **110**, 17806–17812 (2006).

85. X. Gou, G. Wang, X. Kong, D. Wexler, J. Horvat, J. Yang, and J. Park, *Chem. Eur. J.* **14**, 5996–6002 (2008).

86. L. Wang, T. Fei, Z. Lou, and T. Zhang, *ACS Appl. Mater. Interfaces* **3**, 4689–4694 (2011).

87. B. Sun, J. Horvat, H.S. Kim, W.-S. Kim, J. Ahn, and G. Wang, *J. Phys. Chem. C* **114**, 18753–18761 (2010).

88. K. Sivula, R. Zboril, F. Le Formal, R. Robert, A. Weidenkaff, J. Tucek, J. Frydrych, and M. Grätzel, *J. Am. Chem. Soc.* **132**, 7436–7444 (2010).

89. B. Koo, H. Xiong, M.D. Slater, V.B. Prakapenka, M. Balasubramanian, P. Podsiadlo, C.S. Johnson, T. Rajh, and E.V. Shevchenko, *Nano Letters* **12**, 2429–2435 (2012).

90. X. Zhu, Y. Zhu, S. Murali, M.D. Stoller, and R.S. Ruoff, *ACS Nano* **5**, 3333–3338 (2011).

91. C.-W. Lee, K.-W. Lee, and J.-S. Lee, *Mater. Lett.* **62**, 2664–2666 (2008).

92. S. Laurent and M. Mahmoudi, *Int. J. Mol. Epidemiol. Genet.* **2**, 367–390 (2011).

93. S. Laurent, S. Dutz, U.O. Häfeli, and M. Mahmoudi, *Adv. Colloid Interface Sci.* **166**, 8–23 (2011).

94. I. Šafařík and M. Šafaříková, *J. Chromatogr. B* **722**, 33–53 (1999).

95. J. Dobson, *Gene Ther.* **13**, 283–287 (2006).

96. S. Klimkova, M. Cernik, L. Lacinova, J. Filip, D. Jancik, and R. Zboril, *Chemosphere* **82**, 1178–1184 (2011).

97. X. Lv, J. Xu, G. Jiang, J. Tang, and X. Xu, *J. Colloid Interface Sci.* **369**, 460–469 (2012).

98. S.R. Kanel, J.-M. Grenèche, and H. Choi, *Environ. Sci. Technol.* **40**, 2045–2050 (2006).

99. M. Baikousi, A.B. Bourlinos, A. Douvalis, T. Bakas, D.F. Anagnostopoulos, J. Tuček, K. Šafářová, R. Zboril, and M.A. Karakassides, *Langmuir* **28**, 3918–3930 (2012).

3. Synthesis of Iron Particles by Thermal Decomposition of Natural Garnets of Almandine-Pyrope Series

3.1 Garnet

Garnet is a mineral group belonging to the orthosilicates. These minerals are important because they are considered the major rock-forming mineral and are widespread in the earth's crust and upper mantle. In petrology garnets are considered as geobarometers to interpret P-T history of rocks, which is related with the equilibrium and stability of a mineral assembly [1,2]. Garnets are valuable as gemstones, but also in industrial applications principally because of its hardness. The most important uses as abrasive in coarse and fine polishing, sand blasting, water jet cutting, and water filtration [1,3,4]; other uses are as anti-skid material, spark-plug cleaning and artificial gems [5].

3.1.1 Structure and crystal chemistry

The garnet has a cubic structure, space group $Ia\bar{3}d$ and 8 formula molecules per unit cell, with an structural formula $^{VIII}X_3{}^{VI}Y_2{}^{IV}Z_3O_{12}$; where $X = Fe^{2+}$, Mg^{2+}, Mn^{2+}, Ca^{2+}, $Y = Fe^{3+}$, Ti^{3+}, Cr^{3+}, Al^{3+} and $Z = Si^{4+}$, the superscript roman numbers indicate the coordination number for each particular site [2,6,7]. Each cation in the sites *X*, *Y* or *Z*, occupies a specific position in the garnet lattice as specified in table 3.1. In the case of the aluminosilicates, the formula is reduced to $X_3Al_2Si_3O_{12}$ where *X* is replaced by divalent cations (Fe, Mg, Mn, or Ca). The garnet structure can be considered as an array of polyhedra as following: SiO_4 tetrahedra, AlO_6 octahedra, which are connected from the corners as can be seen in Fig. 3.1; the spaces between those polyhedra form dodecahedra XO_8, which is linked to the other polyhedra not only by corners, but also by edges [2,6,8]. The occupancy of the sites depends on the cation sizes, *i.e.* their ionic radii (Mg 0.92 Å, Fe^{2+} 0.92 Å, Mn^{2+} 0.96 Å, and Ca 1.12 Å), and the electrical neutrality when the sum of the oxidation states of all cations gives 24.

Table 3.1 Crystallographic properties for garnet $X_3Y_2Z_3O_{12}$ with space group $Ia\bar{3}d$ [2].

Site	Point symmetry	Atomic coordinates			Site coordination	Wyckoff position
X	222	1/8	0	1/4	8	24c
Y	$\bar{3}$	0	0	0	6	16a
Z	$\bar{4}$	3/8	0	1/4	4	24d
O	1	*x*	*y*	*z*	4	96h

The garnet minerals are rarely found pure, instead they appear forming series between the end-members (table 3.2), for example: almandine-pyrope, almandine-spessartine or almandine-grossular. Intermediate compositions in the series are known as solid solutions, and is possible to write the crystallochemical formula $(Fe^{2+},Mg^{2+},Mn^{2+},Ca^{2+})_3(Fe^{3+},Ti^{3+}Cr^{3+},Al^{3+})_2Si_3O_{12}$, where the atoms per formula unit (*apfu*) of each element is variable, given a total sum of three for dodecahedral sites ($\Sigma X = 3$) and two for octahedral sites ($\Sigma Y = 2$). Other interesting garnets are the andradite ($Ca_3Fe_2Si_3O_{12}$) and the hydrogrossular ($Ca_3Al_2(SiO_4)_{3-x}(OH)_{4x}$).

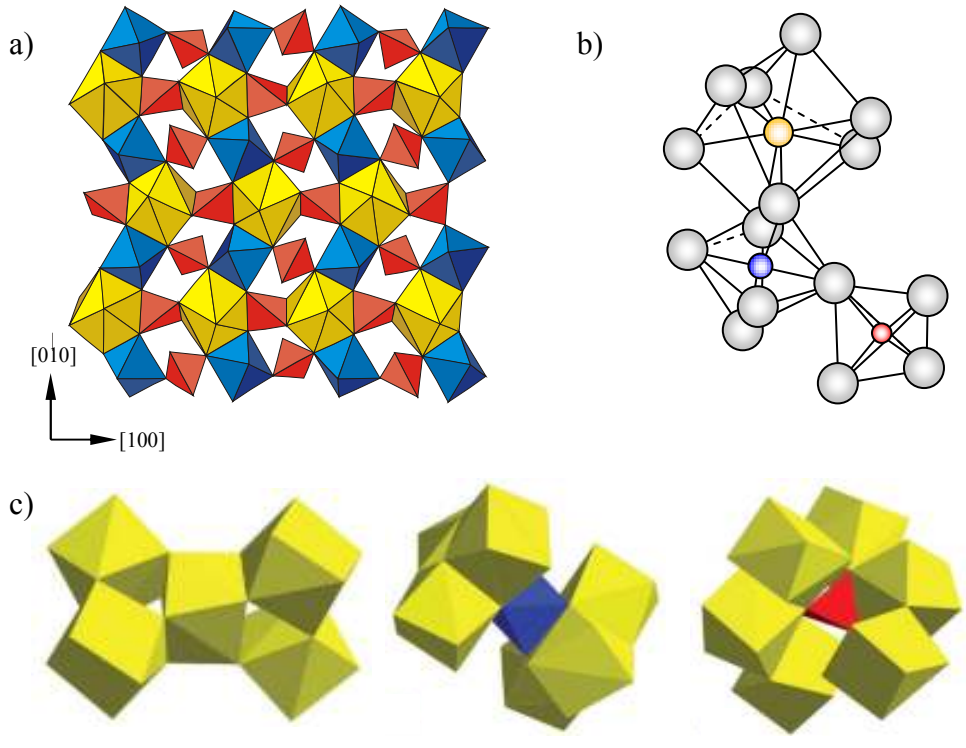

Figure 3.1 Crystalline structure of garnet: a) polyhedral model showing the three coordination polyhedra and their linkages, b) basic polyhedra in the unit cell, c) structural relationship between polyhedra. XO_8 dodecahedron (yellow), AlO_6 octahedron (blue), and SiO_4 tetrahedron (red) [2,8,9].

Table 3.2 End-members of garnet group minerals.

End-Member	Composition	Unit Cell Size a (Å)**
Pyrope (Prp*)	$Mg_3Al_2Si_3O_{12}$	11.459
Almandine (Alm*)	$Fe_3Al_2Si_3O_{12}$	11.526
Spessartine (Sps*)	$Mn_3Al_2Si_3O_{12}$	11.621
Grossular (Grs*)	$Ca_3Al_2Si_3O_{12}$	11.851

* Abbreviations according to Whitney and Evans[10].
** Cell values for synthetic end-members[11].

3.1.2 Polyhedral distortions

According to the polyhedral model the garnet structure can be described as a 3D corner-sharing network conformed by SiO_4 tetrahedra alternating with AlO_8 octahedra, the spaces between them form triangular dodecahedra XO_8 (Fig. 3.1, table 3.3). Consequently, any substitution of cations in the lattice can lead to polyhedral distortions and thus change the lattice constant of the pure end-members [9,12]. Thus, the distortions and rotations inside of the garnet structure are a result of combined factors: X-site cation size, bonding, and internal vibrations [2,12].

The structure adjusts to accommodate cations with different sizes as Ca (1.12 Å) and Mg (0.89 Å), mainly by changes of framework bond angles rather than bond lengths [13]. The inclusion of Ca^{2+} cation in the X-site of Alm-Prp garnet unstabilize its structure, because this cation is not only bigger than Fe^{2+} (0.92 Å) and Mg^{2+} cations, but less massive [12]. Then, to accommodate the shorter bonds, the distortions of the framework are larger in pyrope than in grossular, also the degree of distortion of SiO_4 tetrahedra is less when the adjacent cations are Ca than Mg [13,14].

Table 3.3 Linkages of the polyhedra in the garnet structure [2,6].

Polyhedron	Linkage
Tetrahedron	4 corners with octahedra 4 corners with dodecahedra 2 edges with dodecahedra
Octahedron	6 corners with tetrahedra 6 edges with dodecahedra
Dodecahedron	4 corners with tetrahedra 2 edges with tetrahedra 4 edges with octahedra 4 edges with dodecahedra

The degree of tetrahedral rotation (α) is bigger when the size of X-site cation decreases [6,7,12,15]. The presence of Ca^{2+} cation (> 20%) in the X-site of pyrope causes the deviation of the linear relationship between the angle of tetrahedral rotation and the size of X-site cation. The molar volume increases almost linearly with the mole fraction of iron Fe/(Fe+Mg) and manganese Mn/(Mn+Fe) for the Alm-Prp and Sps-Alm series respectively [12]. Another consequence of the decreasing of α is the increasing of the size of dodecahedra [7].

The temperature is another factor causing distortions in the garnet structure, due mainly to the rotation of tetrahedra and the thermal expansion of the lattice. Temperature effect has been studied in pyrope and grossular by Meagher *et al.* [7]. There is almost no increase of the Si-O bond in pyrope up to 750 °C, but there is a rotation around the $\bar{4}$ axis and the positional angle (tetrahedral rotation) slightly decrease, the dodecahedra edges increase, while the octahedra is barely distorted. In grossular the opposite occurs, there is a slight increase of the Si-O length, and no tetrahedral rotation [7,15]. For almandine there is an increase of the cell dimension and small distortion of the octahedron [15].

In octahedron AlO_6 there are shared corners with dodecahedra and unshared edges. In pyrope the unshared edge is longer than the shared edge at 25 °C, both edges increase with temperature, but not at the same rate, where the shared edge has a bigger expansion. In grossular the shared edge is longer than the unshared edge at 25 °C, both edges increase with temperature at the same rate [7]. On the other hand, the tetrahedral edges shared with dodecahedra are shorter than the unshared edges [13].

3.1.3 Physical properties

Pyralspite garnets (Alm, Prp, Sps) are mostly isotropic, where only spessartine shows a weak anisotropism. They present many colors varying from wine-red to reddish brown, having a vitreous luster, white streak, specific gravity between 3.5 – 4.3, refraction index between 1.71 – 1.83, molar volume between 113 – 118 cm^3/mol, and hardness between 6½ – 7 according to the Moss scale [1,11]. Romano *et al.* [16] studied the variation of the electrical conductivity of almandine-pyrope series with their composition, temperature and pressure. They found that there is an increase of the electrical conductivity with the increase of iron cations in dodecahedral sites, but also the

decrease of this effect with the increase of temperature. Heat capacity in pyralspite garnets vary between 325.3 – 342.8 J/mol.K at 298 K [17], in general with temperature the heat capacity follows a non-linear function $C_p = a – b.T^{-0.5} – c.T^{-2} + c.T^{-3}$ according to Bosenik *et al.* [18].

Magnetic properties of Alm-Prp garnets have been studied basically in almandine, using Mössbauer spectroscopy, magnetization measurements [19], and lately theoretical electronic structural calculations [20]. The paramagnetic suceptibilities of garnets from Alm-Prp series follow the Curie-Weiss law, excluding samples near to pyrope end-member [19]. The Néel temperature (T_N) determined by magnetization measurements varies with the garnet composition (T_N: 10 K for Alm_{100}, 6.7 K for Alm_{67}, and 3.6 K for Alm_{46}). T_N decreases with the increase of Mg ions in dodecahedral sites, thus decreasing the number of superexchange interactions Fe-O-Fe [19]. According to recent studies [20], almandine has two magnetic sub-lattice, which are identical but with opposite orientation of iron spins and the magnetic interaction between then is weakly antiferromagnetic, while each sub-lattice have a ferromagnetic behavior because of Fe-O-Fe interactions.

3.1.4 Point of view from Mössbauer spectroscopy

The Mössbauer parameters, isomer shift (IS) and quadrupole splitting (QS), for ferrous iron in dodecahedral have only small variations as is shown in table 3.4. The large IS and QS values of ferrous iron in dodecahedral sites has been interpreted as an indicator of high degree of ionic bonding, where the Fe^{2+} cation is in the high-spin state (HS). The quadrupole splitting is also one of the highest for ferrous iron [2,21]. The IS value of Fe^{2+} at dodecahedral sites has almost not variation that suggest that Fe-O bond-lengths are nearly the same, without consider the site occupancy [2,21,22]. The hyperfine values for Fe^{3+} are ascribed to a HS cation in octahedral coordination. The QS increases with the increment of octahedra distortions, and it has a negligible dependence on temperature [21].

Almandine spectrum at room temperature has a slightly asymmetric quadrupole split doublet, with almost not variation of IS and QS for different garnet composition. A decreasing of IS and QS is observed with rising temperature in Mössbauer spectra of almandine. At low temperatures the asymmetry is reduced, and the spectrum splits showing two eight-line subspectra indicating the presence of two magnetic sites, where the magnetic order in almandine starts between 9.6 and 10.4 K [2,23].

In Alm-Sps and Alm-Prp series, it is observed an asymmetric doublet, related to the variations in Fe^{2+} vibrational behaviour (*i.e.* recoil-free fraction) as a function of garnet bulk composition, while Alm-Grs series has more symmetric doublets [2,24]. The peak asymmetry of the doublet can be caused by: a) preference in the crystal orientations (texture effect), b) anisotropic recoilless fraction (Goldanskii-Karyagin effect), and c) paramagnetic relaxation (spin-spin). Causes (a) and (b) are excluded because of the poor cleavage and cubic lattice of garnet. From the reduced asymmetry in the peak intensities at low temperatures, the asymmetry is due to spin-spin relaxation [21–23].

Prp-Alm is the only garnet series that presents Fe^{3+} in its structure, which increase with the pyrope content [12]. There is not a noticeable dependence of the IS and QS with the Mg^{2+} content in the garnet X-site [22].

Because of the sensibility of the Mössbauer spectroscopy to notice the change of electronic environment of the cations, it was also used to study the oxidation of ferrous cations inside of the garnet structure [25], not only at room temperature [26], but even to monitor its thermal decomposition [27].

Table 3.4 Hyperfine parameters from Mössbauer spectra for silicate garnets at room temperature (modified from [21]).

Cation	Position	Isomer shift (mm/s)	Quadrupole splitting (mm/s)
Fe^{2+}	24 c (dodec.)	1.20 – 1.39	3.47 – 3.70
Fe^{2+}	24 d (tetr.)	0.68 – 0.79	1.53 – 1.99
Fe^{3+}	16 a (oct.)	0.35 – 0.45	0.29 – 0.75
Fe^{3+}	24 d (tetr.)	0.04 – 0.20	1.05 – 1.28

3.1.5 Thermal behavior at high temperatures

With the increasing of temperature, the structure of garnets starts to expand, and up to 1400 K (1127 °C) the volumetric expansion reach the 3 %. The thermal expansion coefficients for almandine and pyrope have been determined by Thiéblot *et al.* [28] as 3.3×10^{-5} K^{-1} (Alm), and 3.0×10^{-5} K^{-1} (Prp). Not only structure expansion occurs at high temperature, also there are rotations of SiO_4 tetrahedra inside the garnet structure, which are expressed by the variation of the positional angle (γ). The tetrahedron rotation modifies the polyhedral edges of AlO_6 octahedra and XO_8 dodecahedra, as a consequence the Al-O and X-O lengths increase, and the octahedron shared edges increase more than the unshared edges [7].

At temperatures higher than 1000 °C the garnets decompose [28], but it was also reported the decomposition at temperature as low as 750 °C [27]. The thermal decomposition temperature and the decomposition products strongly depend on the chemical composition of garnet. Other factors affecting the decomposition are the kind of atmosphere (inert, oxidant, reductive), the heating regime (dynamic or isothermal) [29,30], high pressure [31].

One of the oldest studies about thermal decomposition of natural garnets was done by Schairer and Yagi [32]. In a close system almandine decomposes into hercynite, Fe-cordierite and fayalite if it is heated between 750 °C and 1050 °C during several days. Experiments under inert atmosphere (N_2) at 1000 °C on samples of mixed composition ($Alm_xPrp_ySps_zGrs_w$) with variable percentage of almandine ($Alm_{91.3}$, $Alm_{69.6}$, and Alm_{40}) were also carried out. After 72 hours the garnets were totally decomposed, Fe-cordierite and fayalite along with melting were identified as decomposition products of garnet with composition close to pure almandine ($Alm_{91.3}$); for the garnet with intermediate composition ($Alm_{69.9}$) the products were olivine, cordierite and spinel, while for (Mg,Ca)-rich garnet (Alm_{40}) Mg-cordierite, clinopyroxene and spinel.

Other studies about thermal decomposition of garnet (almandine) were done under high pressures [31,33,34]. The synthesis of almandine from a mixture of magnetite, quartz, and kyanite at high temperatures (650 – 900 °C) under a pressures greater than 28.5 kbar was described by Harlov and Newton [33]. The reversibility of this process was considered by Anovitz *et al.* [31]; they suggested that in equilibrium almandine decomposes in hercynite, fayalite, and quartz or Fe-cordierite depending on the applied pressure. The oxidation mechanism of almandine was also studied, and depending of the applied pressure it was decomposed in magnetite, quartz and sillimanite or hercynite [31], this reaction also occurs under high oxidation conditions [35]. Under pressures lower than 3.5 kbar and temperatures between 780–1088 °C, almandine decomposes into fayalite, Fe-cordierite and hercynite [34]. Under atmospheric pressure, almandine was decomposed into hematite, sillimanite, and cristobalite [28]. However, studies using Mössbauer spectroscopy [27,36] had shown that hematite is not the original decomposition product of almandine (temperature > 750 °C) but maghemite (γ-Fe_2O_3), which suffers two transformations, first to ε-Fe_2O_3 and second to hematite (α-Fe_2O_3).

Garnets of pyrope-almandine solid solution heated up to 1200 °C in air decompose into spinel ($Mg(Al,Fe^{3+})_2O_4$), anorthite and enstatite when they have composition close to pyrope, while cordierite, anorthite and spinel or maghemite were

detected after the decomposition of garnet of almandine-pyrope intermediate composition [30]. When the chemical composition of garnet is close to ideal end-member pyrope is heated in air, it decomposes into corundum and enstatite [28], while pyrope with some Fe^{2+} in dodecahedral sites decomposes primarily into hematite, enstatite, Fe-spinel, and cristobalite; in this case hematite is also a product of subsequent oxidation of enstatite at high temperature [29].

3.2 Materials and Methods

3.2.1 Preparation of garnet samples

The colours of the garnets used in this study vary from brownish-red and red for garnets compositions near to end-member almandine and pyrope respectively, all crystals were almost free of impurities, transparent, and looking slightly coloured under optical microscope.

Electron microprobe analysis (EMPA) was done on starting garnet samples, in order to know its chemical composition. The averaged results of EMPA analysis (see appendix 1) lead to a crystallochemical formula normalized to twelve oxygen atoms per formula unit, and ignoring the minor components in the structure (Table 3.5).

Under the optical microscopy were selected small pieces of garnet crystal free of impurities, then the pieces were ground in an agate mortar under isopropyl alcohol and air dried at room temperature. The samples were labelled as $Alm_{20}Prp_{80}$, $Alm_{64}Prp_{36}$, $Alm_{82}Prp_{18}$, $Alm_{96}Prp_{4}$, and $Alm_{65}Sps_{35}$ (Table 3.5).

Table 3.5 Crystallochemical formulas of garnets with cations normalized to 12 oxygens.

Sample	Crystallochemical formula
$Alm_{96}Prp_{4}$	$(Fe_{2.85}Mg_{0.15})(Al_{1.99})Si_{2.99}O_{12}$
$Alm_{82}Prp_{18}$	$(Fe_{2.34}Mg_{0.51}Mn_{0.11}Ca_{0.06})(Al_{2.00})Si_{2.97}O_{12}$
$Alm_{64}Prp_{36}$	$(Fe_{1.87}Mg_{1.04}Ca_{0.09})(Al_{1.99})Si_{2.98}O_{12}$
$Alm_{20}Prp_{80}$	$(Fe_{0.47}Mg_{2.22}Ca_{0.33})(Cr_{0.11}Fe_{0.07}Al_{1.81})Si_{2.98}O_{12}$
$Alm_{65}Sps_{35}$	$(Fe_{1.95}Mn_{1.09})(Al_{1.99})Si_{2.94}O_{12}$

3.2.2 Characterization of samples

Both thermogravimetric analysis (TG) and differential scanning calorimetry (DSC) were carried out in a simultaneous thermal analyzer (STA 449 C Jupiter, Netzsch), coupled to mass spectrometer (QMS 403 Aëolos, Netzch) for evolved gas analysis (EGA). The samples were individually heated from room temperature up to chosen temperatures (see table 3.6), under reducing atmosphere of forming gas (H_2 10%, N_2 90%) with a heating rate of 10 K/min in open alumina crucible. After the chosen temperature was reached, the samples were cooling down to room temperature under inert atmosphere of argon, with a heating rate of -40 K/min. The samples resulting of the heating process were labelled according to the temperature of heating, for example: $Alm_{20}Prp_{80}$-1200, $Alm_{64}Prp_{36}$-1200, $Alm_{82}Prp_{18}$-1200, $Alm_{96}Prp_{4}$-1200, and $Alm_{65}Sps_{35}$-1200.

Table 3.6 Temperatures of heating of garnet samples during the TG/DSC analysis.

Sample	Temperature of heating
$Alm_{96}Prp_{4}$	950 °C, 1170 °C, 1200 °C
$Alm_{82}Prp_{18}$	1100 °C, 1115 °C, 1130 °C, 1200 °C
$Alm_{64}Prp_{36}$	1125 °C, 1150 °C, 1180 °C, 1200 °C
$Alm_{20}Prp_{80}$	1000 °C, 1100 °C, 1125 °C, 1200 °C
$Alm_{65}Sps_{35}$	1120 °C, 1140 °C, 1150 °C, 1200 °C

X-ray powder diffraction (XRD) and Mössbauer spectroscopy were used to identify the present phases in all samples, before and after dynamic thermal treatment. XRD patterns were recorded at room temperature using a diffractometer X'Pert PRO MPD (PANalytical) with Co-K_α radiation and step size of 0.017° in the Bragg-Brentano geometry. The identification of crystalline phases in experimental XRD patterns was done using the X'Pert High Score Plus software with PDF-4 database. After phase identification the diffractograms were analyzed using PANalytical HighScore Plus software to perform quantitative Rietveld analysis.

Mössbauer spectra of 1024 channels were collected at room temperature (RT) using a Mössbauer spectrometer in constant acceleration regime with a ^{57}Co(Rh) source. The isomer shift values were calibrated with respect to α-Fe foil, and CONFIT software was used to fit the spectra.

Scanning electron microscopy (SEM) was performed on each sample prepared by thermal heating to study its morphology. The images were obtained using a scanning electron microscope Hitachi SU-6600, with 3 kV secondary electron image.

X-ray diffraction *in-situ* was carried out only in sample $Alm_{20}Prp_{80}$ to monitor the very beginning products of the decomposition reaction. The equipment used for the XRD analysis is a PANalytical X'Pert PRO MPD diffractometer (CoK_α radiation) equipped with Anton Paar HTK-16 reaction chamber. The geometry of the diffractometer is a Bragg-Brentano with 0.01° step size and the angular range of measurements was from 15° to 85°. The collection time of every diffractogram was around 45 min with a sampling time 0.30 s/step. The pyrope powder sample was mixed with ethanol, then the resultant paste was placed directly on a platinum holder filling its central cavity that has 0.1 mm deep, and after the holder was placed inside of the reactor chamber. The heating and cooling rates were 10 °C/min and -100 °C/min respectively with a temperature range from 500 to 1200 °C, the diffractograms were collected every 50 °C until was reached 1050 °C, after this temperature the collection was every 10 °C in order to see in more detail the evolution of the formed products after the decomposition onset. The measurements were performed under forming gas atmosphere. The quantitative Rietveld analysis of the resultant XRD patterns was done using PANalytical HighScore Plus software.

3.3 Results

3.3.1 XRD and MS spectra for starting samples of garnet

Starting samples were characterized by XRD and Mössbauer spectroscopy (MS). All XRD diffractograms (Fig. 3.2, left side) show almost the same profile for garnet structure, the only difference between them are the intensities of the lines situated on the called "identification regions" [37], *i.e.* 2θ(CoK_α) ranging from 41° to 48°, and 2θ(CoK_α) ranging from 63° to 73°.

Mössbauer spectra taken at room temperature (Fig. 3.2, right side) were fitted with one doublet, which have Mössbauer parameters characteristic of garnet *i.e.* isomer shift (IS): 1.28 – 1.30 mm/s and quadrupole splitting (QS): 3.52 – 3.55 mm/s [21,24]. An exception, were spectra of samples $Alm_{20}Prp_{80}$ and $Alm_{96}Prp_4$, which were fitted with two doublets and three doublets respectively. All samples were free of impurities, only

$Alm_{96}Prp_4$ presented a small amount of ilmenite (~ 4%, according to the doublet area), that is a common inclusion in garnets [38]. The doublets for Fe^{2+}, presented certain degree of asymmetry, being this more visible in spectrum of sample $Alm_{20}Prp_{80}$, which has less quantity of iron.

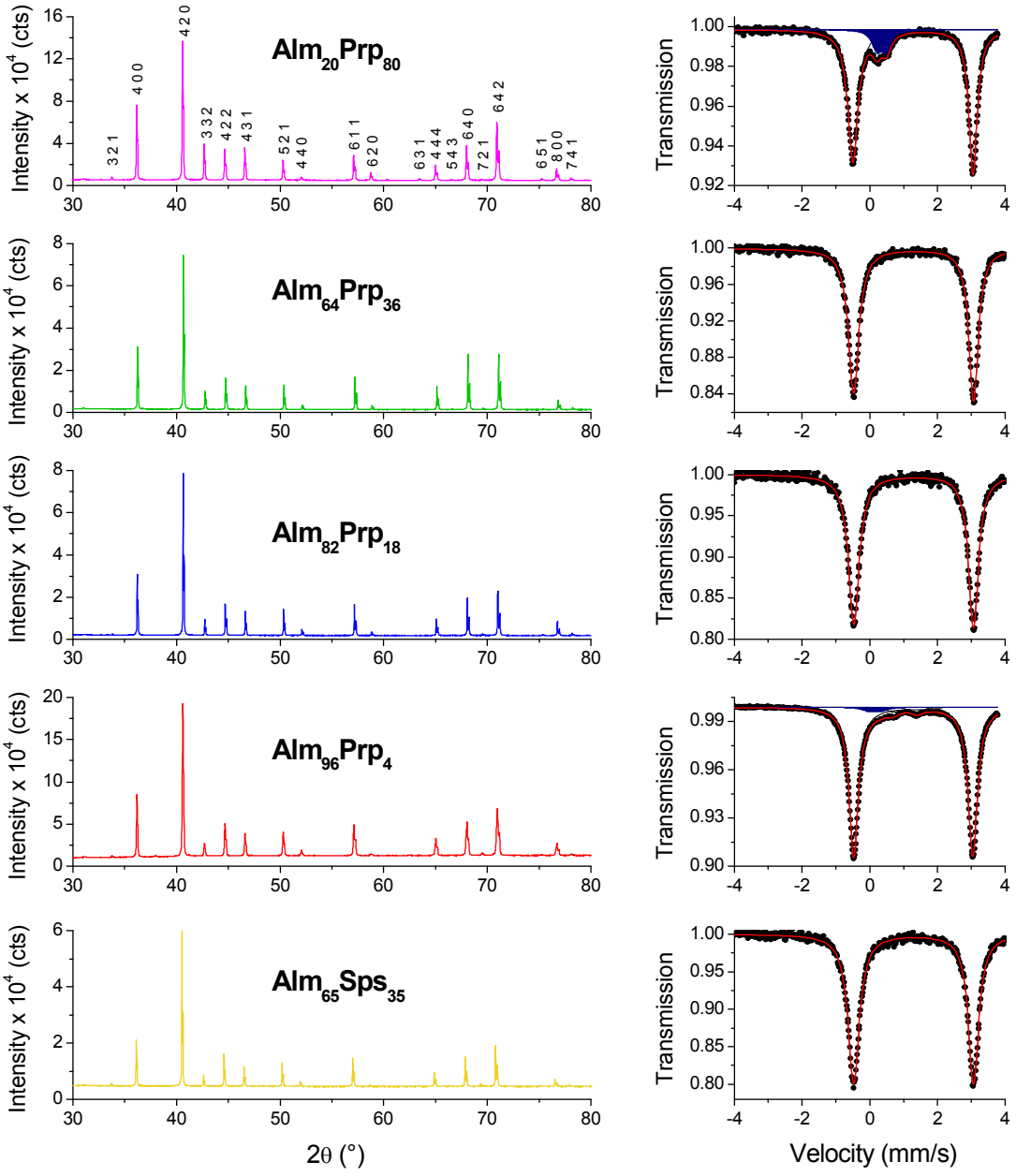

Figure 3.2 XRD patterns (left) and room temperature Mössbauer spectra (right) of natural garnets without any previous thermal treatment. The dark blue shaded doublets in Mössbauer spectra are assigned to Fe^{3+} ions.

3.3.2 Thermal analysis: TG and DSC

According to TG and evolved gases analysis (EGA) (see appendix 2), all studied samples showed a small release of water before thermal decomposition, in most of the cases there were water inclusions in the crystalline garnet or moisture of the sample. Only in the case of almandine ($Alm_{96}Prp_4$) a fraction of the released water corresponded to the thermal decomposition of impurities (ilmenite). The thermal decomposition of garnets in reducing atmosphere starts normally above 1000 °C.

TG curves (see appendix 2) show evident decreases of mass after the beginning of thermal decomposition, they seem to be a "one-step" process, with exception of $Alm_{20}Prp_{80}$ that shows two-steps. The mass loss at the end of TG analysis is different for each garnet (Table 3.7).

DSC analysis (Fig. 3.3) shows clearly endothermic peaks indicating the decomposition process of the garnet. With exception of pyrope, all garnets presented one endothermic peak at temperatures greater than 1000 °C and less than 1200 °C. From these peaks was possible to calculate the beginning temperature of thermal decomposition, *i.e.* the onset temperature for each garnet (Table 3.7).

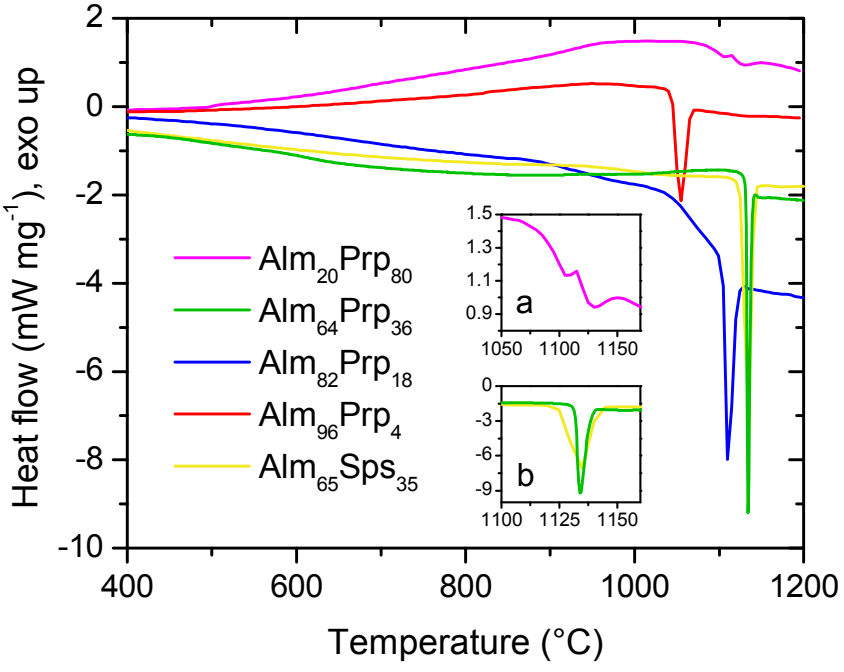

Figure 3.3 DSC heating curves of the studied natural garnets, showing the endothermic peaks of decomposition. Insets: a) closer view of the endothermic effects of $Alm_{96}Prp_4$, b) closer view of the curve for garnets $Alm_{64}Prp_{36}$ and $Alm_{65}Sps_{35}$.

Table 3.7 Onset temperatures and mass decrease of garnets with different contents of iron in X-site. The values in parentheses are the standard deviation.

Sample	X[Fe] (apfu)	Onset (°C)	Δm (wt. %)
$Alm_{20}Prp_{80}$	0.465(05)	1087	-0.69
$Alm_{64}Prp_{36}$	1.864(16)	1131	-4.33
$Alm_{82}Prp_{18}$	2.339(11)	1103	-2.00
$Alm_{96}Prp_{4}$	2.845(11)	1045	-3.51
$Alm_{65}Sps_{35}$	1.946(88)	1125	-1.34

apfu: atoms per formula unit.

3.3.3 Phase composition: XRD and MS

XRD patterns of the samples after heating up to 1200 °C show different phase compositions (Fig. 3.4), despite the all garnets had the same structure prior heating. Even so, there are common phases present between the garnet decomposition products as metallic iron and Fe-spinel ($(Fe,Mg)Al_2O_4$). Fe-cordierite (Fe-Crd) is also observed for almost all garnets with exception of the one with composition close to pyrope ($Alm_{20}Prp_{80}$) and the other one presenting a percentage of spessartine ($Alm_{65}Sps_{35}$). The other identified decomposition products were cristobalite (SiO_2), olivine (fayalite Fe_2SiO_4 or tephroite Mn_2SiO_4), Fe-cordierite ($(Fe,Mg)_2Al_4Si_5O_{18}$), pyroxene (enstatite $(Mg,Fe)SiO_3$ or pigeonite $((Mg,Fe^{2+},Ca)(Mg,Fe^{2+})Si_2O_6$), and anorthite ($CaAl_2Si_2O_8$) depending on chemical composition of starting garnet (all phases are usually well crystallized). Anorthite and pigeonite are present only if there is Ca in the dodecahedral site of the garnet structure.

The Fe-bearing phases present in the phase composition of decomposed garnets were analysed by Mössbauer spectroscopy. The spectra (Fig. 3.5) confirm the presence of metallic iron and Fe-spinel for all decomposed garnets. Cordierite, enstatite, pigeonite, and fayalite were clearly identified; even thephroite phase was identified for $Alm_{65}Sps_{35}$ garnet that was not seen in the XRD pattern. The subspectrum area of metallic iron does not show any correlation between the initial amount of iron cations in the starting garnet.

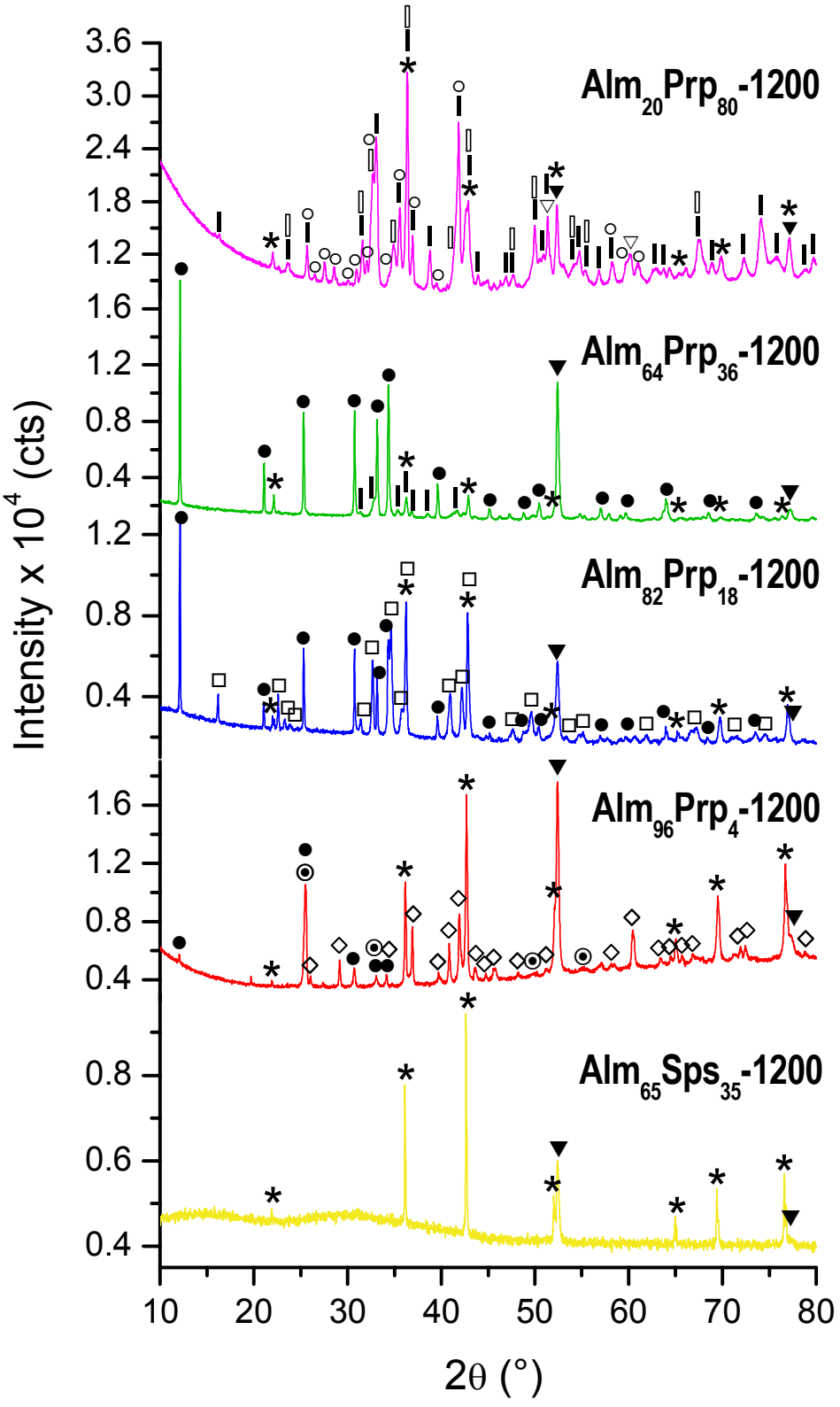

Figure 3.4 XRD patterns showing the decomposition products of garnets after heating up to 1200 °C in reducing atmosphere. The symbols indicate the identified phases: Enstatite (|), clino-enstatite (▯), cordierite (●), hercynite-spinel (★), alpha iron (▼), gamma iron (▽), anorthite (○), pigeonite (□), fayalite (◇), and cristobalite (⦿).

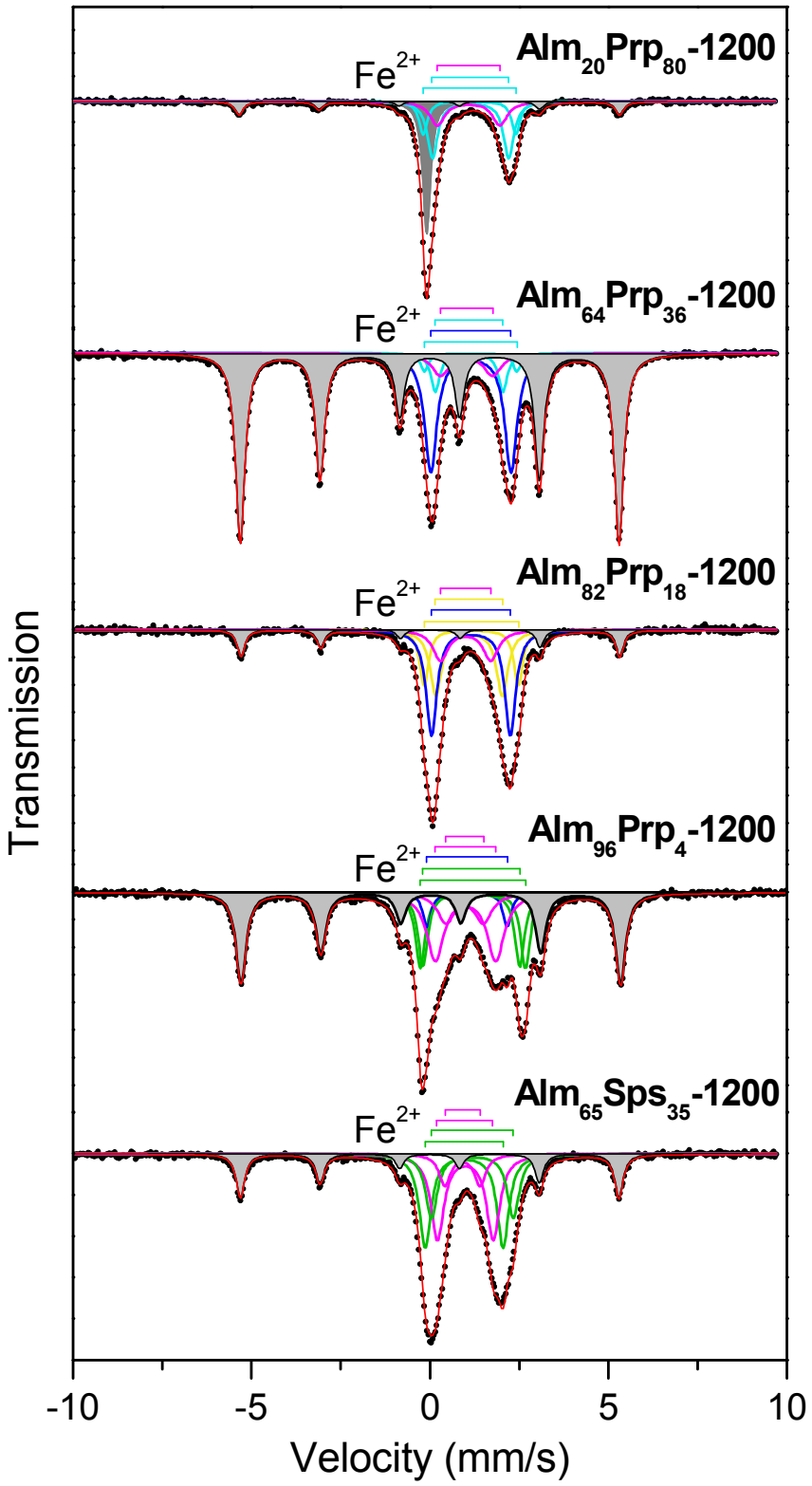

Figure 3.5 MS spectra at room temperature of garnets heated up to 1200 °C. Shadowed sub-spectra correspond to α-Fe (light grey) and γ-Fe (dark grey). Doublets correspond to the other identified phases in each sample: Hercynite-spinel (—), Fe-enstatite (—), cordierite (—), pigeonite (—), and olivine (—).

3.3.4 Samples morphology: SEM

According to SEM images, the surface of samples of garnets heated up to 1200 °C is not smooth, it is non-homogeneous and coarse. It is conformed by irregular particles forming an amalgam, and more regular small particles randomly distributed on the surface of the mineral amalgam. The more regular particles were identified by EDS as metallic iron (see appendix 6). One exception of the observed morphology is the sample $Alm_{65}Sps_{35}$-1200, which looks like more as a smooth glass with fragments with the same composition on its surface. No regular iron particles were observed in this sample, even when the iron presence is proved by XRD and MS.

In sample $Alm_{96}Prp_4$-1200, the mineral amalgam is composed by hercynite, fayalite, cristobalite and Fe-cordierite. In the amalgam were observed very well crystallized cubic particles that are likely to be hercynite, according to the elemental analysis. Sample $Alm_{82}Prp_{18}$-1200, present a very well crystallized particles with regular octahedron shapes, which are most probably hercynite. The other components of the mineral amalgam are cordierite and pigeonite.

Samples $Alm_{64}Prp_{36}$-1200 and $Alm_{20}Prp_{80}$-1200, present a very similar surface, but the composition of the mineral amalgam varies. For sample $Alm_{64}Prp_{36}$-1200 the composition is enstatite, cordierite, and hercynite; and for sample $Alm_{20}Prp_{80}$-1200 is enstatite, anorthite, and spinel. In sample $Alm_{20}Prp_{80}$-1200 there is a presence of Cr, as observed from EDS analysis (appendix 6), which is likely to be allocated into the octahedral sites of the spinel structure.

3.4 Discussion of Results

3.4.1 Thermal behavior of garnets before thermal decomposition

Under atmospheric pressure, the garnets usually decompose at high temperatures above 1000 °C, and according to Thiéblot *et al.* [28] the garnet with the most stable structure is pyrope (onset temperature 1267 °C). It was described also a thermal expansion before decomposition, the expansion results from dilation of Al-O and M-O bonds. Also the Si-O bonds expand at higher temperatures enhancing the distortion of SiO_4 tetrahedron [28]. Another common characteristic is the water release below 300 °C, principally due to the moisture absorbed from the environment, water release at higher

temperatures correspond to chemical reactions or presence of structural water inside of the garnet structure (see appendix 2). The water release was less than -0.5 % of the initial mass of the analyzed garnets.

With exception of the garnet with composition closer to almandine ($Alm_{96}Prp_4$), the others were found to be free of impurities. From XRD patterns of $Alm_{96}Prp_4$, it is possible to see the structure of garnets remains until 950 °C, and also iron (~ 1 %) and titanium dioxide phase (< 1 %). Fe and TiO_2 are supposed to come from decomposition of ilmenite inclusion in almandine [39]. All the other garnets show the stability of the garnet structure before the onset of thermal decomposition, as can be seen from their XRD patterns (see appendix 3). From Mössbauer spectra (Fig. 3.2), the only two samples presenting ferric iron were $Alm_{96}Prp_4$ and $Alm_{20}Prp_{80}$.

The predominant doublet in Mössbauer spectra at room temperature (Fig. 3.2) was ascribed to Fe^{2+} in dodecahedral site, where there is not a big difference of the Mössbauer parameters for garnet samples with different composition. After heating the garnet samples at temperatures below the decomposition temperature, and even at the beginning of the decomposition (only in samples $Alm_{82}Prp_{18}$ and $Alm_{20}Prp_{80}$), there are only slight variations in the values of IS and QS. The reason for the witnessed small variations could be due to a disorder on dodecahedral sites during the heating, which remain after the fast cooling to room temperature of samples prior to Mössbauer measurements [15], also it must be considered that the presence of Ca and Mn in dodecahedral sites, in some samples, could cause distortions or short range strain inside the garnet lattice [7].

In the case of the sample with ilmenite impurity, before heating the sample the Mössbauer spectrum shows two doublets for ilmenite, one for Fe^{2+} and other for Fe^{3+}, both with IS and QS values in the range of published values [40]. The wider doublet disappears in the heated sample, because of decomposition of ilmenite in titanium dioxide and metallic iron, the last component is seen in the spectrum as a magnetic sextet. The other small doublet corresponding to ferric iron, is then assigned to almandine, because is the only structure that remains unchanged. Comparing the areas of the ferric iron doublet for the non-heated sample (2.9 %) and sample heated at 950 °C (4.2 %), they are in the range of its fitting error, and because of that they are almost the same. In conclusion the ferric iron in the starting sample belongs only to almandine, and not to ilmenite.

For sample with composition close to pyrope ($Alm_{20}Prp_{80}$), it is possible to observe the gradual reduction of ferric to ferrous iron according to the results of the

fitting of Mössbauer spectra (see appendices 6 and 7), but when the decomposition starts the doublet for Fe^{3+} disappears indicating that all ferric iron was reduced.

3.4.2 Variation of onset temperature with iron content in garnet

The observed decomposition temperature, determined from differential scanning calorimetry and themogravimetry, is greater than 1000 °C in all cases. An exception is decomposition of garnet with composition close to pyrope ($Alm_{20}Prp_{80}$), which is represented by two weak endothermal effects instead of one strong endothermal effect as in the case of other garnets (Fig. 3.3).

Onset temperature of decomposition from Prp-Alm series shows a negative linear tendency with the increase of iron content in dodecahedral sites of garnet (Fig. 3.6), the same applies to the garnet $Alm_{65}Sps_{35}$. However, sample with the least content of iron ($Alm_{20}Prp_{80}$) does not follow this tendency; instead of that it has a lower onset temperature than garnets of intermediate composition, and around 40 °C greater than for almost pure almandine ($Alm_{96}Prp_4$). Also this sample $Alm_{20}Prp_{80}$ shows a slower decomposition rate than the other samples.

For a better possible explanation of the apparently anomalous thermal behaviour of $Alm_{20}Prp_{80}$, we can assume that garnet structure is build of a polyhedral framework, dodecahedra (XO_8), octahedra (YO_6), tetrahedra (SiO_4) and between them dodecahedral spaces. Because of the larger number of shared polyhedral edges in the garnet structure, the substitution of different X cations at the dodecahedral site produces distortion in all polyhedral. These distortions can cause the increasing of instability of the garnet lattice at high temperatures, and then as a consequence they are decomposed at different temperatures.

The lowest temperature of decomposition is seen for the garnet with composition close to almandine, and this mainly because of the iron reduction. In contrast, the garnet with composition close to pyrope, presents not only Fe^{3+} and Cr^{3+} in octahedral sites, but also Ca^{2+} in dodecahedral sites, which increase the instability of the lattice at high temperatures. The ferric ions reduce to ferrous ions, but apparently they do not remain in the same octahedral site, because there were not evidence of this in Mössbauer spectra, where is not possible to find a doublet assigned to Fe^{2+} in octahedral site. The other cause of instability is the difference of sizes between cations Ca^{2+} (1.12 Å), Fe^{2+} (0.92 Å), and

Mg^{2+} (0.89 Å), which increase the strain and distortion of the garnet lattice, affecting not only the dodecahedral sites, but also the octahedral and even tetrahedral sites [14].

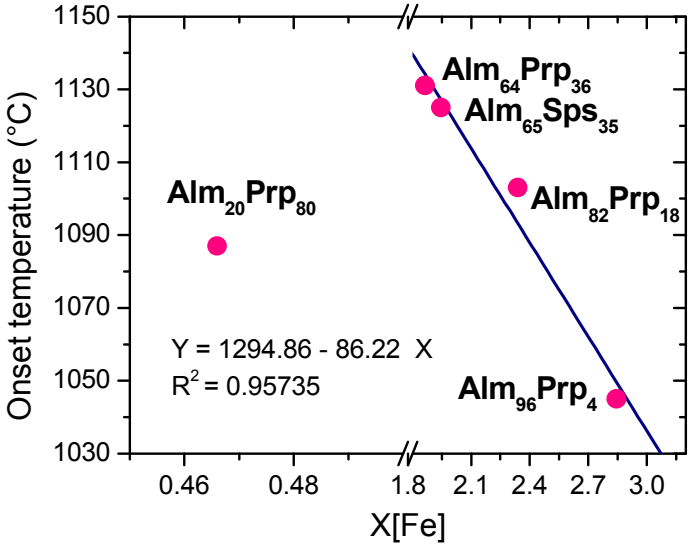

Figure 3.6 Variation of the onset temperature, calculated from DSC, with the iron content in garnet dodecahedral positions.

3.4.3 Difference in phase composition due to iron content

The phase composition analysis shows the variety of the decomposition products of each garnet sample with different iron content in dodecahedral sites (Fig. 3.4, 3.5; for more details see appendices 3, 4, 5, 6, and 7).

The sample with the major amount of iron cations in the dodecahedral site ($Alm_{96}Prp_4$, X[Fe] = 2.845 apfu), when heated at higher temperatures than the decomposition temperature (1055 °C), *i.e.* at 1070 °C and 1200 °C, show a very similar phase composition, but with a different percentage contribution (Fig. 3.7, 3.8).The identified phases were: α-Fe, cristobalite (SiO_2), iron-end-member olivine (fayalite Fe_2SiO_4), and iron-rich cordierite ($(Fe,Mg)_2Al_4Si_5O_{18}$). The variations in phase composition of $Alm_{96}Prp_4$-1070 and $Alm_{96}Prp_4$-1200 samples (Fig. 3.7) indicate consecutive reactions of primary products of almandine decomposition as soon as they were formed: fayalite content increased (+13.1 wt.%) at the expense of alpha iron (-4.5 wt.%) and cristobalite (-11.5 wt.%). Contents of hercynite and Fe-cordierite vary only slightly: hercynite content decreases and Fe-cordierite content increases.

Similar variation of phase percentages was found also with MS, where the sextet corresponding to α-Fe show a decreased area when sample was heated at 1200 °C (Fig. 3.8). Fayalite was fitted with two paramagnetic doublets (M1 and M2 octahedral sites), where the spectral ratio between doublet, for both temperatures, was close to the unity. This result is close to the theoretical occupancy for iron in olivine structure [41]. The hyperfine parameters of two hercynite doublets (T1 and T2 tetrahedral sites) agree with those published for natural Fe-bearing spinel [42]. In the XRD patterns a slight shift of hercynite diffractions of $Alm_{96}Prp_4$-1200 with respect to $Alm_{96}Prp_4$-1070 sample could be due to incorporation of extra iron into the hercynite or some grade of inversion of its structure, as the studied dependence of interplanar distance on iron content according to Vegard's law in the hercynite-spinel series [43]. The most intense diffraction peak of Fe-cordierite (312) showed a shift towards larger d-values with increasing temperature of treatment. This variation in cell parameters can be related to more iron atoms incorporated into the cordierite structure with increasing temperature [44].

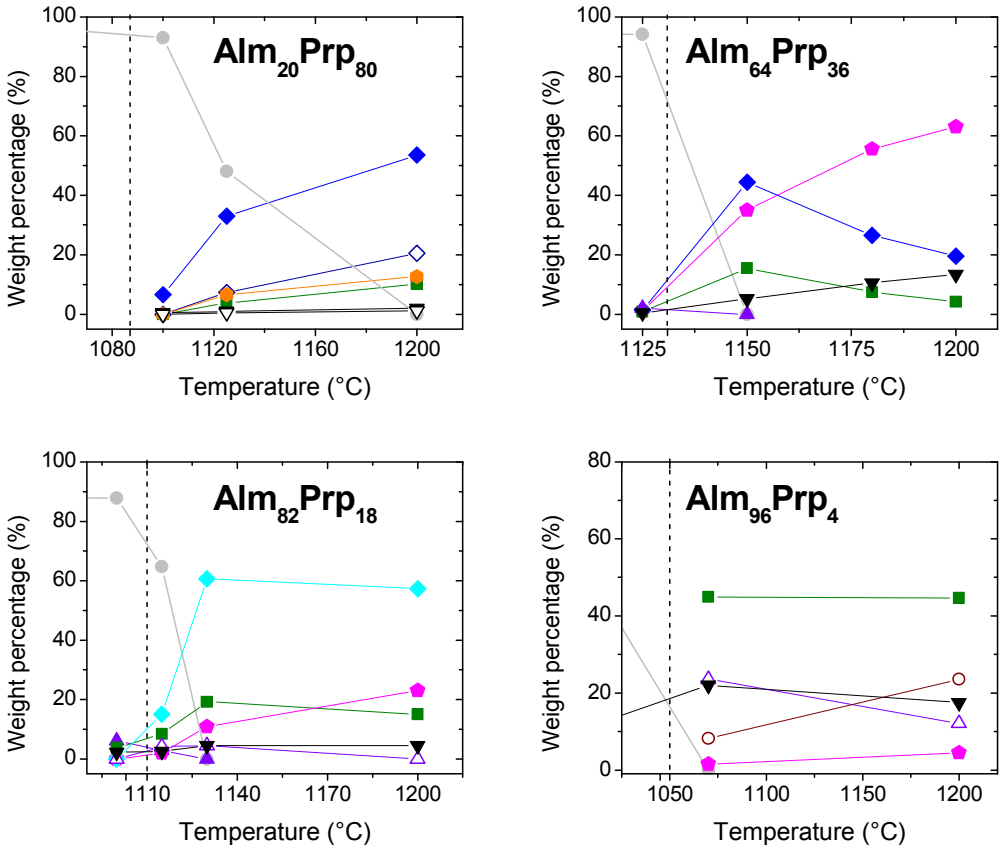

Figure 3.7 Graphs showing the relative weight fraction calculated by Rietveld refinement of samples heated up to 1200 °C. The symbols in the graphs represent the identified phases: Garnet (●), enstatite (◆), clinoenstatite (◇), hercynite-spinel (■), anorthite (⬢), alpha iron (▼), gamma iron (▽), cordierite (⬟), quartz (▲), pigeonite (◆), cristobalite (△), and fayalite (○).

The sample with intermediate composition $Alm_{82}Prp_{18}$ (X[Fe] = 2.339 apfu), heated at high temperatures (1100 °C, 1115 °C, 1130 °C, and 1200 °C), show a similar phase composition when temperatures at higher than 1130 °C (Fig. 3.7). At 1100 °C, the decomposition reaction is already starting, and was possible to identify α-Fe, quartz (SiO_2), spinel-hercynite ($(Mg,Fe)Al_2O_4$) and a high percentage of garnet (87.8 %). At 1115 °C the phase composition is the following: α-Fe, quartz-cristobalite (SiO_2), and spinel-hercynite, Fe-cordierite ($(Fe,Mg)_2Al_4Si_5O_{18}$), pigeonite ($(Mg,Fe,Ca)(Mg,Fe)Si_2O_6$) and still a percentage of the starting garnet (64.7 %).

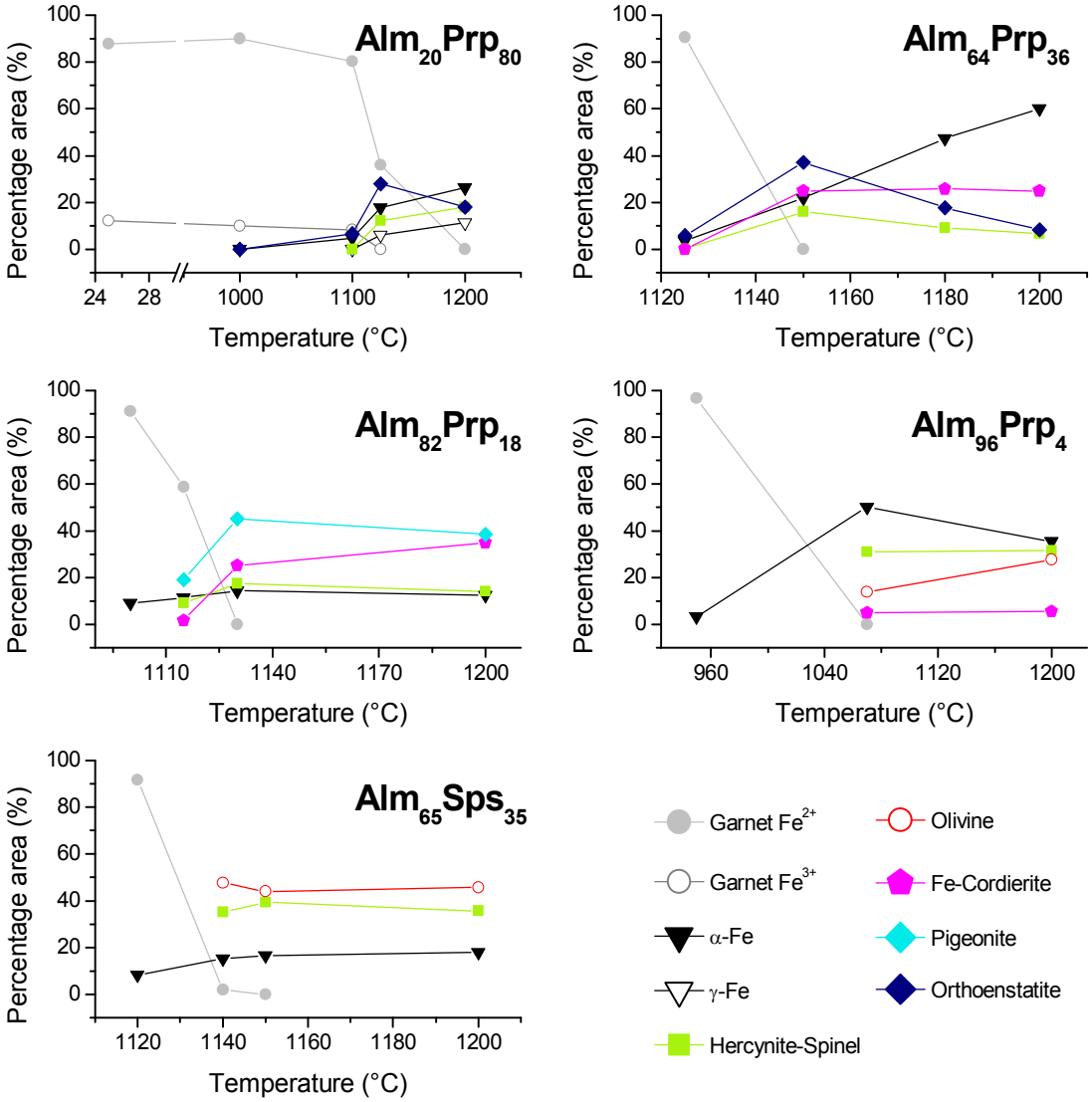

Figure 3.8 Graphs showing the percentage area of Mössbauer sub-spectra of samples heated up to 1200 °C. For garnet $Alm_{96}Prp_4$ was omitted the Fe^{3+} and ilmenite components, and for $Alm_{20}Prp_{80}$ was included the Fe^{3+} component separately.

Finally at 1200 °C all the garnet has been decomposed, remaining only the decomposition products α-Fe, spinel-hercynite, Fe-cordierite, and the Ca-poor pyroxene pigeonite. The slight percentage variation from sample heated up to 1130 °C and 1200 °C of spinel-hercynite, cristobalite, and Fe-cordierite, observed in Fig. 3.7, indicates that there is a secondary reaction taking place. As in the aforementioned sample $Alm_{96}Prp_4$, this reaction corresponds to the formation of Fe-cordierite. Mössbauer spectra also confirm the presence of the bearing-iron phases: hercynite-spinel, iron, Fe-cordierite, and pigeonite (see appendices 6 and 7).

Another garnet with intermediate composition $Alm_{64}Prp_{36}$ (X[Fe] = 1.864 apfu), when heated above the decomposition temperature (1135 °C) has as decomposition products: α-Fe, ortho-enstatite ($(Mg,Fe)SiO_3$), Fe-cordierite ($(Fe,Mg)_2Al_4Si_5O_{18}$), and hercynite-spinel ($(Mg,Fe)Al_2O_4$). In this case, after the decomposition temperature the garnet structure is completely destroyed and the endothermic reaction is one-step. However, carefully observation of the percentage variation of phase composition at different temperatures (1150 °C, 1180 °C, and 1200 °C), suggest again intermediate reactions between the original decomposition products (Fig. 3.7). There is a progressive rise, from 1150 °C to 1200 °C, in the weight percentage of Fe-cordierite (+27.8 %) and α-Fe (+8.5 %), and at the same time a decreasing of the weight percentage of enstatite (-24.4 %) and hercynite-spinel (11.9 %). Only in this case the Mössbauer spectra show a very similar trend of the percentage area of subspectra corresponding to each phase.

The sample $Alm_{20}Prp_{80}$, where Mg^{2+} cations predominantly occupy the dodecahedral site and Fe^{2+} represent a minor contribution (X[Fe] = 0.465 apfu), was heated up to different temperatures (1100 °C, 1125 °C, and 1200 °C). At 1100 °C the decomposition has already started, and the identified phases were zerovalent iron with two different crystallographic arrangements bcc (α-Fe) and fcc (γ-Fe), the orthopyroxene enstatite ($(Mg,Fe)SiO_3$), and a predominant percentage of pyrope-close composition garnet (94.5 %). At higher temperatures, 1125 °C and 1200 °C, besides iron and enstatite were identified Fe-poor spinel ($(Mg,Fe^{2+})(Al,Cr,Fe^{3+})_2O_4$) and anorthite ($CaAl_2Si_2O_8$). In XRD pattern of sample $Alm_{20}Prp_{80}$-1125 (see appendix 3) were also identified diffraction lines belonging to pyrope (48.1 wt. %), indicating a slow decomposition of the garnet. The presence of anorthite is due to the presence of Ca in the starting garnet. In this case there is not a further reaction between the decomposition products. The pyroxene enstatite, identified in samples heated up to 1125 °C and 1200 °C, presented two different

polymorphs: orthoenstatite (space group *Pbca*) and clinoenstatite (space group $P2_1/c$) [45,46].

In the Mössbauer spectra of samples heated up to 1125 °C and 1200 °C (Fig. 3.5, appendix 6), two doublets (M1 and M2 octahedral sites) are assigned to enstatite. The Mössbauer parameters of enstatite for sites M1 (IS = 1.11–1.12 mm/s, QS = 2.59–2.60 mm/s) and M2 (IS = 1.14–1.17 mm/s, QS = 2.13 mm/s), reveals that enstatite is more likely to be orthorhombic and not monoclinic [47,48]; while the sub-spectral area ratio M1/M2 vary with the different temperatures indicating a variation in the site-occupancy of Fe^{2+} cations. One doublet (IS = 1.08–1.15 mm/s, QS = 1.70–1.75 mm/s) was assigned to Fe^{2+} in tetrahedral site of hercynite-spinel. Additional Mössbauer spectra were taken at low temperatures (70 K, 10 K, 5 K), to study the possible presence of clinoenstatite (see appendices 6, 7). In the low-temperature spectra, were not evidence of additional doublets that could be assigned to another phase, and the values of the IS and QS resulted to be closer to those belonging to orthoenstatite and not to clinoenstatite [47,49].

The apparent discrepancy between the graphs showing quantitative results from XRD (Fig. 3.7) and MS (Fig. 3.8), are because XRD take in account all phases present in the sample, while MS only consider the phases having iron in their composition. Also it must be said that the area of the Mössbauer subspectra are proportional to the number of iron cations in the structure of the identified phase [50,51]. This is the reason why in the graphs for $Alm_{20}Prp_{80}$, the enstatite (En) contribution seems to have a different trend, and the other contributing phases iron (α-Fe, γ-Fe) and hercynite (Hc) have the same trend but apparently a bigger contribution to the Mössbauer spectrum at 1200 °C. The same is valid for the other samples, when iron component seems to be the dominant phase ($Alm_{64}Prp_{36}$, $Alm_{82}Prp_{18}$).

A useful characteristic of MS is that make possible not only to know the iron oxidation state, but also quantify the amount of iron cations (Fe^{2+}, Fe^{3+}) in the different crystallographic sites. The last was very useful to monitor the reduction of ferric ion in octahedral sites of sample $Alm_{20}Prp_{80}$. In this sample was seen the progressive reduction of Fe^{3+} to Fe^{2+} before the thermal decomposition (Fig. 3.8).

A garnet sample with intermediate composition from the Alm-Sps series has been also studied, $Alm_{65}Sps_{35}$ (X[Fe] = 1.946 apfu). It has a similar amount of Fe^{2+} cations as sample $Alm_{64}Sps_{36}$, but as is shown from the experimental results the decomposition process was quite different. From XRD pattern of sample heated up to 1120 °C, is possible to see that decomposition has already started and the phases identified are: α-Fe,

hercynite, tephroite ($(Mn,Fe)SiO_4$), quartz (SiO_2), and the starting garnet (92.8 %). However, when sample is heated further to 1140 °C and 1150 °C, the bigger diffraction lines belong to hercynite, while the minor phases are garnet (only in sample $Alm_{65}Sps_{35}$-1140, 14.2 %) and tephroite (in both samples), but in the region $2\theta = 20°–35°$ there is a wide shoulder in the diffractogram that could be ascribed to an amorphous phase, most probably silica (SiO_2). More surprising, is the result of sample heated up to 1200 °C, where the only identified phases were α-Fe, hercynite, and amorphous component (see appendix 3).

In this particular case, Mössbauer spectroscopy was very helpful to identify the amorphous component in sample $Alm_{65}Sps_{35}$-1200, and monitor the variation of the subspectral areas of each Fe-bearing phase. In sample $Alm_{65}Sps_{35}$-1120, the Mössbauer spectrum shows only a doublet corresponding to Fe^{2+} in undecomposed garnet (91.7 %), and a small sextet corresponding to α-Fe (8.3 %). Spectra of samples heated up to 1140 °C, 1150 °C, and 1200 °C – excepting the small doublet for garnet (spectral area 2 %) in sample $Alm_{65}Sps_{35}$-1140 – where fitted with one sextet for α-Fe, two doublets for Fe^{2+} in octahedral sites of tephroite M1 and M2 [52], and two doublets for Fe^{2+} in tetrahedral sites of hercynite T1 and T2. From this it is possible to identify that the amorphous phase in XRD pattern of sample $Alm_{65}Sps_{35}$-1200 is melted tephroite, which is not usual, because minerals melt congruently at higher temperatures. Also from MS, it is noticed that the spectral areas of each phase did not have a great variation in the samples heated at 1150 °C and 1200 °C, and seems that there is not a subsequent secondary reaction between the decomposition products.

3.4.4 Mechanism of thermal decomposition of natural garnets

Natural garnets decompose in reducing atmosphere at temperatures above 1000 °C. When the iron content is very high as in almandine the decomposition is completed below 1100 °C, while for garnets with less iron content the decomposition onset is slightly above 1100 °C.

From the recollected data (XRD, MS) for sample $Alm_{20}Prp_{80}$ heated up to different temperatures, it was seen that before the decomposition onset (1087 °C) there is a slow reduction of Fe^{3+} in octahedral sites, which is a non-destructive process to the garnet structure that remains unaltered. After a slow decomposition process, the result

was a mix of minerals (enstatite polymorphs ortho- and clino-, Fe-spinel, and anorthite) and two iron allotropies (α-Fe, γ-Fe). Because of the complexity and variety of the phase composition after decomposition, a XRD *in-situ* measurement was carried out on sample $Alm_{20}Prp_{80}$ under reducing atmosphere of forming gas from room temperature to 1200 °C (Fig. 3.9).

Rietveld analysis was carried out on each diffractogram, recorded from XRD *in-situ* measurements, in order to quantify the amount of each phase at the corresponding temperature; the results showing the quantitative evolution of phases with the rising temperature were plotted in figure 3.9. As it can be seen from the graph (Fig. 3.9), the decomposition process has started above 1000 °C, a result which agrees with the previous measurements. The identified phases from XRD *in-situ* patterns are the same as the identified from the XRD patterns of samples heated up to 1200 °C.

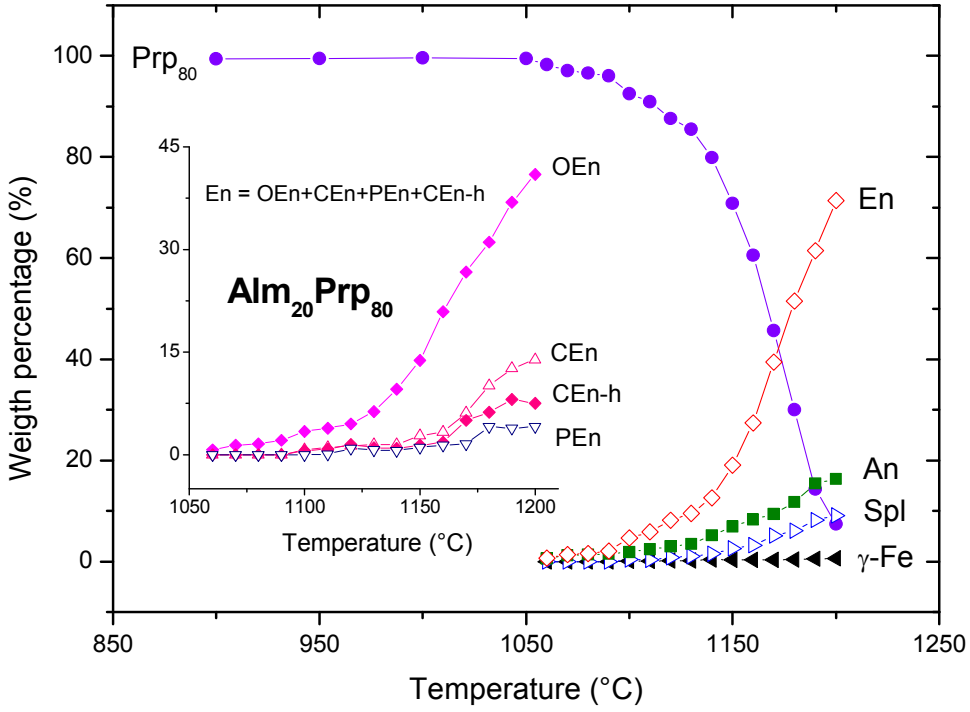

Figure 3.9 Results of Rietveld analysis of XRD patterns collected during the *in-situ* experiment. Pyrope (Prp), anorthite (An), spinel (Spl), gamma iron (γ-Fe), enstatite (En), ortho-enstatite (OEn), clinoenstatite low (CEn), clinoenstatite high (CEn-h), and proto-enstatite (PEn).

From the figure 3.9, there is a progressive decreasing of the weight percentage of the starting garnet at the same time as the increasing of the decomposition products; indicating the slow rate of the reaction, where the decomposition process occurs in a wide

temperature interval from 1080 °C to 1170 °C (Δt = 90 °C) according to DSC measurements. In the very beginning of thermal decomposition (1060 °C) the phases identified, besides garnet (98.3 %), were: orthoenstatite and anorthite. With the increasing of temperature from 1100 °C to 1200 °C the decomposition products included anorthite, γ-Fe, spinel, and enstatite. The identified enstatite was presenting four polymorphs: orthoenstatite (*Pbca*), clinoenstatite low ($P2_1/c$), clinoenstatite high (*C2/c*), and protoenstatite ($P2_1cn$) [45,46].

The garnet structure is expanded progressively before the decomposition, when this expansion goes beyond the bond length between atoms, they are not able to be bonded and the structure collapse and break down. In the case of sample $Alm_{20}Prp_{80}$, at the beginning of the decomposition the first polyhedral site to be broken seems to be the dodecahedral one hosting Ca^{2+} cations, because of the early presence of anorthite as decomposition product. Then the structure slowly collapse because of the increased strain due to presence of cations with different sizes (Ca, Mg, Fe^{2+}), that affect the highly linked network of garnet, producing the aforementioned decomposition products without further reactions.

As it was seen from the Mössbauer spectra, the iron-bearing enstatite was only the polymorph orthoenstatite, and clinoenstatite being the iron-free polymorph. From that, it is possible to assume a slow Fe^{2+} cation reduction in octahedral sites of orthoenstite to produce the iron in zerovalent state, and then the new free-iron enstatite can rearrange its structure giving origin to clinoenstatite polymorph. The only problem of this assumption is the absence of SiO_2 in the diffractograms, but because of the small amount produced it can be hidden by the other phases or be amorphous. This hypotesis can be expressed by the following equation:

$$Mg_{1-x}Fe_xSiO_3 + xH_2 \rightarrow xFe + (1 - x)MgSiO_3 + xSiO_2 + xH_2O \qquad (1)$$

Summarizing all the aforementioned, then the decomposition process of $Alm_{20}Prp_{80}$ sample from 1065 °C to 1200 °C can be expressed as:

$$Alm_{20}Prp_{80} + H_2 \rightarrow Spinel + (\alpha,\gamma)\text{-}Iron + (O, C)\text{-}Enstatite + Anorthite + H_2O$$

The garnet sample with composition close to almandine ($Alm_{96}Prp_4$) has a minor inclusion of ilmenite, which decompose at around 850 °C into rutile and metallic iron according to $FeTiO_3 + H_2\,(g) \rightarrow TiO_2 + \alpha\text{-}Fe + H_2O\,(g)$. When the garnet decomposition occurs, there is a pronounced endothermic peak at 1055 °C and water vapour formation at 1075 °C (see appendix 2). Then, the reaction of $Alm_{94}Prp_4$ with hydrogen between 950 °C to 1200 °C leads to the equation:

$$Fe_{2.85}Mg_{0.15}Al_2Si_3O_{12} + H_2\,(g) \rightarrow 0.90Fe_{1-x}Mg_xAl_2O_4 + Fe + 0.50Fe_2SiO_4 + 2.25SiO_2 + 0.05(Fe_{1-x}Mg_x)_2Al_4Si_5O_{18} + H_2O\,(g); \qquad (0 \leq x \leq 1) \qquad (2)$$

Considering x = 0.15, it is possible to calculate the theoretical mass loss from the equation, which gives a value of -3.21 %. The variable weight percentage of fayalite and Fe-cordierite in samples heated up to 1070°C and 1200 °C, suggest that they were formed by a secondary reaction between the primary products as the themperature increases. The following equations can be written for fayalite [53] and Fe-cordierite [54] formation:

$$2\,Fe + SiO_2 + 2\,H_2O\,(g) \rightarrow Fe_2SiO_4 + 2\,H_2\,(g) \qquad (3)$$

$$2\,Fe_{1-x}Mg_xAl_2O_4 + 5\,SiO_2 \rightarrow (Fe_{1-x}Mg_x)_2Al_4Si_5O_{18} \qquad (4)$$

Based on the experimental data and the previous equations, a general mechanism of reductive decomposition of almandine-close composition garnet (Fe-cordierite and fayalite are formed in amounts indicated as “a” and “b”, respectively):

$$Fe_{3-x}Mg_xAl_2Si_3O_{12} + (2\text{-}b)H_2 \rightarrow (1\text{-}a)Fe_{1-x}Mg_xAl_2O_4 + (2\text{-}b)Fe + (b/2)Fe_2SiO_4 + (3\text{-}5a/2\text{-}b/2)SiO_2 + (a/2)(Fe_{1-x}Mg_x)_2Al_4Si_5O_{18} + (2\text{-}b)H_2O \qquad (5)$$

$$\textit{Alm}_{96}\textit{Prp}_4 + H_2 \rightarrow \textit{Hercynite} + \alpha\textit{-Iron} + \textit{Fayalite} + \textit{Cristobalite} + \textit{Fe-Cordierite} + H_2O$$

In samples with intermediate compositions, samples $Alm_{64}Prp_{36}$ (X[Fe] = 1.864) and $Alm_{82}Prp_{18}$ (X[Fe] = 2.339), the decomposition process is different. In the case of sample $Alm_{82}Prp_{18}$ the TG graph have a two differentiate zones, the first one when the sample is decomposed at 1109 °C, and the second where it is observed a decreasing slope suggesting the occurrence of a secondary reaction (see appendix 2). Using the gathered

data for this sample $Alm_{82}Prp_{18}$ and including also the manganese cations in the model, it is possible to write the mechanism from 1024 °C to 1200 °C.

$$Fe_{2.34}Mg_{0.5}Mn_{0.1}Ca_{0.06}Al_2Si_3O_{12} + 0.45H_2 \rightarrow 0.42Fe_{1-(x1+y1)}Mg_{x1}Mn_{y1}Al_2O_4 + 0.45Fe + 0.29(Fe_{1-(x1+y1)}Mg_{x1}Mn_{y1})_2Al_4Si_5O_{18} + 0.775Fe_{2-(x2+z1)}Mg_{x2}Ca_{z1}Si_2O_6 + 0.45H_2O \quad (6)$$

In this specific case: x1 = 0.3, x2 = 0.26, y1 = 0.1, z1 = 0.08. Using these values the TG mass loss was calulated as -1.51 %. Until 1130 °C, SiO_2 was one of the decomposition products, and it reacted with spinel-hercynite to produce Fe-cordierite in a similar way as produced in sample $Alm_{96}Prp_4$.

$$2Fe_{1-(x1+y1)}Mg_{x1}Mn_{y1}Al_2O_4 + 5SiO_2 \rightarrow (Fe_{1-(x1+y1)}Mg_{x2}Mn_{y1})_2Al_4Si_5O_{18} \quad (7)$$

It is possible also to generalize the decomposition mechanism for $Alm_{80}Prp_{18}$, with "d" representing the formed amount of pigeonite, x = x1 + dx2, y = y1, and z = dz1.

$$Fe_{3-(x+y+z)}Mg_xMn_yCa_zAl_2Si_3O_{12} + 2(1-d)H_2 \rightarrow ((4d-1)/5)Fe_{1-(x1+y1)}Mg_{x1}Mn_{y1}Al_2O_4 + 2(1-d)Fe + ((3-2d)/5)(Fe_{1-x1}Mg_{x1})_2Al_4Si_5O_{18} + dFe_{2-(x2+z1)}Mg_{x2}Ca_{z1}Si_2O_6 + 2(1-d)H_2O \quad (8)$$

$Alm_{82}Prp_{18}$ + H_2 → Hercynite + α-Iron + Fe-Cordierite + Pigeonite + H_2O

For the other sample with intermediate composition $Alm_{64}Prp_{36}$, the DSC graph shows a sharp peak at 1135 °C (Fig. 3.3), which is accompanied with downward peak for hydrogen and a upward peak for water vapour, according to the EGA results (see appendix 2), indicating the decomposition of the garnet. With the information about the phase composition, it was possible to establish a relationship between the phases formed after the $Alm_{64}Prp_{36}$ thermal decomposition from 942 °C to 1200 °C:

$$Fe_{1.87}Mg_{1.13}Al_2Si_3O_{12} + 1.2H_2 \rightarrow 0.12Fe_{1-x2}Mg_{x2}Al_2O_4 + 1.2Fe + 0.80Fe_{1-x1}Mg_{x1}SiO_3 + 0.44Fe_{2-x3}Mg_{x3}Al_4Si_5O_{18} + 1.2H_2O \quad (9)$$

Using the following values: x1 = 0.6, x2 = 0.8, x3 = 1.25, it was calculated the TG mass loss as -4.13%. As was observed in Fig. 3.7, cordierite and iron are the phases that show an increment with the temperature of heating, while enstatite and hercynite decrease. This suggest a reaction between the decomposition products, that can be expresed as:

$$2Fe_{1-x2}Mg_{x2}Al_2O_4 + 5Fe_{1-x1}Mg_{x1}SiO_3 + 5H_2 \rightarrow 5Fe + Fe_{2-x3}Mg_{x3}Al_4Si_5O_{18} + 5H_2O \quad (10)$$

Generalizing the expression for $Alm_{64}Prp_{36}$ decomposition, where "b" is the amount of formed enstatite, it is obtained:

$$Fe_{3-x}Mg_xAl_2Si_3O_{12} + (2-b)H_2 \rightarrow ((2b-1)/5)Fe_{1-x2}Mg_{x2}Al_2O_4 + (2-b)Fe + bFe_{1-x1}Mg_{x1}SiO_3 + ((3-b)/5)Fe_{2-x3}Mg_{x3}Al_4Si_5O_{18} + (2-b)H_2O \quad (11)$$

$$Alm_{64}Prp_{36} + H_2 \rightarrow Hercynite\text{-}Spinel + \alpha\text{-}Iron + Enstatite + Fe\text{-}Cordierite + H_2O$$

A special case is the thermal decomposition of sample $Alm_{65}Sps_{35}$, because of the presence of amorphous phases the XRD quantitative analysis was not very precisely. Here, Mössbauer spectroscopy was a useful tool to monitor the variation of phase composition with the temperature of heating. The XRD patterns of sample heated up to 1140 °C, 1150 °C, and 1200 °C, show hercynite as the predominant component; and the corresponding Mössbauer spectra are almost identical. Because of the slightly variation of the subspectral percentages for each phase, it is assumed that all phases are produced at the beginning of the garnet decomposition. Also it is worthwhile to mention that the TG graphs show a decreasing mass curve, starting from 970 °C that suggest a gradual decomposition followed by melting of SiO_2 first and tephroite after. Taking in account these evidences, it is possible to write:

$$Fe_{1.95}Mn_{1.05}Al_2Si_3O_{12} + 0.35H_2 \rightarrow FeAl_2O_4 + 0.35Fe + 0.825Mn_{2-x2}Fe_{x2}SiO_4 + 2.175SiO_2 + 0.35H_2O \quad (12)$$

$$Alm_{65}Sps_{35} + H_2 \rightarrow Hercynite + \alpha\text{-}Iron + Olivine + Silica + H_2O$$

Where x2 = 0.73, and the calculated TG mass loss is -1.13 %.

The figure 3.10 schematizes the above described decomposition mechanism for natural garnets: $Alm_{96}Prp_4$, $Alm_{82}Prp_{18}$, $Alm_{64}Prp_{36}$, and $Alm_{65}Sps_{35}$. In the schemes it is possible to appreciate the relationships between the decomposition products and their subsequent reactions. For example it is visualized that cordierite is formed by the same kind of reaction in samples $Alm_{96}Prp_4$ and $Alm_{82}Prp_{18}$, while in sample $Alm_{64}Prp_{36}$ the cordierite is formed by another reaction in absence of SiO_2 and hercynite. The last but not the least, the scheme for $Alm_{65}Sps_{35}$ depicts the melting of SiO_2 and tephroite, where the SiO_2 was only detected in sample heated at 1120 °C.

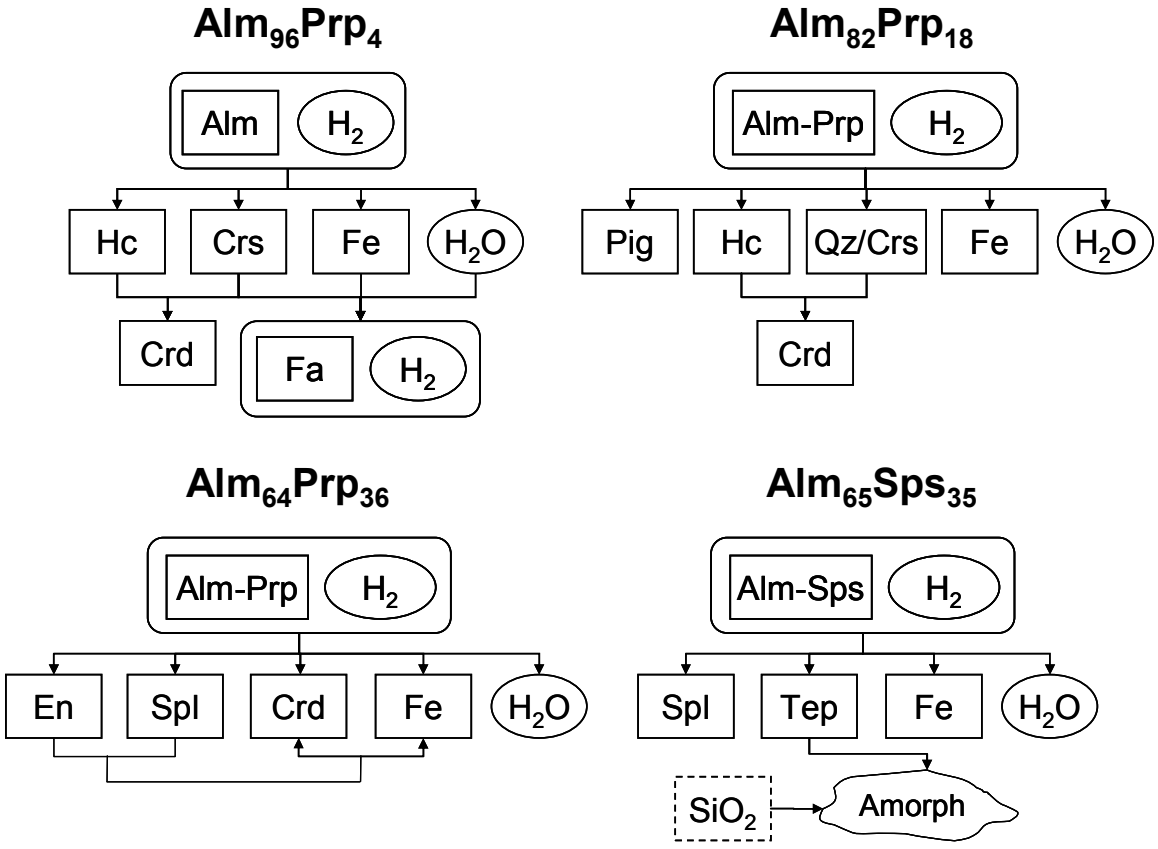

Figure 3.10 Schemes of the decomposition mechanism of the studied natural garnets, showing the relationship between decomposition products and secondary reactions. Almandine (Alm), pyrope (Prp), hercynite (Hc), spinel (Spl), quartz (Qz), cristobalite (Crs), pigeonite (Pig), cordierite (Crd), fayalite (Fa), enstatite (En), tephroite (Tep).

Finally in table 3.8 are given the values of experimental and calculated values of TG mass loss after the thermal decomposition of garnets. The calculation took in account the mass losses from the beginning of decomposition, and after it was added the

percentage value of water release before the decomposition. In the case of garnet $Alm_{20}Prp_{80}$ was not possible to calculate the corresponding mass loss, because the decomposition mechanism could not be quantitatively described.

Table 3.8 Comparison of experimental and theoretical values for mass variation in TG analysis of natural garnet samples.

Sample	Δm_{exp} (wt. %)	Δm_{th} (wt. %)
$Alm_{20}Prp_{80}$	-0.69	n.c.
$Alm_{64}Prp_{36}$	-4.33	-4.26
$Alm_{82}Prp_{18}$	-2.00	-1.97
$Alm_{96}Prp_{4}$	-3.51	-3.57*
$Alm_{65}Sps_{35}$	-1.34	-1.34

n.c. = not calculated
* Here it was considerate 2 wt. % of ilmenite inclusions.

3.4.5 Morphology of iron particles embedded in minerals matrix

The presence of metallic-iron particles was a common result of the thermal decomposed garnets (Fig. 3.11). The shape and size of these particles are variable, depending no only of the quantity of iron, but also of the phases formed during the garnet decomposition. The identification of the iron particles was possible after analysis of the heated samples with energy-dispersive X-ray spectroscopy (EDS) (see appendix 8).

In sample $Alm_{20}Prp_{80}$-1200, the small rounded iron particles have variable sizes (60 – 600 nm) and are spread almost uniformly on the mineral matrix, which is compound of spinel, anorthite, and enstatite. It must be mentioned, that those iron particles have a different crystallographic structure: bcc (α-Fe) and fcc (γ-Fe). Using XRD and MS is not possible to distinguish the kind of particles, neither with EDS. It is not still clear, how to relate the size of the particles with the crystallographic structure of iron. Haneda *et al.* [55] discuss the possibility that fast cooling in ultrafine particles lead to retain fcc lattice, and for relatively large particles the slow transformation in bcc lattice, without specify the particles size; however De Caro *et al.* [56] establish a critical size of 3 nm, below of this size the particles show a bcc structure, and above a fcc structure. Both authors used smaller particles for their studies and it is not possible to compare their results with the present results.

Although sample $Alm_{64}Prp_{36}$-1200 shows iron micrometric particles (0.4 – 2 μm) very well defined and a similar surface as $Alm_{20}Prp_{80}$-1200, the iron particles have a irregular-polyhedral shape almost rounded embedded in a mineral matrix consistent principally of Fe-cordierite and less content of Fe-enstatite and hercynite-spinel.

In sample $Alm_{82}Prp_{18}$, the rounded iron particles (0.5 – 1 μm) appear along with the very well formed regular-octahedral crystals of hercynite with edge length of approximately 1 μm. The octahedral crystals of hercynite have been seen before during the formation of minerals under reducing atmosphere in the system $FeO – Al_2O_3 – SiO_2$ [32]. The remaining mineral matrix is compound of Fe-cordierite and pigeonite.

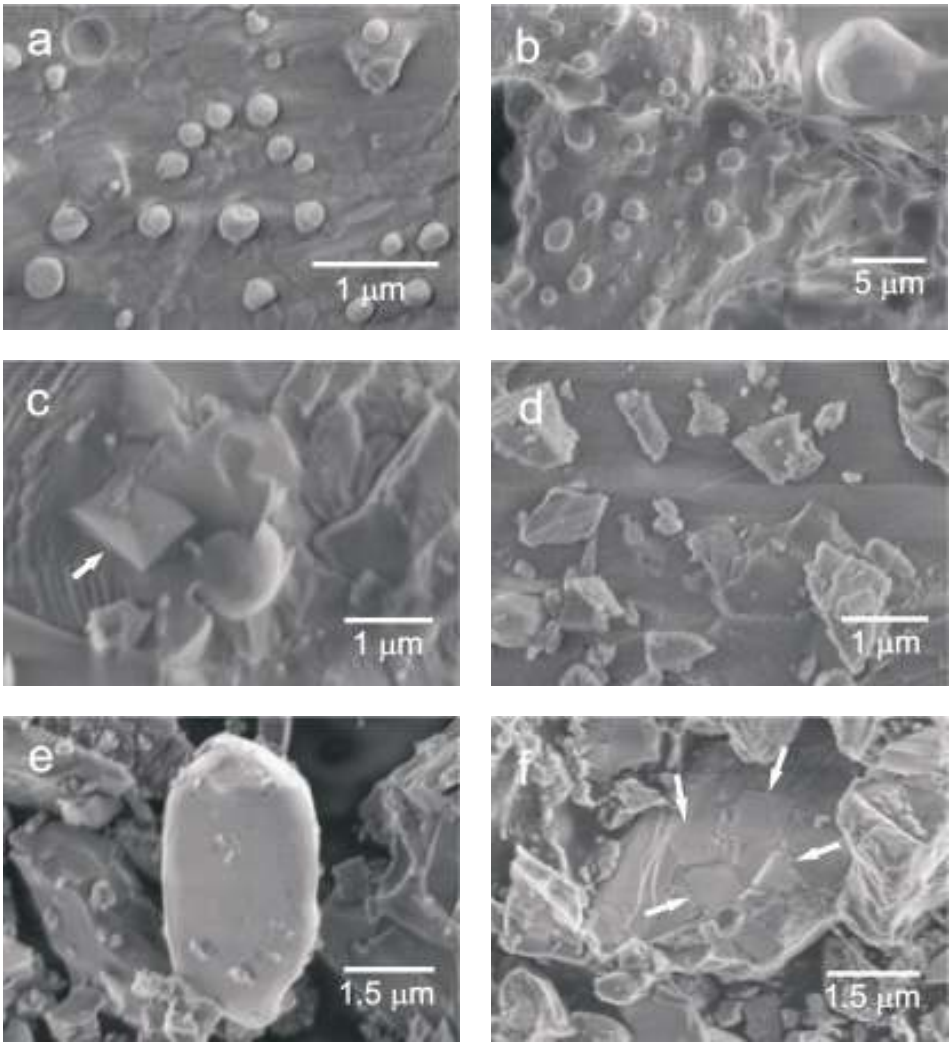

Figure 3.11 SEM photographs showing the morphology of iron particles produced after garnet decomposition. a) $Prp_{80}Alm_{20}$, b) $Prp_{36}Alm_{64}$, c) $Prp_{18}Alm_{82}$, d) $Sps_{35}Alm_{65}$, e) and f) Prp_4Alm_{96}. The arrows point the small hercynite-spinel crystals.

Flat-elongated iron particles were found in sample $Alm_{96}Prp_4$-1200 with variables length (3 – 5.5 μm) and wide (2 – 2.5 μm). These particles seem to be spread over the mixed-mineral surface compound of fayalite, cristobalite, and Fe-cordierite. Embedded in this mineral matrix were found perfect cubic crystals of hercynite-spinel, which have an edge length of approximately 1 μm.

In contrast, it was not possible to identify any iron particle in sample $Sps_{35}Alm_{65}$, even when both XRD and Mössbauer spectroscopy confirm its presence. The mix-mineral object and the smallest pieces over it have the same composition, and they were identified as hercynite mixed with amorphous tephroite and probably SiO_2. The iron particles are probably diffused inside of this mineral-mix.

3.5 Similitude and Differences in Thermal Decomposition of Garnets

All studied garnets, when thermally treated in reduced conditions, have different onset always above 1000 °C. Although the garnets with different chemical composition have the same crystalline structure, the phases obtained after the decomposition visible differ. The main reason could be seen in the occupation of dodecahedral sites with different cations, influencing the strength of inter-atomic bonds, and consequently the thermal stability of the structure. The formation of metallic iron upon reduction of ferric and ferrous cations in hydrogen atmosphere is confirmed to be a common feature of the garnet decomposition.

The common decomposition products observed for all studied garnets are metallic iron (α-Fe) and hercynite-spinel (Hc-Sp). Fe-cordierite (Fe-Crd) is observed for garnets with iron occupancy in dodecahedral sites between 1.864 and 2.845. Other decomposition products are pyroxenes as enstatite (En) and pigeonite (Pig) for garnets with iron occupancy from 0.465 to 2.339, where pigeonite is formed only in presence of Ca cations. Olivines as fayalite (Fa) and tephroite (Tep) are formed only from garnets $Alm_{96}Prp_4$ and $Alm_{65}Sps_{35}$. Cristobalite (Crs) was only found after the $Alm_{96}Prp_4$ decomposition; and anorthite (An) after the decomposition of $Alm_{20}Prp_{80}$, where the Ca amount in dodecahedral sites was significant.

In all studied natural garnets, according with the deduced equations of decomposition mechanism, the molar amount of produced iron is the same as the molar amount of hydrogen participating in the reaction. Therefore, it is possible to conclude that

the amount of metallic iron formed after their thermal decomposition does not depend on the initial iron occupancy in garnets, but on the efficient reaction with hydrogen.

Bibliography

1. W.A. Deer, R.A. Howie, and J. Zussman, *Rock-forming Minerals: Orthosilicates*, Second (Geological Society, London, 1997), p. 932.
2. C.A. Geiger, in *EMU Notes in Mineralogy, Vol. 6*, edited by A. Beran and E. Libowitzky (Eötvös University Press, Budapest, 2004), pp. 589–645.
3. R.R. Rapple, in *Industrial Minerals & Rocks: Commodities, Markets and Uses*, edited by J.E. Kogel, N.C. Trivedi, J.M. Baker, and S.T. Krukowski (Society for mining, metallurgy and exploration Inc., Littleton, CO, 2006), pp. 475–480.
4. K. Barcova, M. Mashlan, and P. Martinec, *Hyperfine Interact.* **139/140**, 463–469 (2002).
5. K.K. Chatterjee, *Uses of Industrial Minerals, Rocks and Freshwater* (Nova Science Publisher Inc., New York, 2009), p. 584.
6. G.A. Novak and G. v. Gibbs, *Am. Mineral.* **56**, 791–825 (1971).
7. E.P. Meagher, *Am. Mineral.* **60**, 218–228 (1975).
8. C.A. Geiger, *Am. Mineral.* **93**, 360–372 (2008).
9. A. Bosenick, M.T. Dove, and C.A. Geiger, *Phys. Chem. Miner.* **27**, 398–418 (2000).
10. D.L. Whitney and B.W. Evans, *Am. Mineral.* **95**, 185–187 (2010).
11. B.J. Skinner, *Am. Mineral.* **41**, 428–436 (1956).
12. C.A. Geiger and A. Feenstra, *Am. Mineral.* **82**, 571–581 (1997).
13. C. Freeman, N. Allan, and W. van Westrenen, *Physical Review B* **74**, 134203 (2006).
14. M. Merli, A. Callegari, E. Cannillo, F. Caucia, M. Leona, R. Oberti, and L. Ungaretti, *Eur. J. Mineral.* **7**, 1239–1249 (1995).
15. T. Armbruster, C.A. Geiger, and G.A. Lager, *Am. Mineral.* **77**, 512–521 (1992).
16. C. Romano, B.T. Poe, N. Kreidie, and C. McCammon, *Am. Mineral.* **91**, 1371–1377 (2006).
17. C.A. Geiger, *Mineral. Petrol.* **66**, 271–299 (1999).
18. A. Bosenick, C.A. Geiger, and L. Cemič, *Geochim. Cosmochim. Acta* **60**, 3215–3227 (1996).
19. J.C.P. de Oliveira, M.I. da Costa Jr., W.H. Schreiner, and A. Vasquez, *J. Magn. Magn. Mater.* **79**, 1–7 (1989).
20. D. Zherebetskyy, S. Lebernegg, G. Amthauer, and M. Grodzicki, *Phys. Chem. Miner.* **39**, 351–361 (2012).

21. G. Amthauer, H. Annersten, and S.S. Hafner, *Zeitschrift Für Kristallographie* **143**, 14–55 (1976).

22. K. Černá, M. Mašláň, and P. Martinec, *Materials Structure* **7**, 6–9 (2000).

23. E. Murad and F.E. Wagner, *Phys. Chem. Miner.* **14**, 264–269 (1987).

24. C.A. Geiger, M. Grodzicki, and G. Amthauer, *Phys. Chem. Miner.* **30**, 280 – 292 (2003).

25. M. Mashlan, R. Zboril, and K. Barcova, in *Material Research in Atomic Scale by Mössbauer Spectrosocopy, Nato Series II Vol. 94*, edited by M. Mashlan, M. Miglierini, and P. Schaaf (Kluwer Academic Publishers, Netherlands, 2003), pp. 271–284.

26. M. Mašláň, Z. Šindelář, P. Martinec, M. Chmielová, and A.L. Kholmetskii, *Czech. J. Phys.* **47**, 571–574 (1997).

27. K. Barcova, M. Mashlan, R. Zboril, P. Martinec, and P. Kula, *Czech. J. Phys.* **51**, 749–754 (2001).

28. L. Thiéblot, J. Roux, and P. Richet, *Eur. J. Mineral.* **10**, 7–15 (1998).

29. R. Zboril, M. Mashlan, K. Barcova, J. Walla, E. Ferrow, and P. Martinec, *Phys. Chem. Miner.* **30**, 620–627 (2003).

30. R. Zboril, M. Mashlan, L. Machala, J. Walla, K. Barcova, and P. Martinec, *Hyperfine Interact.* **156/157**, 403–410 (2004).

31. L.M. Anovitz, E.J. Essene, G.W. Metz, S.R. Bohlen, E.F. Westrum Jr., and B.S. Hemingway, *Geochim. Cosmochim. Acta* **57**, 4191–4204 (1993).

32. J.F. Schairer and K. Yagi, *American Journal of Science* **250-A**, 471–512 (1952).

33. D.E. Harlov and R.C. Newton, *Am. Mineral.* **77**, 558–564 (1992).

34. I. Keesmann, S. Matthes, W. Schreyer, and F. Seifert, *Contrib. Mineral. Petrol.* **31**, 132–144 (1971).

35. R. Grapes, *Pyrometamorphism*, Second (Springer-Verlag Berlin Heidelberg, 2011), p. 365.

36. R. Zboril, M. Mashlan, K. Barcova, and M. Vujtek, *Hyperfine Interact.* **139/140**, 597–606 (2002).

37. M. Chmielová, P. Martinec, and Z. Weiss, *Eur. J. Mineral.* **9**, 403–409 (1997).

38. S. Vrána, *Journal of Geosciences* **53**, 17–30 (2008).

39. Y. Zhao and F. Shadman, *Ind. Eng. Chem. Res.* **30**, 2080–2087 (1991).

40. J.G. Stevens, A.M. Khasanov, J.W. Miller, H. Pollak, and Z. Li, editors, *Mössbauer Mineral Handbook* (Mössbauer Effect Data Center (MEDC), Baltimore Press, Asheville, 1998), p. 624.

41. M.D. Dyar, E.C. Sklute, O.N. Menzies, P. a. Bland, D. Lindsley, T. Glotch, M.D. Lane, M.W. Schaefer, B. Wopenka, R. Klima, J.L. Bishop, T. Hiroi, C. Pieters, and J. Sunshine, *Am. Mineral.* **94**, 883–898 (2009).

42. S. Carbonin, U. Russo, and A. Della Giusta, *Mineral. Mag.* **60**, 355–368 (1996).

43. G.B. Andreozzi and S. Lucchesi, *Am. Mineral.* **87**, 1113–1120 (2002).

44. T. Malcherek, M.C. Domeneghetti, V. Tazzoli, L. Ottonoli, C. McCammon, and M.A. Carpenter, *Am. Mineral.* **86**, 66–79 (2001).

45. J.R. Smyth, *Am. Mineral.* **59**, 345–352 (1974).

46. N. Choudhury and S.L. Chaplot, *Solid State Commun.* **114**, 127–132 (2000).

47. M.D. Dyar, R.L. Klima, D. Lindsley, and C.M. Pieters, *Am. Mineral.* **92**, 424–428 (2007).

48. S.G. Eeckhout, E. De Grave, C.A. McCammon, and R. Vochten, *Am. Mineral.* **85**, 943–952 (2000).

49. J.R. Regnard, J.M. Greneche, and R. Guillen, *Solid State Commun.* **63**, 277–283 (1987).

50. H. Jancke, F. Malz, and W. Haesselbarth, *Accreditation and Quality Assurance* **10**, 421–429 (2005).

51. M. Favre, D. Landolt, K. Hoffman, and M. Stratmann, *Corros. Sci.* **40**, 793–803 (1998).

52. H. Annersten, J. Adetunji, and A. Fillippidis, *Am. Mineral.* **69**, 1110–1115 (1984).

53. T. Ternes, W. Meisel, P. Griesbach, D. Hanžel, and P. Gütlich, *Fresenius Journal of Analytical Chemistry* **341**, 79–82 (1991).

54. S. Liu, Y.-P. Zeng, and D. Jiang, *Ceram. Int.* **35**, 597–602 (2009).

55. K. Haneda, Z.X. Zhou, A.H. Morrish, T. Majima, and T. Miyahara, *Physical Review B* **46**, 13832–13837 (1992).

56. D. de Caro, T.O. Ely, A. Mari, B. Chaudret, E. Snoeck, M. Respaud, J.-M. Broto, and A. Fert, *Chem. Mater.* **8**, 1987–1991 (1996).

4. Synthesis of Iron Nanoparticles by Thermal Decomposition of Prussian Blue

4.1 Prussian Blue: Structure Description and Behavior at High Temperatures

The Prussian blue (PB) complex salt is a common pigment used in painting; PB is also employed in a wide range of applications in industry, pharmaceutics, and science. The chemical name of Prussian blue is iron(III) hexacyanoferrate or ferric ferrocyanide, with an ideal chemical formula of $Fe_4^{+3}[Fe^{+2}(CN)_6]_3 \cdot xH_2O$ (x = 14-16) that crystallizes in $Fm\bar{3}m$ space group [1], where ferrous cations are found in a low-spin (S = 0) state and ferric cations are found in a high-spin (S = 5/2) state. The PB lattice exhibits a vacancy of 25 % of the $[Fe^{2+}(CN)_6]^{4-}$ units, and has water molecules in different sites: shell water structure (O in 24c site), and zeolitic water (O in 32f and 8c sites). Also it is known that sometimes PB has some potassium cations in its structure, that occupy the same crystallographic site as structural water, having the following structure $Fe_4^{3+}[Fe^{2+}(CN)_6]_3 \cdot (K^+_h \cdot OH^-_h \cdot mH_2O)$ [2] (Fig. 4.1). PB shows a ferromagnetic behavior below its Curie temperature T_C = (5.5 ± 0.5) K [3].

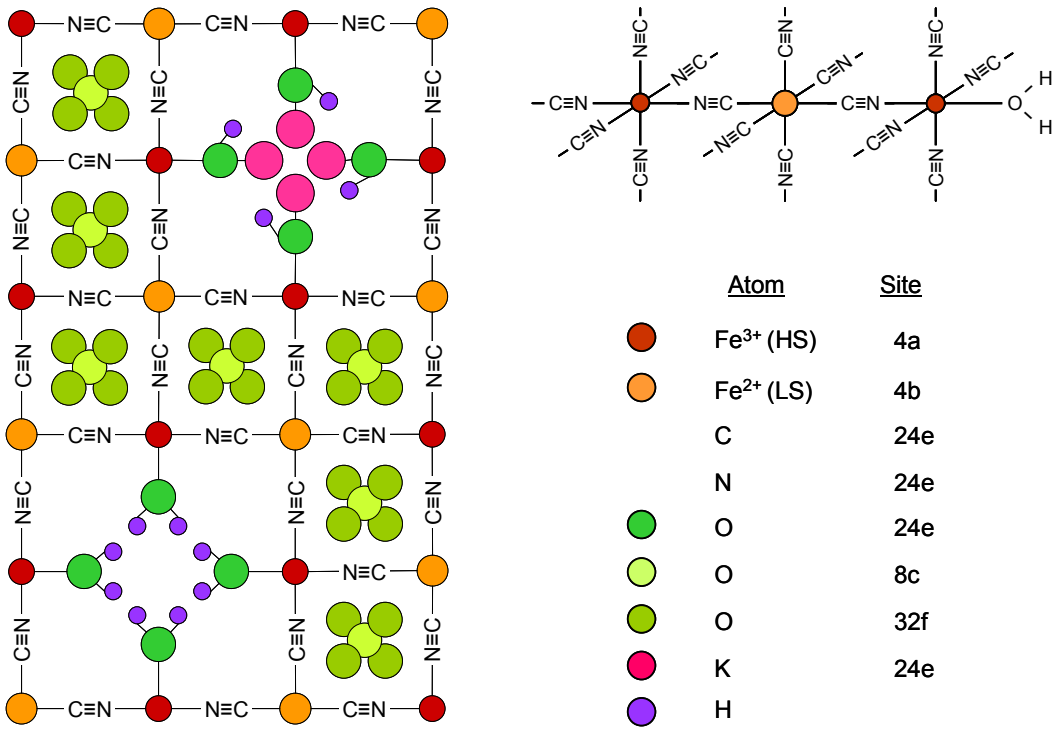

Figure 4.1 Prussian blue structure (2D), including structural water, zeolitic water and K^+ ions (left). In the right is shown the six-fold coordinated Fe ions (octahedral sites).

Physicochemical properties of PB have been investigated by several experimental techniques including infrared spectroscopy [4], X-ray diffraction [1,2,5], neutron diffraction [6], and Mössbauer spectroscopy [3,7,8]. These investigations were devoted to structural analysis [1,6,9], synthesis [10–12], magnetic properties [13], applications [14–16], PB based analogs [17,18], and some of them have been focused on behavior of PB at high temperatures [7,8,19,20].

Gallagher and Prescott [21] studied the thermal decomposition of europium hexacyanoferrate(III) and ammonium europium hexacyanoferrate(II). After the decomposition were obtained europium hydroxide and ferrous cyanide ($Fe(CN)_2$). Further decomposition of $Fe(CN)_2$ to Fe_3C and finally to metallic iron has been observed. Thermal behavior of PB up to 530 °C, in vacuum and in air, was studied by Cosgrove *et al.* [19] using thermal analysis, X-ray diffraction, and Mössbauer spectroscopy. The changes in the iron sites, before and after the cyanide release (~290 °C), were monitored using Mössbauer spectroscopy. Finally, PB heated in vacuum up to 450 °C was partially destroyed and crystalline ferrous ferrocyanide with undetermined crystal structure was formed. On the contrary, when the PB sample was heated in air at 410 °C magnetite was obtained in addition to the aforementioned phases.

The thermal decomposition of Prussian blue in argon was described by Allen and Bonnette [7], they described the successive transformation from the initial Prussian blue to other cyano-compounds, then in the last step ferrous cyanide ($Fe(CN)_2$) was decomposed into cementite (Fe_3C), graphite, and nitrogen as final products. Inoue *et al.* [8] studied the thermal decomposition products of PB in vacuum using Mössbauer spectroscopy. In this paper, Inoue *et al.* explained the thermal behavior of the dried PB from 200 °C to 350 °C and assumed that changes in Mössbauer parameters above 250 °C corresponded to a flipping of cyanoligands or an existence of mixed-valence states. Therefore, it is clear that a full decomposition of PB has not been achieved at such low temperatures.

The thermal decomposition of PB was also studied in oxidant atmosphere (air) by Zboril *et al.* [20]. They confirmed the formation of amorphous Fe_2O_3 at 250 °C, and simultaneous formation of β-Fe_2O_3 and γ-Fe_2O_3 at 350 °C by thermal decomposition of PB in air. Another interesting experimental result of PB thermal decomposition was exposed by Hermanek *et al.* [22], there they discussed the influence of the precursor (PB) layer thickness on its oxidative decomposition towards ferric oxide, allowing to obtain two different iron(III) oxide polymorphs (β and γ) only varying the layer thickness.

4.2 Materials and Methods

4.2.1 Starting material and sample preparation

The Prussian blue was heated up to chosen temperatures under inert atmosphere to study its thermal behavior and subsequent decomposition. The samples were prepared from insoluble Prussian blue ($Fe_4[Fe(CN)_6]_3.xH_2O$), which is manufactured by Sigma Aldrich. The equipment used for heat treatment of the samples is a thermal analyzer (STA 449 C Jupiter, Netzsch), for a simultaneous thermogravimetric analysis (TGA) and differential scanning calorimetry (DSC) coupled to mass spectrometer (QMS 403 Aëolos, Netzsch) for analyze the evolved gases (EGA) during the decomposition reaction.

The Prussian blue powder (PB) was placed inside of an open alumina crucible (volume: 7 ml, bottom internal diameter: 15 mm, height: 25 mm) under argon atmosphere (gas flow 30 ml/min). The heating and cooling rate were 5 K/min and -40 K/min respectively, and the mean mass of the samples was 10 mg. The PB was heated up to the following temperatures: 190 °C, 300 °C, 370 °C, 540 °C, 680 °C, 790 °C and 900 °C. The resultant samples were labeled as PB190, PB300, PB370, PB540, PB680, PB790 and PB900.

Additional samples were prepared in order to investigate the influence of the layer thickness of sample on the decomposition process. The second series of samples were prepared following the same procedure described before, those samples were labeled as PB680-5, PB680-10 and PB680-20, where 680 indicates the final temperature of heating in °C and the number after hyphen represent the mass of the sample in mg.

4.2.2 Samples characterization

All samples were characterized by X-ray powder diffraction (XRD) and Mössbauer spectroscopy (MS). XRD patterns were recorded with a PANalytical X'Pert PRO MPD diffractometer (CoK_α radiation) in the Bragg-Brentano geometry, equipped with an X´Celerator detector and programmable divergence and diffracted beam anti-scatter slits. Samples were placed on a zero-background Si slide, gently pressed and scanned with a step size of 0.017°, with angular range from 15° to 105°. The identification of crystalline phases in experimental XRD patterns was performed using the High Score Plus software (PANalytical) in conjunction with PDF-4+ database.

Transmission ^{57}Fe Mössbauer spectroscopy (1024 channels) was carried out in a constant acceleration mode using a ^{57}Co source in rhodium matrix at room temperature (RT). The spectrometer was calibrated with an α-Fe foil, the isomer shift values were expressed with respect to metallic α-iron at room temperature. The spectra were folded and fitted by Lorentz functions using the computer program CONFIT2000.

Scanning electron microscopy (SEM) was applied on selected samples prepared by thermal heating to study its morphology. The images were obtained using a scanning electron microscope Hitachi SU-6600, the secondary electron images were taken at 5 kV.

4.2.3 High temperature experiments: XRD "*in situ*"

High temperature X-ray diffraction *in situ* was carried out on Prussian blue powder to study its thermal decomposition and thermal transformations of the reaction products under inert atmosphere. The equipment used for the XRD analysis is a PANalytical X'Pert PRO MPD diffractometer (CoK_α radiation) equipped with an X'Celerator high-speed detector and an Anton Paar XRK-900 reaction chamber. The geometry of the diffractometer is a Bragg-Brentano with 0.017° step size. The collection time of each diffractogram was around 10 min with a sampling time of 0.12 s/step. The powder sample was placed directly on a glass ceramic Macor holder (14 mm diameter, 0.5 mm deep) covering completely its surface, then the holder was placed inside of the reactor chamber. The measurements were done in nitrogen atmosphere, under 1 bar of pressure, and the gas flow rate was maintained at 20 ml/min during the experiment. To study the influence of the heating rate were done two different experiments, which are described in table 4.1. The resulting diffractograms were analyzed using PANalytical HighScore Plus software to perform quantitative Rietveld analysis.

Table 4.1 Experimental conditions of the XRD *in situ* experiments.

	Experiment 1	Experiment 2
Heating rate between increase of temperature	40 K/min	40 K/min
Cooling rate	-10 K/min	-40 K/min
Average heating rate	2 K/min	8 K/min
Temperature range	60 – 900 °C	100 – 800 °C
Diffractogram collection every	20 °C	100 °C
Measurement range (2θ)	15° - 105°	5° - 80°

4.3 Results

4.3.1 PB characterization

The commercial Prussian blue was characterized by XRD and ^{57}Fe Mössbauer spectroscopy (MS). Both techniques showed that PB powder, without any treatment, contained a minor phase (~ 3%) identified as mineral jarosite ($(K,Na)Fe_3(SO_4)_2(OH)_6$) (see Fig. 4.2).

The Mössbauer spectrum taken at room temperature (Fig. 4.2b) was fitted with two doublets and one singlet. The singlet and the narrow doublet correspond to low-spin (LS) Fe^{2+} octahedrally coordinated to six C atoms (IS = –0.14 mm/s, 50.6 %) and high-spin (HS) Fe^{3+} ions octahedrally coordinated to N atoms (IS = 0.41 mm/s, QS = 0.17 mm/s, 47.0 %) in Prussian blue [20,23]. The wider doublet corresponds to Fe^{3+} (IS = 0.32 mm/s, QS = 1.13 mm/s, 2.4%) in octahedral sites of jarosite [24].

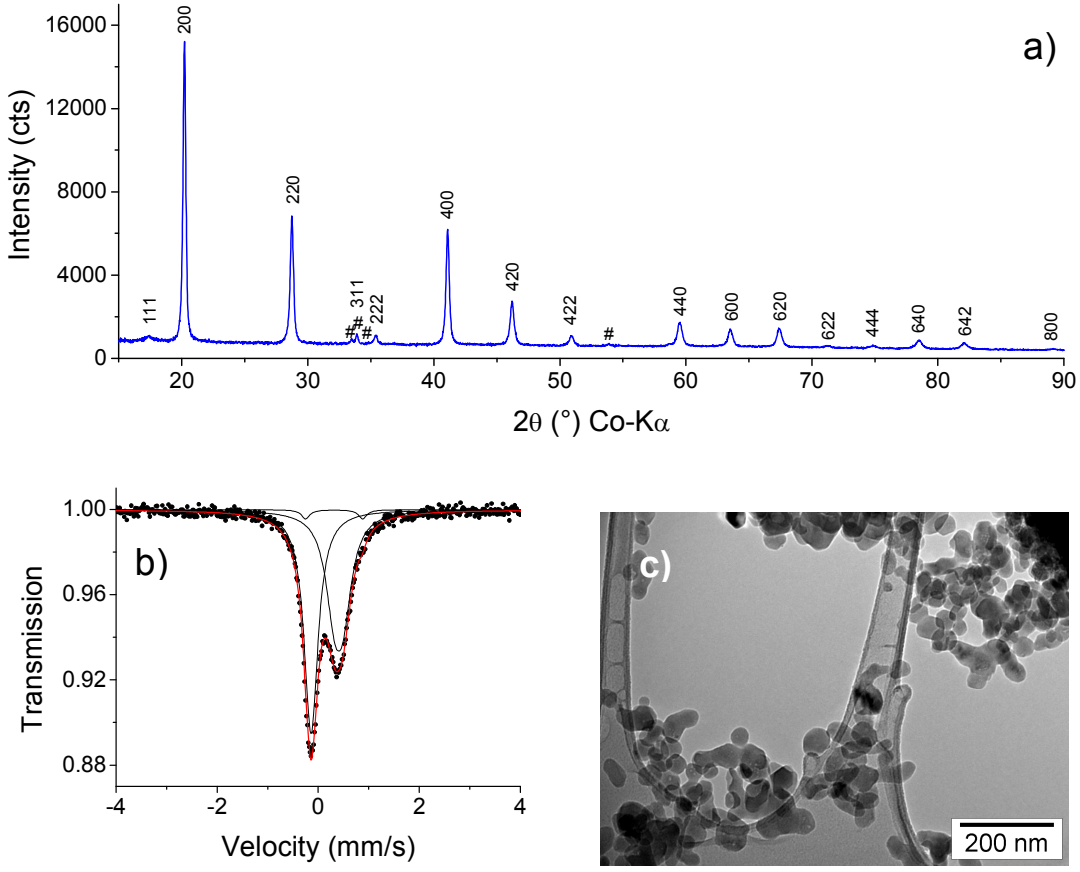

Figure 4.2 Results of the characterization of non-heated PB: a) XRD pattern, besides PB a small diffraction lines of jarosite (#) are present, b) room temperature Mössbauer spectrum, and c) TEM photography.

The XRD pattern of PB has a wide diffraction lines, typical for small particles. TEM photography shows the PB nanoparticles having sizes between 30–60 nm, where the particles showed low agglomeration (see Fig. 4.2c).

4.3.2 PB under argon atmosphere: TG/DSC measurements

The thermogravimetric curve shows clearly six differentiated steps (Fig. 4.3, table 4.2). According to the evolved gases analysis (EGA), there is a release of water (m/z = 18) starting from 55 °C to 300 °C, it corresponds well with the mass decreasing (-9.65 %) in step I and part of the step II, and with the wide endothermic peak at 150 °C. Because of the small amount of jarosite in the sample (~ 3%), it is not considered in the calculus of water content (structural and zeolitic) in the structure of Prussian blue. The calculus gave as result 5 water molecules per unit cell, being this result less than in the ideal number of water molecules in the PB structure.

The thermal decomposition of PB in argon atmosphere starts above 300 °C (step II), with release of cyanide groups (CN^-, m/z = 26), forming after hydrogen cyanide HCN (m/z = 27) and cyanogen gas $(CN)_2$ (m/z = 52) and small amount of carbon dioxide CO_2 (m/z = 44) according to the EGA results. It is reflected by the two small downward peaks in DSC (endo-effect) at 330 °C and 360 °C.

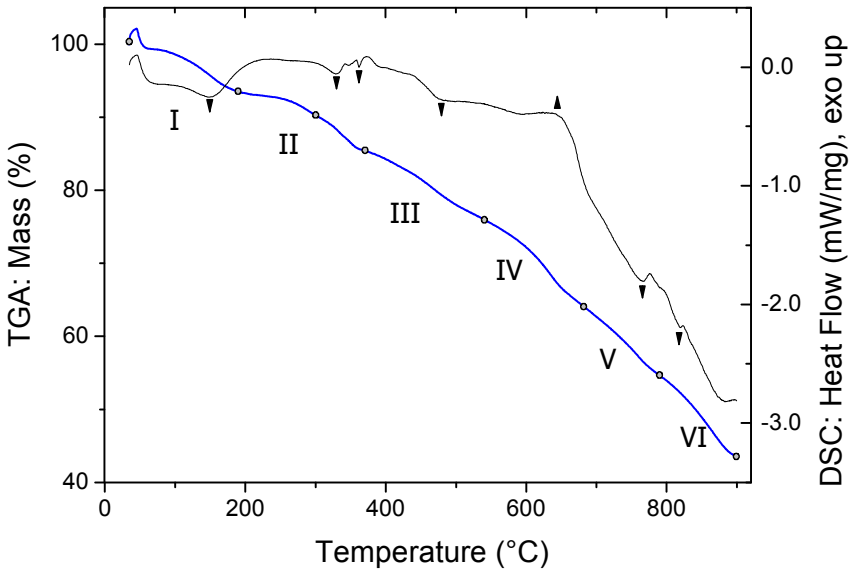

Figure 4.3 TGA (blue line) and DSC (black line) of PB sample carried out under argon atmosphere with a heating rate of 5 °C/min. Roman numbers indicate the different stages of the decomposition, up and down arrows indicate the exothermal or endothermic effect respectively, and the grey circles indicate the temperatures where samples were taken.

In contrast, the mass decreasing in the other steps (III to VI) is accompanied by release of nitrogen (N_2, m/z = 28) and carbon dioxide basically, during the iron carbides formation.

Table 4.2 Mass loss estimated from TG curve for PB sample heated up to 900 °C in Ar.

Step	Temperature range (°C)	Mass loss (%)
I	35 – 189	-6.39
II	189 – 361	-7.85
III	361 – 505	-7.96
IV	505 – 649	-11.01
V	649 – 775	-10.98
VI	775 – 899	-12.19
	Total:	-56.39

4.3.3 XRD "*ex situ*" patterns from samples heated in argon at selected temperatures

The phase composition of the samples taken at different stages of decomposition was variable, showing clearly not only the Prussian blue thermal decomposition, but also the transformation of iron carbides and their decomposition (Fig. 4.4).

The XRD pattern of sample PB190 is basically the same as the starting PB, and still present traces of jarosite. At 300 °C, the Prussian blue is dehydrated and maintains its crystalline structure unchanged. After 350 °C the decomposition of PB starts, and from the diffractogram of sample PB370 were identified as iron(II) hexacyanoferrate(II) ($Fe_2[Fe(CN)_6]$), also known as ferrous ferrocyanide or Berlin white (BW), potassium sulfate (K_2SO_4) and ferric sulfate ($Fe_3(SO_4)_3$), both from the thermal decomposition of jarosite [24]. Also is surprising the presence of the organic phase carbamide or urea ($CO(NH_2)_2$).

In samples PB540 and PB680, the presence of ferrous ferrocyanide seems to be dominant without any traces of the original Prussian blue. Other phases present in sample PB540 are iron carbide (Fe_2C, orthorhombic (ζ, *Pbcn*) and hexagonal (ε', $P6_322$)), iron oxalate (FeC_2O_4), iron sulfate (Fe_2SO_4), and trisulfur dinitrogen dioxide ($S_3N_2O_2$), while in sample PB680 are present iron carbides (both Fe_2C; Fe_7C_3 $P6_3mc$), and $S_3N_2O_2$.

At higher heating temperatures, the samples almost exclusively show different iron carbides in the phase composition. In sample PB790 were identified Fe_2C, Eckstrom-

Adcock carbide (Fe_7C_3), Hägg carbide (Fe_5C_2, space group *C*2/*c*), cementite (Fe_3C, space group *Pnma*), and also small amount of $K_4[Fe(CN)_6]$. In sample PB900 the predominant phase is cementite, also diffraction lines from metallic iron (α-Fe) were present.

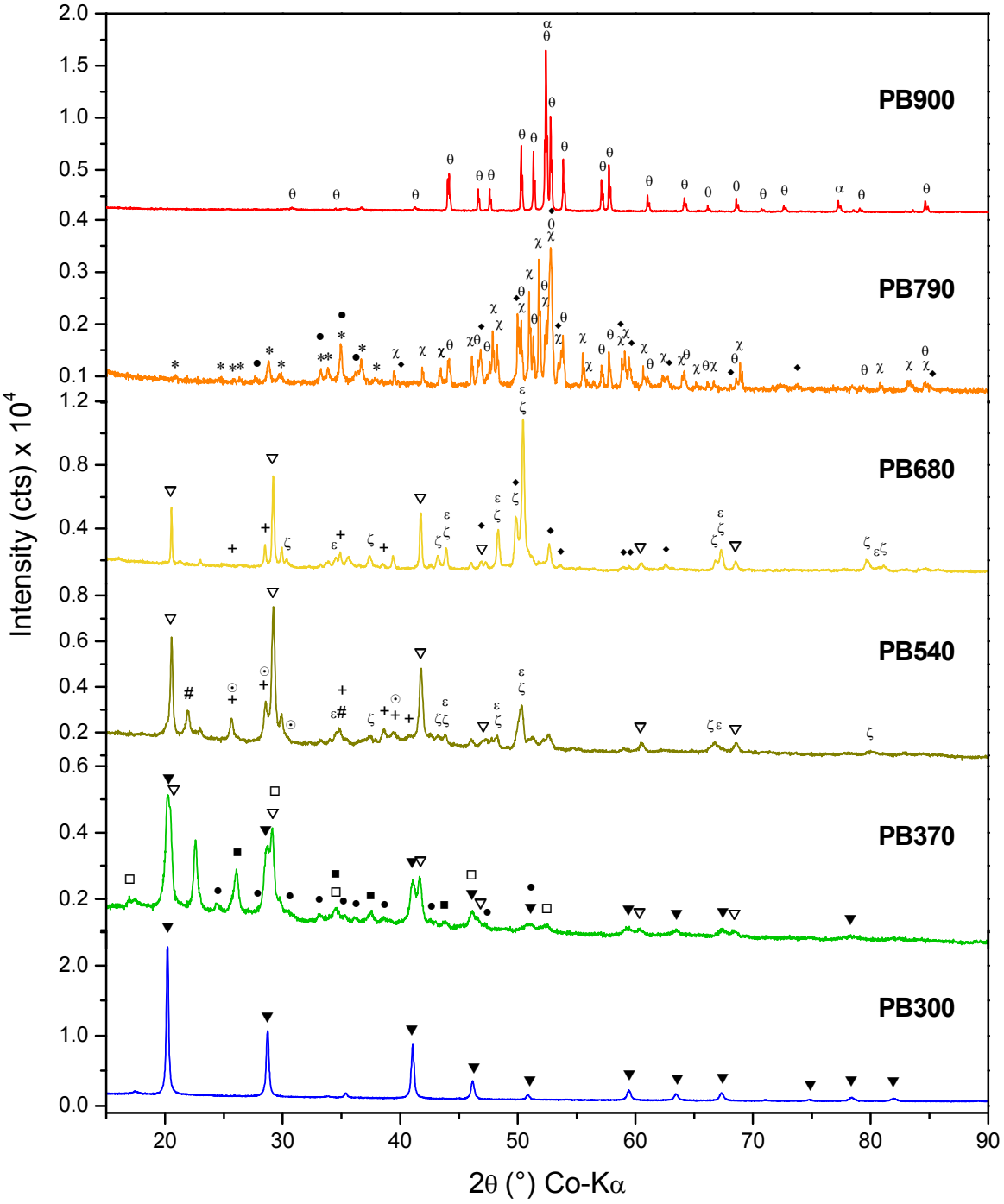

Figure 4.4 XRD patterns for samples heated up to selected temperatures under Ar. The symbols represent the identified phases: $Fe_4[Fe(CN)_6]_3$ (▼), $Fe_2[Fe(CN)_6]$ (▽), $Fe_{2+x}C$ (ε'), Fe_2C (ζ), Fe_7C_3 (◆), Fe_2C_5 (χ), Fe_3C (θ), Fe^0 (α), $K_4Fe(CN)_6$ (*), K_2SO_4 (●), $CO(NH_2)_2$ (■), $Fe_2(SO_4)_3$ (□), $FeSO_4$ (⊙), $Fe_2C_2O_4$ (#), $S_3N_2O_2$ (+).

4.3.4 Mössbauer spectra of the samples heated in argon at selected temperatures

Mössbauer spectra at room temperature were taken for all PB samples heated up to the chosen temperatures (Fig. 4.5). Mössbauer spectrum of sample PB190 is similar to the spectrum of unheated PB sample; it was fitted with one singlet (IS = -0.14 mm/s, 48.6%) and one doublet (IS = 0.40 mm/s, QS = 0.22 mm/s, 51.4%) both assigned to ferrous and ferric ions in PB structure. The spectrum of sample PB300 (Fig. 4.5) is also similar to this of sample PB190, having a similar Mössbauer parameters (Table 4.3).

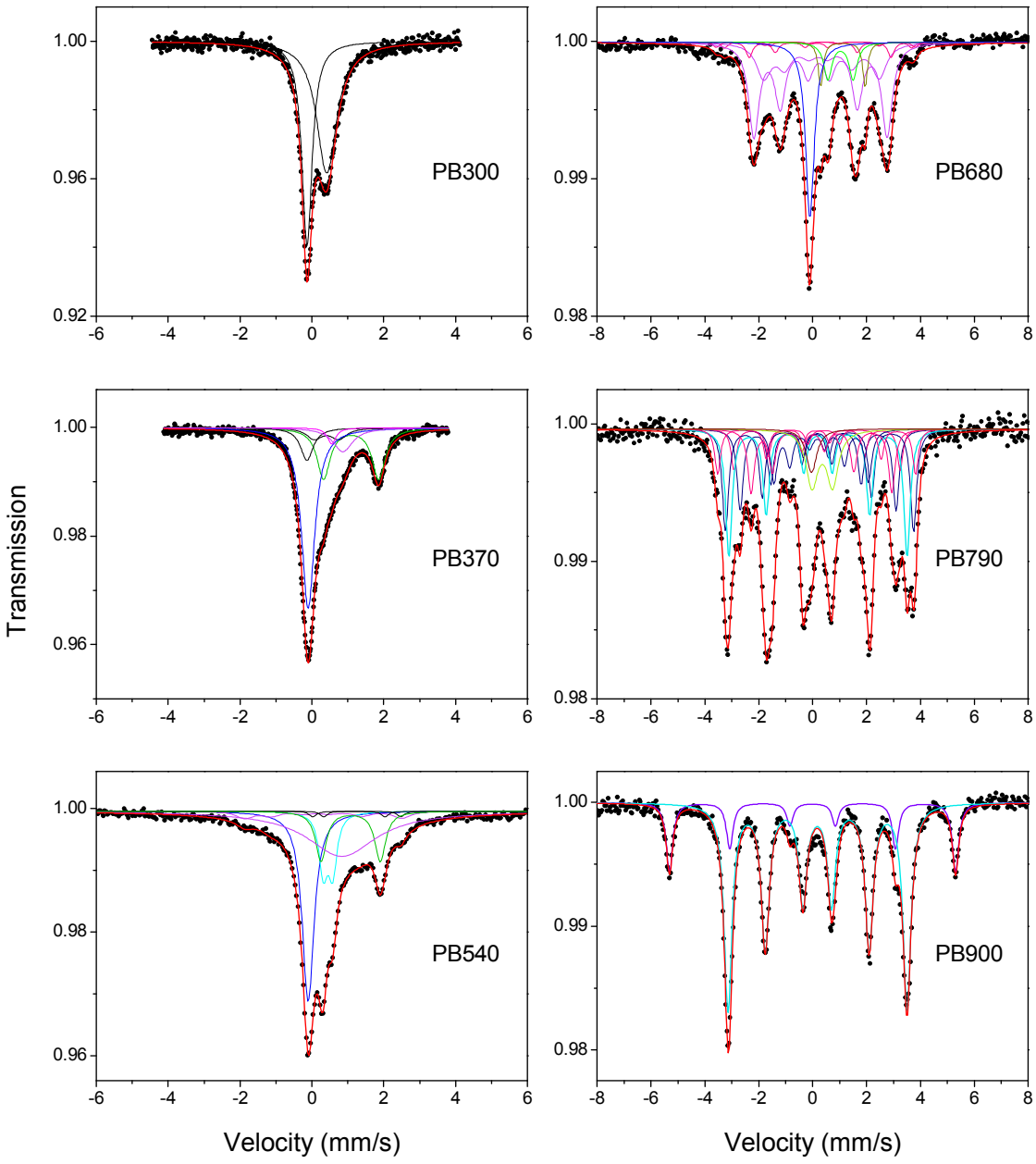

Figure 4.5 Mössbauer spectra for samples heated up to selected temperatures under Ar.

With the raising of temperature the Mössbauer spectra become more complicated, as can be seen for samples PB370 and PB540 (Fig. 4.5). Mössbauer spectrum of sample PB370 was fitted with four singlets and two doublets; one singlet (L1) and one doublet (D1) are abscribed to the undecomposed PB, where the bigger QS suggest a bigger strain in the PB structure [25]; the other couple of singlet (L2) and doublet (D2) are assigned to Berlin white (BW); there is one singlet (L3) abscribed to ferric ion in octahedral sites of ferric sulfate ($Fe_2(SO_4)_3$) [26], the last singlet (L4) with a broad linewidth correspond to ferrous ions from unknown provenance.

Sample PB540 has a Mössbauer spectrum that was fitted with one sextet, four doublets and two singlets. As in the previous sample, it is possible to identify BW (D2, L1), where the doublet has a bigger value of quadrupole splitting, denoting a deformation of the octahedral site of ferrous ions. It was not possible to assign the doublet D1 to any compound identified in the XRD pattern, where the ferric ions are most probably to have tetrahedral coordination. Doublet D3 is assigned to Fe^{2+} in octahedral sites of ferrous sulfate (Fe_2SO_4), produced from the reduction of ferric sulfate. Surprising is the presence of ferrous oxalate at this high temperature (D4), when it normally decompose in inert atmosphere at around 370 °C [27]. The singlet L2 with a very wide linewidth, which has a similar value to singlet L4 in sample PB370, seems to reflect the arrangement of iron cations prior to the formation of iron carbides, fact that agrees with the poor crystallization observed in the respective XRD pattern; where the presence of a sextet shows the small fraction (5.8 %) of crystallized Fe_2C. Then, relating to the singlet L4 in the previous sample, at 370 °C there is an agglomeration of iron cations with a poor arrangement.

Sample heated up to 680 °C (PB680) has a Mössbauer spectrum, in which a doublet (D1) and singlet (L1) belonging to BW are still present; and a doublet (D2) corresponding to ferrous ion in octahedral coordination is likely to belong to some unidentified iron compound. Three sextets (S1, S2, S3) with hyperfine fields varying between 16.3 – 22.9 T are ascribed to the hexagonal iron carbide with three inequivalent sites (Fe_7C_3) [28–31]. The last two sextets (S4, S5) are assigned to Fe_2C, representing the major contribution to the spectrum (64.8 %).

There is a disagreement of the found values of hyperfine magnetic field of Fe_2C (13.3 – 15.3 T) in comparison to values published by other authors. These values are smaller than those measured for hexagonal ε-carbides (between 17 and 24 T) [28,32].

Table 4.3 Mössbauer parameters obtained from the fit of spectra for samples PB300, PB370, PB540, PB680, PB790, and PB900 heated under Ar atmosphere.

	Phase	IS (mm/s)	QS (mm/s)	W (mm/s)	B (T)	Area (%)
PB300						
D2	PB Fe^{3+} (HS)	0.41	0.09	0.66	-	55.8
L1	PB Fe^{2+} (LS)	-0.14	-	0.34	-	44.2
PB370						
D1	PB Fe^{3+} (HS)	0.41	0.68	0.52	-	6.6
D2	BW Fe^{2+} (HS)	1.09	1.53	0.44	-	26.2
L1	PB Fe^{2+} (LS)	-0.14	-	0.43	-	8.1
L2	BW Fe^{2+} (LS)	-0.10	-	0.44	-	46.8
L3	$Fe_2(SO_4)_3$	0.55	-	0.28	-	2.7
L4	Fe^{2+}	0.86	-	0.67	-	9.4
PB540						
S1	Fe_2C	0.22	0.19	0.58	13.6	5.8
D1	Fe^{3+}	0.45	0.26	0.28	-	12.3
D2	BW Fe^{2+} (HS)	1.08	1.65	0.36	-	13.2
D3	$FeSO_4$	1.25	2.44	0.25	-	1.0
D4	$Fe_2C_2O_4$	1.18	1.70	0.25	-	1.0
L1	BW Fe^{2+} (LS)	-0.10	-	0.39	-	27.9
L2	Fe^{2+}	0.83	-	2.33	-	38.7
PB680						
S1	Fe_7C_3	0.24	-0.25	0.28	22.9	1.5
S2	Fe_7C_3	0.32	-0.23	0.28	21.6	1.7
S3	Fe_7C_3	0.21	0.14	0.28	16.3	4.2
S4	Fe_2C	0.26	0.07	0.47	15.3	42.9
S5	Fe_2C	0.26	0.13	0.65	13.3	21.9
D1	BW Fe^{2+} (HS)	1.12	1.65	0.22	-	4.7
D2	Fe^{2+}	1.03	0.94	0.36	-	6.5
L1	BW Fe^{2+} (LS)	-0.10	-	0.38	-	16.5
PB790						
S1	Fe_7C_3	0.28	-0.26	0.25	22.8	7.0
S2	Fe_7C_3	0.15	0.03	0.25	19.1	6.3
S3	Fe_7C_3	0.17	0.30	0.29	16.2	11.5
S4	Fe_5C_2	0.21	0.10	0.27	21.7	17.2
S5	Fe_5C_2	0.16	0.08	0.28	18.0	14.0
S6	Fe_5C_2	0.24	0.15	0.30	10.9	9.8
S7	Fe_3C	0.20	0.00	0.29	20.5	22.4
D1	Fe^{3+} (SP)	0.36	0.76	0.52	-	8.9
L1	$K_4[Fe(CN)_6]$	-0.04	-	0.46	-	3.0
PB900						
S1	Fe^0	0.00	0.00	0.29	33.0	20.0
S2	Fe_3C	0.18	0.01	0.35	20.6	80.0

Notes: IS: isomer shift, QS: quadrupole splitting, W: experimental linewidth, HS: high spin, LS: low spin, D: doublet, L: singlet, SP: superparamagnetic.

The lowest hyperfine magnetic field of 17 T has been obtained by Niemantsverdriet *et al.* [33] and Amelse *et al.* [34], both describe the iron carbide as hexagonal iron carbide ε'-$Fe_{2.2}C$. In samples PB540 and PB680, the hyperfine values are even smaller, where an alternative ordering of iron and carbon atoms in the structure or a different crystalline symmetry can be the reason for a smaller hyperfine field [35]. It is known that iron-carbides and iron-nitrides are isostructural [36]; the XRD pattern measured by Niemantsverdriet *et al.* [33] is almost identically to the one described by Barton and Gale [37], and very close to the pattern of ζ-Fe_2N (space group *Pbcn*), then one of the iron carbides identified in PB680 sample can be better explain by the orthorhombic carbide ζ-Fe_2C.

In sample PB790, the spectra was fitted with 3 sextets (S1, S2, S3, sum of subspectral areas: 24.8 %) for Fe_7C_3, 3 sextets (S4, S5, S6, sum of subspectral areas: 41 %) corresponding to three inequivalent magnetic sites of Fe_5C_2 [30,33,38], a one sextet (S7) ascribed to cementite [28,39]. Cementite has two magnetic sites, but because its Mössbauer parameters have very close values it was fitted with only one sextet [30]. The presence of one doublet (D1) can be assigned to Fe^{3+} or a superparamagnetic phase (SP) [38]. Finally, one singlet (L1) is ascribed to potassium ferrocyanide, but its presence at this high temperature is very unusual because this compound normally decompose around 400 °C.

The last Mössbauer spectrum (sample PB900), is quite simple to fit with two sextets, one for metallic iron (S1) and the other one for cementite (S2).

4.3.5 Phase composition of samples heated at 680 °C with variable layer thickness

Samples of PB with different masses (layer thickness) were heated up to 680 °C under Ar atmosphere: PB680-20 (20 mg, 1.55 mm), PB680-10 (10 mg, 0.78 mm), and PB680-5 (5 mg, 0.39 mm). Phase composition was monitored using XRD and MS (Fig. 4.6).

The phase composition after the heating was different for the sample with the thinnest layer thickness (PB680-5), where it is composed almost exclusively for iron carbide ($Fe_{2+x}C$). On the other hand, the samples with thicker layer thickness (PB680-20 and PB680-10) have an almost identical phase composition, as can be seen from the XRD patterns and Mössbauer spectra; there were identified two different iron carbides (Fe_7C_3

and Fe_2C), ferrous ferrocyanide (BW), and some unknown phases as indicated by small diffraction lines in XRD pattern and 2 doublets in the Mössbauer spectrum.

The values of Mössbauer parameters for samples PB680-20 and PB680-10 are similar (Table 4.4), in both samples the major subspectral contributions comes from Fe_2C (mixed disordered hexagonal ε'-$Fe_{2+x}C$ and orthorhombic ζ-Fe_2C): 59.9 % for sample PB680-20 and 64.8 % for sample PB680-10.

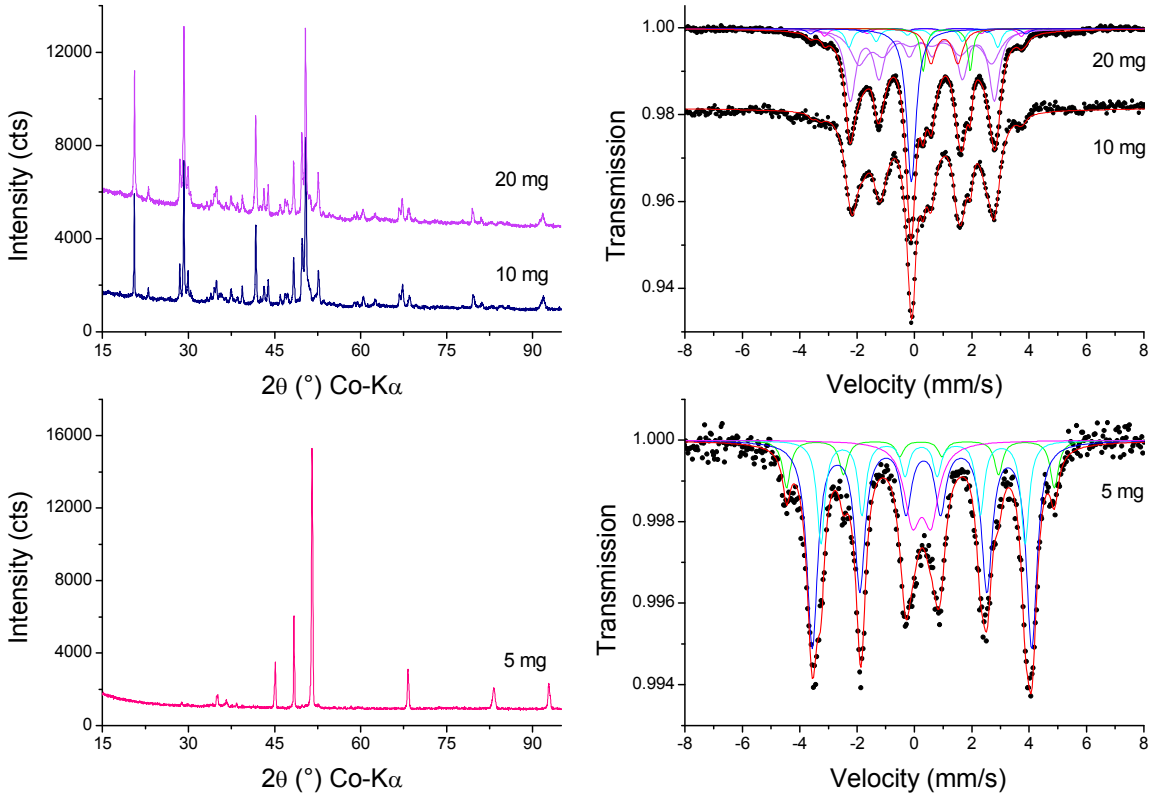

Figure 4.6 XRD patterns (left side) and Mössbauer spectra (right side) for samples with different masses heated up 680 °C under Ar.

In contrast, sample PB680-5 has a dominant component as showed by the XRD pattern, while the fitting of the Mössbauer spectrum shows three sextets (sum of subspectra areas: 85.3 %) and one doublet. The high values of magnetic hypefine field suggest that iron carbide is a pure hexagonal phase with ordered structure ε-$Fe_{2+x}C$. The doublet present in the spectra can be assigned to an unidentified iron compound or to a superparamagnetic component of the iron carbide [28].

Table 4.4 Mössbauer parameters obtained from the fit of spectra for sample PB680 with different masses heated under Ar atmosphere.

PB680	Phase	IS (mm/s)	QS (mm/s)	W (mm/s)	B_{hf} (T)	Area (%)
20 mg						
S1	Fe_7C_3	0.25	-0.24	0.33	23.3	2.0
S2	Fe_7C_3	0.32	-0.04	0.28	21.3	2.4
S3	Fe_7C_3	0.24	0.14	0.28	16.1	5.9
S4	Fe_2C	0.25	0.06	0.44	15.6	34.1
S5	Fe_2C	0.31	0.13	0.72	14.4	25.8
D1	BW Fe^{2+} (HS)	1.13	1.65	0.22	-	5.2
D2	Fe^{2+}	1.05	0.94	0.41	-	7.8
L1	BW Fe^{2+} (LS)	-0.11	-	0.39	-	16.7
10 mg						
S1	Fe_7C_3	0.24	-0.25	0.28	22.9	1.5
S2	Fe_7C_3	0.32	-0.23	0.28	21.6	1.7
S3	Fe_7C_3	0.21	0.14	0.28	16.3	4.2
S4	Fe_2C	0.26	0.07	0.47	15.3	42.9
S5	Fe_2C	0.26	0.13	0.65	13.3	21.9
D1	BW Fe^{2+} (HS)	1.12	1.65	0.22	-	4.7
D2	Fe^{2+}	1.03	0.94	0.36	-	6.5
L1	BW Fe^{2+} (LS)	-0.10	-	0.38	-	16.5
5 mg						
S1	Fe_2C	0.22	-0.02	0.33	29.0	9.4
S2	Fe_2C	0.29	-0.06	0.44	23.8	52.2
S3	Fe_2C	0.27	0.06	0.35	22.2	23.7
D1	Fe^{3+}	0.25	0.64	0.70	-	14.7

Notes: IS: isomer shift, QS: quadrupole splitting or quadrupole shift, W: experimental linewidth, HS: high spin, LS: low spin, D: doublet, L: singlet.

4.3.6 Morphology of the samples heated under argon atmosphere

The samples heated up to different temperatures have different morphologies (Fig. 4.7). For example sample PB540 have a granular structure, apparently composed by the same material; the elemental composition show the presence of Na, S, K besides Fe and C. It helped to identify Fe_2SO_4 and $S_3N_2O_2$ in the XRD pattern, but it was not possible to identify any phase with the elements Na or K.

The SEM photography of sample PB680 show two different sizes of particles (bigger ones ~ 150 nm and small ones < 50 nm), but it was not possible to distinguish differences in composition because the EDS profiles showed almost identical chemical composition for both particles.

Sample PB790 have a different morphology in comparison with the other samples, there were observed rounded particles, but also lengthened particles with approximated dimensions of 5 μm x 500 nm, which are more likely to be monoclinic iron carbide χ-Fe_5C_2.

The last sample, PB900 has also particles with different sizes, according to the XRD pattern both phases (Fe_3C and α-Fe) are very well crystallized, being cementite the prevailing phase (83.1 %). EDS analysis of the sample showed that the rounded particles are compound almost exclusively of Fe and C, and the small particles have K and S in addition to Fe and C (see appendix 11). However no crystalline phase containing K and S was identify from the XRD pattern. Additional TEM photography shows the rounded particles have a core shell structure, and it suggests that the particles have a cementite core with a thin shell of metallic iron (Fig. 4.7).

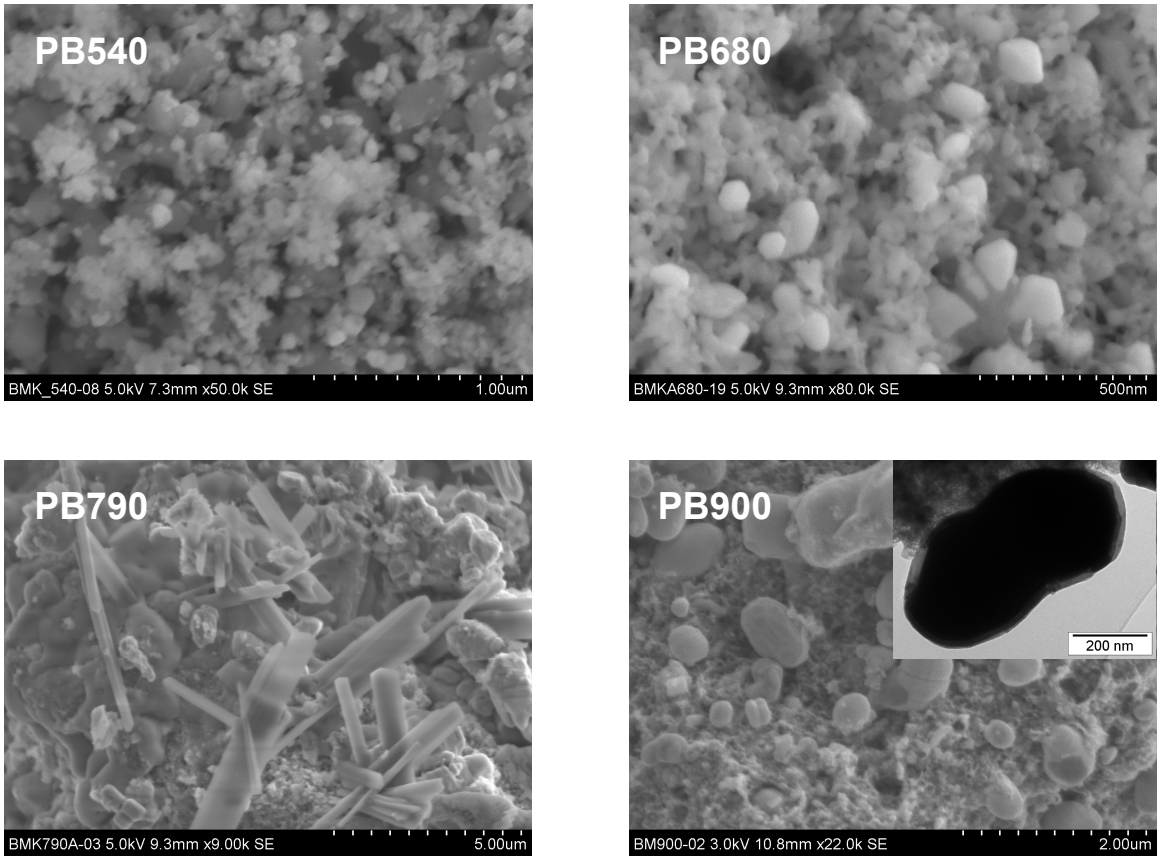

Figure 4.7 SEM pictures showing the sample morphology of samples PB540, PB680, PB790, and PB900. The inset in PB900 shows a close view of a single particle with core-shell structure.

4.3.7 PB under nitrogen atmosphere: XRD "*in situ*" measurements

The XRD *in situ* allowed following the thermal decomposition under nitrogen atmosphere of a PB sample with a layer thickness of 0.5 mm (details of the experiment are in table 4.1). The resultant 43 diffractograms were grouped in 7 groups which are well corresponded with the steps observed in TGA graph (for details see appendix 10). Selected diffractograms from each group are shown in Fig. 4.8.

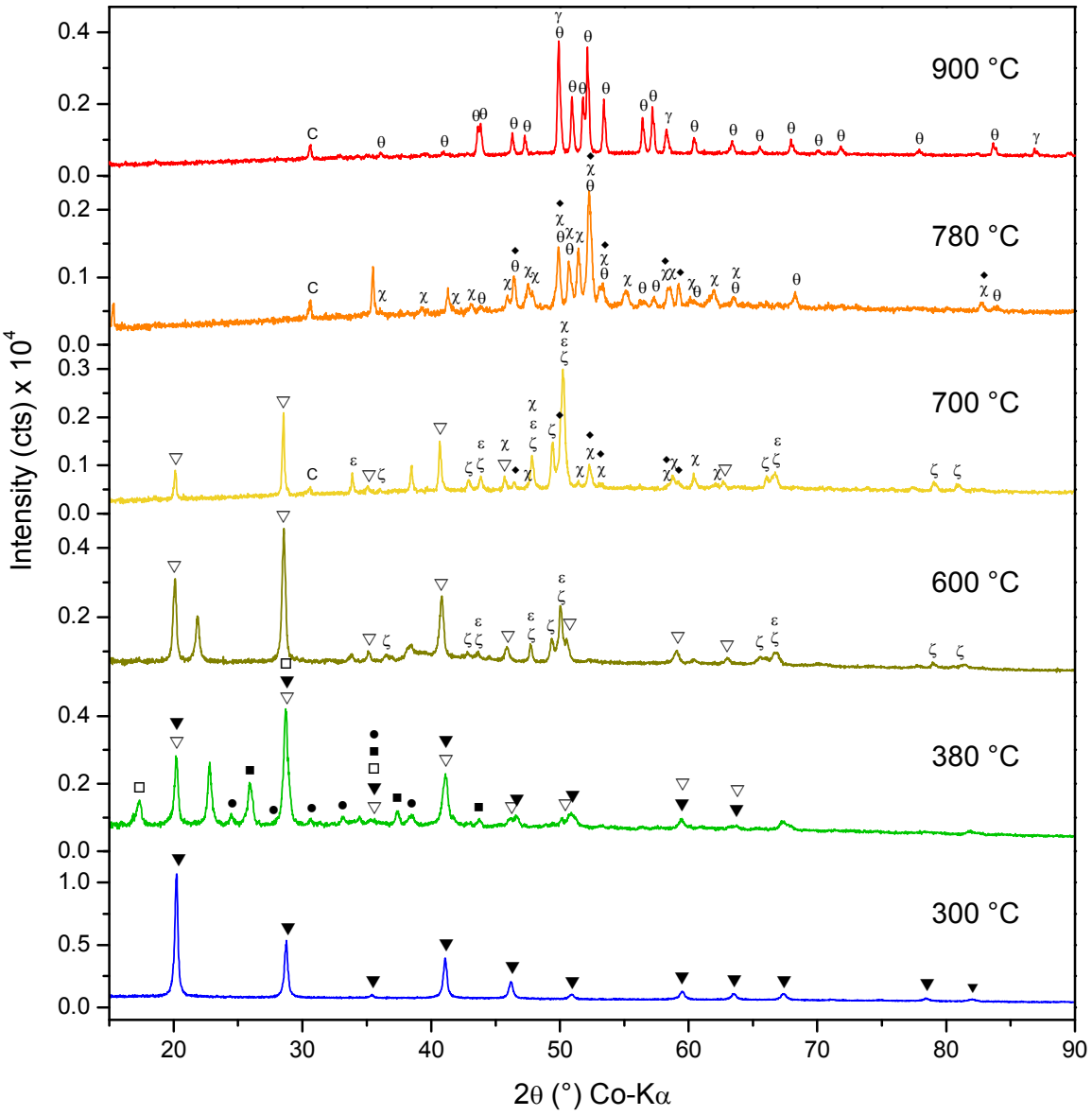

Figure 4.8 Selected XRD patterns from *in situ* measurements of Prussian blue heated under N_2. The average heating rate was 2 K/min. The symbols represent the identified phases: $Fe_4[Fe(CN)_6]_3$ (▼), $Fe_2[Fe(CN)_6]$ (▽), $Fe_{2+x}C$ (ε'), Fe_2C (ζ), Fe_7C_3 (◆), Fe_2C_5 (χ), Fe_3C (θ), Fe^0 (α),K_2SO_4 (●), $CO(NH_2)_2$ (■), $Fe_2(SO_4)_3$ (□).

Quantitative phase analysis was performed in all diffractograms using the Rietveld method. For the analysis were considered only the known phases, excluding the unidentified phases in the XRD patterns. The results show the transformation of PB into BW, and after its decomposition the formation and posterior transformation of iron carbides, leading to the final products cementite, iron and carbon (Fig. 4.9).

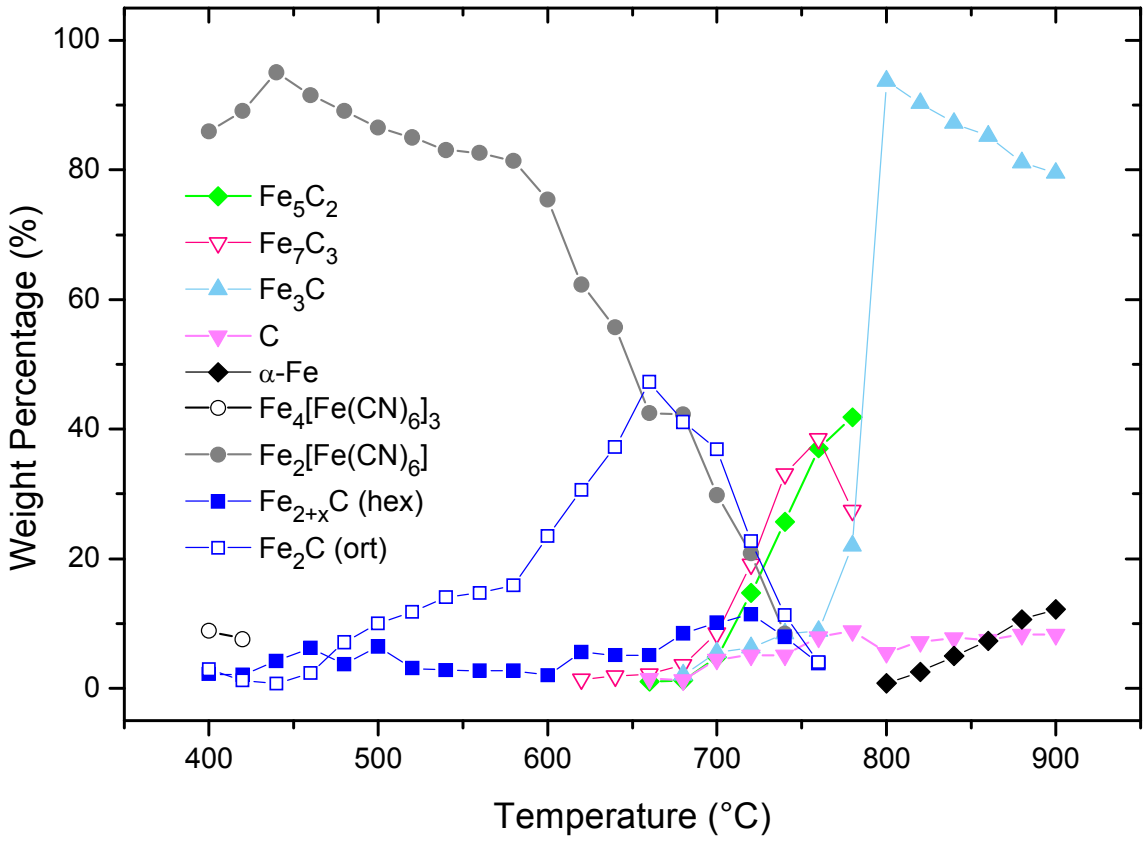

Figure 4.9 Results of Rietveld analysis of XRD patterns collected *in-situ* during the thermal decomposition of commercial Prussian blue under N_2 atmosphere. The final products of decomposition are Fe_3C, Fe and C.

4.4 Discussion of Results

4.4.1 Similitude in phase composition from samples in argon and nitrogen

It was investigated the influence of atmosphere on thermal decomposition of PB. Additionally to the samples heated in argon atmosphere, two samples were heated up to 790 °C and 900 °C in nitrogen atmosphere under the same experimental conditions. The samples were labeled as PB790-Ar, PB900-Ar, PB790-N_2, and PB900-N_2.

According to the diffractograms, there are no differences in the phase composition of the samples heated in different atmospheres and temperatures (Fig. 4.10, upper side). In samples PB790-Ar and PB790-N_2 were found a mixture of iron carbides as majority phases, potassium sulfate and potassium ferrocyanide as minor phases. Cementite, iron, and carbon, were found in samples PB900-Ar and PB900-N_2. Rietveld analysis was performed on all aforementioned samples considering only the iron and iron carbides, giving the following quantitative results: Fe_7C_3 (25.1 %), Fe_5C_2 (43.5 %), Fe_3C (31.4 %) for sample PB790-Ar; Fe_7C_3 (39.4 %), Fe_5C_2 (38.0 %), Fe_3C (22.6 %) for sample PB790-N_2; Fe_3C (83.1 %), α-Fe (16.9 %) for sample PB900-Ar; and Fe_3C (89.3 %), α-Fe (10.7 %) for sample PB900-N_2.

Difference in the percentage contribution to samples phase composition, suggest a slower thermal decomposition of PB when it is heated in nitrogen atmosphere than in argon, as can be inferred from XRD in-situ measurements (Fig. 4.9).

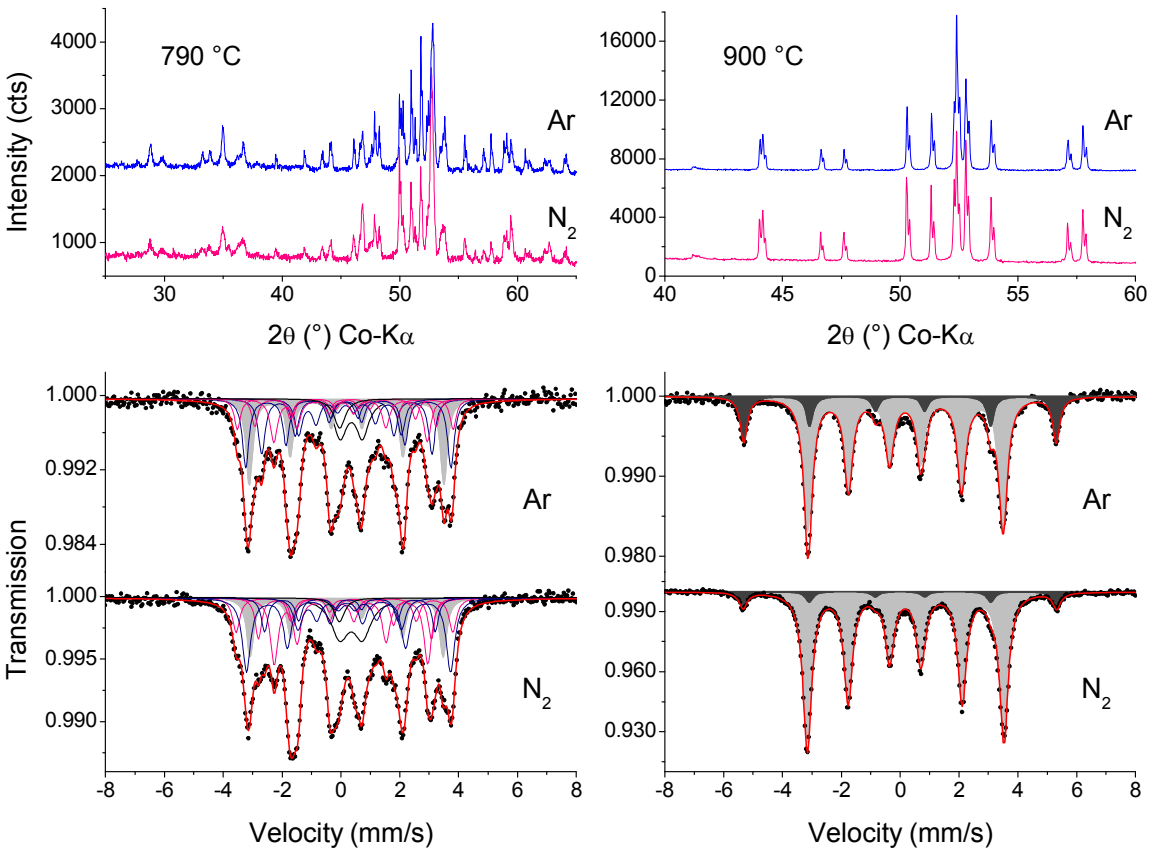

Figure 4.10 XRD patterns (upper side) and Mössbauer spectra (lower side) for PB samples heated up to 790 °C (left side) and 900 °C (right side) under argon (Ar) and nitrogen (N_2) atmospheres.

Mössbauer spectra of the samples PB790-Ar and PB790-N_2 are also very similar (Fig. 4.10, lower left side), and quantitatively follow the same trend as the results from XRD. The sub-spectral contributions of iron carbides are as follow: Fe_7C_3 (24.8 %), Fe_5C_2 (41.0 %), Fe_3C (22.4 %) for sample PB790-Ar; Fe_7C_3 (34.3 %), Fe_5C_2 (38.2 %), Fe_3C (14.6 %) for sample PB790-N_2. Both spectra present a doublet assigned to a paramagnetic component with very similar hyperfine parameters (table 4.5), where the sub-spectral area is slightly bigger (+2.2 %) in the case of sample heated under nitrogen.

It is clear from the spectra of samples PB900-Ar and PB900-N_2 the presence of two sextets for Fe_3C and α-Fe (Fig. 4.10, lower right side). The hyperfine parameters for the two sextets on both samples are identical, where the only difference is the less amount of α-Fe in the sample heated under nitrogen, as was previously explained (table 4.5).

Table 4.5 Mössbauer parameters obtained from the fit of spectra for samples PB790 and PB900 heated under Ar and N_2 atmospheres.

	Phase	IS (mm/s)	QS (mm/s)	W (mm/s)	B_{hf} (T)	Area (%)
PB790-Ar						
S1	Fe_7C_3	0.28	-0.26	0.25	22.8	7.0
S2	Fe_7C_3	0.15	0.03	0.25	19.1	6.3
S3	Fe_7C_3	0.17	0.30	0.29	16.2	11.5
S4	Fe_5C_2	0.21	0.10	0.27	21.7	17.2
S5	Fe_5C_2	0.16	0.08	0.28	18.0	14.0
S6	Fe_5C_2	0.24	0.15	0.30	10.9	9.8
S7	Fe_3C	0.20	0.00	0.29	20.5	22.4
D1	Fe^{3+} (SP)	0.36	0.76	0.52	-	8.9
L1	$K_4[Fe(CN)_6]$	-0.04	-	0.46	-	3.0
PB790-N_2						
S1	Fe_7C_3	0.28	-0.30	0.30	22.9	8.5
S2	Fe_7C_3	0.11	0.05	0.26	18.4	8.9
S3	Fe_7C_3	0.18	0.32	0.31	16.2	16.9
S4	Fe_5C_2	0.23	0.07	0.35	21.6	21.4
S5	Fe_5C_2	0.28	0.06	0.27	18.0	7.6
S6	Fe_5C_2	0.25	0.11	0.34	10.9	8.9
S7	Fe_3C	0.20	0.00	0.30	20.4	14.6
D1	Fe^{3+} (SP)	0.35	0.77	0.71	-	11.1
L1	$K_4[Fe(CN)_6]$	-0.05	-	0.42	-	2.1
PB900-Ar						
S1	Fe^0	0.00	0.00	0.29	33.0	20.0
S2	Fe_3C	0.18	0.01	0.35	20.6	80.0
PB900-N_2						
S1	Fe^0	0.00	0.00	0.32	33.1	8.1
S2	Fe_3C	0.18	0.01	0.36	20.8	91.9

Notes: IS: isomer shift, QS: quadrupole splitting or quadrupole shift, W: experimental linewidth, HS: high spin, LS: low spin, D: doublet, L: singlet, SP: superparamagnetic.

4.4.2 Dependence of phase composition on heating rate

As described above (table 4.1), a second set of *in situ* XRD measurements were done on PB sample heated up to 800 °C with an average heating rate of 8 K/min. The resultant diffractograms are shown in Fig. 4.11. From the figure, it is possible to see the changes of phase composition with the increase of temperature; from room temperature to 300 °C the PB structure remains unaltered, and after 300 °C starts the transformation to BW. From Rietveld quantitative analysis: at 300 °C there is 61.6 % of the starting PB and 38.4 % of BW; at 400 °C the PB percentage decrease to 30.8 % and there is an increase of BW to 56.8 %, at this temperature also the BW decomposition leads to the formation of hexagonal iron carbide ε'-$Fe_{2+x}C$ (12.4 %). At 500 °C the phase composition is the same, where the weight percentage of each phase is: 12.1 % for PB, 46.9 % for BW, and 41.4 % for ε'-$Fe_{2+x}C$.

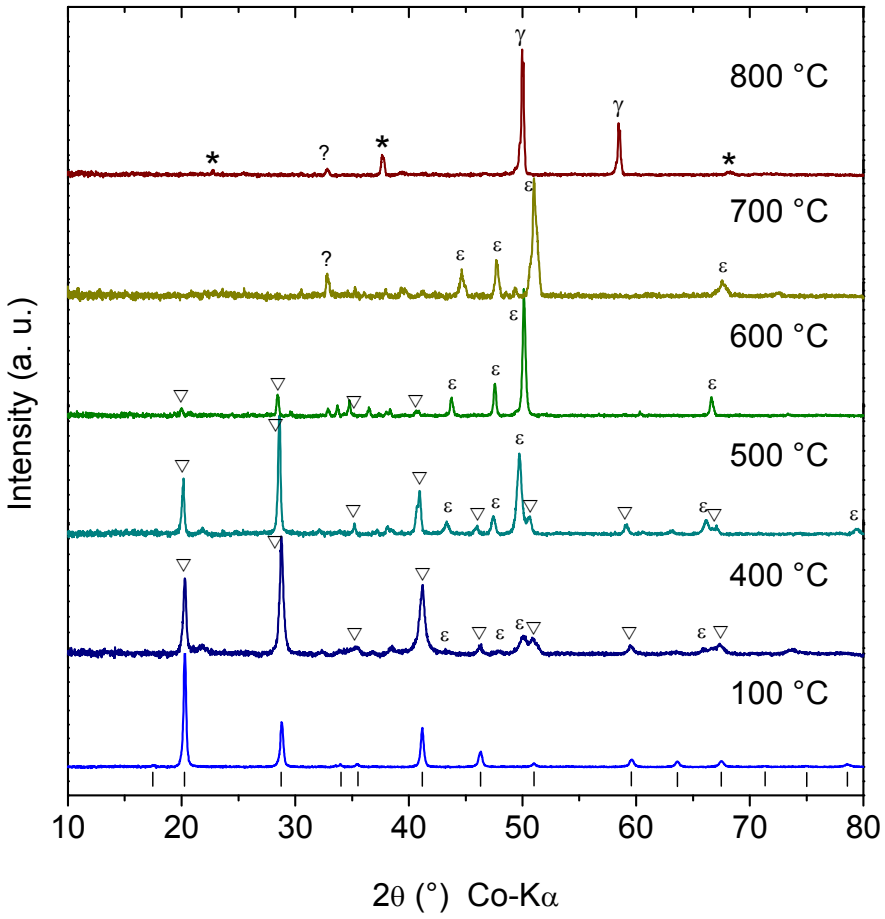

Figure 4.11 Selected XRD patterns from *in situ* measurements of Prussian blue heated under N_2. The average heating rate was 8 K/min. The symbols represent the identified phases: $Fe_4[Fe(CN)_6]_3$ (|), $Fe_2[Fe(CN)_6]$ (▽), $Fe_{2+x}C$ (ε'), Fe^0 (γ), $KFeO_2$ (*).

At 600 °C the remains of PB transformed to BW (17.2 %), and the presence of ε'-$Fe_{2+x}C$ is majority (82.8 %); they are also small unidentified diffraction lines that probably belong to some potassium compound. Neglecting the small contribution of unknown phases, it can be said that at 700 °C the phase composition is compose exclusively of ε'-$Fe_{2+x}C$. This hexagonal iron carbide shows a shifting of the diffraction lines, and can be interpreted as thermal expansion of the unit cell prior to decomposition. Finally, at 900 °C the predominant phase if γ-Fe and there is also diffraction lines belonging to $KFeO_2$.

Comparing both in situ measurements on PB sample heated under nitrogen atmosphere (table 4.1), it is seen that the thermal decomposition of PB occurs above 300 °C in both cases. However, the phase composition is quite different at higher temperatures; where the slower heating rate (2 K/min) allows the formation of different iron carbides and finally the formation of zerovalent iron (ZVI), whereas a faster heating rate (8 K/min) was obtained exclusively hexagonal iron carbide (ε'-$Fe_{2+x}C$) with a posterior formation of iron. This can be resumed by the following schema.

2 K/min: $Fe_4[Fe(CN)_6]_3 \rightarrow Fe_2[Fe(CN)_6] \rightarrow Fe_2C \rightarrow Fe_5C_2, Fe_7C_3 \rightarrow Fe_3C \rightarrow Fe$

8 K/min: $Fe_4[Fe(CN)_6]_3 \rightarrow Fe_2[Fe(CN)_6] \rightarrow Fe_{2+x}C \rightarrow Fe$

4.4.3 Influence of layer thickness on phase composition

From the results shown in Fig. 4.6, the variation of the sample mass appears to play an important role in the thermal decomposition of Prussian blue. It agrees with the concept of "critical sample layer thickness (weigth)" introduced by Hermanek and Zboril [22]. These authors studied the thermal decomposition thermal decomposition of iron(II) acetate, where for mass sample of 50 mg was obtained pure hematite, while for mass sample of 500 mg was obtained pure maghemite. Similar results were also obtained from Prussian blue heated in air, with narrow sample layer (1 mm) was obtained a mixture of iron oxides (β-Fe_2O_3 and maghemite), whereas almost pure maghemite was obtained with a thick sample layer (4 mm) [20,22].

Similarly, for sample PB680, when the used sample mass was above 10 mg (layer thickness 0.78 mm) was obtained a mix of iron carbides (Fe_7C_3, ε'-$Fe_{2+x}C$, ζ-Fe_2C) and

ferrous ferrocyanide as decomposition products; whereas only ε-$Fe_{2+x}C$ was obtained when sample mass was 5 mg (layer thickness 0.39 mm). The absence of other iron carbides and ferrous ferrocyanide in sample PB680-5, suggest that the decomposition reaction was faster in comparison to the other samples (PB680-10 and PB680-20). In fact, this can be an advantage because it allows the synthesis of pure iron carbide phase.

4.4.4 Relationship between iron-carbide phases

Above 300 °C most of the PB has been transformed into ferrous ferrocyanide (BW), and when it decomposes iron carbides are formed. From the results showed in figures 4.8 and 4.9, all the known iron carbides are present when PB sample if heated up to temperatures greater than 400 °C in reducing atmosphere.

The first formed iron carbides were the orthorhombic Fe_2C and hexagonal $Fe_{2+x}C$. They are first formed slowly up to 580 °C, then from 580 °C to 660 °C there is an steadily increase of the amount of Fe_2C indicating a faster decomposition of BW, in the same temperature range (from 620 °C) it can be observed the formation of the hexagonal iron carbide Fe_7C_3. It can be explained by the following equations:

$$7\ Fe_2C \rightarrow 2\ Fe_7C_3 + C \quad (1)$$

$$3\ Fe_{2+x}C \rightarrow Fe_7C_3, \text{ where } x \leq 0.33 \quad (2)$$

With the increase of temperature, from 620 °C to 760 °C, the weight percentage of Fe_2C continually decrease and at the same time there is a small increase of $Fe_{2+x}C$. Another iron carbide has been formed, Fe_5C_2, and its weight percentage grows steeply at the same rate as Fe_7C_3, the percentage of both iron carbides increase to the detriment of Fe_2C, this suggest a transformation of the primary iron carbide (Fig. 4.9). Besides Fe_2C, $Fe_{2+x}C$, Fe_7C_3, and Fe_5C_2, there is also a small percentage of Fe_3C and C. The possible relation between carbides can be expressed by:

$$6\ Fe_2C \rightarrow Fe_7C_3 + Fe_5C_2 + C \quad (3)$$

$$4\ Fe_2C \rightarrow Fe_5C_2 + Fe_3C + C \quad (4)$$

From 760 °C to 780 °C, there is a percentage decrease of Fe_7C_3, and increase of weight percentage of Fe_5C_2 and Fe_3C. This could probably be explained by the equations:

$$3\ Fe_7C_3 \rightarrow 7\ Fe_3C + 2\ C \quad (5)$$

$$3\ Fe_5C_2 \rightarrow 5\ Fe_3C + C \quad (6)$$

Equation (6) has been proposed by many authors [38,40,41], during the studies of kinetics of iron carbides [40], origin and behavior of iron carbides under reducing atmospheres [38]. It was reported by Cohn and Hofer [41] that formation of cementite occurs at temperatures higher than 480 °C and that Fe_5C_2 always precede Fe_3C and never the opposite.

Finally, between 800 °C and 900 °C, there are present only Fe_3C, γ-Fe, and C. It is pretty clear from Fig. 4.9 the decrease of weight percentage of Fe_3C to form γ-Fe and C (Eq. 7); that result has been already observed by many other authors, because of the instability of cementite at temperatures higher than 700 °C [40,42].

$$3\ Fe_3C \rightarrow 3\ Fe + C \quad (7)$$

The transformations between carbides or its decomposition, agrees with the statement that the stability of iron carbides increases when the carbon contents decreases: $Fe_2C < Fe_{2.2-2.4}C < Fe_5C_2 < Fe_3C$ [35,43]. The aforementioned relationships between iron carbides can be summarized in the schema depicted in Fig. 4.12.

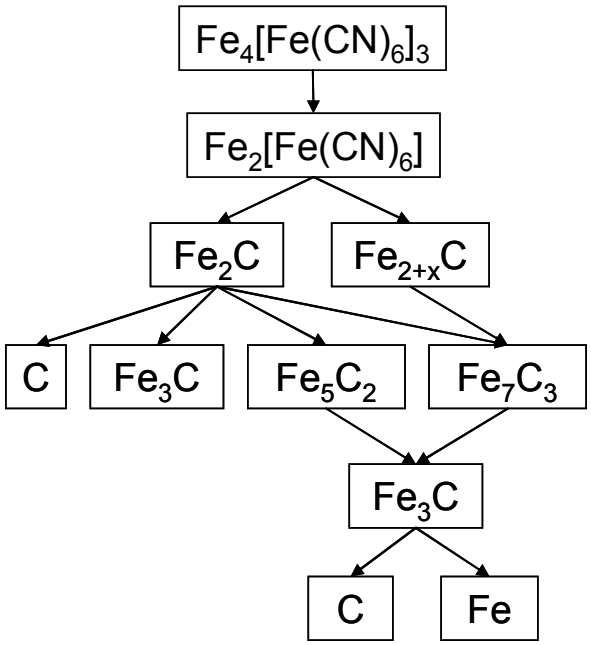

Figure 4.12 Schema showing the decomposition of Prussian blue and subsequent formation and transformation of iron carbide phases.

4.5 Overall Mechanism of Thermal Decomposition

Considering a pure sample of Prussian blue, from TGA/DSC analysis (Fig. 4.3, table 4.2), the first step had a mass loss between 35 °C and 189 °C corresponding to the release of zeolitic water in PB structure (Eq. 8, Δm_{th} = -6.64 %), then a second release of water until 300 °C, corresponding to the release of structural water (Eq. 9, Δm_{th} = -9.48 %):

$$Fe_4[Fe(CN)_6]_3 \cdot 5H_2O \rightarrow Fe_4[Fe(CN)_6]_3 \cdot 1.5H_2O + 3.5\ H_2O \quad (8)$$

$$Fe_4[Fe(CN)_6]_3 \cdot 5H_2O \rightarrow Fe_4[Fe(CN)_6]_3 + 5\ H_2O \quad (9)$$

Between 300 °C and 420 °C, starts the transformation of ferric ferrocyanide (PB) into ferrous ferrocyanide (BW), then the following reaction takes place:

$$Fe_4[Fe(CN)_6]_3 \rightarrow 7/3\ Fe_2[Fe(CN)_6] + 2\ (CN)_2 \quad (10)$$

For example, at 370 °C (PB370) as can be seen in Fig. 4.4, both kinds of ferrocyanide (PB, BW) are present, it can be described by the equation:

$$Fe_4[Fe(CN)_6]_3 \rightarrow 1.4\ Fe_2[Fe(CN)_6] + 0.4\ Fe_4[Fe(CN)_6]_3 + 1.2\ (CN)_2 + 5\ H_2O$$

(Δm_{th} = -16.06 %, Δm_{exp} = -14.57 %) (11)

At higher temperatures, i.e. from 420 °C to 900 °C, occurs the formation and transformation of iron carbides as was explained in the previous section, and the final formation of iron resulting from the thermal decomposition of cementite. The overall PB mechanism of decomposition in argon atmosphere can be resumed by the following equation:

$$Fe_4[Fe(CN)_6]_3 \cdot 5H_2O \rightarrow 2\ Fe_3C + Fe + 2\ C + 7\ (CN)_2 + 2\ N_2 + 5\ H_2O \quad (12)$$

From the Eq. 11, it was calculated the theoretical mass loss as -53.74 %, which differs with the experimental mass loss of -56.39 %. The reason of the differences could be attributed to the fact that it was not consider the minor phases present during the PB decomposition. The nitrogen was included in the Eq. 11, because it was released during

the formation and transformation of iron carbides (at 500 °C, 642 °C, 763 °C, 842 °C, and 885 °C), although its provenance is not well understood, also a little amount of CO_2 was release at 418 °C, 471 °C, 579 °C, 704 °C, and 826 °C, according to the EGA analysis.

Bibliography

1. H.J. Buser, D. Schwarzenbach, W. Petter, and A. Ludi, *Inorg. Chem.* **16**, 2704–2710 (1977).
2. P.R. Bueno, F.F. Ferreira, D. Giménez-Romero, G.O. Setti, R.C. Faria, C. Gabrielli, H. Perrot, J.J. Garcia-Jareño, and F. Vicente, *J. Phys. Chem.* **112**, 13264–13271 (2008).
3. A. Ito, M. Suenaga, and K. Ono, *J. Chem. Phys.* **48**, 3597–3599 (1968).
4. R.E. Wilde, S.N. Ghosh, and B.J. Marshall, *Inorg. Chem.* **9**, 2512–2516 (1970).
5. H.B. Weiser, W.O. Milligan, and J.B. Bates, *J. Phys. Chem.* **46**, 99–111 (1942).
6. F. Herren, P. Fischer, A. Ludi, and W. Hälg, *Inorg. Chem.* **19**, 956–959 (1980).
7. J.F. Allen and A.K. Bonnette, *J. Inorg. Nucl. Chem.* **36**, 1011–1016 (1974).
8. H. Inoue, T. Nakazawa, T. Mitsuhashi, T. Shirai, and E. Fluck, *Hyperfine Interact.* **46**, 725–731 (1989).
9. A. Ludi and H.U. Güdel, *Struct. Bond.* **14**, 1–21 (1973).
10. S. Vaucher, M. Li, and S. Mann, *Angewandte Chemie (International Ed. in English)* **39**, 1793–1796 (2000).
11. P.A. Fiorito, V.R. Gonçales, E.A. Ponzio, and S.I.C. de Torresi, *Chemical Communications* **2005**, 366–368 (2005).
12. X. Shen, S. Wu, Y. Liu, K. Wang, Z. Xu, and W. Liu, *J. Colloid Interface Sci.* **329**, 188–95 (2009).
13. P.H. Zhou and D.S. Xue, *J. Appl. Phys.* **96**, 610–614 (2004).
14. A.A. Karyakin and E.E. Karyakina, *Russ. Chem. Bull., Int. Ed.* **50**, 1811–1817 (2001).
15. R. Koncki, *Crit. Rev. Anal. Chem.* **32**, 79–96 (2002).
16. E.A. Puganova and A.A. Karyakin, *Sens. Actuators B* **109**, 167–170 (2005).
17. P.G. Rasmussen and E.A. Meyers, *Polyhedron* **3**, 183–190 (1984).
18. M. Verdaguer and G. Girolami, in *Magnetism: Molecules to Materials V*, edited by J.S. Miller and M. Drillon (Willey-VCH Verlag GmbH & Co. KGaA, Weinheim (Germany), 2005), pp. 283–346.
19. J.G. Cosgrove, R.L. Collins, and D.S. Murty, *J. Am. Chem. Soc.* **95**, 1083–1086 (1973).
20. R. Zboril, L. Machala, M. Mashlan, and V. Sharma, *Cryst. Growth Des.* **4**, 1317–1325 (2004).

21. P.K. Gallagher and B. Prescott, *Inorg. Chem.* **9**, 2510–2512 (1970).

22. M. Hermanek and R. Zboril, *Chem. Mater.* **20**, 5284–5295 (2008).

23. E. Reguera, J. Fernández-Bertrán, A. Dago, and C. Díaz, *Hyperfine Interact.* **73**, 295–308 (1992).

24. K. Nomura, M. Takeda, T. Iiyama, and H. Sakai, *Hyperfine Interact.* **166**, 657–664 (2006).

25. L. Samain, F. Grandjean, G.J. Long, P. Martinetto, P. Bordet, and D. Strivay, *J. Phys. Chem. C* **117**, 9693–9712 (2013).

26. R. Zboril, M. Mashlan, D. Petridis, D. Krausova, and P. Pikal, *Hyperfine Interact.* **139/140**, 437–445 (2002).

27. M. Hermanek, R. Zboril, M. Mashlan, L. Machala, and O. Schneeweiss, *J. Mater. Chem.* **16**, 1273 (2006).

28. J. a. L. Lodya, H. Gericke, J. Ngubane, and T.H. Dlamini, *Hyperfine Interact.* **190**, 37–42 (2009).

29. Y. Yamada, H. Yoshida, K. Kouno, and Y. Kobayashi, *J. Phys. Conf. Ser.* **217**, 012096 (2010).

30. X.-X. Bi, B. Ganguly, G.P. Huffman, F.E. Huggins, M. Endo, and P.C. Eklund, *J. Mater. Res.* **8**, 1666–1674 (1993).

31. F.H. Herbstein and J.A. Snyman, *Inorg. Chem.* **3**, 894–896 (1964).

32. M. Ron, in *Applications of Mössbauer Spectroscopy II*, edited by R.L. Cohen (Academic Press, New York, 1980), pp. 329–392.

33. J.W. Niemantsverdriet, a. M. Van der Kraan, W.L. Van Dijk, and H.S. Van der Baan, *J. Phys. Chem.* **84**, 3363–3370 (1980).

34. J.A. Amelse, G. Grynkewich, J.B. Butt, and L.H. Schwartz, *J. Phys. Chem.* **85**, 2484–2488 (1981).

35. G. Le Caer, J.M. Dubois, M. Pijolat, V. Perrichon, and P. Bussiere, *J. Phys. Chem.* **86**, 4799–4808 (1982).

36. C.M. Fang, M. a. van Huis, and H.W. Zandbergen, *Scr. Mater.* **63**, 418–421 (2010).

37. G.H. Barton and B. Gale, *Acta Crystallogr.* **17**, 1460–1462 (1964).

38. T. Herranz, S. Rojas, F. Pérez-Alonso, M. Ojeda, P. Terreros, and J. Fierro, *J. Catal.* **243**, 199–211 (2006).

39. O. Schneeweiss, R. Zbořil, B. David, M. Heřmánek, and M. Mashlan, *Hyperfine Interact.* **189**, 167–173 (2009).

40. Y. Iguchi, T. Kouda, and T. Shibata, *ISIJ International* **44**, 243–249 (n.d.).

41. E.M. Cohn and L.J.E. Hofer, *J. Chem. Phys.* **21**, 354 (1953).

42. D. Chaira, S. Sangal, and B.K. Mishra, *Mater. Manuf. Processes* **22**, 492–496 (2007).

43. H. Jung and W.J. Thomson, *J. Catal.* **134**, 654–667 (1992).

5. Synthesis of iron oxide nanoparticles by thermal decomposition of chemical synthesized Prussian blue

5.1 Introduction

Prussian blue (PB) is an iron salt that can be synthesized chemically by many routes. The most used is the direct method, where are mixed an aqueous solution of ferric or ferrous salt and hexacyanoferrate(II) or hexacyanoferrate(III) ($K_4Fe(CN)_6 \cdot 3H_2O$, $K_3Fe(CN)_6 \cdot 6H_2O$) [1–4]. The salts commonly used are ferrous or ferric chloride, although iron nitrate and iron sulfate has been used too, but in that case were used ammonium hexacyanoferrate or ferrocyanide acid [3]. Cubic crystals of PB can be also prepared, but in contrast to the direct method it takes longer time (three weeks) [5]. Using ultrasound [6] or by addition of surfactants some authors had controlled the morphology of PB particles, some of the surfactants used in the PB synthesis are polyvinylpyrrolidone (PVP) [7–9] and citric acid [10].

The control of the size and morphology of nanoparticles has been one of the goals in the synthesis of nanoparticles or nanocrystals. The variation of these two parameters (size and shape), leads to the variation of the optical, thermal, electrical, magnetic, and even catalytic properties of the materials [11,12]. In the case of magnetic nanoparticles, the shape of nanoparticles has influence on the coercitivity of the material because of the shape anisotropy [13,14]. Usually, the preparation of nanoparticles with defined shapes is done by colloidal or thermal decomposition methods [11], where the shapes of the particles can be controlled by means of a surfactant [8,15] or ultrasound during the synthesis [6]. If well, there is known that particles sizes affect the melting point of the particles [11], there are no experimental results of the morphology effect.

Iron salts and minerals had been used in the preparation of iron oxides by solid state thermal decomposition [4,16,17], In general, the particles size of the precursor and even the thickness of the layer on the crucible affect the temperature of the thermal decomposition, and the kind of iron oxides produced [18]. Another factor to consider is the morphology of the precursor, which could influence in the kind of iron oxide produced after the thermal decomposition of the precursor material.

5.2 Materials and Methods

5.2.1 Synthesis of Prussian blue (PB) with spherical and cubic morphology

Prussian blue (PB) spherical nanoparticles were synthesized using a modified version of the synthesis described by Shen *et al.* [8]. For the synthesis, 7.5 g (67.5 mmol of monomer units) of polyvinylpyrrolidone (PVP, K-30, Mw = 40 000, Fluka) were dissolved in 100 ml of hydrochloric acid (HCl, 0.01 M, PH = 2). After the total dissolution of PVP, 225 mg (0.68 mmol) of potassium ferricyanide ($K_3[Fe(CN)_6]$, Lachema) were slowly added to the former solution under stirring. The new solution was put into a boiling flask, joined to the bulb condenser, and then the aqueous solution was refluxed at 80 °C during 2 hours. When the time of reaction has finished, the solution was cooled to room temperature. Then, the PB nanoparticles were separated from the solution using centrifuge equipment (Sigma Sartorius 4-16 K) (13500 rpm, 25 min), the resulting precipitate was washed three times alternating between absolute ethanol and water (13500 rpm, 20 min). Finally, the precipitate was dry in vacuum for 20 h. The blue powder sample was labeled as PB-S.

Prussian blue cubic microparticles were synthesized using a sonochemical synthesis described by Wu *et al.* [6]. For the synthesis, 423 mg (1 mmol) of potassium ferrocyanide ($K_4[Fe(CN)_3]\cdot 3H_2O$, Penta) were dissolved in 100 ml of hydrochloric acid (HCl, 0.1 M, PH = 1). Then, the solution was put into an ultrasound bath at 40 °C for 4 hours. After that, the cooled solution was centrifuged at 13500 rpm during 15 min; the blue precipitate was washed two times with water and one time with absolute ethanol (13500 rpm, 30 min). Finally, the precipitate was dried in air. The dark blue powder sample was labeled as PB-C.

5.2.2 Preparation of iron oxide nanoparticles by thermal decomposition of PB

Two PB samples, each one with approx. weight of 26 mg, were heated in a muffle furnace (Linn Hightherm Gmbh LM 112.07) at 350°C for 1 hour. The furnace was set to have an ascending temperature from room temperature to 350 °C with a heating rate of 5 K/min. The sample containing micro-cubes of Prussian blue has a dark blue color, and the sample of nano-spheres has a brilliant blue color. After heating, both samples changed their color to reddish brown color and dark brown color, respectively. The samples

obtained after the heating were labeled as PBC350 and PBS350. In order to remove undesired compounds in the samples, they were washed with deionized water four times.

Three other set of samples were prepared using sample PB-C. The first set consists of three samples W5KC350a, W5KC350b, and W5K350c; PB-C sample was heated up to 350 °C with a heating rate of 5 K/min, where the mean mass sample was 35 mg. In the second set three samples were prepared at different temperatures: a) 330 °C, 5 K/min, 2 hours (W5KC3302); b) 400 °C, 5 K/min, 1 hour (W5KC400); and c) 350 °C, 2 K/min, 1 hour (W2KC350). The third set consist of two samples with different mass density (mean mass sample was 33 mg for each sample, but the alumina crucible had different diameters 15 mm and 33 mm): a) 350 °C, 5 K/min, 1 hour, 4.2 mg/cm^2 (W5KC350L); b) 320 °C, 5 K/min, 3 hours, 20.3 mg/cm^2 (W5KC320). All samples were washed with deionized water after the thermal treatment.

5.2.3 Samples characterization

Thermogravimetric analysis (TGA) and differential scanning calorimetry (DSC) were carried out simultaneously on PB-C and PB-S samples, using a thermal analyzer STA 449 C Jupiter from Netzsch. Analyses were done under oxidant atmosphere (air) from 35 °C to 900 °C with a heating rate of 5 K/min in open alumina crucible; the average mass of samples was 10 mg. After heating, samples were cooling down to room temperature under inert atmosphere of nitrogen. Additional analyses were up to chosen temperatures for PB-C (350 °C, 450 °C) and PB-S (310 °C, 400 °C) samples.

All samples were characterized by X-ray powder diffraction (XRD) and ^{57}Fe Mössbauer spectroscopy (MS). XRD patterns were recorded with a PANalytical X'Pert PRO MPD diffractometer (CoK_α radiation) in the Bragg-Brentano geometry, equipped with an X´Celerator detector and programmable divergence and diffracted beam anti-scatter slits. The measurement range was 2θ: 15° - 90°, with a step size of 0.017°. The identification of crystalline phases and the Rietveld refinement were performed using the High Score Plus software (PANalytical) in conjunction with PDF-4+ and ICSD databases.

Transmission ^{57}Fe Mössbauer spectroscopy on powdered samples was carried out in a constant acceleration mode using a ^{57}Co(Rh) source at room temperature (RT) and 15 K. Spectra were folded and fitted using the CONFIT2000 software; the isomer shift values were expressed with respect to metallic alpha-iron.

Scanning electron microscopy (SEM) was performed on each sample, as synthesizes and after heating, to study its morphology. The images were obtained using a scanning electron microscope Hitachi SU-6600, with 5 kV and 15 kV secondary electron image. Also was performed energy dispersive X-ray analysis (EDS) to check the elemental composition of the sample.

5.3 Results

5.3.1 Prussian blue: Cubic and spherical shapes

The Prussian blue samples were analyzed by XRD, MS, and SEM. The XRD patterns confirm the presence of pure Prussian blue on both samples, *i.e.* PB-S and PB-C (Fig. 5.1a). The FWHM of XRD reflections in sample PB-S are wider than in sample PB-C, indicating the minor size of the particles as confirmed by SEM images (Fig. 5.2a and 5.2b). The particles sizes follow a normal distribution (Fig. 5.2c and 5.2d), with average sizes of 1.45 μm for cubic particles (PB-C) and 160 nm for spherical particles (PB-S). Also, according to the energy dispersive X-ray spectroscopy (EDS) results (Fig. 5.2e and 5.2f), the particles contain K besides the usual elements present in the PB composition (Fe, C, N), where the PB-C sample contains more amount of potassium than PB-S sample, which could affect the decomposition mechanism. Due to the presence of potassium in the samples, it could be inferred that K was incorporated into the PB lattice, as was proposed by Bueno *et al.* [19].

The Mössbauer spectra of the samples are slightly different (Fig. 5.1b). The spectrum of sample PB-S was fitted with one doublet (IS = 0.38 mm/s, QS = 0.51 mm/s, sub-spectral area 57.6%) and one singlet (IS = -0.15 mm/s, sub-spectral area 42.4%), corresponding to the high-spin (HS) ferric ion 6-fold coordinated by N and the low-spin (LS) ferrous ion 6-fold coordinated by C in the PB structure, respectively [4]. On the other hand, the spectrum of sample PB-C, besides of the described doublet (IS = 0.34 mm/s, QS = 0.37 mm/s, sub-spectral area 50.9%) and singlet (IS = -0.15 mm/s, sub-spectral area 41.9%), has another doublet (IS = 0.54 mm/s, QS = 0.31 mm/s, sub-spectral area 7.2%) corresponding to the HS ferric ion 6-fold coordinated by five N, and one OH-K or O-H_2, which substitute the $[Fe^{2+}(CN)_6]^{4-}$ vacancies.

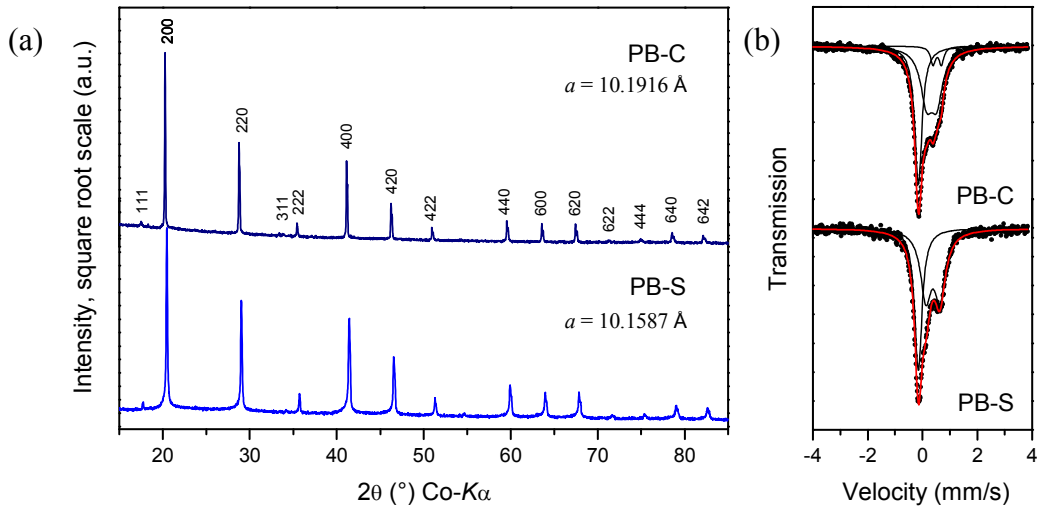

Figure 5.1 XRD patterns (a) and Mössbauer spectra (b) at room temperature of cubic (PB-C) and spherical (PB-S) particles of Prussian blue. Lattice constants (*a*) for each sample are shown.

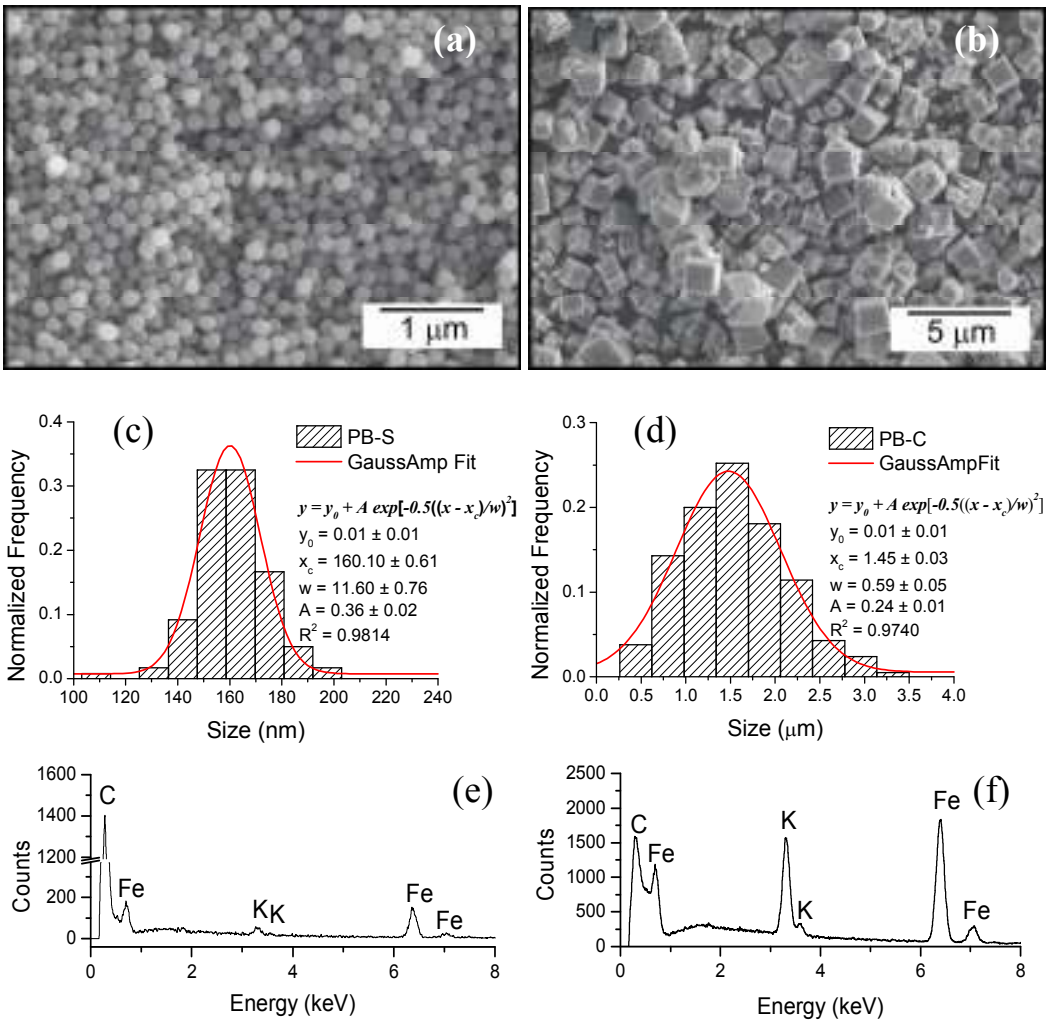

Figure 5.2 SEM photographs, histogram for particle size distribution, and EDS spectra of samples PB-S (a, c, e) and PB-C (b, d, f).

5.3.2 Thermal analysis: TG and DSC

The thermal decomposition of Prussian blue in air starts above 250 °C, after the liberation of the structural water and the cyanide groups from the PB lattice. Studies using simultaneously thermogravimetric analysis (TGA) and differential scanning calorimetry (DSC) from 35 °C to 900 °C (heating rate 5 K/min), show differences in the results obtained for spherical and cubic particles of PB (Fig. 5.3). First, the estimated water molecules from TGA differs for both particles, being less H_2O in cubic particles (4) than in spherical particles (9.5), fact that could be influenced by the presence of K^+ ions in the PB lattice as was discussed in the previous section. Second, the decomposition temperature (estimated from the exothermic peak of DSC curve) is smaller for spherical nanoparticles (269 °C) than for cubic particles (334 °C), but it seems more a size effect consequence rather than a morphology effect [11]. Third, the mass losses -obtained from TGA- in both samples are different, principally because of the K presence, which lead to a formation of potassium compounds as KNO_3 besides iron oxide in the case of the cubic particles. Similar TGA curves were published by Samain *et al.* [1] without further explanation about the decomposition mechanism of Prussian blue.

The endothermic peak, on step I, for both samples indicates the release of water molecules from the Prussian blue lattice. The endothermic peak, on step IV, present in the DSC graph of sample PB-C corresponds to the formation of the ferrite $KFe_{11}O_{17}$, surprisingly this peak is not present in the sample PB-S, even when the same ferrite is formed. Step II corresponds to the Prussian blue decomposition, with formation of iron oxides. In the step III, crystallization of the amorphous iron oxides is likely to happen, as suggested by the presence of two exothermal effects in DSC for PB-C and PB-S samples (table 5.1).

Table 5.1 Comparative data from TGA (mass loss: Δm) and DSC analysis of samples PB-S and PB-C. The arrows represent the endothermic (↓) and exothermic (↑) effects.

	PB-S			**PB-C**		
Step	Temp. range (°C)	Δm (%)	DSC peak (°C)	Temp. range (°C)	Δm (%)	DSC peak (°C)
I	35 – 171	-16.63	144 (↓)	35 – 268	-8.25	221 (↓)
II	171 – 272	-28.95	245, 269 (↑)	268 – 335	-25.14	278, 334 (↑)
III	272 – 339	-3.01	298, 329 (↑)	335 – 402	1.46	360, 386 (↑)
IV	339 – 900	-3.06	none	402 – 900	-8.63	664 (↓)
	Sum:	-51.66		Sum:	-40.56	

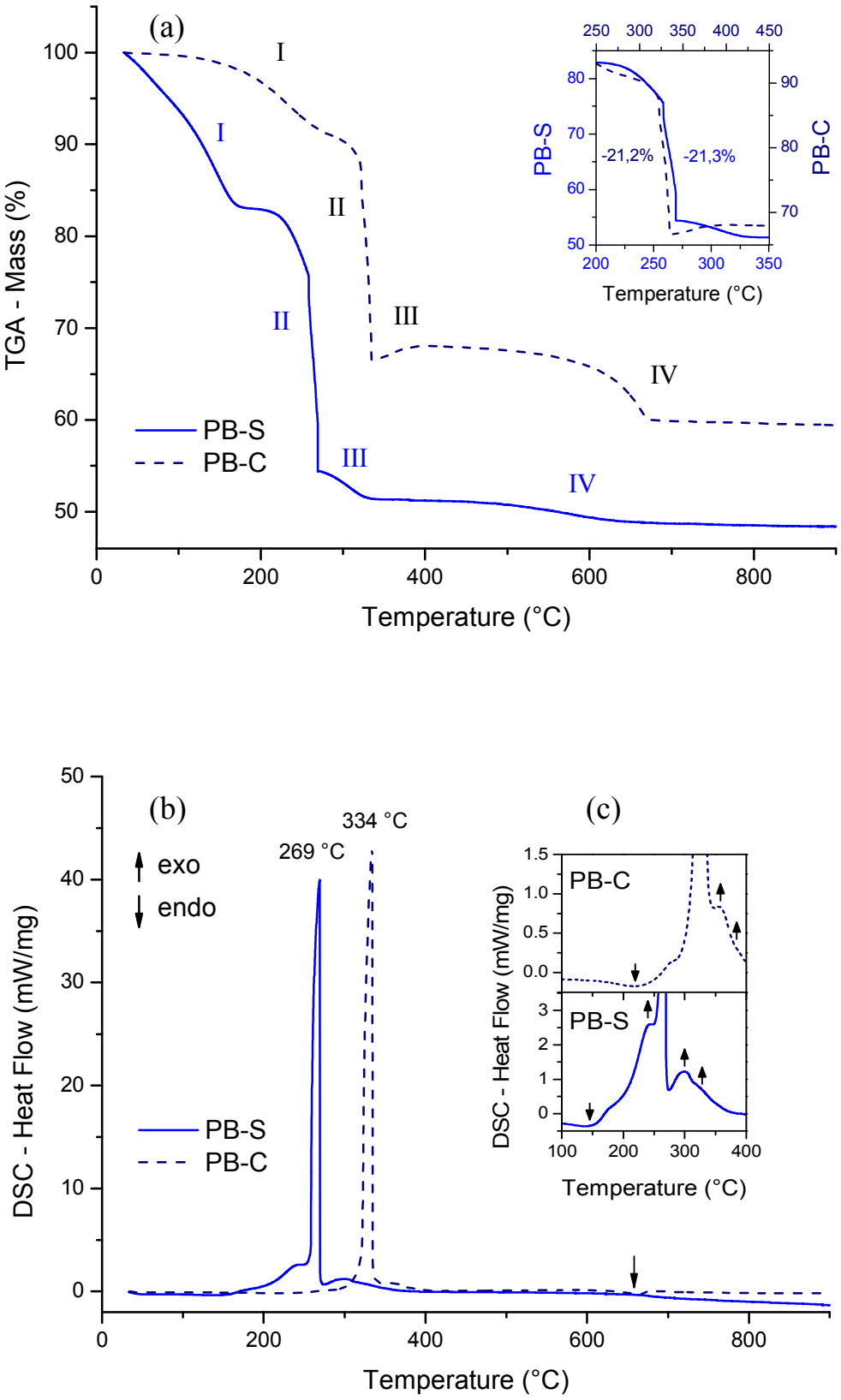

Figure 5.3 TGA (a), DSC (b) for samples PB-S (solid line) and PB-C (dashed line). A closer view of DSC (c), where the arrows represent the endothermic (↓) and exothermic (↑) effects.

5.3.3 Phase composition: XRD and MS

The evaluation of the phase composition of the samples heated up to chosen temperatures (PB-S: 310 °C, 400 °C and 900 °C; PB-C: 350 °C, 450 °C and 900 °C), was done using XRD and MS (Fig. 5.4, 5.5 and 5.6). Quantitative phase analysis was done using the Rietveld analysis on XRD patterns (Table 5.2).

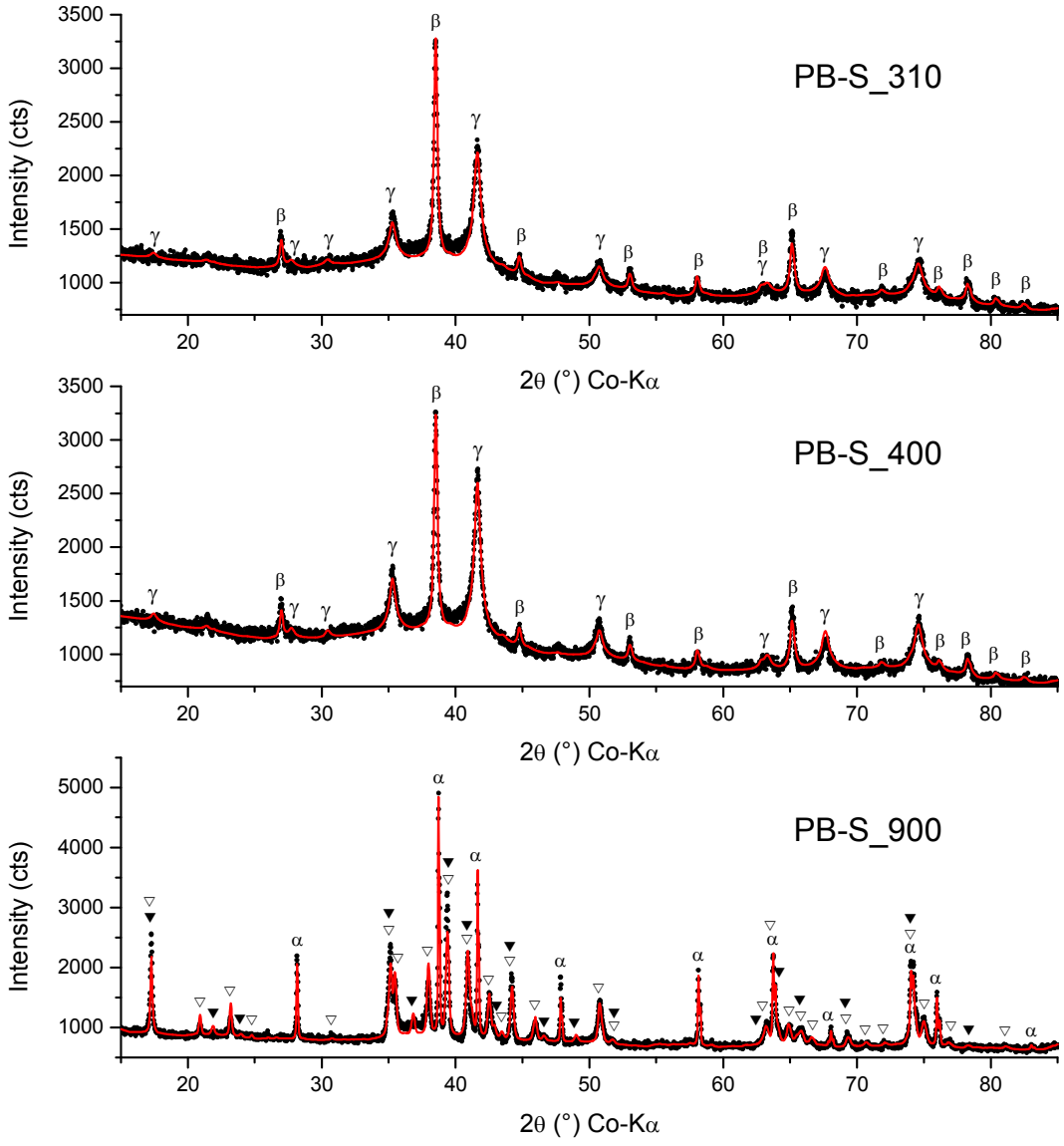

Figure 5.4 XRD patterns for PB-S_310 (top), PB-S_400 (middle), and PB-S_900 (bottom). The symbols represent each phase present in the samples: β-Fe_2O_3 (β), maghemite (γ), $KFe_{11}O_{17}$–hex (▼), $KFe_{11}O_{17}$–trig (▽).

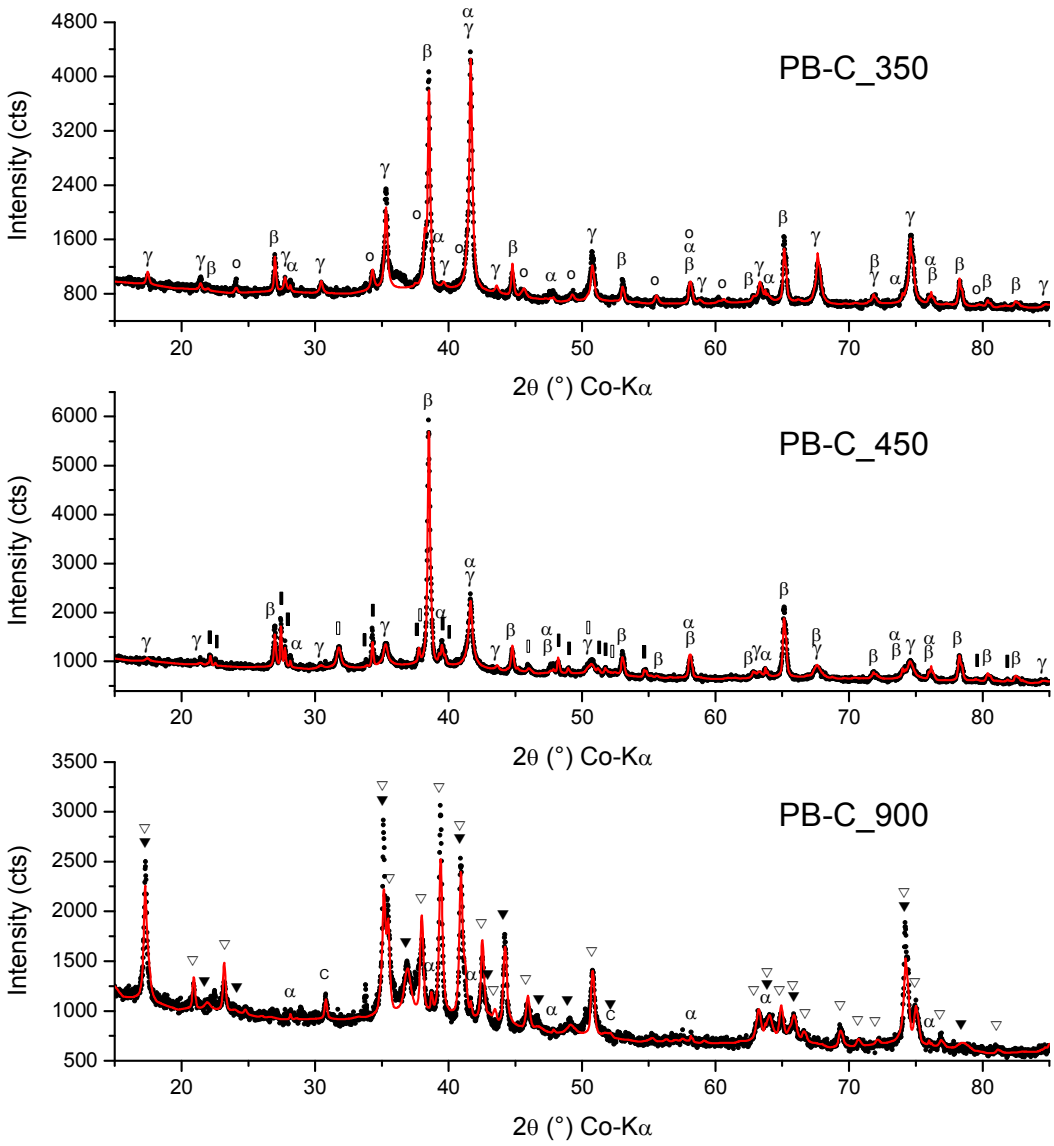

Figure 5.5 XRD patterns for PB-C_350 (top), PB-C_450 (middle), and PB-C_900 (bottom). The symbols represent each phase present in the samples: hematite (α), β-Fe_2O_3 (β), maghemite (γ), KOCN (o), α-KNO_3 (▮), γ-KNO_3 (▯), $KFe_{11}O_{17}$–hex (▼), $KFe_{11}O_{17}$–trig (▽), graphite (C).

PB-S samples after heating at 310 °C and 400 °C, have a similar phase composition presenting a mixture of iron oxides (γ-Fe_2O_3 and β-Fe_2O_3) (Fig. 5.4), only the weight percentage is different, for example at 400 °C the gamma polymorph is the major phase present, that could reflect the slow transformation of beta to gamma polymorph (table 5.2). Mössbauer spectra of the aforementioned samples are quite similar (Fig. 5.6), in addition to the beta and gamma polymorphs, there is one sub-spectral

component ascribed to superparamagnetic maghemite with isomer shift of 0.35-0.36 mm/s and quadrupole splitting 1.05-1.08 mm/s (table 5.3). Beta polymorph was more crystalline in comparison to maghemite, according to the full width at half maximum of diffraction peaks and the experimental linewidth of Mössbauer sub-spectra. Sample PB-S_900, have a completely different phase composition than the previous samples, the major phase was potassium ferrite with two different crystallographic arrangements (hexagonal and trigonal), and hematite (Fig. 5.4).

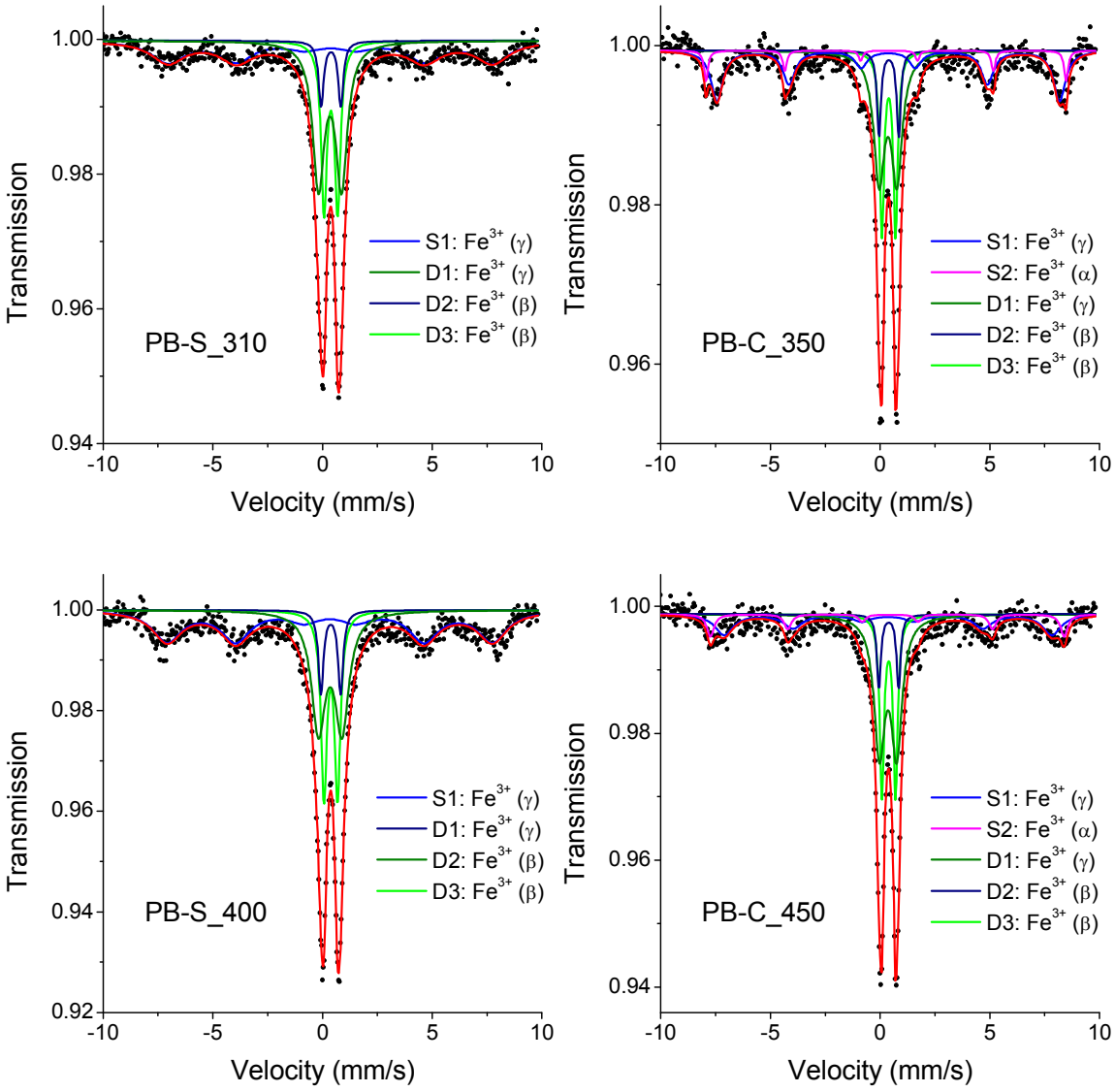

Figure 5.6 Mössbauer spectra, taken at room temperature, of samples PB-S_310 (left top side), PB-S_400 (left bottom side), PB-C_350 (right top side), and PB-C_450 (right bottom side).

Table 5.2 Quantitative results from Rietveld refinement of the PB-C and PB-S samples heated up to chosen temperatures. The numbers between parentheses indicate the estimated standard deviations.

Phase	PDF-file	Space group	PB-C_350	PB-C_450	PB-C_900
α-Fe_2O_3	161291	R-3c	2.5(2) %	3.0(1) %	1.4(1) %
β-Fe_2O_3	108905	Ia-3	25.4(4) %	37.7(4) %	-
γ-Fe_2O_3	87119	$P4_132$	55.4(4) %	27.7(7) %	-
KOCN	24008	I4/mcm	16.6(6) %	-	-
α-KNO_3	10289	Pnma	-	14.0(2) %	-
γ-KNO_3	36113	R3m	-	17.7(4) %	-
$KFe_{11}O_{17}$	83285	$P6_3/mmc$	-	-	17.4(4) %
$KFe_{11}O_{17}$	174323	R-3m	-	-	78.1(6) %
C	76767	$P6_3/mmc$	-	-	3.1(4) %
			PB-S_310	PB-S_400	PB-S_900
α-Fe_2O_3	161291	R-3c	-	-	24.2(2) %
β-Fe_2O_3	108905	Ia-3	46.7(9) %	39.9(7) %	-
γ-Fe_2O_3	87119	$P4_132$	53.3(1) %	60.1(9) %	-
$KFe_{11}O_{17}$	83285	$P6_3/mmc$	-	-	10.8(4) %
$KFe_{11}O_{17}$	174323	R-3m	-	-	65.0(6) %

Table 5.3 Mössbauer parameters obtained from the fit of spectra for samples PB-C and PB-S heated up to different temperatures in air.

Sample	Sub-spectra	IS (mm/s)	QS (mm/s)	W (mm/s)	B_{hf} (T)	Area (%)	Assignment
PB-C_350	S1	0.37	*0.00*	0.66	48.5	30.8	Fe^{3+} (γ-Fe_2O_3)
	S2	0.34	-0.14	0.22	51.0	6.1	Fe^{3+} (α-Fe_2O_3)
	D1	0.36	0.81	*0.59*	-	34.1	Fe^{3+} (γ-Fe_2O_3 SP)
	D2	0.40	*0.90*	*0.22*	-	8.7	Fe^{3+} b (β-Fe_2O_3)
	D3	0.39	*0.62*	*0.24*	-	20.2	Fe^{3+} d (β-Fe_2O_3)
PB-C_450	S1	0.36	*0.00*	1.01	46.4	21.1	Fe^{3+} (γ-Fe_2O_3)
	S2	0.39	-0.13	0.39	50.1	8.9	Fe^{3+} (α-Fe_2O_3)
	D1	0.36	0.79	*0.59*	-	39.9	Fe^{3+} (γ-Fe_2O_3 SP)
	D2	0.39	*0.90*	*0.22*	-	8.3	Fe^{3+} b (β-Fe_2O_3)
	D3	0.39	*0.62*	*0.24*	-	21.8	Fe^{3+} d (β-Fe_2O_3)
PB-S_310	S1	0.36	*0.00*	1.83	46.0	35.1	Fe^{3+} (γ-Fe_2O_3)
	D1	0.34	1.05	0.63	-	36.2	Fe^{3+} (γ-Fe_2O_3 SP)
	D2	0.38	*0.90*	0.28	-	7.3	Fe^{3+} b (β-Fe_2O_3)
	D3	0.38	*0.62*	0.32	-	21.4	Fe^{3+} d (β-Fe_2O_3)
PB-S_400	S1	0.33	*0.00*	1.60	46.0	40.0	Fe^{3+} (γ-Fe_2O_3)
	D1	0.35	1.08	0.76	-	31.0	Fe^{3+} (γ-Fe_2O_3 SP)
	D2	0.38	*0.90*	0.28	-	8.1	Fe^{3+} b (β-Fe_2O_3)
	D3	0.37	*0.62*	0.33	-	20.9	Fe^{3+} d (β-Fe_2O_3)

Notes: IS: isomer shift (± 0.01), QS: quadrupole splitting or quadrupole shift (± 0.01), W: experimental linewidth (± 0.01), B_{hf}: magnetic hyperfine field (± 0.1), Area (± 0.5), S: sextet, D: doublet, L: singlet, SP: superparamagnetism, numbers in cursive are the fixed values during the fitting.

Unlike the prior sample (PB-S), the phase composition of the heated PB-C at 350 °C includes an iron oxide mixture (α, β and γ), and potasium cyanate (KOCN), while at 450 °C there were identified potassium nitrides (α-KNO_3 and γ-KNO_3), and the iron oxide mixture (Fig. 5.5). In this case the three iron oxide polymorphs apparently are produced simultaneously. If only the Fe-bearing phases are considered, then the percentages of iron oxides are the following: α-Fe_2O_3 (3.0%), β-Fe_2O_3 (30.5%), γ-Fe_2O_3 (66.5%) for sample PB-C_350; and α-Fe_2O_3 (4.4%), β-Fe_2O_3 (55.1%), γ-Fe_2O_3 (40.5%) for sample PB-C_450. From these results apparently there is an increment of beta iron oxide at higher temperature, resulting from the unlikely transformation of gamma to beta polymorph or due to the inhomogeneity of the analyzed sample. In sample PB-C_900 were identified two polymorphs of potassium ferrite, hematite and carbon (table 5.2).

Mössbauer spectra of samples PB-C_350 and PB-C_450 at the first sight are similar to the spectra obtained for samples PB-S_310 and PB-S_400. However, the main difference lies in the presence of an extra sextet for hematite, both iron oxide polymorphs were also identified, including the superparamagnetic component of maghemite.

The phase composition of samples PBC350 and PBS350 (PB-C and PB-S heated at 350 °C in a furnace) was analyzed by XRD and Mössbauer spectroscopy. XRD patterns (Fig. 5.7) show different phase compositions for both samples after washing them with deionized water. All potassium compounds were removed by washing of the both samples with the aim to obtain only the ferric oxide phases. Nevertheless, an unidentified phase still remained in the sample PBC350.The quantitative phase composition was calculated by Rietveld refinement, giving the following quantities: hematite (3.8%), maghemite (62.1%) and β-Fe_2O_3 (34.1%) for sample PBC350, and 100% of maghemite for sample PBS350.

The RT Mössbauer spectra of samples PBC350 and PBS350 (Fig. 5.8a and 5.8b) are very similar; but according to the phases identified by XRD in the sample PBC350, there are 3 different iron oxide polymorphs (α-, β- and γ- Fe_2O_3), while in the sample PBS350 there is only maghemite (γ-Fe_2O_3). The values of quadrupole splitting (QS) for both doublets of β-Fe_2O_3 were fixed, to avoid the no-convergence during the fitting, using values given in the literature [16,20]. Values of subspectra areas, in sample PBC350, reveal that the dominant phase is the superparamagnetic maghemite represented by a doublet with 70.3 %, and the minor phase is hematite with 3.1 %, hematite is weakly ferromagnetic according to its Mössbauer parameters (Table 5.4).

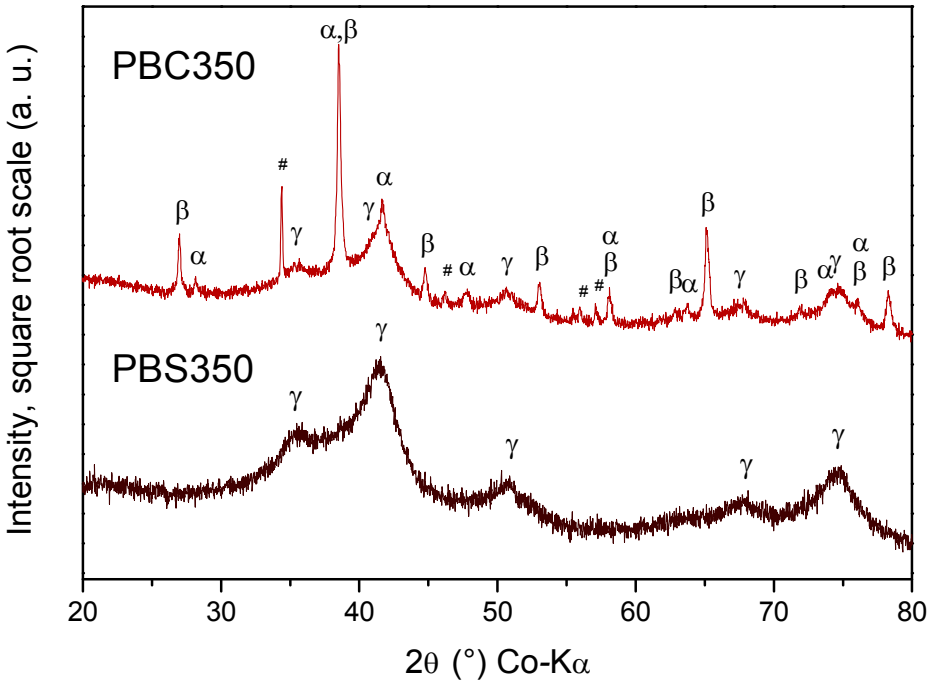

Figure 5.7 XRD patterns of the samples PBC350 (top) and PBS350 (bottom). The phases identified were maghemite (γ), hematite (α), β-Fe_2O_3 (β), and one unknown phase (#).

Low temperature Mössbauer spectra confirmed the presence of maghemite in both samples (Fig. 5.8c and 5.8d), indicated by two sextets: one for the tetrahedral sites and the other for octahedral sites. In the fitting of the Mössbauer spectrum at 15 K, were used two distributions of hyperfine magnetic fields for both iron sites of maghemite, and single sextets for the other ferric oxides (table 5.4). In sample PBC350, two sextets correspond to d-sites and b-sites of the crystalline phase β-Fe_2O_3, with Mössbauer parameters close to those measured at 20 K by Zboril *et al.* [16]. The hematite in sample PBC350, represented by a sextet with the highest hyperfine field, corresponds to a crystalline phase with an antiferromagnetic behavior below the Morin temperature (T_M ~ 260 K) [16,21].

The ratio of ferric ions in octahedral (O) and tetrahedral (T) sites was determined from their corresponding sub-spectral areas for both samples: PBC350 ($[Fe^{3+}]_O/[Fe^{3+}]_T$ = 1.62) and PBS350 ($[Fe^{3+}]_O/[Fe^{3+}]_T$ = 1.67). The $[Fe^{3+}]_O/[Fe^{3+}]_T$ ratio, for sample PBC350, slightly differs from the ratio for stoichiometric maghemite (5/3), then the maghemite present in the sample is non-stoichiometric with an excess of vacancies in the octahedral sites. A more detailed study was done on sample PBS350, where Mössbauer spectra were taken at different temperatures and even under external magnetic field (for details see appendices 12 and 13).

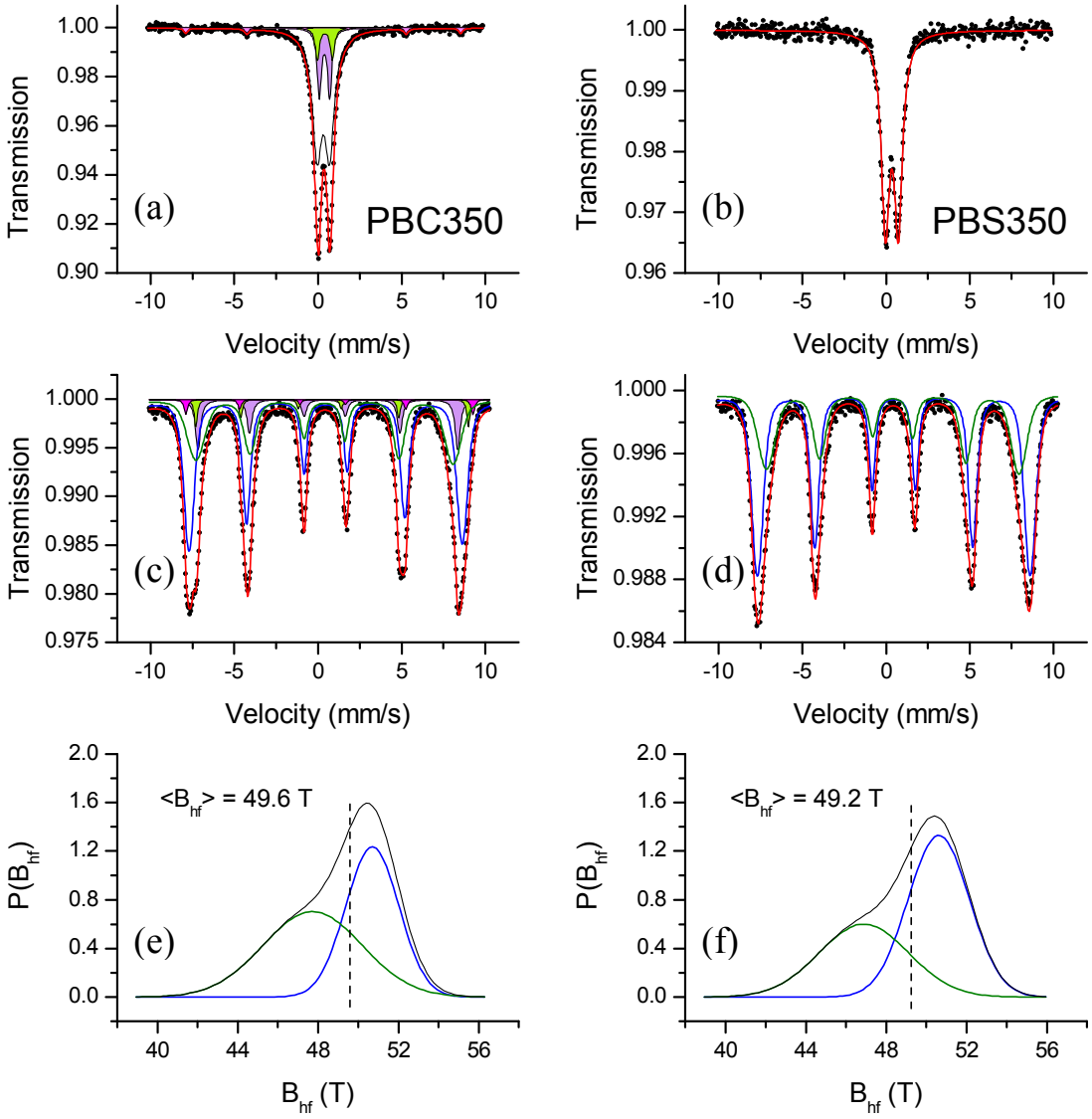

Figure 5.8 Mössbauer spectra: at room temperature for samples PBC350 (a) and PBS350 (b), at 15 K without external magnetic field for samples PBC350 (c) and PBS350 (d). Resulting distribution of hyperfine magnetic fields from fitting of Mössbauer spectra taken at 15 K: PBC350 (e) and PBS350 (f). Sub-spectra assignment: hematite (pink fill), β-Fe_2O_3 b site (green fill), β-Fe_2O_3 d site (purple fill), maghemite octahedral (blue line) and tetrahedral (green line) sites.

The group of Mössbauer spectra taken for sample PBS350 is typical for a powder sample with a strong interaction of particles [22]. At 150 K, the presence of one sextet with magnetic hyperfine field of 45.1 T indicates the fraction of ordered spins in the core of the maghemite nanoparticles (28.5 %), while the doublet represents the superparamagnetic contribution. When the measurement temperature decreases to 70 K, the superparamagnetic contribution disappears, instead three sextets were used to fit the

spectra (<B_{hf}> = 40.9 T); two sextets are ascribed to the tetrahedral and octahedral sites of maghemite, and the sextet with a decreased magnetic hyperfine field (28 T) is related to disordered spins at the surface of maghemite nanoparticles and size distribution of the nanoparticles [23]. The Mössbauer spectrum at 5 K is quite similar to the spectra taken at 15 K, which was discussed in the previous paragraph. Finally, Mössbauer spectrum of sample PBS350 shows that it contains pure stoichiometric maghemite with existence of canted spins, as was revealed from the presence of the lines 2 and 5 in the Mössbauer spectrum measured under an external magnetic field (details in appendices 12 and 13). Using the relationship $\theta_c = \arcsin\sqrt{6r/(4+3r)}$ (where: r = $A_{2,5}/A_{1,6}$) it was calculated the canting angle for each sub-lattice of maghemite: $\theta_{c,A}$ = 44.6° (tetrahedral site), $\theta_{c,B}$ = 59.0° (octahedral site) [22]. The observed spin-canting effect observed in PBS350 sample is most probably due to finite-size effects of the particles.

Table 5.4 Mössbauer parameters of the samples PBC350 and PBS350 after washing. IS: isomer shift (± 0.01), QS: quadrupole splitting or quadrupole shift (± 0.01), W: experimental linewidth (± 0.01), B_{hf}: magnetic hyperfine field (± 0.1), Area (± 0.5), SP: superparamagnetism, WF: weak-ferromagnetism, AF: anti-ferromagnetism, numbers in cursive are the fixed values during the fitting.

Sample	T (K)	Phase	IS (mm/s)	QS (mm/s)	W (mm/s)	B_{hf} (T)	Area (%)
PBC350	300	β-Fe_2O_3 b	0.41	*0.90*	0.29	-	8.2
		β-Fe_2O_3 d	0.39	*0.62*	0.30	-	18.2
		γ-Fe_2O_3 SP	0.32	0.75	0.69	-	70.5
		α-Fe_2O_3 WF	0.42	-0.20	0.28	51.1	3.1
PBS350	300	γ-Fe_2O_3 SP	0.35	0.77	0.59	-	100.0
PBC350	15	β-Fe_2O_3 d	0.50	0.19	0.36	48.2	9.9
		β-Fe_2O_3 b	0.48	0.74	0.22	50.6	3.3
		α-Fe_2O_3 AF	0.49	0.40	0.24	53.3	2.0
		γ-Fe_2O_3 O[a]	0.46	*0.00*	0.43	50.7[b]	52.4
		γ-Fe_2O_3 T[a]	0.39	*0.00*	0.47	47.7[b]	32.4
PBS350	15	γ-Fe_2O_3 O	0.46	*0.00*	0.43	50.6[b]	62.6
		γ-Fe_2O_3 T	0.40	*0.00*	0.56	46.9[b]	37.4

[a] The sub-spectrum was fitted with a distribution of hyperfine magnetic fields.
[b] Average hyperfine magnetic field.

Additional experiments were performed on samples PB-C. Results of the first set of experiments, with samples heated up to 350 °C, show that it is not always possible to

have the same percentage of the respective iron oxide polymorph (α, β, γ), as is shown in figure 5.9. The phase composition for each sample was: 12.1 % (α), 49.8 % (β), 38.1 (γ) for sample W5KC350a; 27.4 % (α), 30.4 % (β), 42.2 (γ) for sample W5KC350b; and 18.1 % (α), 38.0 % (β), 43.9 (γ) for sample W5KC350c.

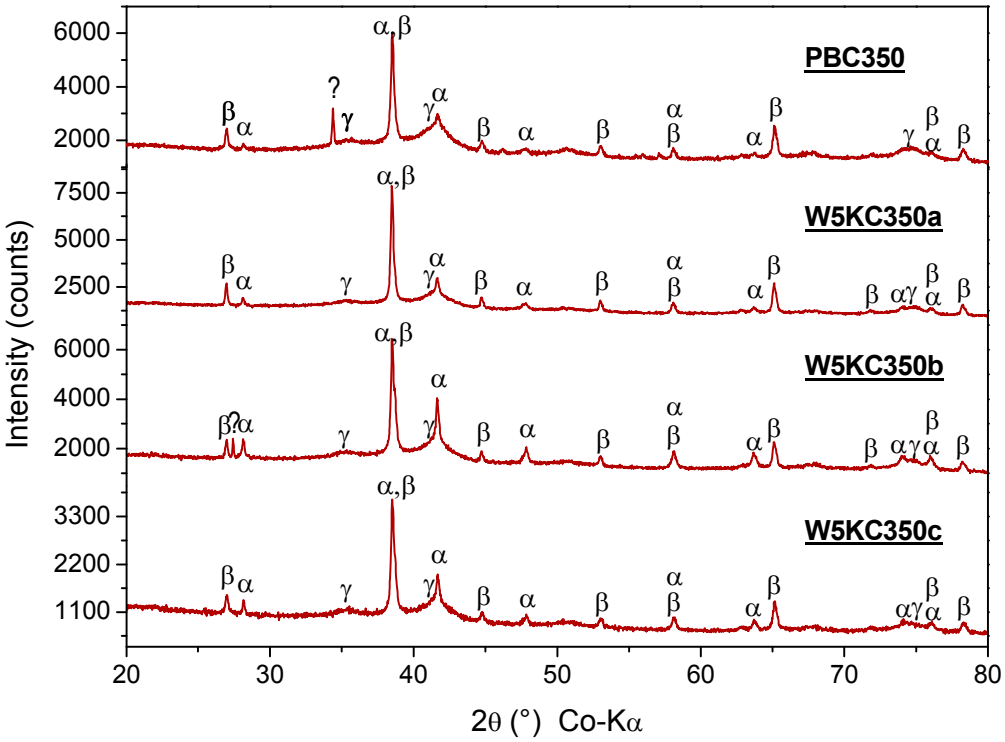

Figure 5.9 Diffractograms of samples W5KC350a, W5KC350b, and W5KC350c. PBC350 is shown only for comparison. Greek letters stand for each identified iron oxide polymorph.

The second set of experiments, when samples were heated under different heating regimes, had as a result the same phase composition with variable weight percentage of each phase (Fig. 5.10). The phase composition for each sample was: 35.9 % (α), 18.5 % (β), 45.6 (γ) for sample W5KC3302; 17.5 % (α), 38.8 % (β), 43.7 (γ) for sample W5KC400; and 27.4 % (α), 4.6 % (β), 68.0 (γ) for sample W2KC350. When the sample was heated at lower temperature (330 °C) and for longer time (2 h) was obtained a major weight percentage of hematite than in the other samples. With a higher temperature (400 °C) of heating was found a bigger weight percentage of beta polymorph than in the other samples. However, when the sample is heated with a lower heating rate (2 K/min) and 350 °C the major weight percentage corresponds to maghemite.

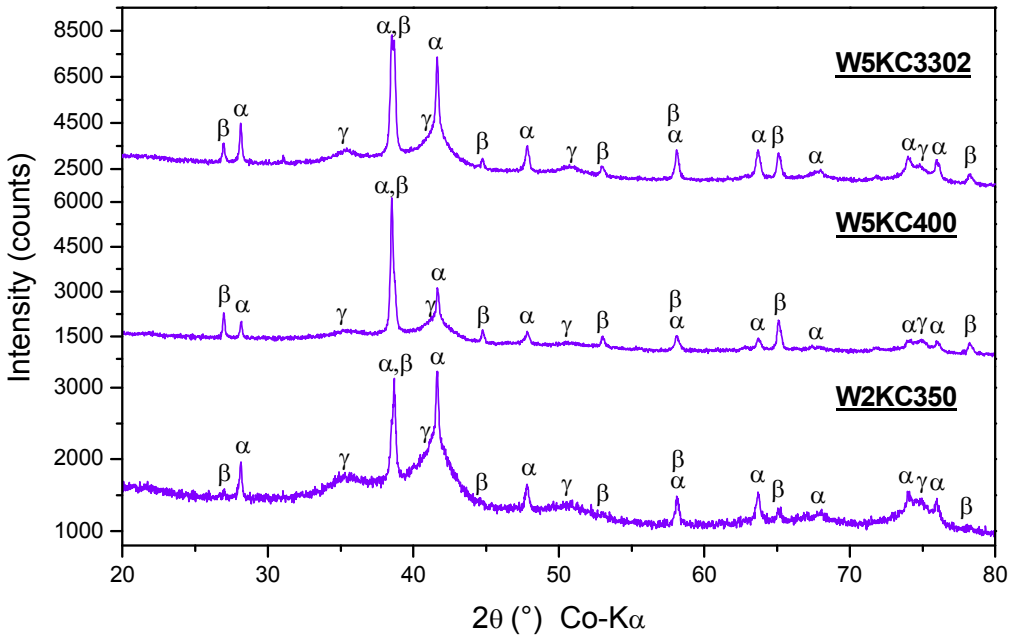

Figure 5.10 Diffractograms of samples W5KC3302, W5KC400, and W2KC350. PBC350 is shown only for comparison. Greek letters stand for each identified iron oxide polymorph.

The results of the third set of experiments were the same; both samples (W5KC350L and W5KC320) consisted of a fine powder of maghemite, even when the experimental conditions were different.

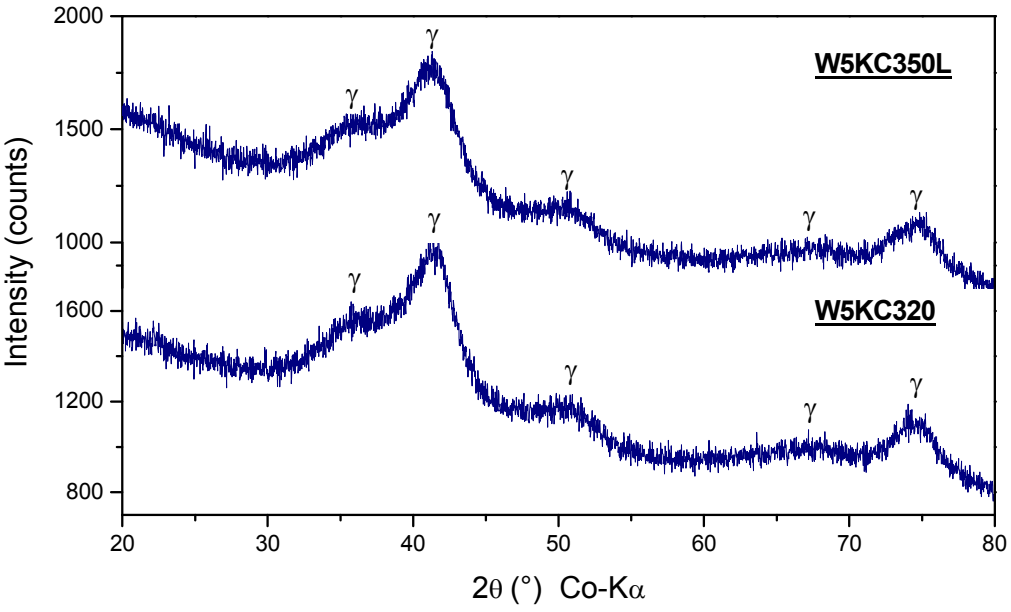

Figure 5.11 Diffractograms of samples W5KC350L and W5KC320. Both samples contain pure maghemite (γ).

5.3.4 Morphology of the iron oxide particles: SEM and TEM

The morphology of the ferric oxide samples varies, depending on the PB precursor morphology. Particularly, when the particles of PB are spherical, the maghemite form spherical clusters with a size of (~116 nm), which is slightly smaller than the particle size precursor (~160 nm) (Fig. 5.12b), it is probably due to the decomposition of the PVP coating of the PB nanoparticles. In the case of cubic PB particles, the maghemite forms cubic clusters with similar sizes as the PB-C precursor particles (Fig. 5.12a), the same was also seen for sample W5KC320 (Fig. 5.12g). The identified β-Fe_2O_3 particles have an angular shape with a mean size of 70 nm (Fig. 5.12c), this also agrees with the narrow lines in the XRD pattern. In figure 5.12c, it is observed groups of β-Fe_2O_3 particles in the surface of the cubic cluster, it suggests that the particles grow on the surfaces where the surface energy permit the polymorph transformation from γ- to β- ferric oxide. It is interesting that the occurrence of polymorph transformation instead of sintering or agglomeration of the clusters. Even more interesting is the that our β-Fe_2O_3 exceed the size limit (~ 30 nm) for polymorph transformation as described by Sakurai [24].

Maghemite clusters – cubic and spherical – are conformed by small nanoparticles as can be seen from TEM photographs (Fig. 5.12e and g), the size of these particles was estimated from XRD patterns as 4 nm. Because of their reduced sizes, each particle behaves as a single magnetic domain, and at room temperature they exhibit superparamagnetism. At room temperature, the thermal energy is greater than the barrier energy between the magnetization axes, and the magnetizations of these magnetic domains are randomly oriented, this behaviour is indicate by the measured doublet in Mössbauer spectrum. At low temperatures, the thermal fluctuations decrease and the magnetic moment of the nanoparticles are blocked in a specific direction, given a measurable magnetization, indicated by a sextet in the Mössbauer spectrum.

The retention of the morphology during thermal transformation was addressed in the work of Itoh [25], but a difference with our work is that they only observed that between polymorph transformation of iron oxides (from hematite to magnetite, and posterior transformation to maghemite). This offers us the possibility of morphology control of the precursor materials and makes more efficient the solid state thermal decomposition method.

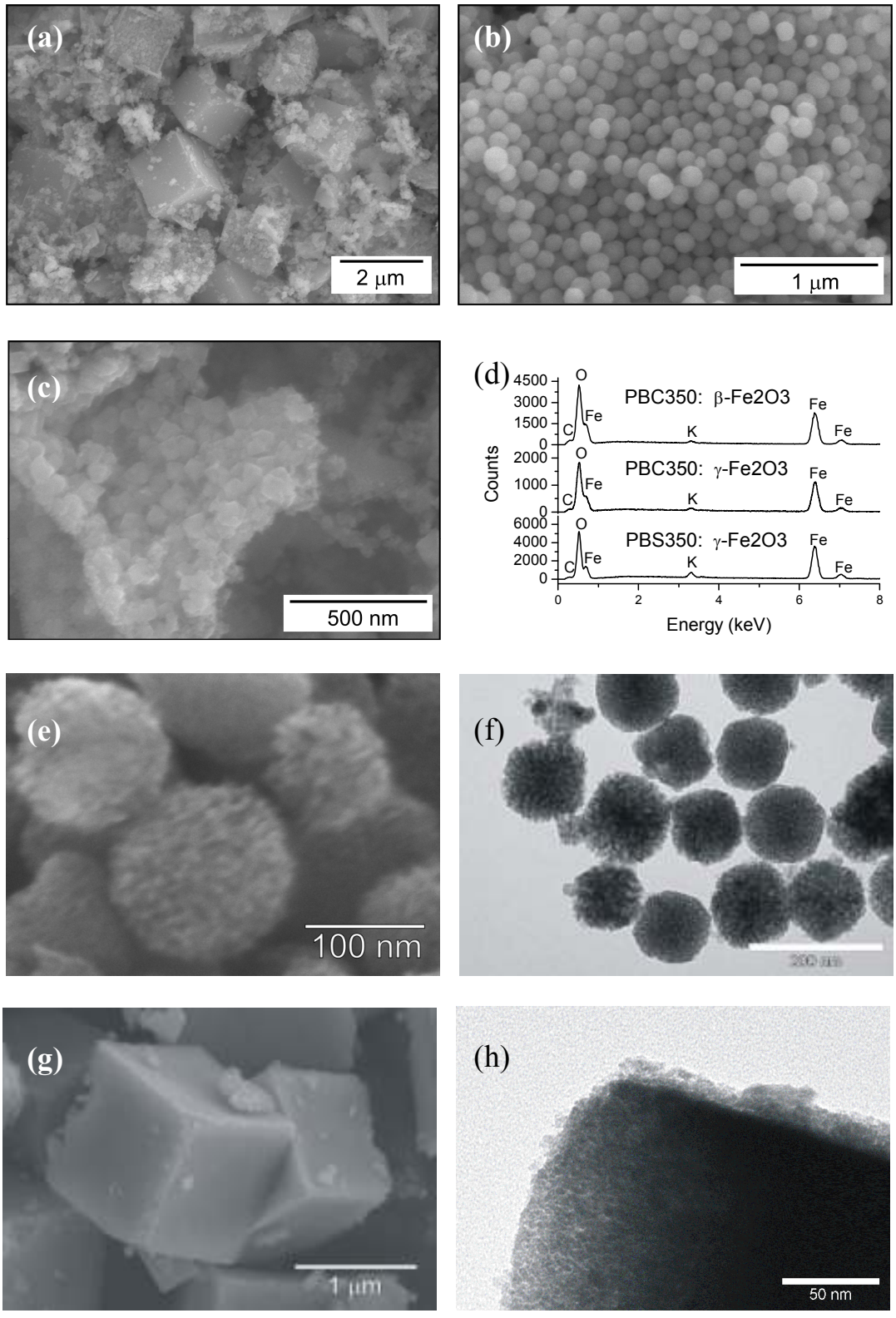

Figure 5.12 SEM images of the samples PBC350 (a, c) and PBS350 (b) showing the clusters of maghemite nanoparticles (a, b) and the β-Fe_2O_3 nanoparticles (c), and their respective EDS analysis (d). Detail view of spherical maghemite clusters in sample PBS350 from SEM (e) and TEM (f) images. SEM (g) and TEM (h) image of cubic maghemite clusters in sample W5KC320.

5.3.5 Magnetic properties of the produced maghemite nanoclusters

Magnetic properties of sample PBS350 were studied using a superconducting quantum interference device (SQUID). The obtained spherical maghemite clusters, in sample PBS350, behave as superparamagnets at room temperature (300 K) as can be seen from the hysteresis loop with a very small coercivity (16 Oe) and saturation magnetization of 21.8 emu/g, which is lower than the bulk magnetization (~74 emu/g) (Fig. 5.13a and table 5.5). At 5 K the nanoparticles are in a blocked state and show a magnetic coercivity and a higher saturation magnetization (28.3 emu/g). It is also observed a slight asymmetry in the hysteresis loop, which suggests particles with a core/shell structure due to exchange bias field phenomenon (Fig. 5.13b and table 5.5) [26].

Zero field cooling (ZFC) and field cooling (FC) were measured on sample PBS350 under external magnetic field of 100 Oe and 1000 Oe respectively (Fig. 5.13c, 5.13d). In ZFC measurement the sample is cooled to 5 K without any external magnetic field, then a external field is added and the magnetization curve is collected from 5 K to 300 K. In FC measurement, the sample is cooled down to 5 K under an external magnetic field, and then from 5 K to 300 K the magnetization curve is collected.

The ZFC/FC measurements under magnetic field of 100 Oe, reveals a wide distribution of particles size, FC curve shows that magnetization seems to come from two different phases: crystallized maghemite, and amorphous ferric oxide. The blocking temperature (T_B) was 117 K and the irreversibility temperature (T_{irr}) was 293 K. When the ZFC/FC measurements were taken under magnetic field of 1000 Oe, there is a shift of T_B to 95 K because of the interaction of the particles under the magnetic field, while T_{irr} was 220 K. The flat part of the FC curve is typical for a highly interacting particle system, as a powder.

Table 5.5 Parameters of the hysteresis loop of sample PBS350, measured at 300 K and 5 K, where M_{max+} (7 T) is the saturation magnetization at 7 T, M_{max-} (7 T) is the saturation magnetization at -7 T, H_{C+} is the positive coercivity field, H_{C-} is the negative coercivity field, M_{R+} is the positive remanent magnetization, and M_{R-} is the negative remanent magnetization.

T (K)	M_{max+} (7 T) (emu/g)	M_{max-} (– 7 T) (emu/g)	H_{C+} (Oe)	H_{C-} (Oe)	M_{R+} (emu/g)	M_{R-} (emu/g)
300	21.7912	– 21.7917	16	– 15	0.0952	– 0.0938
5	28.2824	– 28.3225	741	– 1413	7.2334	– 6.5715

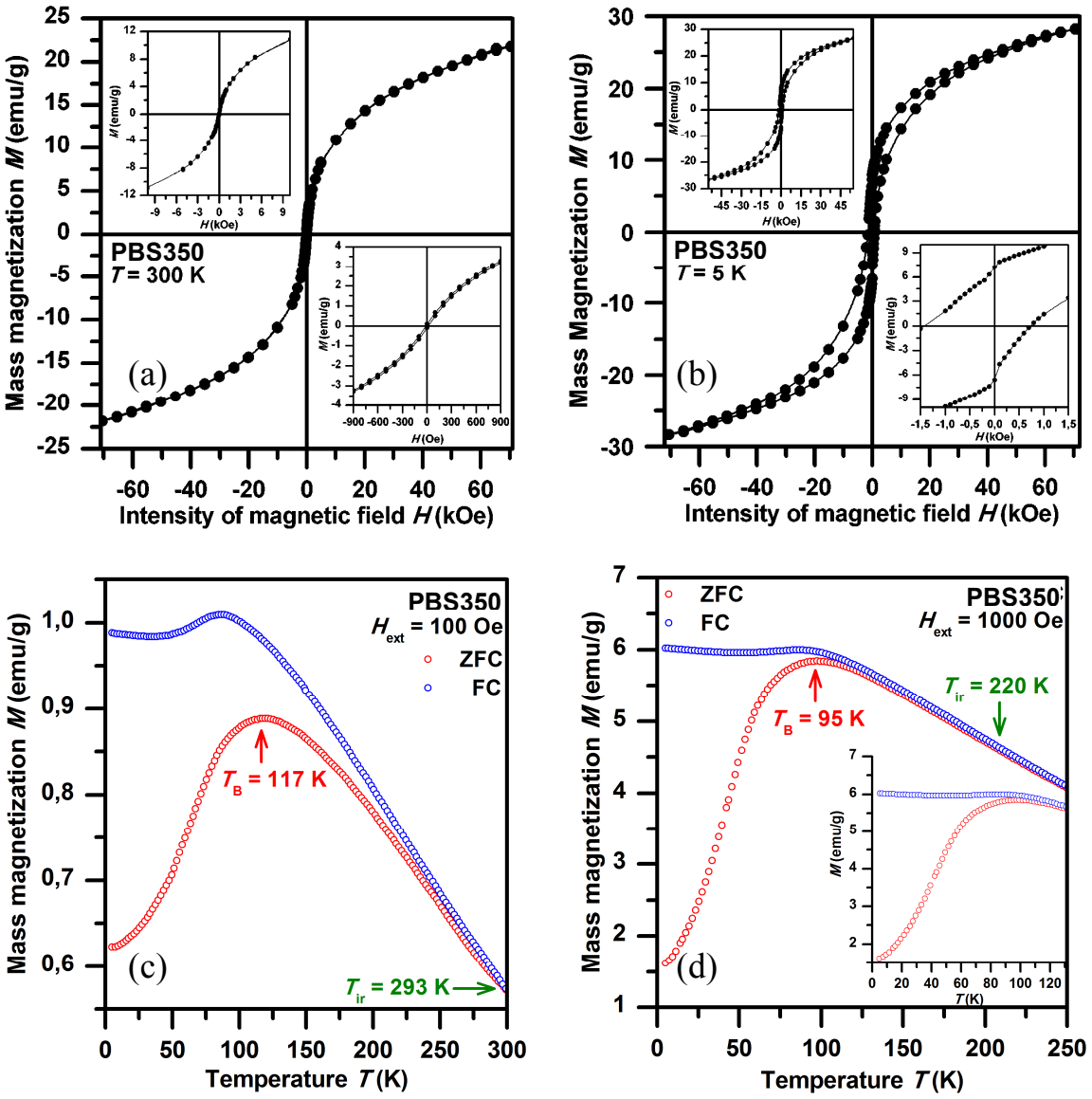

Figure 5.13 Hysteresis loop measured at 300K (a) and 5 K (b) under external magnetic field from -7 T to 7 T. ZFC and FC magnetization curves measured under external magnetic field with induction 100 Oe (c) and 1000 Oe (d).

5.4 Discussion of Results

5.4.1 Models of thermal decomposition of PB in air and formation of iron oxides

To explain the thermal decomposition of Prussian blue (PB) in air, two models are proposed: a) one assuming no presence of K in PB for spherical particles, and b) another for PB structure with K for cubic particles, using the PB model with 25% of $Fe(CN)_6$ vacancies $Fe_4[Fe(CN)_6]_3 \cdot [K^+_h \cdot OH^-_h \cdot mH_2O]$ proposed by Bueno *et al.* [19].

For the first model the Eq. 1 can be written for the PB dehydration and decomposition considering the steps I, II and III of the TGA graph. The theoretical mass loss according to Eq. 1 is estimated as Δm_{th}(PB-S) = 45.73 %, which is close to the experimental mass loss 48.59 % up to 400 °C. It should be underlined that at 900 °C according to the experimental results, there is a presence of potassium ferrite ($KFe_{11}O_{17}$), and its formation correspond to the slight mass decrease (-3.06 %) observed in step IV. The formation for potassium ferrite is not completely understood because it was not possible to identify any potassium-bearing phase in the corresponding diffractogram (Fig. 5.4), either some potassium compound was in amorphous state or the percentage weight was too small in the sample and the corresponding diffraction lines were unnoticed. The discrepancies between theoretical and experimental values, in sample PB-S, are probably due to humidity in the samples, or undetected potassium compounds in the samples.

$$Fe_4[Fe(CN)_6]_3 \cdot 9.5H_2O + 5.25\ O_2 \rightarrow 3.5\ Fe_2O_3 + 9\ (CN)_2 + 9.5\ H_2O \qquad (1)$$

In the case of PB-C, the first step on the TGA curve (Fig. 5.3a) corresponds to release of water from the PB structure with and experimental mass loss of -8.25 % (Δm_{th}(PB-C) = -8.16 %). Then the thermal decomposition occurs during the second step, between 268 °C – 335 °C, with a considerable loss mass (-25.14 %), then it is resume in the following equation:

$$Fe_4[Fe(CN)_6]_3 \cdot K^+_x OH^-_x + (5.25 + x/4)\ O_2 \rightarrow 3.5\ Fe_2O_3 + x\ KOCN + (9 - x/2)\ (CN)_2 + x/2\ H_2O \qquad (x = 1.3) \qquad (2)$$

$$Fe_4[Fe(CN)_6]_3 \cdot K^+_{1.3} OH^-_{1.3} \cdot 4.6H_2O + 5.575\ O_2 \rightarrow 3.5\ Fe_2O_3 + 1.3\ KOCN + 8.35\ (CN)_2 + 5.25\ H_2O \qquad (3)$$

Theoretical mass loss was calculated from Eq. 3, giving as a result -34.51 %, a slight higher value than the experimental one Δm_{exp}(PB-C) = -33.39 %. There was observed a rise in the TGA curve (step III) with the corresponding increment of mass (+1.46 %). It can be explained by the thermal decomposition of potassium cyanate to potassium nitrate:

$$KOCN + 2\ O_2 \rightarrow KNO_3 + CO_2 \qquad (4)$$

Combining Eq. 4 with Eq. 3 is obtained Eq. 5, where the theoretical mass loss is Δm_{th}(PB-C) = 31.95% and the experimental mass loss from TGA is 31.93%.

$$Fe_4[Fe(CN)_6]_3 \cdot K^+_{1.3}OH^-_{1.3} \cdot 4.6H_2O + 8.175\ O_2 \rightarrow 3.5\ Fe_2O_3 + 1.3\ KNO_3 + 8.35\ (CN)_2 + 5.25\ H_2O + 1.3\ CO_2 \quad (5)$$

In the temperature range from 402 °C to 900 °C (step IV) of the TGA curve there is a visible decrease of mass (-8.36 %), which can be explained by de formation of potassium ferrite ($KFe_{11}O_{17}$) as a result from the solid state reaction between ferric oxide and potassium nitrate (Eq. 6). This reaction is endothermic as can be noticed from the downward peak in the DSC curve at 664 °C. At temperatures higher than 500 °C can decompose into potassium dioxide (K_2O) as in Eq. 7 [27].

$$5.5\ Fe_2O_3 + KNO_3 \rightarrow KFe_{11}O_{17} + NO + 0.75\ O_2 \quad (6)$$

$$2\ KNO_3 \rightarrow K_2O + 2\ NO_2 + 0.5\ O_2 \quad (7)$$

Then the whole process can be described with Eq. 8. Using this final equation was calculated the theoretical mass loss as -38.88 %, which differs with the experimental mass loss of -40.56 %.

$$Fe_4[Fe(CN)_6]_3 \cdot K^+_{1.3}OH^-_{1.3} \cdot 4.6H_2O + 8.175\ O_2 \rightarrow 0.75\ Fe_2O_3 + 0.5\ KFe_{11}O_{17} + 0.4\ K_2O + 8.35\ (CN)_2 + 5.25\ H_2O + 1.3\ CO_2 + 0.5\ NO + 0.8\ NO_2 + 0.575\ O_2 \quad (8)$$

5.4.2 Kinds of iron oxide polymorphs produced during thermal decomposition of Prussian blue

From the same precursor, Prussian blue (PB) with cubic and spherical morphologies has been prepared different iron oxide polymorphs. In both samples, it has been formed clusters of superparamagnetic maghemite nanoparticles, which retained the morphology and size of the precursor material (cubic or spherical, depending on the heating conditions). The origin of β-Fe_2O_3 seems to come from the posterior transformation of the maghemite nanoparticles in the surfaces of the cubic clusters, but in some cases is more likely that both phases (α and β) were formed simultaneously. For

example in heated PB-C samples, where in some cases were visible two layers (the top layer was dark red, while the bottom layer was red), but unfortunately it was not possible to analyze independently each layer; the formation of such layers can attributed to the inhomogeneous reaction within the sample as explained by Machala *et al.* [21].

Also was investigated the influence of the powder-sample layer thickness on the thermal decomposition of PB-C samples. Samples heated under the same conditions (heating rate 5 K/min, 350 °C for 1 hour, average mass 34 mg), but with different mass density (19.8 mg/cm^2 for samples W5KC350 (Fig. 5.9) and 4.2 mg/cm^2 for sample W5KC350L (Fig. 5.11, upper part)) had very different phase composition. In the samples with a higher mass density the phase composition consisted of three iron oxide polymorphs (α, β, and γ), while for the sample with a low mass density it was obtained pure maghemite. It is worthy to be mentioned that pure maghemite cubic-clusters can be obtained by heating the PB-C at lower temperature (320 °C), for a longer time (3 hours), with a higher mass density (20.3 mg/m^2); then it can be inferred the lower temperature prevents the transition $\gamma \rightarrow \beta$ in iron oxide (Fig. 5.11, lower part).

5.4.3 Maghemite clusters and its possible applications

Cubic and spherical clusters of maghemite were obtained from PB heated under the adequate conditions, as was explained in the previous sections. These clusters are composed of small rounded nanoparticles of maghemite (~ 4 nm in size), and they retained the original shape of the original precursor. Both maghemite clusters behave as superparamagnets at room temperature (see sections 5.3.4 and 5.3.5), making then interesting for potential applications.

Because of the smaller size (~ 116 nm) and narrower particles size distribution the spherical nanoclusters of maghemite (Fig. 5.12) seem to be more adequate for some practical applications. For example they could be used for cell separation processes, only after a surface modification of the clusters or functionalization; but they are not suitable for use as a contrast agent or hyperthermia, principally because of their low remanent magnetization (21.8 emu/g).

Another interesting feature of the spherical maghemite nanoclusters is their big surface area (239.11 m^2/g obtained by the BET method), that make maghemite clusters interesting for catalytic applications or for removing pollutants from water. Also is possible to deposit Prussian blue diluted in ethanol on glass substrates to produce

hematite thin films after a thermal treatment, using a similar conditions as for preparing maghemite powders (see details in appendix 14). The produced hematite thin films could also be used for water splitting or gas sensing, but it needs further investigation that is beyond the purpose of this thesis.

Bibliography

1. L. Samain, F. Grandjean, G.J. Long, P. Martinetto, P. Bordet, and D. Strivay, *J. Phys. Chem. C* **117**, 9693–9712 (2013).
2. B. V. Borshagovskii, V.I. Gol'danskii, G.B. Seifer, and R.A. Stukan, *Bulletin of the Academy of Sciences of the USSR Division of Chemical Science* **20**, 933–939 (1971).
3. E. Reguera, J. Fernández-Bertrán, A. Dago, and C. Díaz, *Hyperfine Interact.* **73**, 295–308 (1992).
4. R. Zboril, L. Machala, M. Mashlan, and V. Sharma, *Crystal Growth & Design* **4**, 1317–1325 (2004).
5. H.J. Buser, D. Schwarzenbach, W. Petter, and A. Ludi, *Inorg. Chem.* **16**, 2704–2710 (1977).
6. X. Wu, M. Cao, C. Hu, and X. He, *Crystal Growth & Design* **6**, 26–28 (2006).
7. M. Hu, S. Furukawa, R. Ohtani, H. Sukegawa, Y. Nemoto, J. Reboul, S. Kitagawa, and Y. Yamauchi, *Angewandte Chemie (International Ed. in English)* **51**, 984–988 (2012).
8. X. Shen, S. Wu, Y. Liu, K. Wang, Z. Xu, and W. Liu, *J. Colloid Interface Sci.* **329**, 188–95 (2009).
9. T. Uemura and S. Kitagawa, *J. Am. Chem. Soc.* **125**, 7814–7815 (2003).
10. M. Shokouhimehr, E.S. Soehnlen, J. Hao, M. Griswold, C. Flask, X. Fan, J.P. Basilion, S. Basu, and S.D. Huang, *J. Mater. Chem.* **20**, 5251 (2010).
11. C. Burda, X. Chen, R. Narayanan, and M. a El-Sayed, *Chem. Rev.* **105**, 1025–102 (2005).
12. Y. Xia, Y. Xiong, B. Lim, and S.E. Skrabalak, *Angew. Chem., Int. Ed.* **48**, 60–103 (2009).
13. A.-H. Lu, E.L. Salabas, and F. Schüth, *Angew. Chem., Int. Ed.* **46**, 1222–1244 (2007).
14. D.L. Leslie-Pelecky and R.D. Rieke, *Chem. Mater.* **8**, 1770–1783 (1996).
15. L. Wang and L. Gao, *Journal of Physical Chemistry C* **113**, 15914–15920 (2009).
16. R. Zboril, M. Mashlan, and D. Petridis, *Chem. Mater.* **14**, 969–982 (2002).
17. R. Zboril, M. Mashlan, K. Barcova, and M. Vujtek, *Hyperfine Interact.* **139/140**, 597–606 (2002).

18. M. Hermanek and R. Zboril, *Chem. Mater.* **20**, 5284–5295 (2008).

19. P.R. Bueno, F.F. Ferreira, D. Giménez-Romero, G.O. Setti, R.C. Faria, C. Gabrielli, H. Perrot, J.J. Garcia-Jareño, and F. Vicente, *J. Phys. Chem.* **112**, 13264–13271 (2008).

20. R. Zboril, M. Mashlan, D. Krausova, and P. Pikal, *Hyperfine Interact.* **120/121**, 497–501 (1999).

21. L. Machala, J. Tuček, and R. Zbořil, *Chem. Mater.* **23**, 3255–3272 (2011).

22. J. Tuček, R. Zboril, and D. Petridis, *J. Nanosci. Nanotechnol.* **6**, 926–947 (2006).

23. A.M. Pereira, C. Pereira, A.S. Silva, D.S. Schmool, C. Freire, J.-M. Grenèche, and J.P. Araujo, *J. Appl. Phys.* **109**, 114319 (2011).

24. S. Sakurai, A. Namai, K. Hashimoto, and S. Ohkoshi, *J. Am. Chem. Soc.* **131**, 18299–18303 (2009).

25. H. Itoh and T. Sugimoto, *J. Colloid Interface Sci.* **265**, 283–295 (2003).

26. O. Iglesias, A. Labarta, and X. Batlle, *J. Nanosci. Nanotechnol.* **8**, 2761–2780 (2008).

27. Y.Z. Shen, K.H. Oh, and D.N. Lee, *Materials Science and Engineering: A* **434**, 314–318 (2006).

6. Summary and conclusions

The principal aim of this thesis was the preparation of iron and iron oxides using the solid state reaction method. To reach this goal two different materials has been used as precursors: a) natural garnets from Alm-Prp and Alm-Sps series, and b) iron(III) hexacyanoferrate (Prussian blue). The thermal decomposition of the aforementioned materials was studied using thermogravimetry analysis (TGA) and differential scanning calorimetry (DSC), where complementary techniques as X-ray diffraction (XRD) and Mössbauer spectroscopy (MS) were used to studied the phase composition of samples before and after heating.

The main contribution of this work is the detailed study of the thermal decomposition of the chosen precursors, and its better understanding to determine a more accurate mechanism of decomposition in reducing and oxidant atmospheres. The principal conclusions can be summarized as follow:

1.

Natural garnets decompose in reducing atmosphere at temperatures above 1000 °C. When the iron content is very high as in almandine the decomposition is completed below 1100 °C, while for garnets with less iron content the decomposition onset is slightly above 1100 °C.

The common decomposition products observed for all studied garnets are metallic iron (α-Fe) and hercynite-spinel (Hc-Spl), Fe-cordierite (Fe-Crd) is also observed for almost all garnets with exception of pyrope. Other decomposition products are pyroxenes as enstatite (En), clinoenstatite (Cen) and pigeonite (Pgt), cristobalite (Crs), fayalite (Fa), and anorthite (An) only if the Ca amount in dodecahedral sites is significant.

The onset temperature of decomposition has a linear dependence with the iron content in dodecahedral sites of garnet; the only exception is observed for pyrope, which has an onset temperature around 40 °C greater than for almandine, but it shows a slower decomposition rate than the other garnets. It could be caused for the presence of Ca in dodecahedral sites, also Fe^{3+} and Cr in octahedral sites destabilizing the garnet structure.

The thermal stability of garnets decrease with the increase of iron content, but when the iron content is very low, i.e. for garnet composition close to pyrope, the thermal stability decreases, but it is still greater than for almandine. Although this is contradictory

to the linear tendency observed for the other garnets, it could probably be explained for local distortion produced by the presence of Ca in the X-sites.

2.

Prussian blue (PB), when heated under reducing atmosphere of argon, starts to decompose above 300 °C, and is fully decomposed at 440 °C. According to TGA/DSC analysis, at temperatures around 150 °C water molecules are released from PB structure, following by a degradation of the structure that leads to the emission of cyanide groups (CN^-), thus initiating first a rearrangement of the former PB structure to and analogue PB form (ferrous ferrocyanide), and finally to the breakdown of PB.

The decomposition products formed after decomposition of PB, heated under inert atmosphere with a low heating rate, are mainly iron carbides; where Fe_2C (hexagonal and orthorhombic crystallographic structure) is first formed, then the former iron carbides have a rearrangement and decomposition of their structures and originate other crystalline forms of iron carbides Fe_5C_2, Fe_7C_3 a Fe_3C. Iron is formed lastly, as a result of the decomposition of cementite (Fe_3C) at temperatures higher than 800 °C.

The kind of inert atmosphere (nitrogen, argon) does not have any influence on the phase composition obtained after the decomposition, as long as the sample mass and heating rate are similar when heated under the different atmospheres.

The mass of the sample (layer thickness) influences the kind of phases produced. When the sample mass is small (< 10 mg, with layer thickness < 0.78 mm) is obtained only the hexagonal form of iron carbide ε-$Fe_{2+x}C$, but if the mass is greater than 10 mg are obtained Fe_2C (hexagonal and orthorhombic) and Fe_7C_3.

The heating rate also has influence on the kind of iron carbides obtained. Low heating rate (2 K/min) allows the obtention of many kinds of iron carbides, on the contrary with a higher heating rate (8 K/min) is obtained only hexagonal $Fe_{2+x}C$, which at the end is reduced to metallic iron.

2 K/min: $Fe_4[Fe(CN)_6]_3 \rightarrow Fe_2[Fe(CN)_6] \rightarrow Fe_2C \rightarrow Fe_5C_2, Fe_7C_3 \rightarrow Fe_3C \rightarrow Fe$

8 K/min: $Fe_4[Fe(CN)_6]_3 \rightarrow Fe_2[Fe(CN)_6] \rightarrow Fe_{2+x}C \rightarrow Fe$

3.

The synthesized Prussian blue, with cubic and spherical morphologies, when heated in air decomposes above 250 °C. Cubic particles of Prussian blue (PB-C) have

potassium incorporated in their structure, while the spherical particles (PB-S) have only traces of potassium. The differences in the TGA curves for both samples seem to be due to the potassium presence and not because of the morphology, but the difference between decomposition temperatures (T_d) is rather a consequence of the different size of the particles.

PB-S: $Fe_4[Fe(CN)_6]_3 \cdot mH_2O$, 160 nm, T_d = 269 °C

PB-C: $Fe_4[Fe(CN)_6]_3 \cdot [K^+_h \cdot OH^-_h \cdot mH_2O]$, 1.45 μm, T_d = 334 °C

At the beginning of the thermal decomposition of PB, amorphous iron oxide is first obtained, then the first polymorph to be formed is maghemite, in the case of sample PB-S; but in the case of PB-C maghemite and beta polymorph seems to be formed simultaneously. In the earlier stages of the decomposition (between 300 °C and 350 °C) the initial morphology and size of the PB precursor is maintained, and usually the formed iron oxide is maghemite.

When PB-S was heated up to 350 °C in a furnace it was obtained maghemite agglomerates that kept the initial morphology of the precursor; the same result was also obtained after heating PB-C but only when the layer thickness was thin (mass density 4.2 mg/cm^2), otherwise β-Fe_2O_3 was additionally obtained. Using a thin layer thickness was not the only way to obtain cubic clusters of maghemite, also it was possible using a thickest layer (20.3 mg/cm^2) but heating it up to lower temperature (320 °C). However using very slow heating rate (2 K/min) on sample PB-C promotes the formation of hematite and maghemite.

The clusters of ferric oxides, both cubic and spherical, are composed of small rounded maghemite nanoparticles (~ 4 nm in size). The magnetic behavior of the produced maghemite clusters was probed to be superparamagnetic at room temperature, with a very small coercitivity, and a big surface area (239.11 m^2/g). These properties make them interesting for possible applications, but it is necessary to carry on more research in that direction.

Appendices

Appendix 1: Localities of garnets and its **c**hemical composition obtained by EMPA.

Label	Locality
Grt1	Měrunice, Teplice, Czech Republic
Grt2	Ceylon, Sri Lanka
Grt3	Starkoč, Kutná hora, Czech Republic
Grt4	Dolní Bory, Žďár nad Sázavou, Czech Republic
Grt5	Zlatý Chlum, near Jeseník, Czech Republic

	Oxide	TiO_2	Cr_2O_3	CaO	FeO	MnO	Na_2O	P_2O_5	SiO_2	Al_2O_3	MgO	Y_2O_3	*Total*
Grt5	Wt.%	0.04	0.01	0.56	41.19	0.21	0.01	0.01	36.09	20.44	0.91	0.01	99.49
	± SD	0.02	0.01	0.11	0.15	0.06	0.02	0.01	0.22	0.14	0.05	0.01	0.35
Grt3	Wt.%	0.02	0.03	0.71	34.48	1.64	0.02	0.08	36.50	20.94	4.24	0.07	98.73
	± SD	0.01	0.01	0.01	0.17	0.07	0.02	0.01	0.45	0.03	0.06	0.04	0.37
Grt2	Wt.%	0.02	0.02	1.10	28.68	0.54	0.02	0.08	38.37	21.81	8.96	0.01	99.61
	± SD	0.03	0.01	0.03	0.27	0.02	0.01	0.01	0.16	0.11	0.09	0.01	0.23
Grt1	Wt.%	0.63	1.98	4.29	8.85	0.32	0.08	0.04	41.24	20.73	20.37	0.00	98.53
	± SD	0.03	0.04	0.04	0.09	0.02	0.02	0.01	0.26	0.10	0.11	0.00	0.28
Grt4	Wt.%	0.05	0.00	0.09	27.97	15.15	0.03	0.41	35.34	20.32	0.09	0.00	99.46
	± SD	0.01	0.00	0.01	1.30	1.18	0.01	0.12	0.18	0.09	0.02	0.00	0.24

Cations normalized to 12 oxygens

	Cation	Ti^{4+}	Cr^{3+}	Ca^{2+}	Fe^{2+}	Mn^{2+}	Na^{2+}	P^{5+}	Si^{4+}	Al^{3+}	Mg^{2+}	Y^{3+}	*Total*
Grt5	Apfu	0.002	0.001	0.050	2.851	0.015	0.002	0.006	2.986	1.994	0.113	0.001	8.020
	± SD	0.001	0.000	0.010	0.011	0.005	0.003	0.005	0.007	0.007	0.006	0.001	0.006
Grt3	Apfu	0.001	0.002	0.061	2.339	0.114	0.003	0.005	2.973	2.002	0.513	0.003	8.017
	± SD	0.001	0.000	0.001	0.011	0.004	0.003	0.001	0.008	0.004	0.007	0.002	0.008
Grt2	Apfu	0.001	0.001	0.092	1.867	0.036	0.003	0.005	2.978	1.996	1.037	0.000	8.016
	± SD	0.000	0.001	0.002	0.016	0.001	0.002	0.000	0.006	0.006	0.010	0.000	0.006
Grt1	Apfu	0.035	0.114	0.334	0.537	0.020	0.011	0.002	2.995	1.775	2.205	0.000	8.028
	± SD	0.002	0.002	0.003	0.005	0.001	0.001	0.000	0.011	0.009	0.016	0.000	0.010
Grt4	Apfu	0.003	0.000	0.008	1.949	1.069	0.005	0.029	2.944	1.996	0.011	0.000	8.013
	± SD	0.000	0.000	0.001	0.088	0.084	0.002	0.009	0.014	0.008	0.003	0.000	0.009

Notes: SD= Standard deviation. Wt%= weight percentage of oxide. Apfu= Atoms per formula unit.
Grt1: $Alm_{20}Prp_{80}$, Grt2: $Alm_{64}Prp_{36}$, Grt3: $Alm_{82}Prp_{18}$, Grt4: $Alm_{65}Sps_{35}$, Grt5: $Alm_{96}Prp_{4}$

Appendix 2: Thermal analysis (TG/DSC) and evolved gases analysis (EGA) of the natural garnets of almandine-pyrope and almandine-spessartine series.

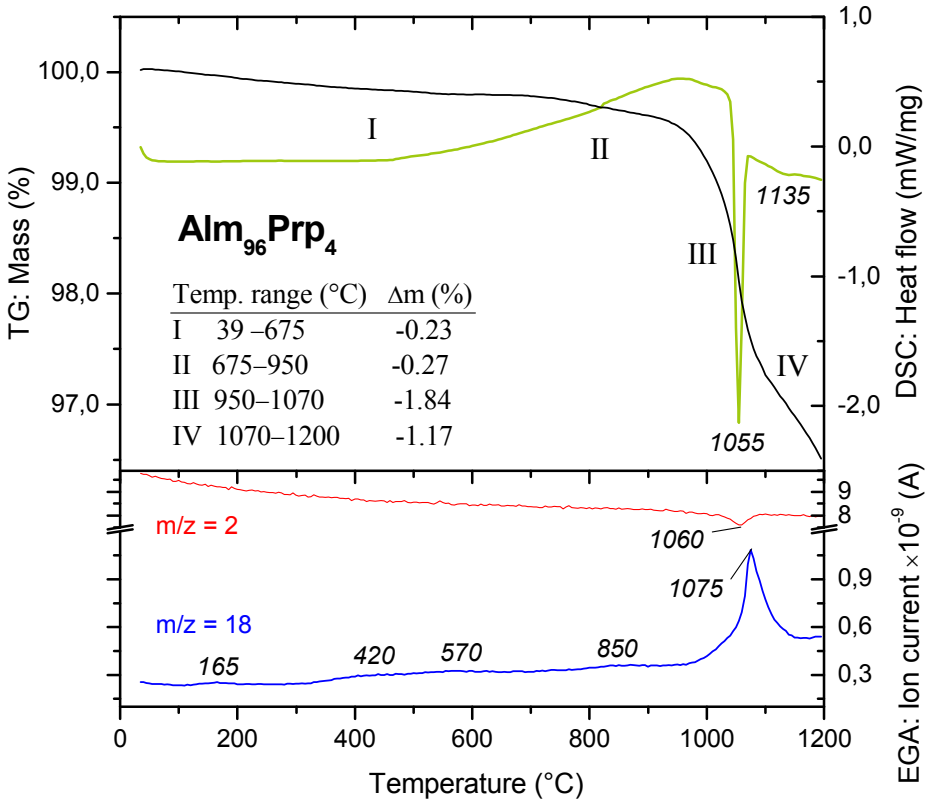

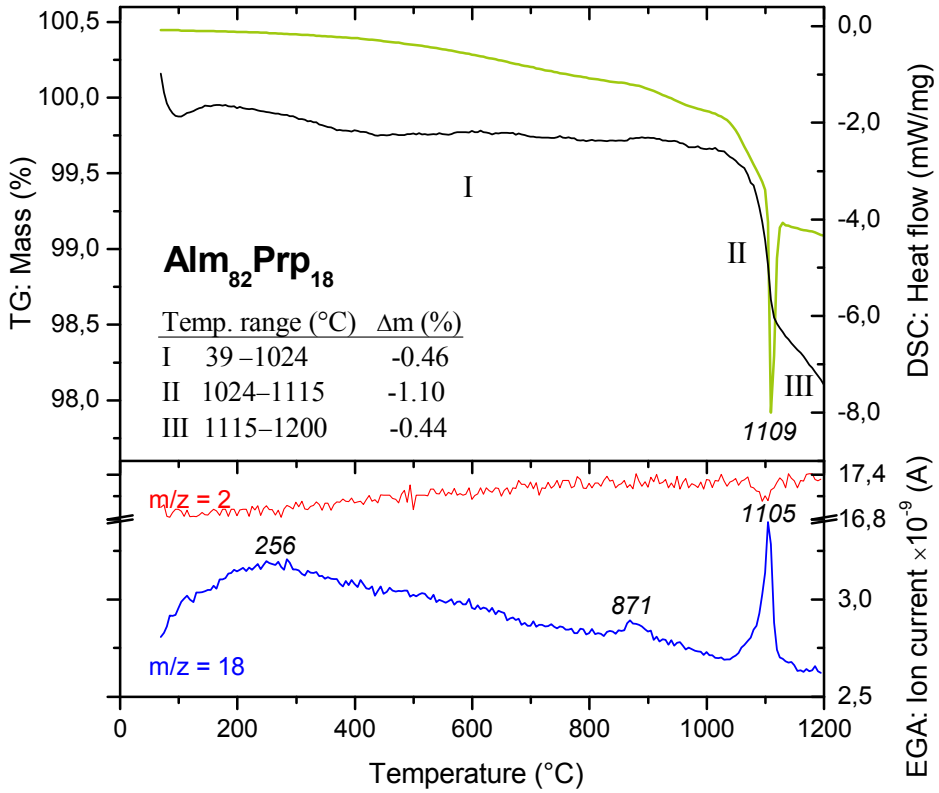

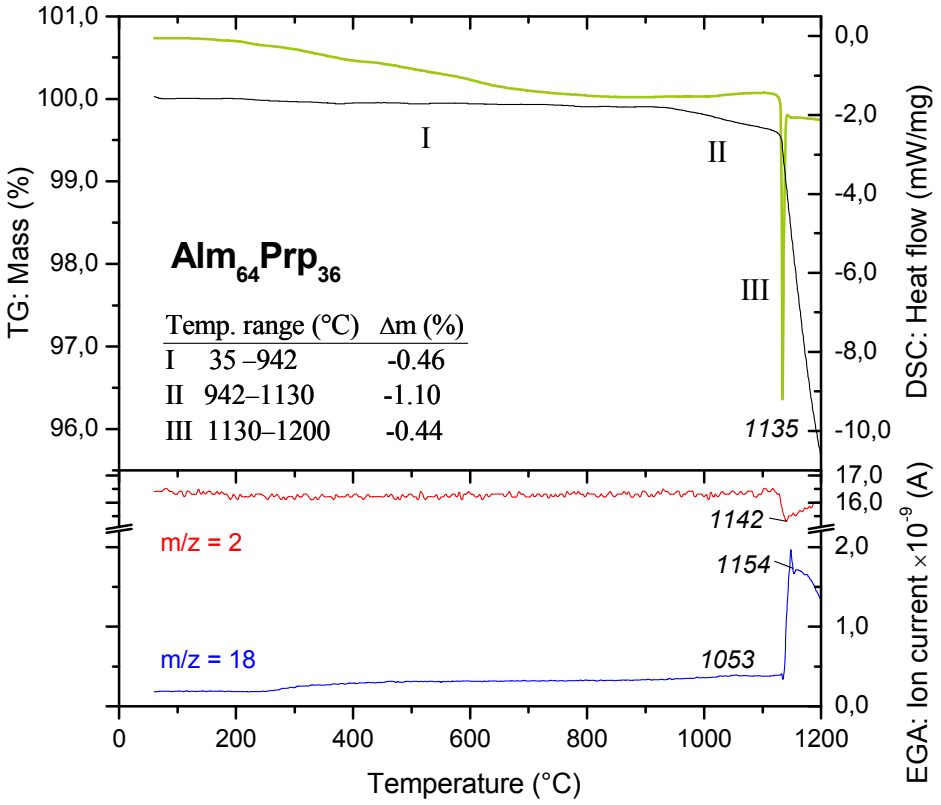
Alm64Prp36
Temp. range (°C) Δm (%)
I 35 –942 -0.46
II 942–1130 -1.10
III 1130–1200 -0.44
I
II
III
1135
1142
1154
1053
m/z = 2
m/z = 18
TG: Mass (%)
DSC: Heat flow (mW/mg)
EGA: Ion current ×10-9 (A)
Temperature (°C)

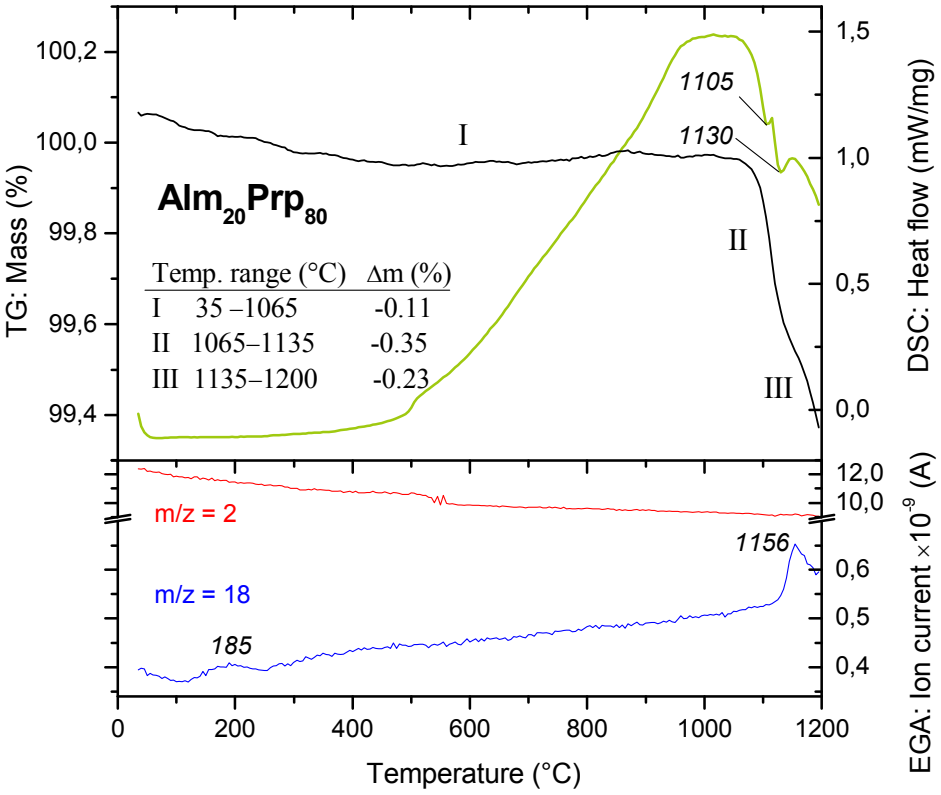
Alm20Prp80
Temp. range (°C) Δm (%)
I 35 –1065 -0.11
II 1065–1135 -0.35
III 1135–1200 -0.23
I
II
III
1105
1130
1156
185
m/z = 2
m/z = 18
TG: Mass (%)
DSC: Heat flow (mW/mg)
EGA: Ion current ×10-9 (A)
Temperature (°C)

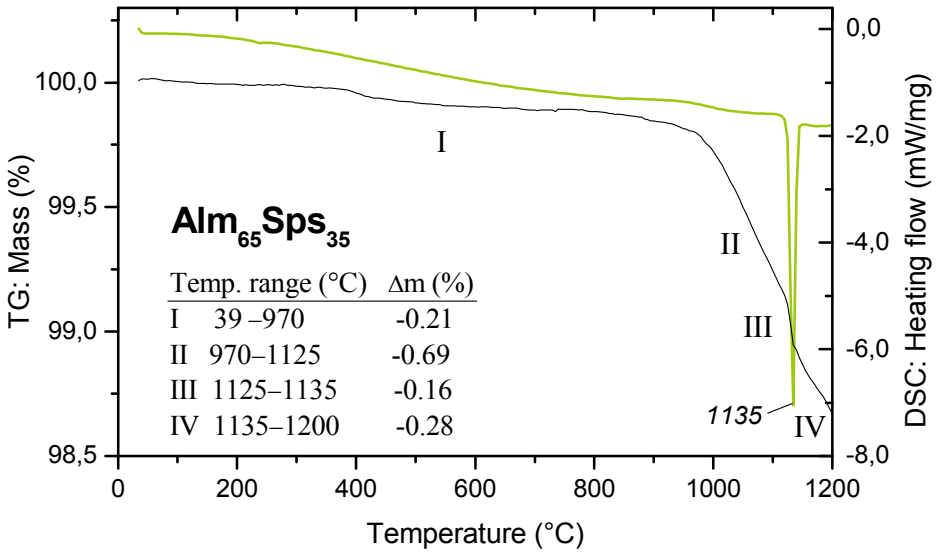
TG: Mass (%)
DSC: Heating flow (mW/mg)
Temperature (°C)
100,0
99,5
99,0
98,5
0,0
-2,0
-4,0
-6,0
-8,0
0
200
400
600
800
1000
1200
I
II
III
IV
1135
Alm65Sps35
Temp. range (°C) Δm (%)
I 39 –970 -0.21
II 970–1125 -0.69
III 1125–1135 -0.16
IV 1135–1200 -0.28

Appendix 3: Phase identification and Rietveld refinement of the garnet samples.

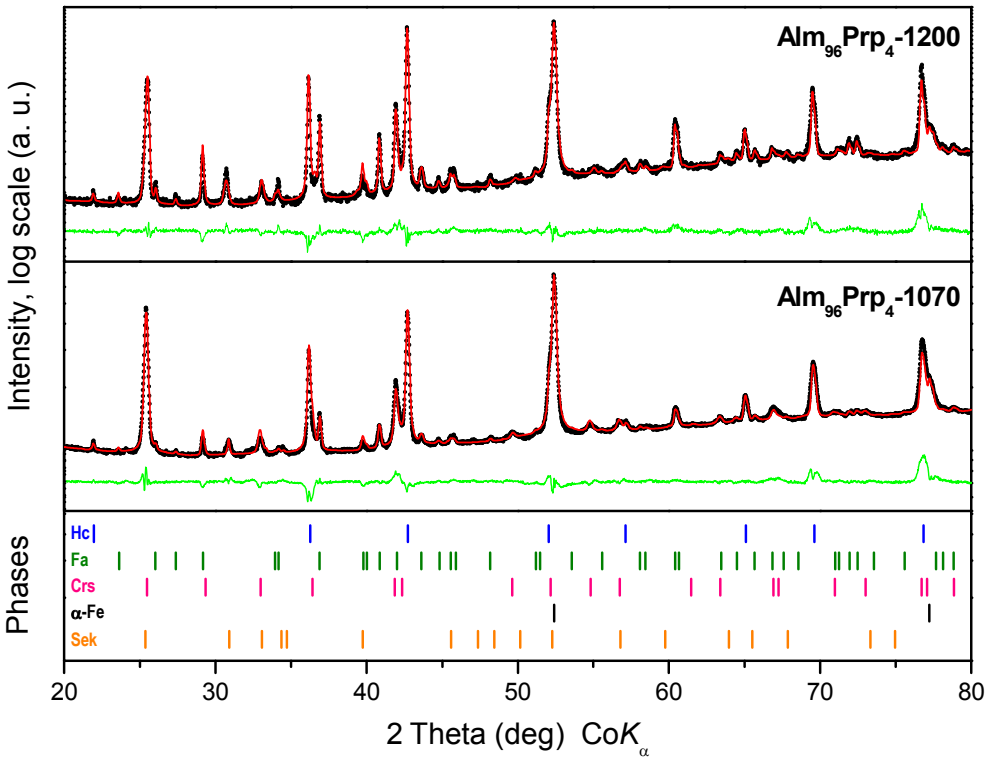

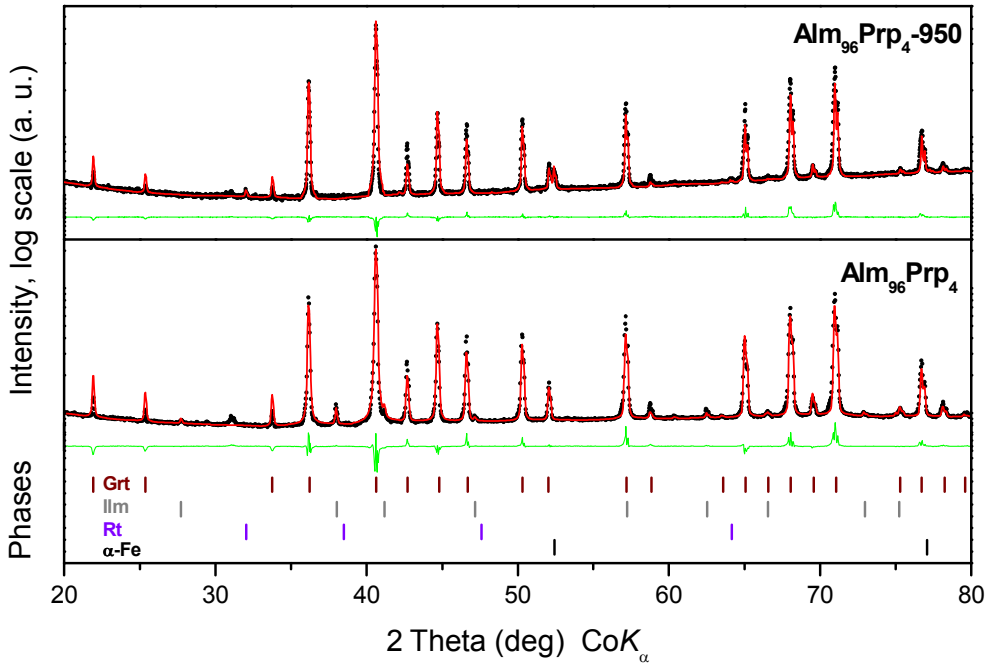

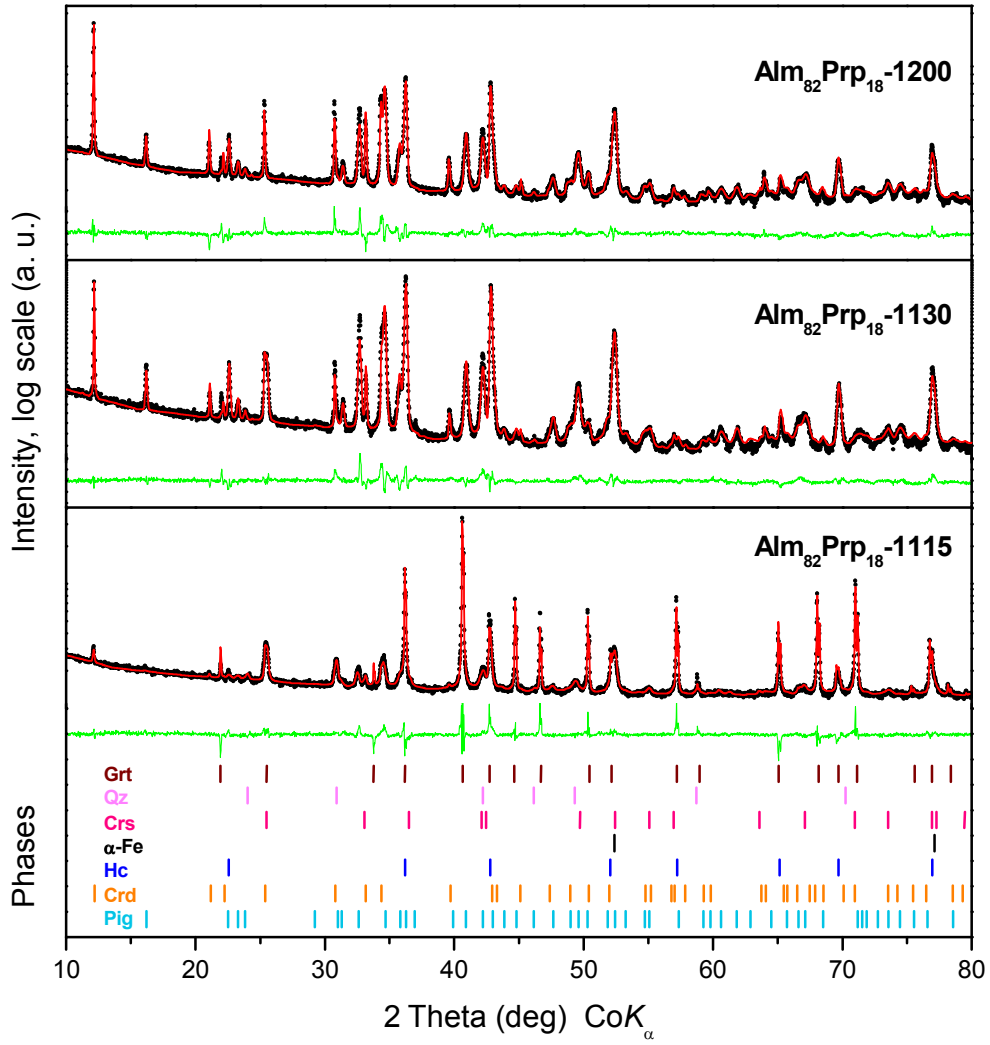
Alm82Prp18-1200
Alm82Prp18-1130
Alm82Prp18-1115
Intensity, log scale (a. u.)
Phases
Grt
Qz
Crs
α-Fe
Hc
Crd
Pig
10
20
30
40
50
60
70
80
2 Theta (deg) CoKα

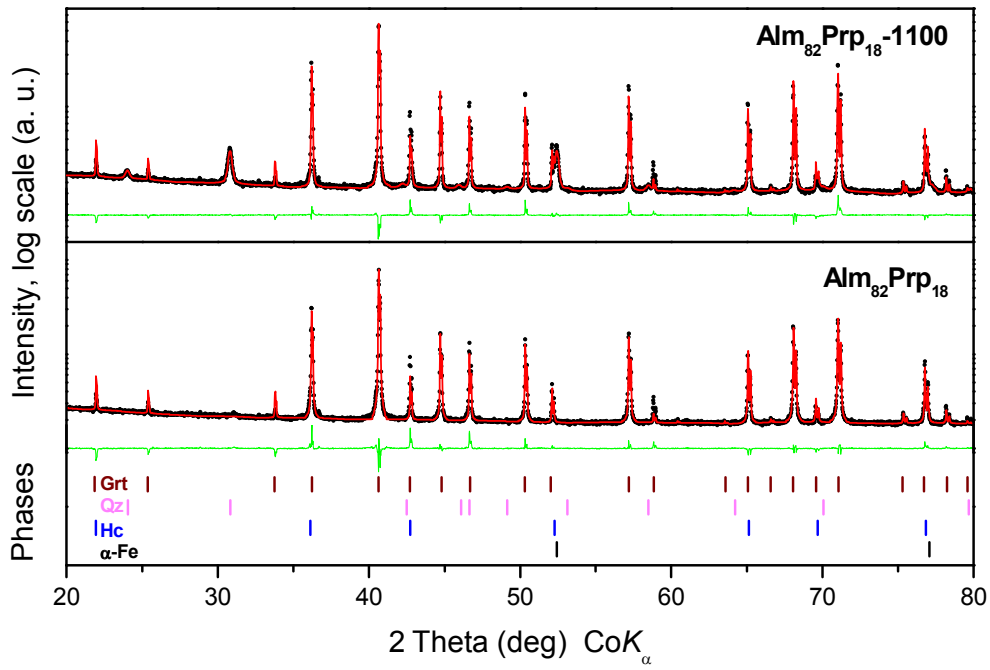
Alm82Prp18-1100
Alm82Prp18
Intensity, log scale (a. u.)
Phases
Grt
Qz
Hc
α-Fe
20
30
40
50
60
70
80
2 Theta (deg) CoKα

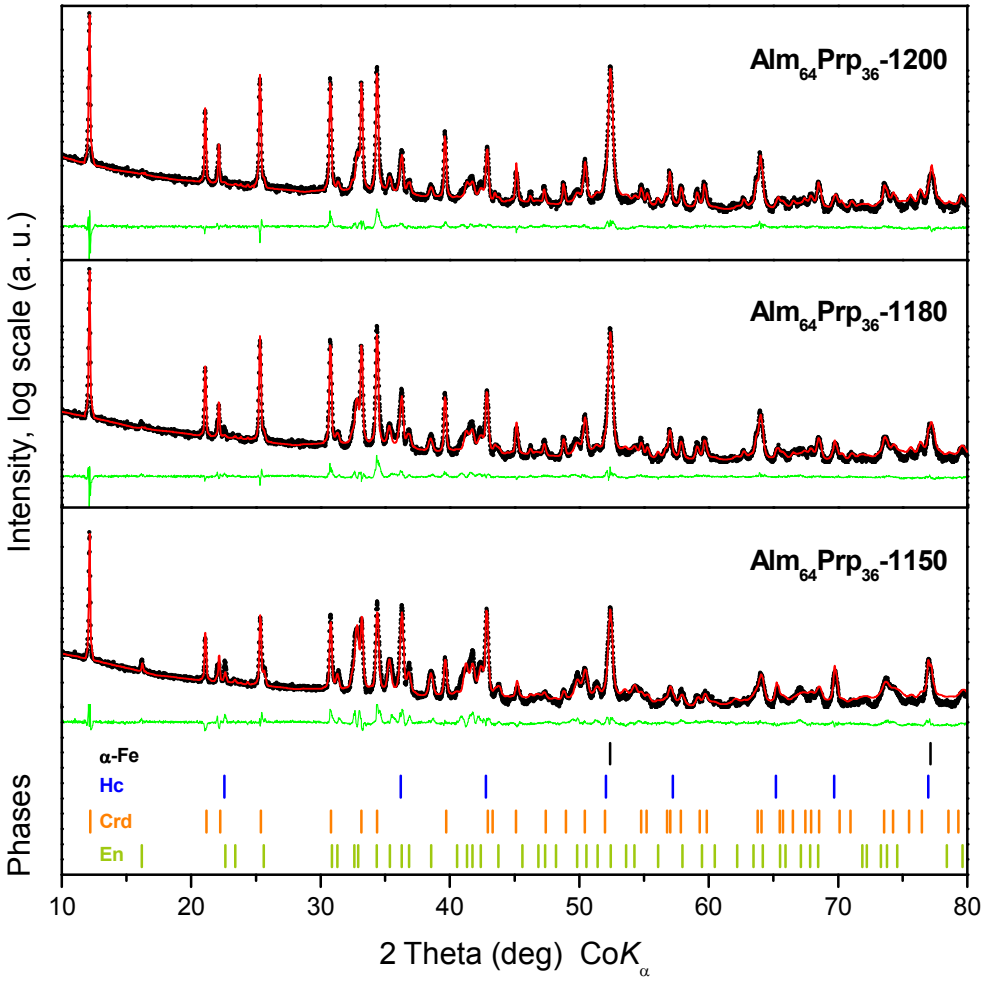
Alm64Prp36-1200
Alm64Prp36-1180
Alm64Prp36-1150
Intensity, log scale (a. u.)
Phases
α-Fe
Hc
Crd
En
10
20
30
40
50
60
70
80
2 Theta (deg) CoKα

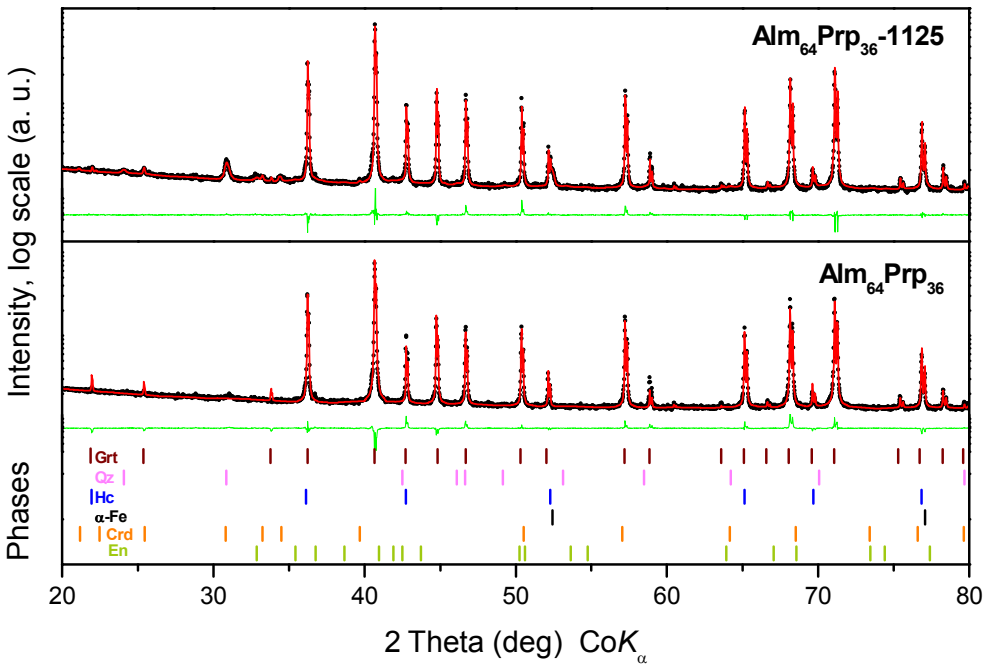
Alm64Prp36-1125
Alm64Prp36
Intensity, log scale (a. u.)
Phases
Grt
Qz
Hc
α-Fe
Crd
En
20
30
40
50
60
70
80
2 Theta (deg) CoKα

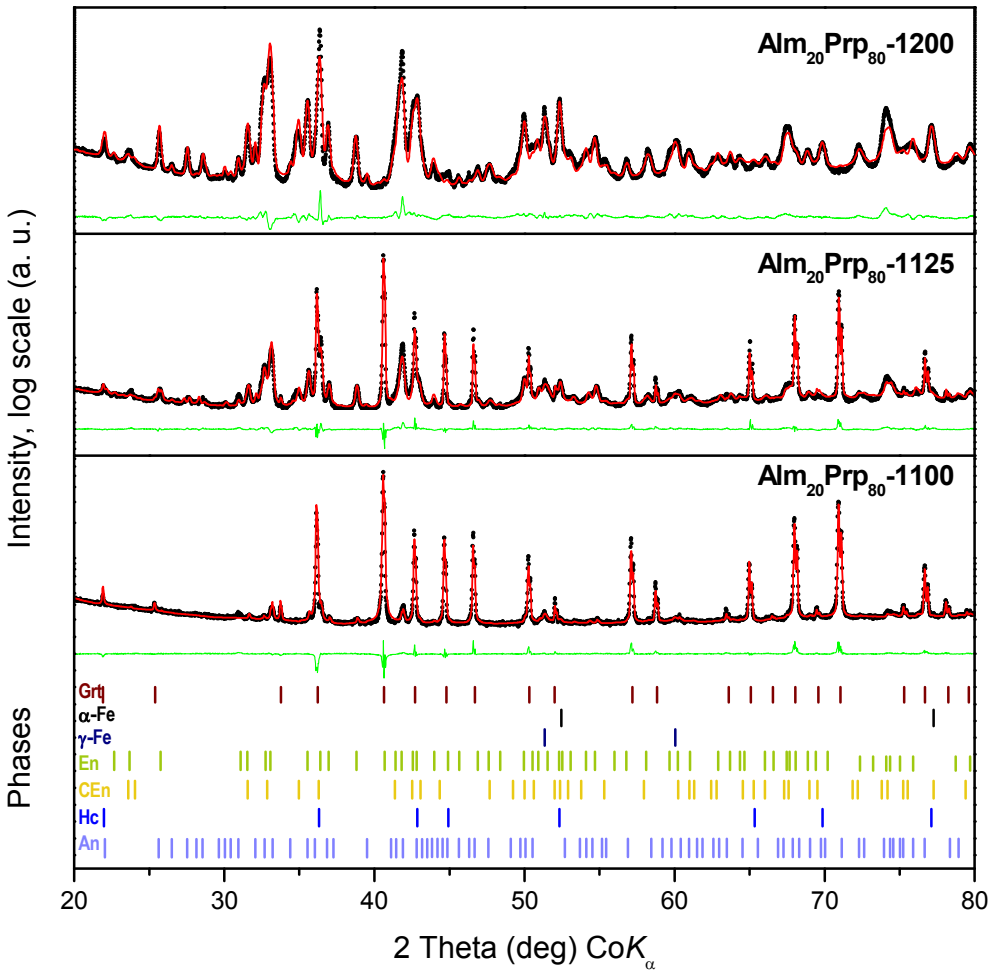
Alm20Prp80-1200
Alm20Prp80-1125
Alm20Prp80-1100
Intensity, log scale (a. u.)
Phases
Grt
α-Fe
γ-Fe
En
CEn
Hc
An
20
30
40
50
60
70
80
2 Theta (deg) CoKα

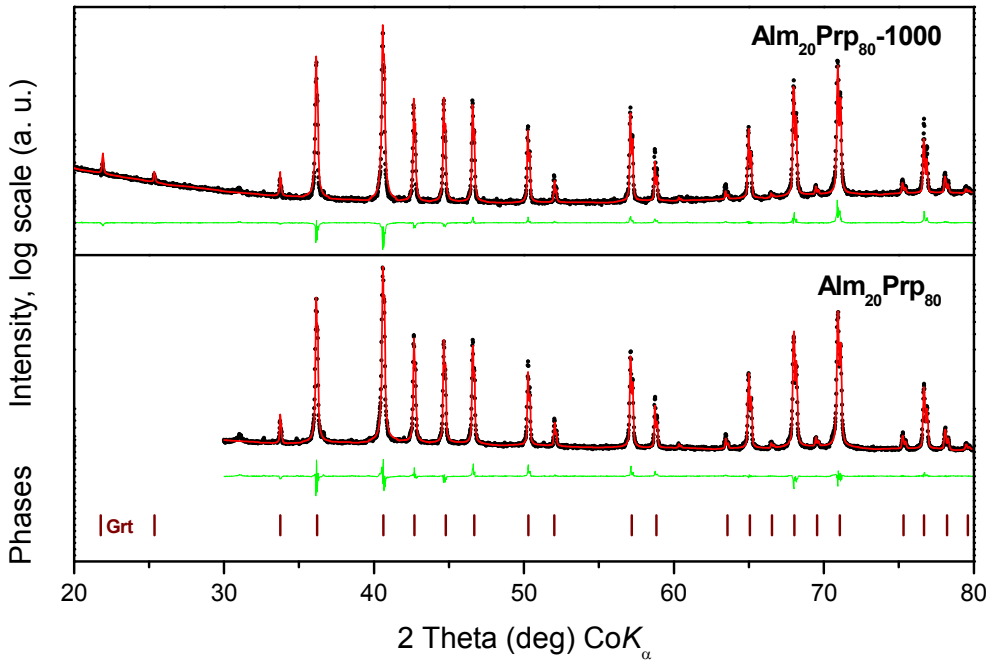
Alm20Prp80-1000
Alm20Prp80
Intensity, log scale (a. u.)
Phases
Grt
20
30
40
50
60
70
80
2 Theta (deg) CoKα

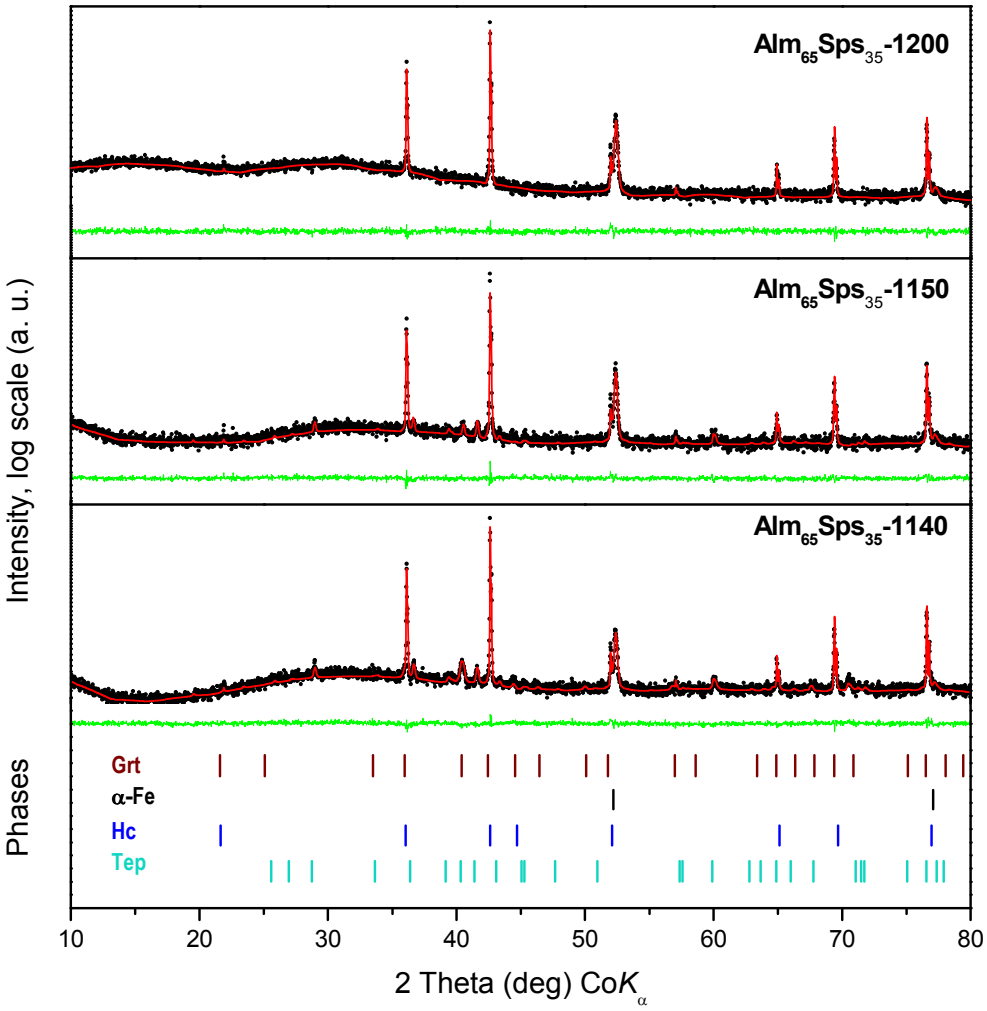
Alm65Sps35-1200
Alm65Sps35-1150
Alm65Sps35-1140
Intensity, log scale (a. u.)
Phases
Grt
α-Fe
Hc
Tep
10
20
30
40
50
60
70
80
2 Theta (deg) CoKα

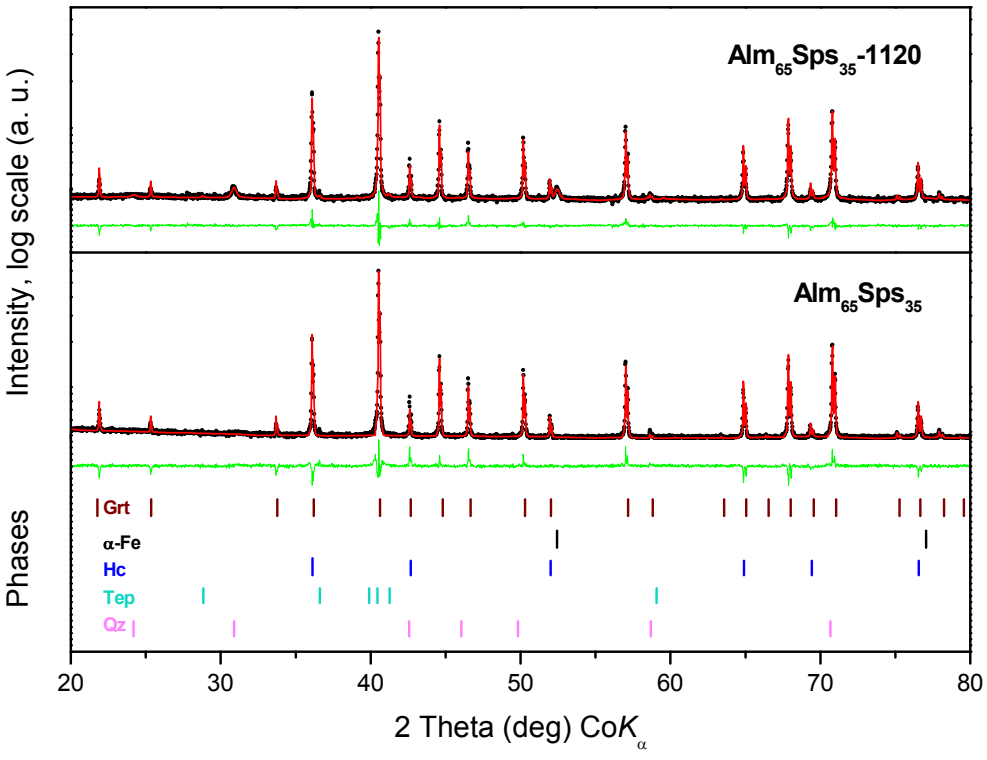
Alm65Sps35-1120
Alm65Sps35
Intensity, log scale (a. u.)
Phases
Grt
α-Fe
Hc
Tep
Qz
20
30
40
50
60
70
80
2 Theta (deg) CoKα

Appendix 4: Quantitative results from Rietveld refinement of the garnet samples.

$Alm_{96}Prp_4$

Phase	Chemical formula	Weight fractions (%)			
		$Alm_{96}Prp_4$	$Alm_{96}Prp_4$-950	$Alm_{96}Prp_4$-1070	$Alm_{96}Prp_4$-1200
Garnet	$(Fe,Mg)_3Al_2Si_3O_{12}$	99.2(6)	98.8(7)	-	-
Ilmenite	$FeTiO_3$	0.8(1)	-	-	-
Rutile	TiO_2	-	0.5(2)	n.d.	n.d.
α-iron	Fe	-	0.7(1)	22.0(1)	17.5(1)
Hercynite	$(Fe,Mg)Al_2O_4$	-	-	44.9(2)	44.6(2)
Fayalite	Fe_2SiO_4	-	-	8.2(2)	21.3(1)
Cristobalite	SiO_2	-	-	23.6(2)	12.1(2)
Sekaninaite	$(Fe,Mg)_2Al_4Si_5O_{18}$	-	-	1.3(1)	4.5(1)

n.d. - not determined

$Alm_{82}Prp_{18}$

Phase	Chemical formula	Weight fractions (%)				
		$Alm_{82}Prp_{18}$	$Alm_{82}Prp_{18}$ -1100	$Alm_{82}Prp_{18}$ -1115	$Alm_{82}Prp_{18}$ -1130	$Alm_{82}Prp_{18}$ -1200
Garnet	$(Fe,Mg)_3Al_2Si_3O_{12}$	100.0	87.8(3)	64.7(2)	-	-
Quartz	SiO_2	-	6.2(1)	2.9(1)	-	-
Cristobalite	SiO_2	-	-	4.2(1)	4.4(1)	-
α-iron	Fe	-	2.3(1)	2.6(1)	4.4(1)	4.5(1)
Hercynite	$(Fe,Mg)Al_2O_4$	-	3.7(2)	8.5(1)	19.7(1)	17.9(1)
Cordierite	$(Fe,Mg)_2Al_4Si_5O_{18}$	-	-	2.0(1)	11.3(1)	23.4(1)
Pigeonite	$(Mg,Fe,Ca)(Mg,Fe)Si_2O_6$	-	-	15.0(3)	60.2(3)	54.2(2)

$Alm_{64}Prp_{36}$

Phase	Chemical formula	Weight fractions (%)				
		$Alm_{64}Prp_{36}$	$Alm_{64}Prp_{36}$ -1125	$Alm_{64}Prp_{36}$ -1150	$Alm_{64}Prp_{36}$ -1180	$Alm_{64}Prp_{36}$ -1200
Garnet	$(Fe,Mg)_3Al_2Si_3O_{12}$	100.0	94.5(2)	-	-	-
Quartz	SiO_2	-	1.8(1)	-	-	-
α-iron	Fe	-	0.6(1)	5.2(1)	11.3(1)	13.7(1)
Enstatite	$(Mg,Fe)SiO_3$	-	1.2(1)	43.6(4)	25.3(4)	19.2(3)
Cordierite	$(Fe,Mg)_2Al_4Si_5O_{18}$	-	1.3(1)	34.5(1)	55.6(2)	62.3(2)
Hercynite	$(Fe,Mg)Al_2O_4$	-	0.6(1)	16.7(1)	7.9(1)	4.8(1)

$Alm_{20}Prp_{80}$

Phase	Chemical formula	Weight fractions (%)				
		$Alm_{20}Prp_{80}$	$Alm_{20}Prp_{80}$ -1000	$Alm_{20}Prp_{80}$ -1100	$Alm_{20}Prp_{80}$ -1125	$Alm_{20}Prp_{80}$ -1200
Garnet	$(Fe,Mg,Ca)_3Al_2Si_3O_{12}$	100.0	100.0	94.5(3)	48.1(2)	-
α-iron	Fe	-	-	0.1(1)	0.4(1)	1.1(1)
γ-iron	Fe	-	-	0.4(1)	1.0(1)	2.0(1)
Enstatite	$(Mg,Fe)SiO_3$	-	-	5.1(3)	32.9(3)	53.7(3)
Clinoenstatite	$Mg_2Si_2O_6$	-	-	-	7.3(3)	20.5(3)
Anorthite	$CaAl_2Si_2O_8$	-	-	-	6.6(2)	12.6(2)
Spinel	$(Fe,Mg)Al_2O_4$	-	-	-	3.7(2)	10.1(2)

$Alm_{65}Sps_{35}$

Phase	Chemical formula	Weight fractions (%)				
		$Alm_{65}Sps_{35}$	$Alm_{65}Sps_{35}$ -1120	$Alm_{65}Sps_{35}$ -1140	$Alm_{65}Sps_{35}$ -1150	$Alm_{65}Sps_{35}$ -1200
Garnet	$(Fe,Mg,Ca)_3Al_2Si_3O_{12}$	100.0	92.8(2)	14.2(5)	-	-
α-iron	Fe	-	1.2(1)	10.7(2)	14.8(2)	78.8(5)
Hercynite	$FeAl_2O_4$	-	1.2(1)	58.7(3)	70.1(5)	21.2(3)
Tephroite	$(Mn,Fe)SiO_4$	-	1.2(2)	16.5(5)	15.1(6)	-
Quartz	SiO_2	-	3.6(1)	-	-	-

Appendix 5: Lattice parameters of the garnets and its decomposition products.

Phase	ICSD file	Space group	Refined cell parameters			
			$Alm_{96}Prp_4$	**$Alm_{96}Prp_4$-950**	**$Alm_{96}Prp_4$-1070**	**$Alm_{96}Prp_4$-1200**
Garnet	27364	Ia-3d	a = b = c = 11.5341(2) Å α = β = γ =90°	a = b = c = 11.5318(2) Å α = β = γ =90°	-	-
Ilmenite	153491	R3-H	a = b = 5.0893(8) Å c = 14.0770(40) Å α = β = 90°, γ = 120°	-	-	-
Rutile	16636	P42/mnm	-	a = b = 4.5900(40) Å c = 2.9610(60) Å α = β = γ =90°	-	-
α-Iron	631729	Im-3m	-	a = b = c = 2.8665(4) Å α = β = γ = 90°	a = b = c = 2.8669(1) Å α = β = γ = 90°	a = b = c =2.86713(7) Å α = β = γ = 90°
Hercynite	95322	Fd-3m	-	-	a = b = c =8.1532(2) Å α = β = γ = 90°	a = b = c = 8.1568(2) Å α = β = γ = 90°
Fayalite	158572	Pnma	-	-	a = 10.4729(14) Å b = 6.0941(9) Å c = 4.8232(8) Å α = β = γ = 90°	a = 10.4710(6) Å b = 6.0953(3) Å c = 4.8239(3) Å α = β = γ = 90°
Cristobalite	47220	$P4_12_12$	-	-	a = b = 5.0044(5) Å c = 6.9920(12) Å α = β = γ = 90°	a = b = 4.9909(8) Å c = 6.953(2) Å α = β = γ = 90°
Cordierite-Sekaninaite	100490	Cccm	-	-	a = 9.8451(156) Å b = 16.8523(145) Å c = 9.2824(50) Å α = β = γ = 90°	a = 9.8378(193) Å b = 17.1454(180) Å c = 9.2721(40) Å α = β = γ = 90°

Phase	ICSD file	Space group	Refined cell parameters				
			$Alm_{82}Prp_{18}$	**$Alm_{82}Prp_{18}$-1100**	**$Alm_{82}Prp_{18}$-1115**	**$Alm_{82}Prp_{18}$-1130**	**$Alm_{82}Prp_{18}$-1200**
Garnet	27364	Ia-3d	a = b = c = 11.5299(1) Å α = β = γ =90°	a = b = c = 11.5298(1) Å α = β = γ =90°	a = b = c = 11.5287(1) Å α = β = γ =90°	-	-
Quartz	201354	P3121	-	a = b = 4.9754(19) Å c = 5.4236(34) Å α = β = 90°, γ = 120°	a = b = 4.9693(24) Å c = 5.3831(42) Å α = β = 90°, γ = 120°	-	-
Cristobalite	47220	$P4_12_12$	-	-	a = b = 4.9953(18) Å c = 6.9539(47) Å α = β = γ = 90°	a = b = 4.9678(15) Å c = 7.0617(41) Å α = β = γ =90°	-
α-Iron	631729	Im-3m	-	a = b = c = 2.8674(2) Å α = β = γ =90°	a = b = c = 2.8676(2) Å α = β = γ =90°	a = b = c = 2.8685(1) Å α = β = γ =90°	a = b = c = 2.8677(1) Å α = β = γ =90°
Hercynite-spinel	95322	Fd-3m	-	a = b = c = 8.1436(6) Å α = β = γ =90°	a = b = c = 8.1424(3) Å α = β = γ =90°	a = b = c = 8.1379(6) Å α = β = γ =90°	a = b = c = 8.1386(6) Å α = β = γ =90°
Cordierite-Sekaninaite	100490	Cccm	-	-	a = 9.7967(79) Å b = 16.9807(131) Å c = 9.3232(42) Å α = β = γ = 90°	a = 9.8024(15) Å b = 16.9417(26) Å c = 9.3332(7) Å α = β = γ = 90°	a = 9.7897(8) Å b = 17.0066(12) Å c = 9.3270(4) Å α = β = γ = 90°
Pigeonite	9242	$P12_1/c1$	-	-	a = 9.3923(26) Å b = 8.9466(28) Å c = 5.2508(14) Å β = 103.09(2)° α = γ = 90°	a = 9.3896(6) Å b = 8.8747(6) Å c = 5.2662(4) Å β = 102.94(1)° α = γ = 90°	a = 9.3897(5) Å b = 8.8742(6) Å c = 5.2621(3) Å β = 102.98(1)° α = γ = 90°

Phase	ICSD file	Space group	Refined cell parameters				
			$Alm_{64}Prp_{36}$	**$Alm_{64}Prp_{36}$-1125**	**$Alm_{64}Prp_{36}$-1150**	**$Alm_{64}Prp_{36}$-1180**	**$Alm_{64}Prp_{36}$-1200**
Garnet	27364	Ia-3d	a = b = c = 11.5172(1) Å α = β = γ =90°	a = b = c = 11.5183(1) Å α = β = γ =90°	-	-	-
Quartz	201354	P3121	-	a = b = 4.9622(31) Å c = 5.4041(56) Å α = β = 90°, γ = 120°	-	-	-
α-Iron	631729	Im-3m	-	a = b = c = 2.8689(3) Å α = β = γ =90°	a = b = c = 2.8675(1) Å α = β = γ =90°	a = b = c = 2.8676(1) Å α = β = γ =90°	a = b = c = 2.8670(1) Å α = β = γ =90°
Enstatite	79762	Pbca	-	a = 5.2163(28) Å b = 18.3849(91) Å c = 8.7978 (47) Å α = β = γ = 90°	a = 5.2272(8) Å b = 18.2633(25) Å c = 8.8448(12) Å α = β = γ = 90°	a = 5.2317(11) Å b = 18.2897(36) Å c = 8.8351(16) Å α = β = γ = 90°	a = 5.2284(12) Å b = 18.2897(40) Å c = 8.8175 (22) Å α = β = γ = 90°
Cordierite	100490	Cccm	-	a = 9.7714(67) Å b = 16.9977(110) Å c = 9.3083(54) Å α = β = γ = 90°	a = 9.7816(25) Å b = 16.9673(43) Å c = 9.3207(6) Å α = β = γ = 90°	a = 9.7842(9) Å b = 16.9698(17) Å c = 9.3286(3) Å α = β = γ = 90°	a = 9.7817(4) Å b = 16.9729(7) Å c = 9.3299(2) Å α = β = γ = 90°
Spinel	95322	Fd-3m	-	a = b = c = 8.1353(8) Å α = β = γ =90°	a = b = c = 8.1324(2) Å α = β = γ =90°	a = b = c = 8.1312(4) Å α = β = γ =90°	a = b = c = 8.1281(5) Å α = β = γ =90°

Phase	ICSD file	Space group	Refined cell parameters				
			$Alm_{20}Prp_{80}$	**$Alm_{20}Prp_{80}$-1000**	**$Alm_{20}Prp_{80}$-1100**	**$Alm_{20}Prp_{80}$-1125**	**$Alm_{20}Prp_{80}$-1200**
Garnet	31238	Ia-3d	a = b = c = 11.5387(1) Å α = β = γ =90°	a = b = c = 11.5396(1) Å α = β = γ =90°	a = b = c = 11.5391(1) Å α = β = γ =90°	a = b = c = 11.5388(-) Å α = β = γ =90°	-
α-Iron	631729	Im-3m	-	-	a = b = c = 2.8685(33) Å α = β = γ =90°	a = b = c = 2.8681(-) Å α = β = γ =90°	a = b = c = 2.8674(3) Å α = β = γ =90°
γ-Iron	53449	Fm-3m	-	-	a = b = c = 3.5777(13) Å α = β = γ =90°	a = b = c = 3.5796(-) Å α = β = γ =90°	a = b = c = 3.5773(3) Å α = β = γ =90°
Enstatite	79762	Pbca	-	-	a = 5.2020(17) Å b = 18.1757(52) Å c = 8.6961(29) Å α = β = γ =90°	a = 5.2085(-) Å b = 18.2104(-) Å c = 8.7135(-) Å α = β = γ =90°	a = 5.2046(4) Å b = 18.2071(13) Å c = 8.7325(6) Å α = β = γ =90°
Clinoenstatite	24270	$P12_1/c1$	-	-	-	a = 9.33489(-) Å b = 8.9012(-) Å c = 5.1744(-) Å β = 103.70(-)° α = γ = 90°	a = 9.3601(18) Å b = 8.7928(22) Å c = 5.2055(12) Å β = 103.26(2)° α = γ = 90°
Anorthite	86317	P-1	-	-	-	a = 8.2006(-) Å b = 12.8573(-) Å c = 12.9161(-) Å α = 86.63(-)° β = 80.72(-)° γ = 90.03(-)°	a = 8.1521(12) Å b = 12.8219(21) Å c = 12.8843(19) Å α = 86.02(2)° β = 81.08(1)° γ = 89.33(2)°
Spinel	95317	Fd-3m	-	-	-	a = b = c = 8.1482(-) Å α = β = γ =90°	a = b = c = 8.1207(5) Å α = β = γ =90°

Phase	ICSD file	Space group	Refined cell parameters				
			$Alm_{65}Sps_{35}$	**$Alm_{65}Sps_{35}$-1120**	**$Alm_{65}Sps_{35}$-1140**	**$Alm_{65}Sps_{35}$-1150**	**$Alm_{65}Sps_{35}$-1200**
Garnet	27364	Ia-3d	a = b = c = 11.5614(1) Å α = β = γ =90°	a = b = c = 11.5625(1) Å α = β = γ =90°	a = b = c = 11.6060(10) Å α = β = γ =90°	-	-
α-Iron	631729	Im-3m	-	a = b = c = 2.8669(4) Å α = β = γ =90°	a = b = c = 2.8691(1) Å α = β = γ =90°	a = b = c = 2.8676(1) Å α = β = γ =90°	a = b = c = 2.8675(1) Å α = β = γ =90°
Hercynite	86560	Fd-3m	-	a = b = c = 8.1736(2) Å α = β = γ =90°	a = b = c = 8.1684(1) Å α = β = γ =90°	a = b = c = 8.1658(1) Å α = β = γ =90°	a = b = c = 8.1674(1) Å α = β = γ =90°
Tephroite	91450	Pnma	-	a = 10.5528(-) Å b = 6.2150(-) Å c = 4.8810(-) Å α = β = γ = 90°	a = 10.5520(30) Å b = 6.1480(20) Å c = 4.8470(20) Å α = β = γ = 90°	a = 10.5600(20) Å b = 6.1430(20) Å c = 4.8461(10) Å α = β = γ = 90°	-
Quartz	201354	P3121	-	a = b = 4.9370(40) Å c = 5.4620(70) Å α = β = 90°, γ = 120°	-	-	-

Appendix 6: Mössbauer spectra for garnet samples before and after heating.

$Alm_{96}Prp_4$

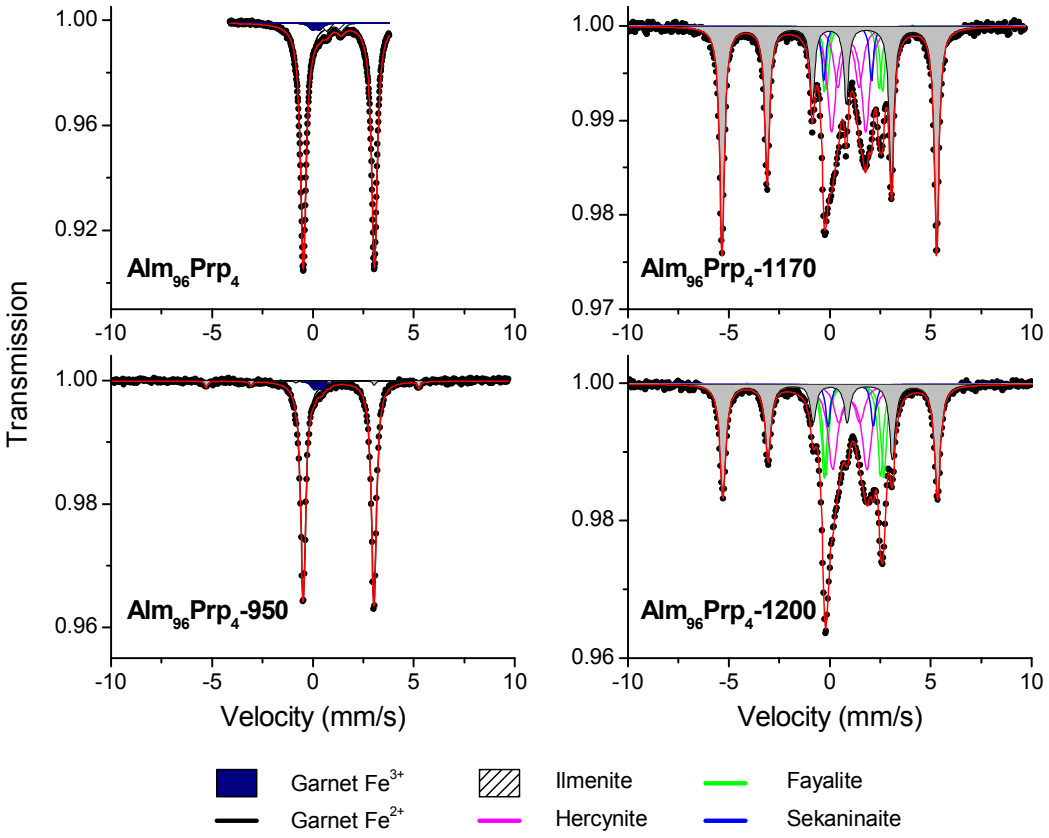

$Alm_{82}Prp_{18}$

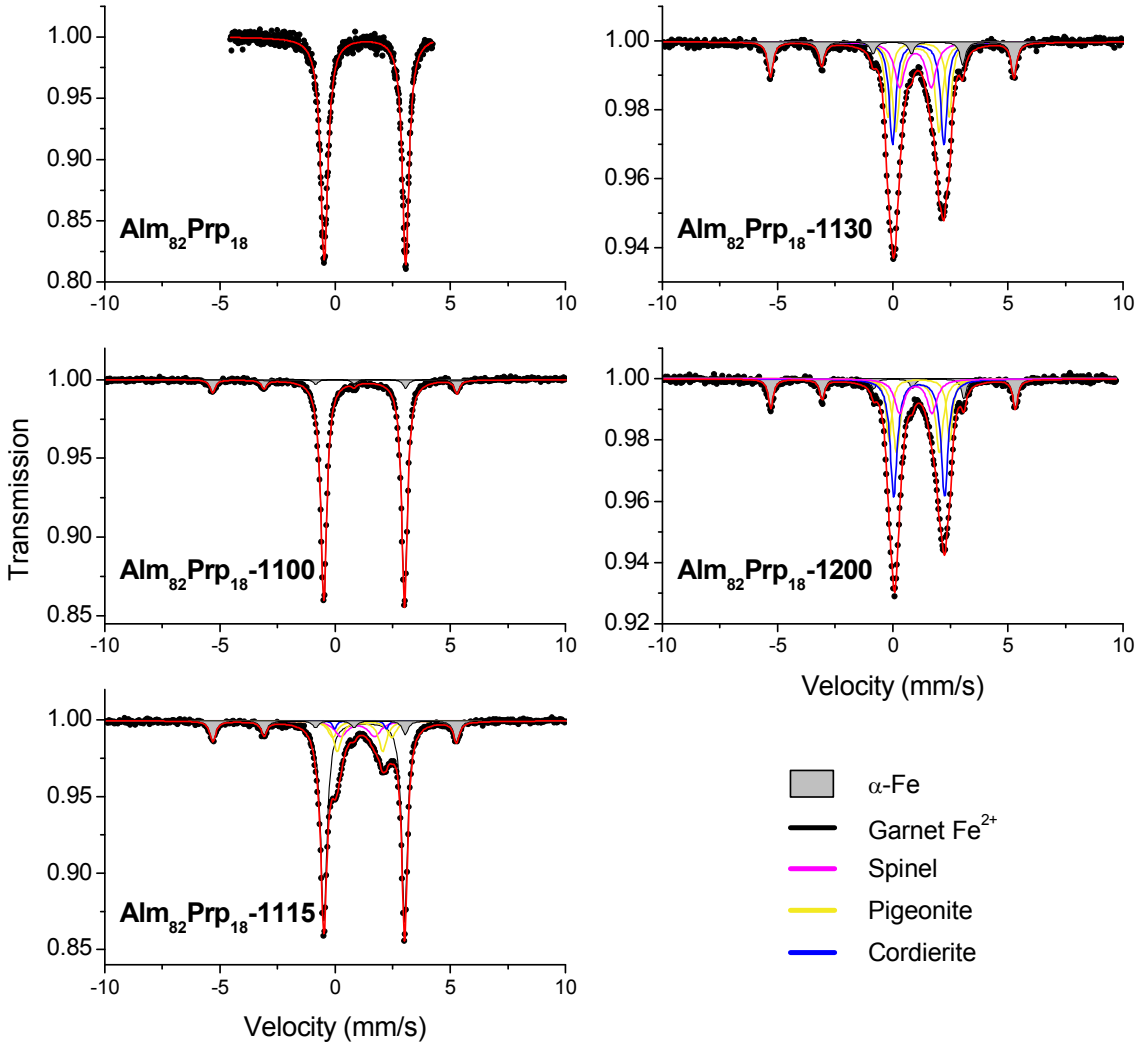
Alm82Prp18
Alm82Prp18-1130
Alm82Prp18-1100
Alm82Prp18-1200
Alm82Prp18-1115
Transmission
Velocity (mm/s)
Velocity (mm/s)
α-Fe
Garnet Fe2+
Spinel
Pigeonite
Cordierite

$Alm_{64}Prp_{36}$

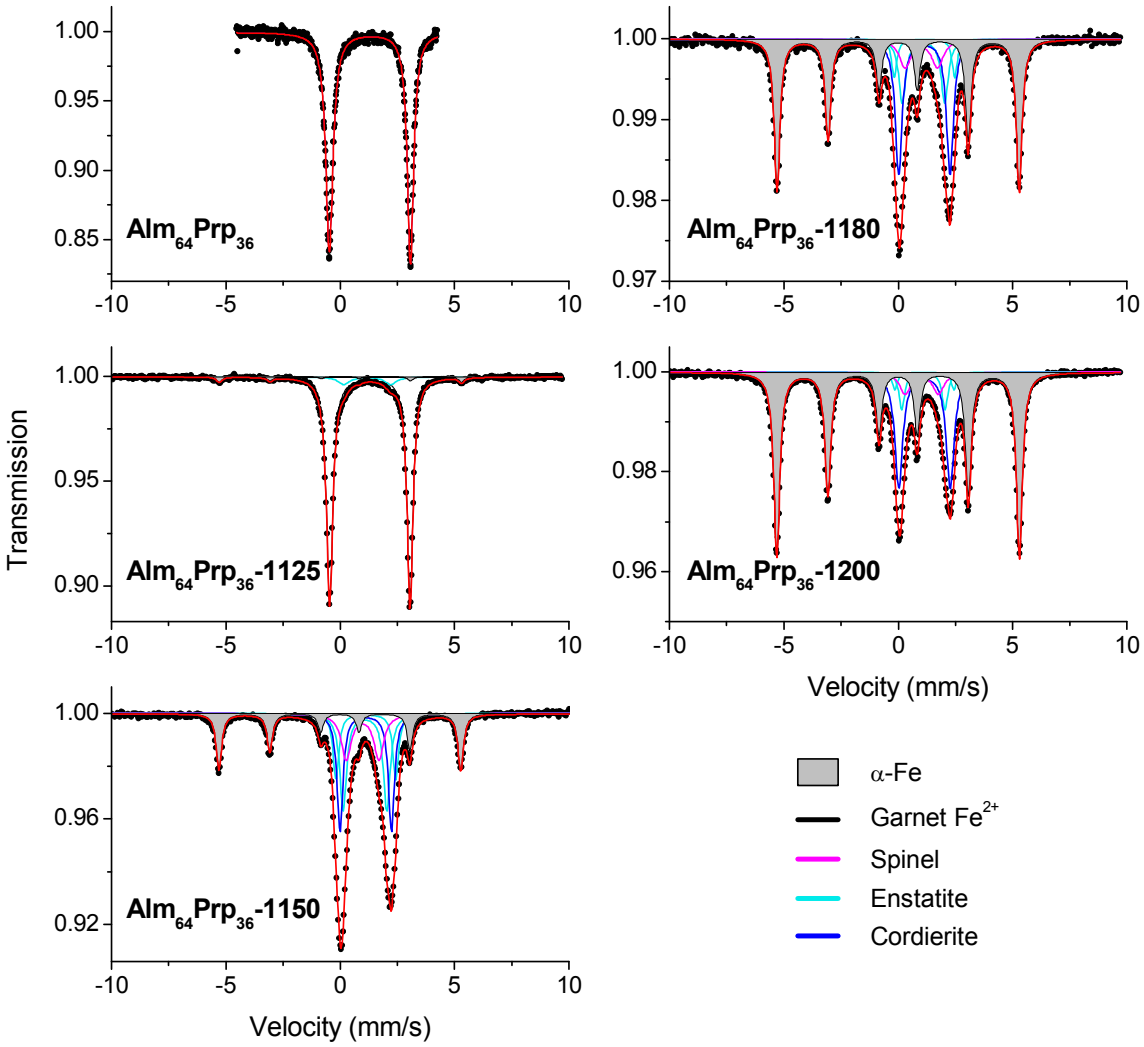
Alm64Prp36
Alm64Prp36-1180
Alm64Prp36-1125
Alm64Prp36-1200
Alm64Prp36-1150
Transmission
Velocity (mm/s)
α-Fe
Garnet Fe2+
Spinel
Enstatite
Cordierite

$Alm_{20}Prp_{80}$

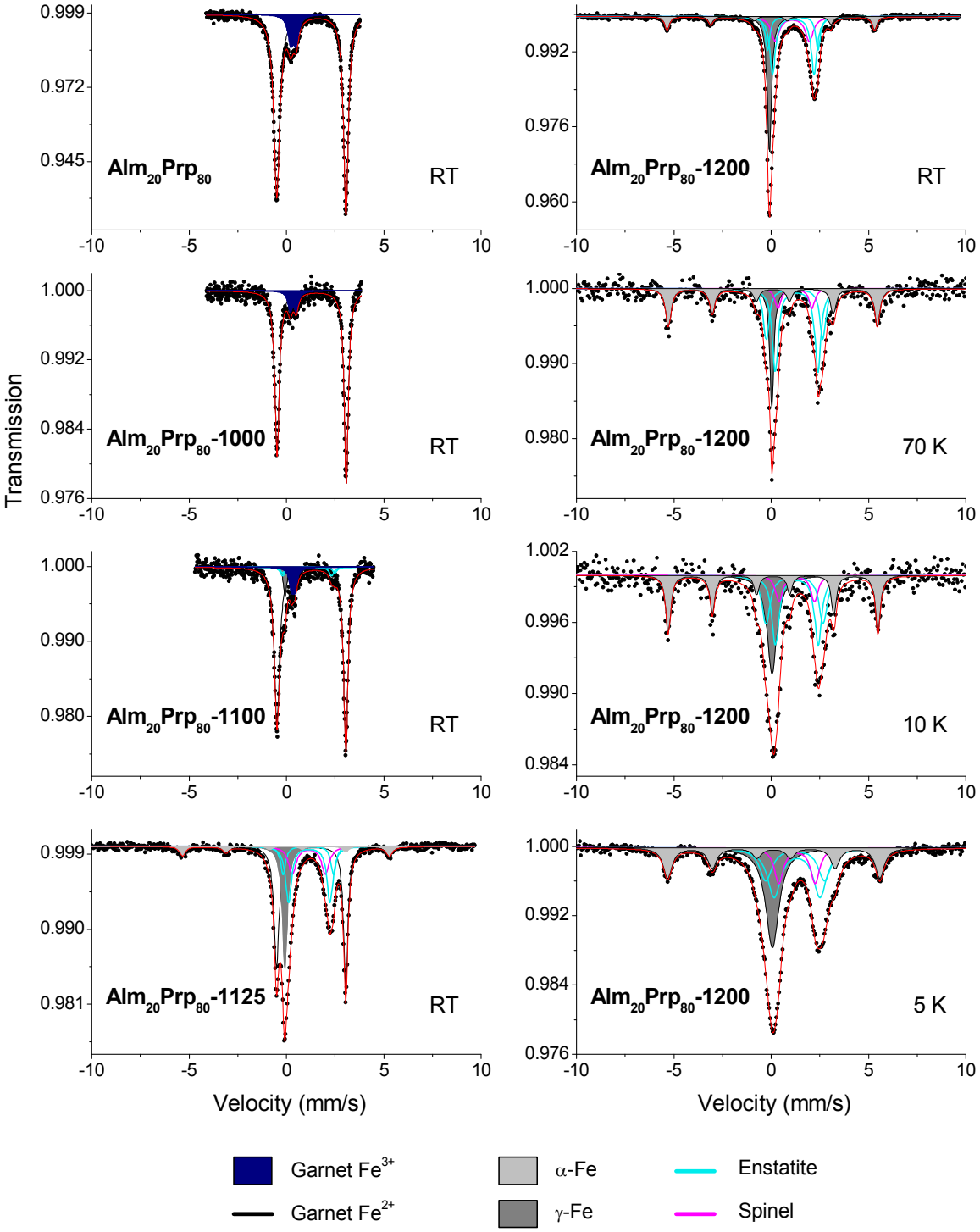
Alm20Prp80
RT
Alm20Prp80-1200
RT
Alm20Prp80-1000
RT
Alm20Prp80-1200
70 K
Alm20Prp80-1100
RT
Alm20Prp80-1200
10 K
Alm20Prp80-1125
RT
Alm20Prp80-1200
5 K
Transmission
Velocity (mm/s)
Velocity (mm/s)
Garnet Fe3+
Garnet Fe2+
α-Fe
γ-Fe
Enstatite
Spinel

$Alm_{65}Sps_{35}$

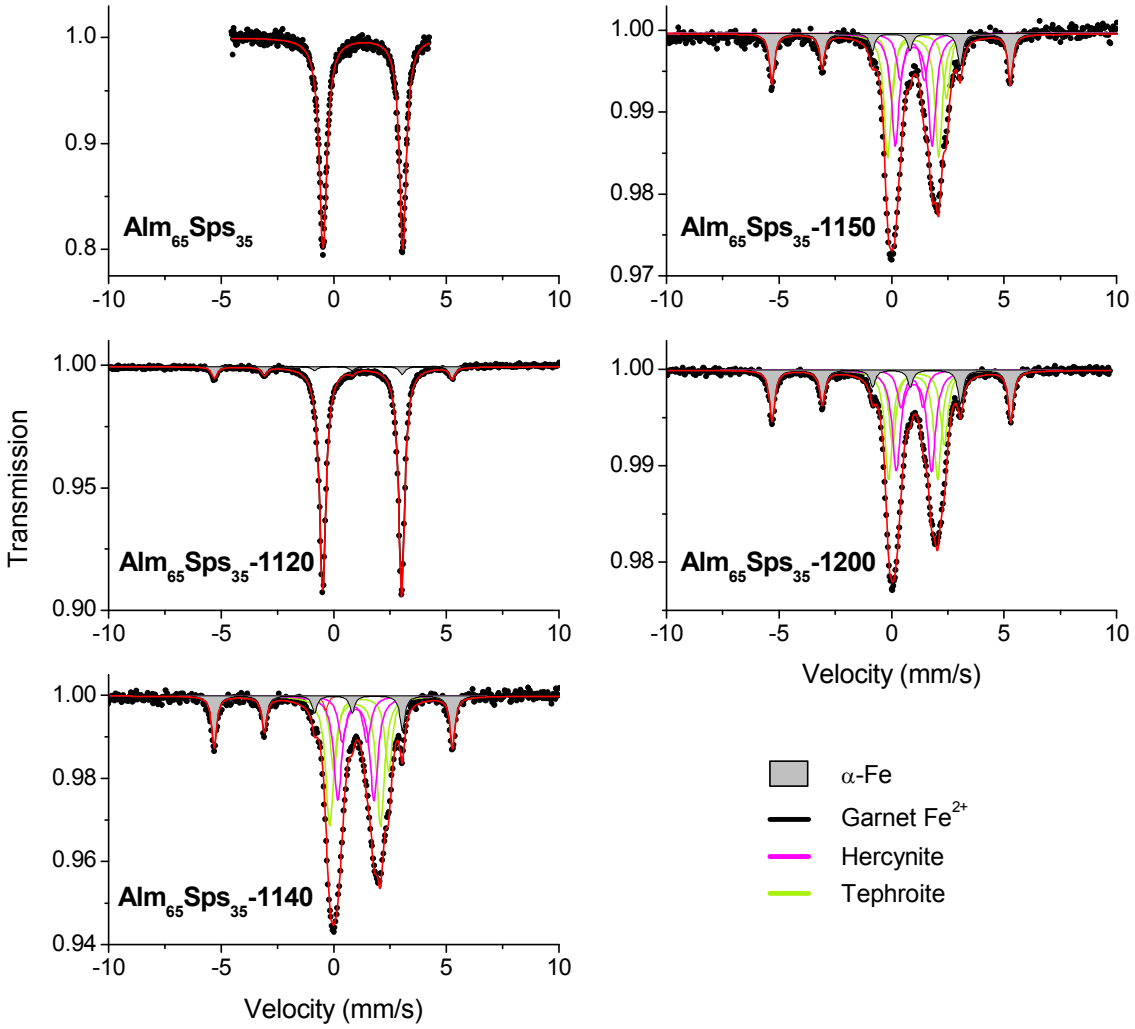
Alm65Sps35
Alm65Sps35-1150
Alm65Sps35-1120
Alm65Sps35-1200
Alm65Sps35-1140
Transmission
Velocity (mm/s)
α-Fe
Garnet Fe2+
Hercynite
Tephroite

Appendix 7: Mössbauer parameters for garnet samples before and after heating.

$Alm_{96}Prp_4$

Component	Assignment	Parameter	NH	950	1170	1200
$Alm_{96}Prp_4$	$^{VIII}Fe^{2+}$	δ (mm/s)	1.29	1.27	-	-
		Δ (mm/s)	3.52	3.51	-	-
		Γ (mm/s)	0.34	0.30	-	-
		A (%)	93.3	92.4	-	-
$Alm_{96}Prp_4$	$^{VI}Fe^{3+}$	δ (mm/s)	0.15	0.25	-	-
		Δ (mm/s)	0.37	0.38	-	-
		Γ (mm/s)	0.45	0.40	-	-
		A (%)	2.9	4.2	-	-
Ilmenite	$^{VI}Fe^{3+}$	δ (mm/s)	1.05	-	-	-
		Δ (mm/s)	0.70	-	-	-
		Γ (mm/s)	0.42	-	-	-
		A (%)	3.8	-	-	-
α-iron	Fe^0	δ (mm/s)	-	0.00	-0.02	0.02
		2ε (mm/s)	-	0.00	0.00	0.00
		B (T)	-	32.7	33.0	33.0
		Γ (mm/s)	-	0.19	0.28	0.34
		A (%)	-	3.4	50.2	35.4
Fayalite	$^{VI}Fe^{2+}$ M1	δ (mm/s)	-	-	1.17	1.20
		Δ (mm/s)	-	-	2.89	2.95
		Γ (mm/s)	-	-	0.28	0.33
		A (%)	-	-	7.0	14.0
Fayalite	$^{VI}Fe^{2+}$ M2	δ (mm/s)	-	-	1.16	1.16
		Δ (mm/s)	-	-	2.61	2.72
		Γ (mm/s)	-	-	0.28	0.33
		A (%)	-	-	6.8	13.6
Hercynite	$^{IV}Fe^{2+}$ T1	δ (mm/s)	-	-	0.94	1.00
		Δ (mm/s)	-	-	1.69	1.70
		Γ (mm/s)	-	-	0.50	0.58
		A (%)	-	-	20.0	22.0
Hercynite	$^{IV}Fe^{2+}$ T2	δ (mm/s)	-	-	0.93	0.97
		Δ (mm/s)	-	-	1.06	1.05
		Γ (mm/s)	-	-	0.49	0.58
		A (%)	-	-	11.0	9.6
Sekaninaite	$^{VI}Fe^{2+}$	δ (mm/s)	-	-	0.89	1.04
		Δ (mm/s)	-	-	2.37	2.25
		Γ (mm/s)	-	-	0.26	0.28
		A (%)	-	-	5.0	5.4

Notes: # Fixed parameter. δ: isomer shift (± 0.03), Δ: quadrupole splitting (± 0.03), 2ε: quadrupole shift (± 0.03), Γ: experimental line width (± 0.03), B: hyperfine magnetic field (± 0.2), A: relative area (± 0.5). Superscript roman numbers indicates the coordination number.

$Alm_{82}Prp_{18}$

Component	Assignment	Parameter	NH	1100	1115	1130	1200
$Alm_{82}Prp_{18}$	Fe^{2+}	δ (mm/s)	1.30	1.26	1.27	-	-
		Δ (mm/s)	3.54	3.51	3.51	-	-
		Γ1 (mm/s)	0.39	0.32	0.33	-	-
		Γ 2 (mm/s)	0.35	0.30	0.30	-	-
		A (%)	100.0	91.0	58.7	-	-
α-iron	Fe^{0}	δ (mm/s)	-	-0.01	-0.02	-0.02	0.01
		2ε (mm/s)	-	0.00	0.00	0.00	0.00
		B (T)	-	32.9	32.9	32.8	33.0
		Γ (mm/s)	-	0.26	0.30	0.28	0.26
		A (%)	-	9.0	11.4	14.4	12.4
Pigeonite	$^{VI}Fe^{2+}$ M1	δ (mm/s)	-	-	1.18	1.12	1.16
		Δ (mm/s)	-	-	2.57	2.66	2.64
		Γ (mm/s)	-	-	0.48	0.32	0.30
		A (%)	-	-	7.3	17.6	15.1
Pigeonite	$^{VI}Fe^{2+}$ M2	δ (mm/s)	-	-	1.08	1.07	1.11
		Δ (mm/s)	-	-	1.98	1.88	1.86
		Γ (mm/s)	-	-	0.42	0.38	0.39
		A (%)	-	-	11.8	24.9	23.3
Cordierite	$^{VI}Fe^{2+}$	δ (mm/s)	-	-	1.11	1.11	1.15
		Δ (mm/s)	-	-	2.25	2.23	2.21
		Γ (mm/s)	-	-	0.21	0.34	0.36
		A (%)	-	-	1.6	25.5	34.9
Fe-Spinel	Fe^{2+}	δ (mm/s)	-	-	0.99	0.99	1.00
		Δ (mm/s)	-	-	1.46	1.37	1.41
		Γ (mm/s)	-	-	0.66	0.53	0.51
		A (%)	-	-	9.2	17.5	14.2

Notes: # Fixed parameter. δ: isomer shift (± 0.03), Δ: quadrupole splitting (± 0.03), 2ε: quadrupole shift (± 0.03), Γ: experimental line width (± 0.03), B: hyperfine magnetic field (± 0.2), A: relative area (± 0.5). Superscript roman numbers indicates the coordination number.

$Alm_{64}Prp_{36}$

Component	Assignment	Parameter	NH	1125	1150	1180	1200
$Alm_{64}Prp_{36}$	Fe^{2+}	δ (mm/s)	1.30	1.29	-	-	-
		Δ (mm/s)	3.55	3.52	-	-	-
		Γ1 (mm/s)	0.38	0.33	-	-	-
		Γ2 (mm/s)	0.34	0.31	-	-	-
		A (%)	100.0	90.6	-	-	-
α-iron	Fe^{0}	δ (mm/s)	-	0.01	-0.02	-0.01	-0.01
		2ε (mm/s)	-	0.00	0.00	0.00	0.00
		B (T)	-	32.9	32.8	32.9	33.0
		Γ (mm/s)	-	0.26	0.28	0.30	0.31
		A (%)	-	3.7	21.8	47.4	60.2
Enstatite	$^{VI}Fe^{2+}$ M1	δ (mm/s)	-	-	1.12	1.15	1.14
		Δ (mm/s)	-	-	2.61	2.65	2.59
		Γ (mm/s)	-	-	0.30	0.27	0.26
		A (%)	-	-	13.7	5.4	2.4
Enstatite	$^{VI}Fe^{2+}$ M2	δ (mm/s)	-	1.18	1.08	1.10	1.10
		Δ (mm/s)	-	2.05	1.91	1.86	1.89
		Γ (mm/s)	-	0.60	0.36	0.37	0.30
		A (%)	-	5.7	23.5	12.4	5.8
Cordierite	$^{VI}Fe^{2+}$	δ (mm/s)	-	-	1.12	1.14	1.15
		Δ (mm/s)	-	-	2.25	2.25	2.25
		Γ (mm/s)	-	-	0.31	0.36	0.42
		A (%)	-	-	24.9	25.8	25.0
Fe-Spinel	$^{IV}Fe^{2+}$	δ (mm/s)	-	-	0.98	1.01	1.02
		Δ (mm/s)	-	-	1.43	1.42	1.46
		Γ (mm/s)	-	-	0.52	0.62	0.59
		A (%)	-	-	16.1	9.0	6.6

Notes: # Fixed parameter. δ: isomer shift (± 0.03), Δ: quadrupole splitting (± 0.03), 2ε: quadrupole shift (± 0.03), Γ: experimental line width (± 0.03), B: hyperfine magnetic field (± 0.2), A: relative area (± 0.5). Superscript roman numbers indicates the coordination number.

$Alm_{20}Prp_{80}$

Component	Assignment	Parameter	NH RT	1000 RT	1100 RT	1125 RT	1200 RT	1200 70 K	1200 10 K	1200 5 K
$Alm_{20}Prp_{80}$	$^{VIII}Fe^{2+}$	δ (mm/s)	1.28	1.29	1.28	1.27	-	-	-	-
		Δ (mm/s)	3.55	3.55	3.54	3.55	-	-	-	-
		Γ1 (mm/s)	0.36	0.27	0.33	0.32	-	-	-	-
		Γ 2 (mm/s)	0.30	0.25	0.27	0.26	-	-	-	-
		A (%)	87.7	90.0	80.2	35.9	-	-	-	-
$Alm_{20}Prp_{80}$	$^{VI}Fe^{3+}$	δ (mm/s)	0.35	0.34	0.34	-	-	-	-	-
		Δ (mm/s)	0.28	0.31	0.17	-	-	-	-	-
		Γ (mm/s)	0.34	0.28	0.28	-	-	-	-	-
		A (%)	12.3	9.9	8.4	-	-	-	-	-
α-iron	Fe^0	δ (mm/s)	-	-	-	-0.02	-0.02	0.09	0.10	0.13
		2ε (mm/s)	-	-	-	0.00	0.00	0.00	0.00	0.00
		B (T)	-	-	-	33.0	33.1	33.3	33.5	33.8
		Γ (mm/s)	-	-	-	0.35	0.29	0.34	0.31	0.55
		A (%)	-	-	-	6.1	11.2	26.7	26.8	20.9
γ-iron	Fe^0	δ (mm/s)	-	-	-0.08	-0.08	-0.09	0.03	0.05	0.06
		Γ (mm/s)	-	-	0.20	0.31	0.26	0.24	0.61	0.82
		A (%)	-	-	4.7	17.7	26.4	15.2	22.7	25.7
Enstatite	$^{VI}Fe^{2+}$ M1	δ (mm/s)	-	-	1.14	1.12	1.11	1.20	1.22	1.23
		Δ (mm/s)	-	-	2.69	2.59	2.60	2.91	2.93	3.01
		Γ (mm/s)	-	-	0.26	0.30	0.28	0.36	0.51	0.79
		A (%)	-	-	2.5	8.2	14.0	19.2	18.4	16.0
Enstatite	$^{VI}Fe^{2+}$ M2	δ (mm/s)	-	-	1.06	1.17	1.14	1.31	1.32	1.33
		Δ (mm/s)	-	-	2.51	2.13	2.13	2.19	2.20	2.35
		Γ (mm/s)	-	-	0.29	0.37	0.35	0.36	0.45	0.83
		A (%)	-	-	4.2	19.7	30.3	31.5	23.4	25.2
Fe-Spinel	$^{IV}Fe^{2+}$	δ (mm/s)	-	-	-	1.15	1.08	1.22	1.32	1.33
		Δ (mm/s)	-	-	-	1.70	1.75	1.74	1.81	1.86
		Γ (mm/s)	-	-	-	0.48	0.50	0.35	0.44	0.55
		A (%)	-	-	-	12.3	18.1	7.2	8.6	12.2

Notes: # Fixed parameter. δ: isomer shift (± 0.03), Δ: quadrupole splitting (± 0.03), 2ε: quadrupole shift (± 0.03), Γ: experimental line width (± 0.03), B: hyperfine magnetic field (± 0.2), A: relative area (± 0.5), RT: measured at room temperature. Superscript roman numbers indicates the coordination number.

$Alm_{65}Sps_{35}$

Component	Assignment	Parameter	NH	1120	1140	1150	1200
$Alm_{65}Sp_{35}$	Fe^{2+}	δ (mm/s)	1.30	1.26	1.33	-	-
		Δ (mm/s)	3.54	3.51	3.38	-	-
		Γ1 (mm/s)	0.41	0.35	0.24	-	-
		Γ 2 (mm/s)	0.37	0.33	0.24	-	-
		A (%)	100.0	91.7	2.0	-	-
α-iron	Fe^{0}	δ (mm/s)	-	-0.02	-0.02	-0.02	-0.01
		2ε (mm/s)	-	0.00	0.00	0.00	0.00
		B (T)	-	32.8	32.9	32.9	32.9
		Γ (mm/s)	-	0.29	0.26	0.27	0.28
		A (%)	-	8.3	15.3	16.7	18.0
Tephroite	$^{VI}Fe^{2+}$ M1	δ (mm/s)	-	-	0.95	0.96	0.96
		Δ (mm/s)	-	-	2.26	2.27	2.18
		Γ (mm/s)	-	-	0.43	0.39	0.40
		A (%)	-	-	31.0	29.3	27.0
Tephroite	$^{VI}Fe^{2+}$ M2	δ (mm/s)	-	-	1.22	1.22	1.19
		Δ (mm/s)	-	-	2.44	2.44	2.30
		Γ (mm/s)	-	-	0.39	0.36	0.40
		A (%)	-	-	16.5	14.7	18.7
Hercynite	$^{IV}Fe^{2+}$ T1	δ (mm/s)	-	-	0.98	0.98	0.99
		Δ (mm/s)	-	-	1.61	1.63	1.56
		Γ (mm/s)	-	-	0.43	0.42	0.44
		A (%)	-	-	24.7	28.7	27.4
Hercynite	$^{IV}Fe^{2+}$ T2	δ (mm/s)	-	-	0.92	0.92	0.91
		Δ (mm/s)	-	-	1.10	1.06	0.99
		Γ (mm/s)	-	-	0.42	0.38	0.39
		A (%)	-	-	10.5	10.6	8.2

Notes: # Fixed parameter. δ: isomer shift (± 0.03), Δ: quadrupole splitting (± 0.03), 2ε: quadrupole shift (± 0.03), Γ: experimental line width (± 0.03), B: hyperfine magnetic field (± 0.2), A: relative area (± 0.5). Superscript roman numbers indicates the coordination number.

Appendix 8: EDS of the garnet samples after heating at 1200 °C, showing the iron particles.

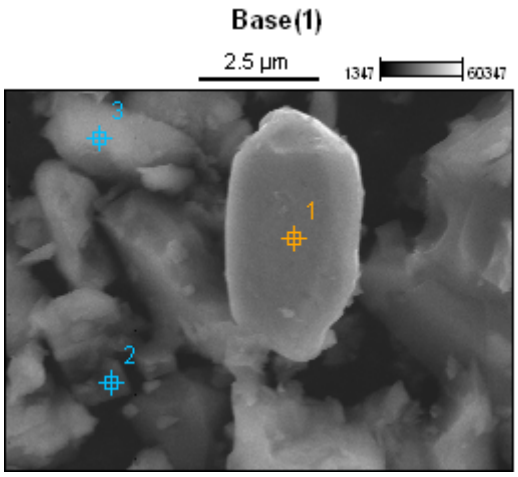

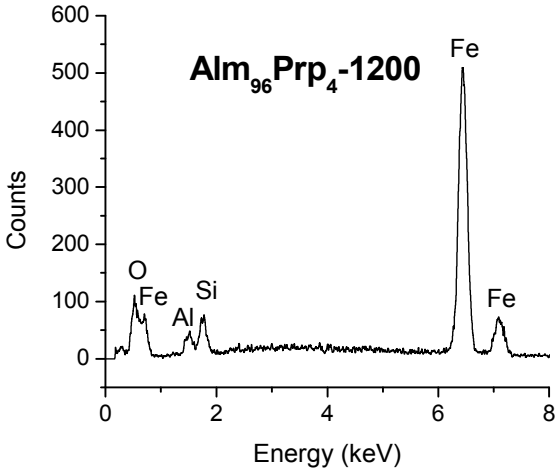

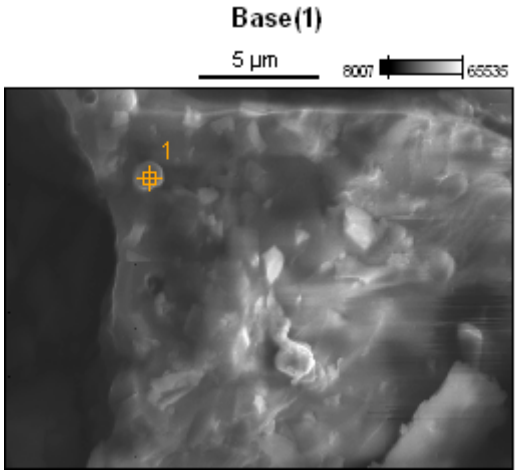

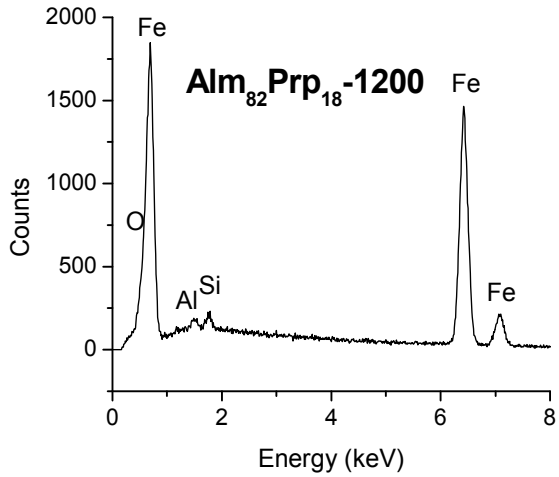

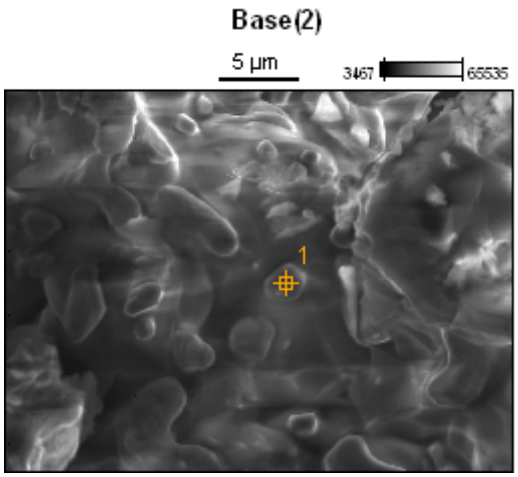

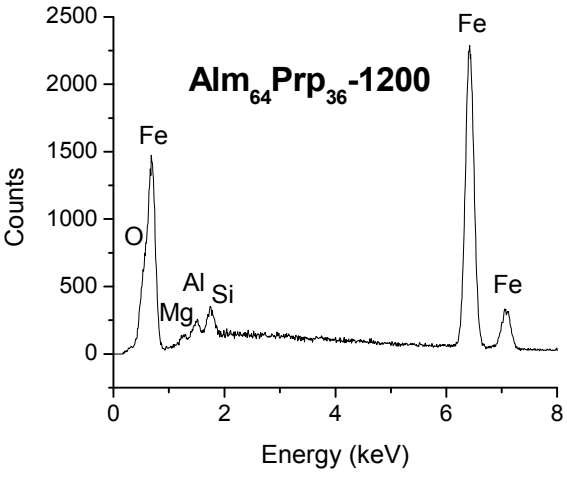

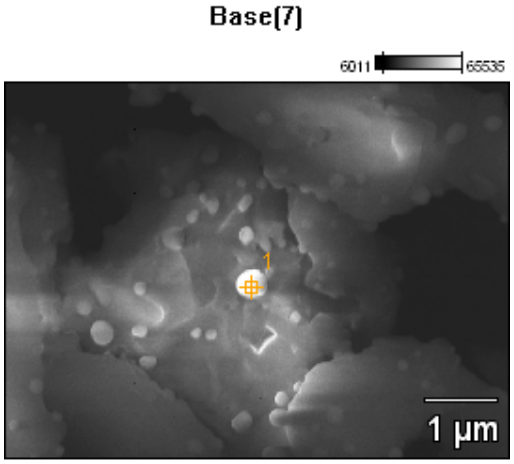
Base(7)
6011
65535
1
1 µm

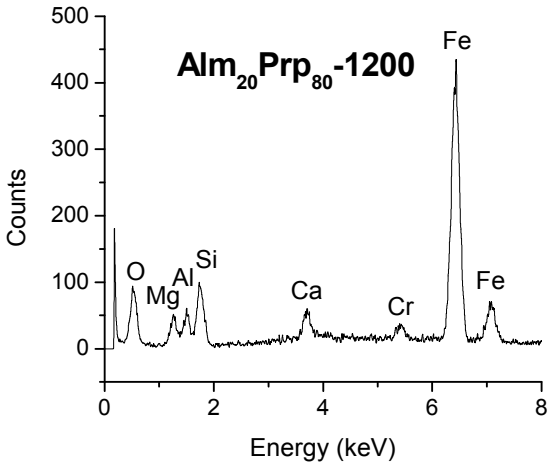
Alm20Prp80-1200
Counts
Energy (keV)
O
Mg
Al
Si
Ca
Cr
Fe
Fe

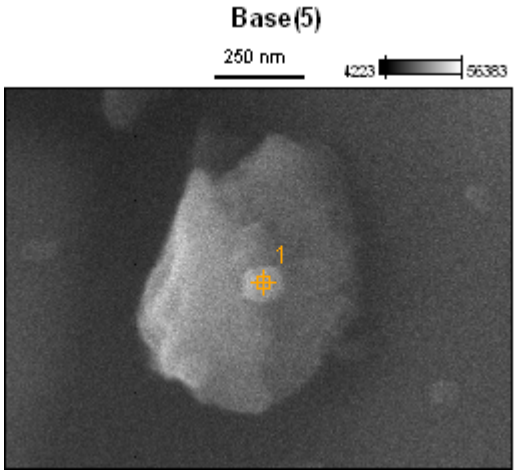
Base(5)
250 nm
4223
56383
1

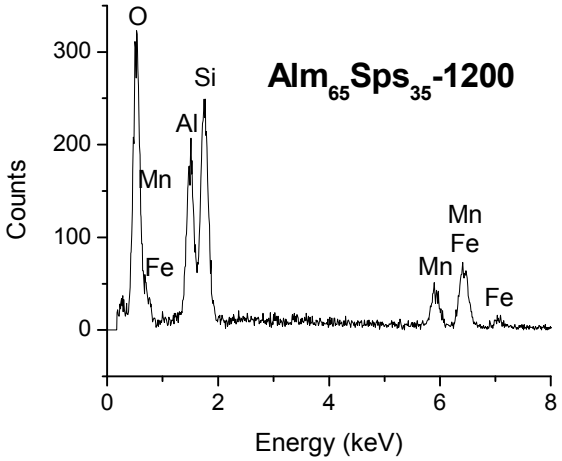
Alm65Sps35-1200
Counts
Energy (keV)
O
Si
Al
Mn
Fe
Mn
Fe
Mn
Fe

Appendix 9: SQUID results of sample $Alm_{20}Prp_{80}$-1200.

Hysteresis loops were obtained for the sample at room temperature (300 K) and 5 K under a variable magnetic field from -7 T to 7 T. At room temperature, are noticed two different sections in the hysteresis loop, corresponding to two different magnetic ordering. There is one magnetic ordered phase and a second paramagnetic phase, both corresponding to iron. At 5 K, there is a predominance of magnetic ordering of the phases.

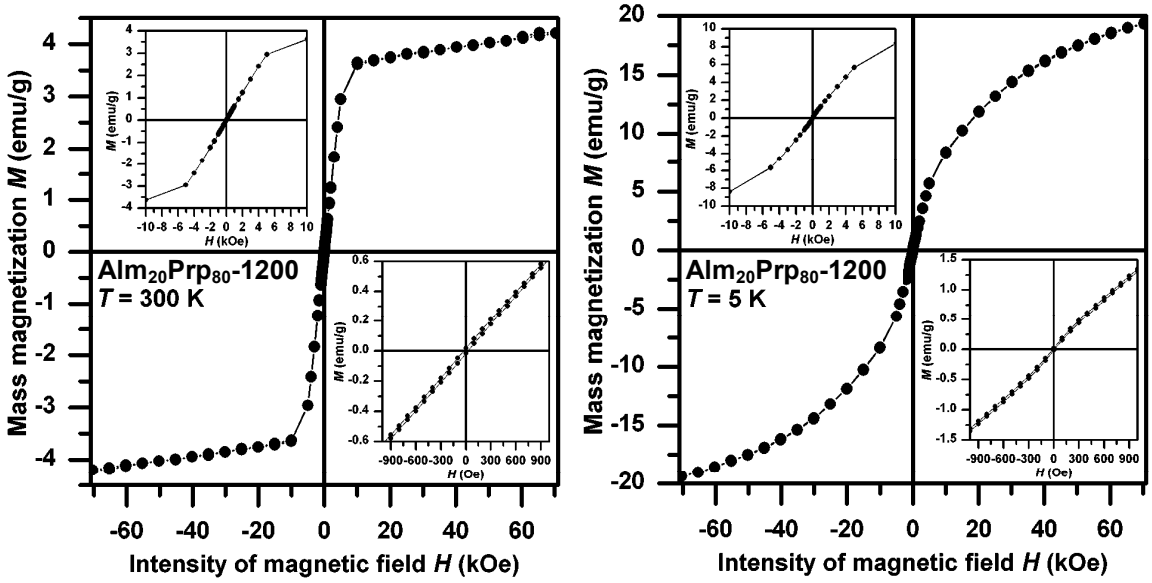

In the table are presented the parameters of the hysteresis loops of the $Alm_{20}Prp_{80}$ sample. Where M_{max+} (7 T) is a maximum magnetization at 7 T, M_{max-} (7 T) is a maximum magnetization at – 7 T, H_{C+} is a positive coercivity, H_{C-} is negative coercivity, M_{R+} is a positive remanent magnetization and M_{R-} is a negative remanent magnetization.

T (K)	M_{max+} (7 T) (emu/g)	M_{max-} (7 T) (emu/g)	H_{C+} (Oe)	H_{C-} (Oe)	M_{R+} (emu/g)	M_{R-} (emu/g)
5	19.4234	– 19.4234	20	– 20	0.0181	– 0.0164
300	4.2069	– 4.2069	17	– 17	0.0156	– 0.0156

Appendix 10: XRD patterns in-situ collected during heating of Prussian blue under nitrogen atmosphere with an average heating rate of 2 K/min.

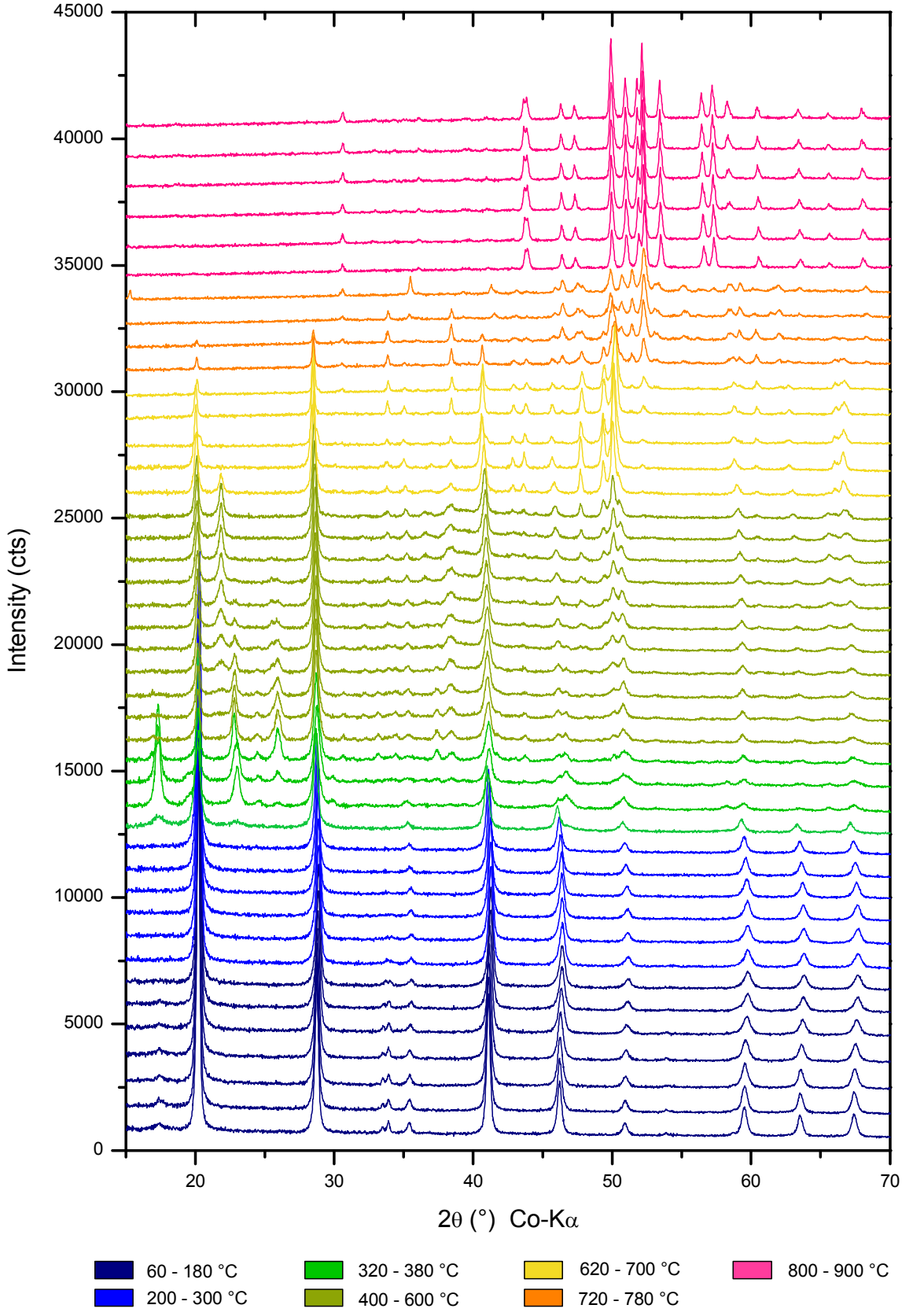

Appendix 11: EDS analysis of sample PB900 showing its elemental composition. Image taken with electron beam accelerating voltage of 15 kV and magnification 20000X.

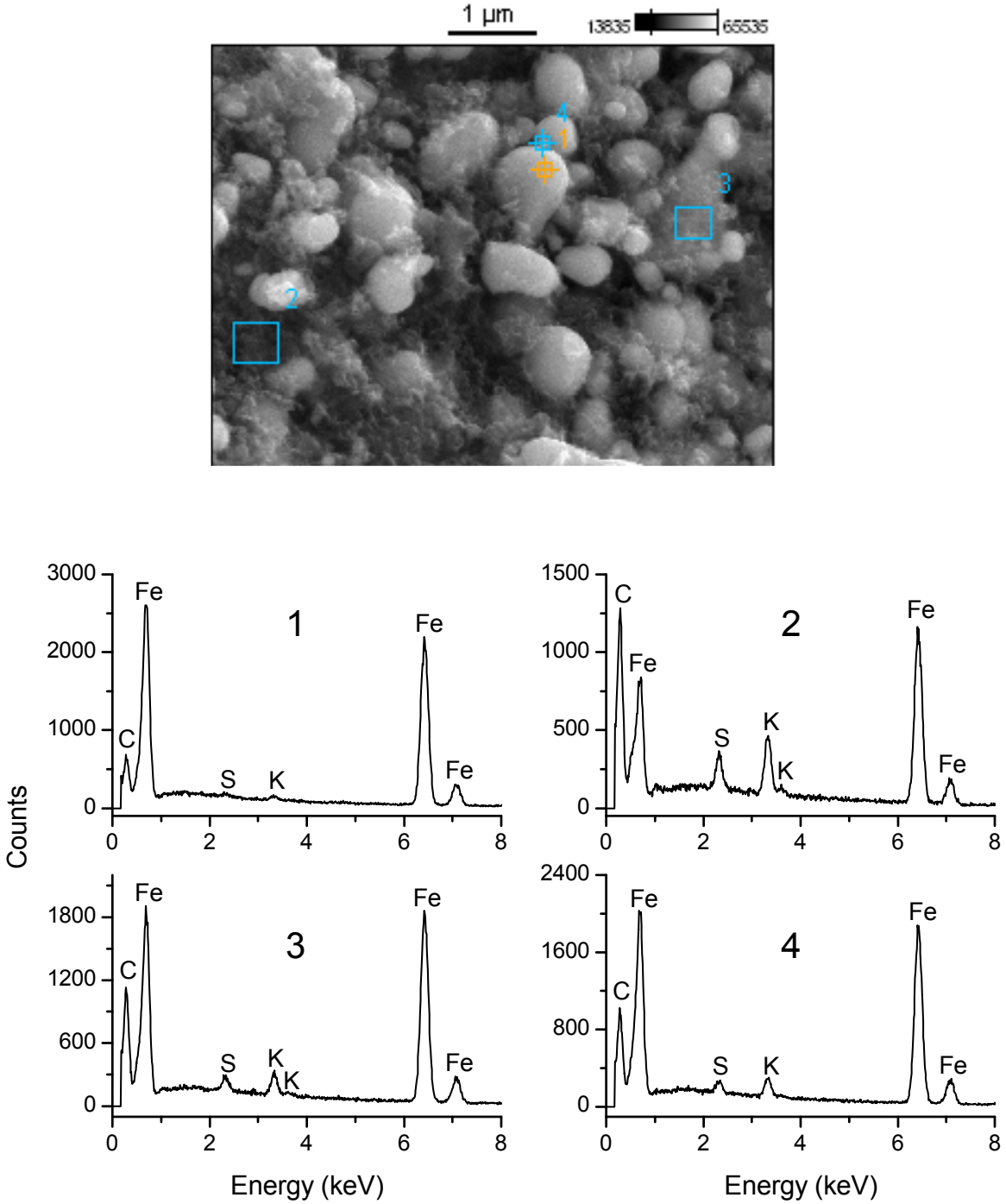

Appendix 12: Mössbauer spectra of maghemite clusters prepared from Prussian blue.

Mössbauer spectra taken at different temperatures (300 K, 150 K, 70 K, 15 K, 5 K) on sample PBS350. Sub-spectra assignment of maghemite: octahedral sites (blue line) and tetrahedral sites (green line).

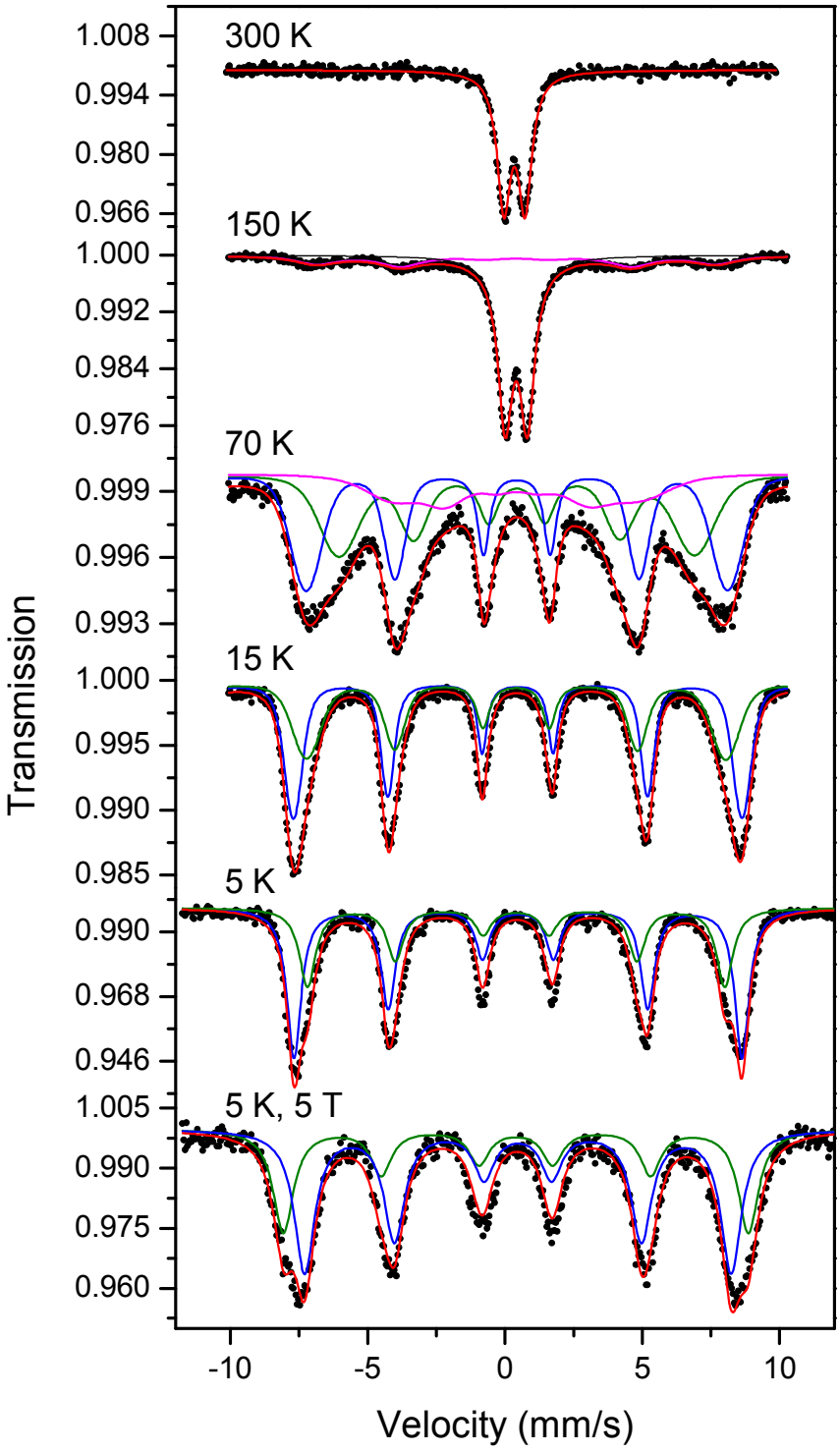

Appendix 13: Mössbauer parameters of maghemite clusters prepared from Prussian blue.

Mössbauer parameters of the samples PBC350 and PBS350 after washing. IS: isomer shift (± 0.01), QS: quadrupole splitting or quadrupole shift (± 0.01), W: experimental line width (± 0.01), B_{hf}: magnetic hyperfine field (± 0.1), Area (± 0.5), SP: superparamagnetism, numbers in cursive are the fixed values during the fitting.

Sample	T (K)	Phase	IS (mm/s)	QS (mm/s)	W (mm/s)	B_{hf} (T)	Area (%)
PBS350	300	γ-Fe_2O_3 SP	0.35	0.77	0.59	-	100.0
	150	γ-Fe_2O_3	0.40	*0.00*	1.84	45.1	28.5
		γ-Fe_2O_3 SP	0.41	0.80	0.64	-	71.5
	70	γ-Fe_2O_3 O[a]	0.42	*0.00*	0.80	40.2[b]	37.9
		γ-Fe_2O_3 T[a]	0.43	*0.00*	0.48	47.7[b]	42.1
		γ-Fe_2O_3[a]	0.43	*0.00*	1.56	28.0[b]	19.9
	15	γ-Fe_2O_3 O[a]	0.46	*0.00*	0.43	50.6[b]	62.6
		γ-Fe_2O_3 T[a]	0.40	*0.00*	0.56	46.9[b]	37.4
	5	γ-Fe_2O_3 O	0.47	*0.00*	0.62	50.7	62.4
		γ-Fe_2O_3 T	0.40	*0.00*	0.71	47.2	37.6
	5[c]	γ-Fe_2O_3 O	0.47	*0.00*	0.91	48.3[d]	62.5
		γ-Fe_2O_3 T	0.40	*0.00*	0.89	52.6[d]	37.5

[a] The sub-spectrum was fitted with a distribution of hyperfine magnetic fields.
[b] Average hyperfine magnetic field.
[c] Measurement at 5 K under an external magnetic field of 5 T.
[d] Effective magnetic field.

Appendix 14: Hematite thin films prepared from Prussian blue.

Prussian blue synthesis

For the synthesis of Prussian blue spherical (PBS) nanoparticles, 3 g (27 mmol of monomer units) of polyvinylpyrrolidone (PVP, K-30, M_w = 40 000, Fluka) were dissolved in 40 ml of hydrochloric acid (HCl, 0.01 M, PH = 2). After the total dissolution of PVP, 90 mg (0.27 mmol) of potassium ferricyanide ($K_3[Fe(CN)_6]$, Lachema) were slowly added to the former solution under stirring. The new solution was put into a boiling flask, joined to the bulb condenser, and then the aqueous solution was refluxed at 80 °C during 2 hours. When the time of reaction has finished, the solution was naturally cooled to room temperature. Then, the PB nanoparticles were separated from the solution using centrifuge equipment (Sigma Sartorius 4-16 K) (13500 rpm, 25 min), the resulting precipitate was washed three times alternating between absolute ethanol and water (13500 rpm, 20 min). Finally, the precipitate was dried in vacuum for 20 h.

Thin films preparation by Spin-coating method

A concentrated alcoholic solution of PBS was prepared adding 90 mg of the before synthesized PB to 2 ml of ethanol, and after ultrasonicated during one minute with power 98 W.
A glass substrate was collocated inside of the spin-coater, after 100 µl of the PBS solution was added to the substrate. Then two steps were carried out, the first one to homogenize the tick of the liquid drop over the substrate surface creating a thin film (1000 rpm, 30 s, 2200 rpm/s), and the second to make thinner the film (4500 rpm, 120 s, 2200 rpm/s). These two steps were repeated two times more, to increase the thickness of the film.

Transformation to hematite

The films are heated up from room temperature to 350 °C, with a heating rate of 5 K/min, then the samples were maintained at 350 °C for one hour. After the heating, the samples were cooled in air, rinsed with water three times to eliminate the presence of some potassium compounds. The previously heated films were again heated up to 650 °C in a muffle furnace during one hour, with a heat rate of 5 K/min.

Results

The thin films of PBS were homogeneous as it is shown in the Fig. 1. After the first heating at 350 °C, the films have an orange-brown color (not shown here), but after the second heating at 650 °C the color change to orange-red (Fig. 1).
The identification of the phases present in the samples was determinate using XRD. For the sample heated up to 350 °C, it was found $KFeO_2$ with a preferred orientation along [010] direction, and Fe_2O_3 amorphous component (Fig. 2a). Pure hematite (α-Fe_2O_3) was obtained after the second heating up to 650 °C (Fig. 2b), result also confirmed by Mössbauer spectroscopy (Fig. 3). The thickness of the hematite thin film (~ 370 nm) was measured using AFM. The surface of the film was irregular with empty spaces forming channels. A closer view of it reveals rounded nanoparticles, with sizes around 100 nm, without a preferred orientation. Because of the thinness of the film, EDS analyses also show elements belonging to the glass substrate composition (Fig. 4).

Fig. 1 PB (left), amorphous Fe_2O_3 (center), and hematite (rigth) thin films.

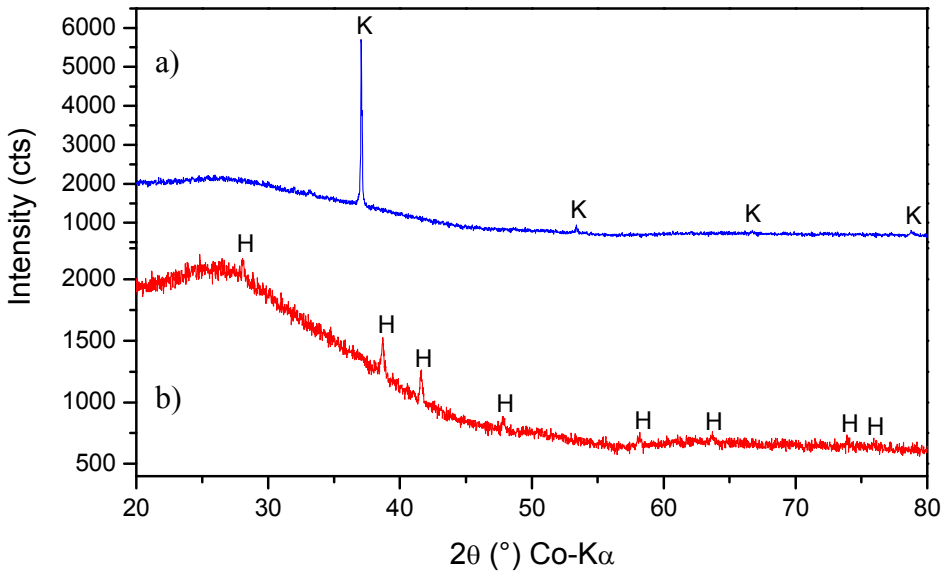

Fig. 2 XRD patterns of PB sample after first heating at 350 °C (a), after second heating at 650 °C (b). K stands for $KFeO_2$, and H stands for hematite.

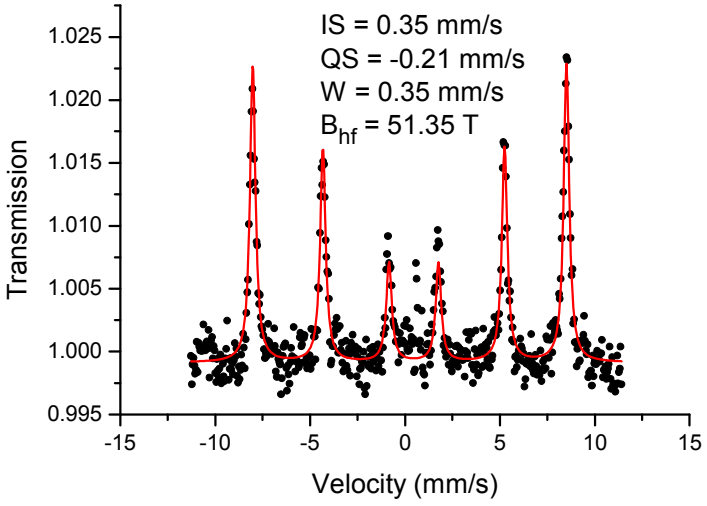

Fig. 3 CEMS spectrum of the hematite film.

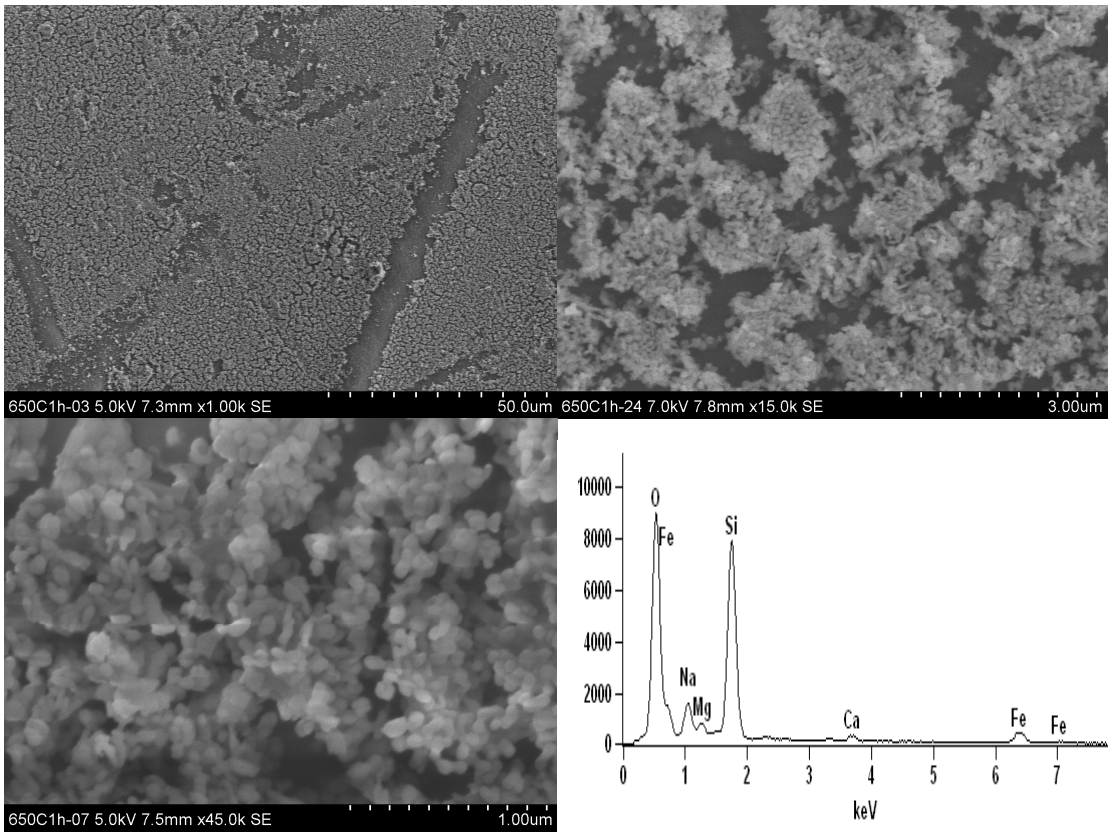

Fig. 4 SEM images of hematite thin film with different magnificents and EDS analysis.

Annexes

Annex 1

High temperature decomposition of almandine and pyrope in reducing atmosphere

C. Aparicio, J. Filip & M. Mashlan

MSMS 2010, *AIP Conference Proceedings* **1258**, 47–54 (2010)

High Temperature Decomposition of Almandine and Pyrope in Reducing Atmosphere

C. Aparicio, J. Filip and M. Mashlan

Centre for Nanomaterial Research, Palacky University in Olomouc, 17. listopadu 1192/12, 771 46 Olomouc, Czech Republic

Abstract. Thermal decomposition of two garnets of near end-member composition – almandine $(Fe_{2.85}Mg_{0.15})(Al_{1.99})Si_{2.99}O_{12}$ and pyrope $(Mg_{2.22}Fe_{0.47}Ca_{0.33})(Cr_{0.11}Fe_{0.06}Al_{1.81})Si_{2.98}O_{12}$ – has been carried out in reducing atmosphere (forming gas: 10% of H_2 in N_2). High-temperature behavior of both samples was monitored using simultaneous thermogravimetry and differential scanning calorimetry. The decomposition of almandine and pyrope turned out to proceed at slightly different temperatures above 1000 °C. Therefore, two series of samples were prepared based on the results of thermal analysis: almandine heated up to 950 °C, 1070 °C and 1200 °C, and pyrope heated up to 1000 °C, 1100 °C, 1125 °C and 1200 °C. The identification of the decomposition products was performed by X-ray powder diffraction and Mössbauer spectroscopy. The common feature of the decomposition of both garnets is the presence of metallic iron and spinel phase, while the other products include fayalite, cristobalite, and cordierite for almandine; and enstatite and anorthite for pyrope. The formation of this last component was enabled due to Ca content in pyrope.

Keywords: Fe-bearing garnet, thermal decomposition, reducing atmosphere.
PACS: 81.40.-z, 81.70.Pg, 82.80.Ej

INTRODUCTION

Garnets of the pyrope-almandine series have been widely studied since many years ago because they are present in the Earth crust as accessory to major rock-forming silicates. Moreover, it is commonly used in industry, e.g., as an abrasive material. The garnet with a cubic structure and space group Ia-3d has a structural formula of $^{VIII}X_3{}^{VI}Y_2{}^{IV}Z_3O_{12}$; where X = Fe^{2+}, Mg^{2+}, Mn^{2+}, Ca^{2+}, Y = Fe^{3+}, Ti^{3+}, Cr^{3+}, Al^{3+} and Z = Si^{4+}, the superscript Roman numbers indicate the coordination number for each particular site [1]. The idealized formulae for almandine and pyrope are $Fe_3Al_2Si_3O_{12}$ and $Mg_3Al_2Si_3O_{12}$, respectively.

Published studies dealing with a decomposition of garnets belonging to pyrope-almandine series were performed under various experimental conditions: oxidizing or inert atmosphere, isothermal or non-isothermal regime [2,3], and non-ambient pressure [4]. However, no data have been published for the high-temperature behavior of garnet in reducing conditions so far. The most frequently used techniques employed in aforementioned studies involved X-ray powder diffraction [5] and Mössbauer spectroscopy [6,7,8]. The results of the high-temperature treatment of garnet in air demonstrate that the decomposition occurs between 750 °C and 1200 °C, but the decomposition products for almandine and pyrope differ. The thermal decomposition

CP1258, *Mossbauer Spectroscopy in Materials Science – 2010,* edited by J. Tuček and M. Miglierini

of garnets, principally of almandine, has been investigated first under high pressures [4,9]. In 1992, Harlov and Newton described the synthesis of almandine from a mixture of magnetite, quartz and kyanite in pressures greater than 28.5 kbar [9]. Anovitz et al. [4] considered the possibility of reversibility of this process; in equilibrium conditions, they suggested the following products of almandine decomposition: hercynite, fayalite, and quartz or Fe-cordierite depending on the applied pressure. They also investigated the oxidation mechanism of almandine leading to the formation of magnetite, quartz, and sillimanite or hercynite depending on the applied pressure [4]. According to Thiéblot et al. [5], almandine was decomposed into hematite, sillimanite, and cristobalite in air under atmospheric pressure. However, based on Mössbauer spectroscopy [7,10], it was demonstrated that maghemite (γ-Fe_2O_3) is the original product of almandine decomposition at temperatures higher than 750 °C and it is subsequently transformed to ε-Fe_2O_3 and finally to hematite (α-Fe_2O_3). The decomposition mechanism of pyrope differs mainly due to a low amount of iron and sometimes the presence of calcium in the dodecahedral sites. Pyrope with the chemical composition close to the ideal end-member shows two decomposition products in air: corundum and enstatite [5], while pyrope with Fe^{2+} in the dodecahedral sites decomposes primarily into hematite, enstatite, Fe-spinel, and cristobalite; in this case, hematite is also a product of subsequent oxidation of enstatite at high temperature [2]. At 1200 °C, garnets of pyrope-almandine solid-solution show spinel ($Mg(Al,Fe^{3+})_2O_4$), anorthite and enstatite as decomposition products for the composition close to pyrope, while cordierite, anorthite, and spinel or maghemite were detected after the decomposition of garnet of almandine-pyrope intermediate composition [3].

The aim of this work is to describe the high-temperature decomposition of both end-member garnets under the reducing atmosphere and to characterize the Fe-bearing decomposition products by means of Mössbauer spectroscopy.

EXPERIMENTAL METHODS

Preparation of Samples

Two natural garnets of near end-member composition (almandine and pyrope) were used in this study. Their respective crystal-chemical formulae, normalized to twelve oxygen atoms, are:

almandine - $(Fe_{2.85}Mg_{0.15})(Al_{1.99})Si_{2.99}O_{12}$ and
pyrope - $(Mg_{2.22}Fe_{0.47}Ca_{0.33})(Cr_{0.11}Fe_{0.06}Al_{1.81})Si_{2.98}O_{12}$,

as analyzed by electron microprobe (EMPA – Cameca SX100 operating in the wavelength dispersive mode; an accelerating voltage of 15 kV, a beam currents of 10 nA and a spot size of ~ 5 μm). The inclusion-free fragments of respective garnet samples were hand-picked under the binocular microscope, subsequently ground in an agate mortar under isopropyl alcohol and finally air-dried at room temperature. The

powdered samples of almandine and pyrope were labeled as ALM-NH and PY-NH, respectively.

The high–temperature behavior of garnet in the reducing atmosphere (forming gas: 10 % H_2 in N_2; atmospheric pressure) was observed using a simultaneous thermal analyzer STA 449 C (Jupiter, Netzsch) involving thermogravimetric analysis (TGA) and differential scanning calorimetry (DSC). Samples were placed into an open alumina crucible and dynamically heated with a heating rate of 10 °C/min. Using this approach, the two series of samples were prepared based on the results of full range of TGA and DSC measurements: almandine heated up to 950 °C (ALM-950), 1070 °C (ALM-1070) and 1200 °C (ALM-1200), and pyrope heated up to 1000 °C (PY-1000), 1100 °C (PY-1100), 1125 °C (PY-1125) and 1200 °C (PY-1200). The samples were cooled down to room temperature within approximately two hours.

Characterization of Samples

Both series of samples, including samples without the thermal treatment, were characterized using X-ray powder diffraction (XRD) and Mössbauer spectroscopy (MS). XRD patterns were recorded with a PANalytical X'Pert PRO MPD diffractometer (CoK_α radiation) in the Bragg-Brentano geometry, equipped with an X´Celerator detector and programmable divergence and diffracted beam anti-scatter slits. Samples were placed on a zero-background Si slides, gently pressed and scanned with a step size of 0.017°. The identification of crystalline phases in the experimental XRD patterns and the Rietveld analysis were carried out using the High Score Plus software (PANalytical) in conjunction with PDF-4+ and ICSD databases.

Transmission ^{57}Fe Mössbauer spectroscopy on powdered samples was performed in the constant acceleration mode using a ^{57}Co source in Rh matrix and 1024 channel detector at room temperature. The spectrometer was calibrated with an α-Fe foil, the isomer shift values were expressed with respect to the metallic iron at room temperature. The spectra were folded and fitted by the Lorentz functions using the computer program CONFIT2000 [11].

RESULTS AND DISCUSSION

Thermal Analysis: TG and DSC

The near end-member almandine and pyrope samples have shown different high-temperature behaviors (i.e., decomposition), as reflected in their respective DSC curves (see Fig. 1). While almandine showed one pronounced and sharp endothermic peak (1055 °C), the pyrope decomposition results in two weak endothermic peaks at higher temperatures than in the case of almandine (1105 °C and 1130 °C). Both samples also differ in the TG analysis (not shown), where the mass loss of – 3.51 % (between RT and 1200 °C) in the case of almandine is approximately five times bigger than the mass loss for pyrope (– 0.69 %).

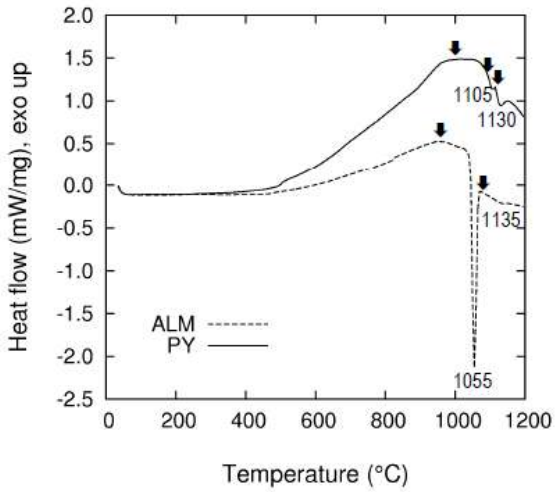

FIGURE 1. DSC curves comparing the almandine (ALM) and pyrope (PY) decomposition endothermic peaks. Arrows indicate the temperatures of preparation of ALM-950, ALM-1070, PY-1000, PY-1100 and PY-1125 samples.

Phase Analysis: XRD and MS

XRD patterns of ALM-NH and PY-NH samples are typical for almandine and pyrope [12], respectively. The PY-NH sample turned out to be impurity-free. However, in the XRD pattern of the ALM-NH sample, there were identified diffractions from ilmenite ($FeTiO_3$) representing inclusions in almandine grains (less than 2 wt. % of ilmenite according to the Rietveld analysis). Similarly, Mössbauer spectra at room temperature of untreated almandine and pyrope showed Mössbauer parameters typical for garnet [13]. The almandine spectrum was fitted with three doublets, D1: IS = 1.29 mm/s and QS = 3.52 mm/s for Fe^{2+} in the dodecahedral 24*c* position (the relative area of 93.3 % or 97 % excluding ilmenite contribution); D2: IS = 0.15 mm/s and QS = 0.37 mm/s for Fe^{3+} in the octahedral 16*a* position (the relative area of 2.9 % or 3 % excluding ilmenite contribution), and D3: IS = 1.05 mm/s and QS = 0.70 mm/s assigned to Fe^{2+} in ilmenite (the relative area of 3.8 % of total spectral area). Pyrope, containing 8.85 wt. % of Fe_{tot} according to EMPA, gave the Mössbauer spectrum with the following components – one asymmetric doublet D1: IS = 1.28 mm/s and QS = 3.55 mm/s for Fe^{2+} in the dodecahedral 24*c* position (the relative area of 87.7 %), and D2: IS = 0.35 mm/s and QS = 0.27 mm/s for Fe^{3+} in the octahedral 16*a* position (the relative area of 12.3 %). A slightly larger value of the quadrupole splitting of D1 doublet in pyrope compared to that observed for almandine evidence the distortion of this site [13,14]; the asymmetry of D1 doublet could be attributed to a spin-spin relaxation [13,15].

XRD diffractograms (see Fig. 2) and Mössbauer spectra (see Fig. 3) for ALM-950, ALM-1070, ALM-1200, PY-1000, PY-1100, PY-1125, and PY-1200 samples represent the crucial data for solving the thermally-induced decomposition mechanism of both garnets. Below 1000 °C, the structure of both almandine and pyrope is preserved unchanged; the MS spectrum of pyrope revealed the partial non-destructive reduction of Fe^{3+} to Fe^{2+} (see Fig. 3, right). In the ALM-950 sample, we identified D1

and D2 doublets for almandine and a very weak sextet of alpha-iron (IS = – 0.02 mm/s, QS = 0.00 mm/s and B = 32.7 T) being, together with rutile TiO_2 (confirmed by XRD), the products of decomposition of ilmenite inclusions at temperatures lower than 950 °C [16]. The weight ratio of α-Fe and rutile derived from the Rietveld analysis implies that all α-Fe present in the ALM-950 sample originates exclusively from ilmenite. Such a decomposition of ilmenite inclusions seems to be partially responsible for the different weight loss observed in TGA for respective garnets. Indeed, the different amount of Fe being reduced into the metallic form (see below) is the main reason of different weight loss in both samples.

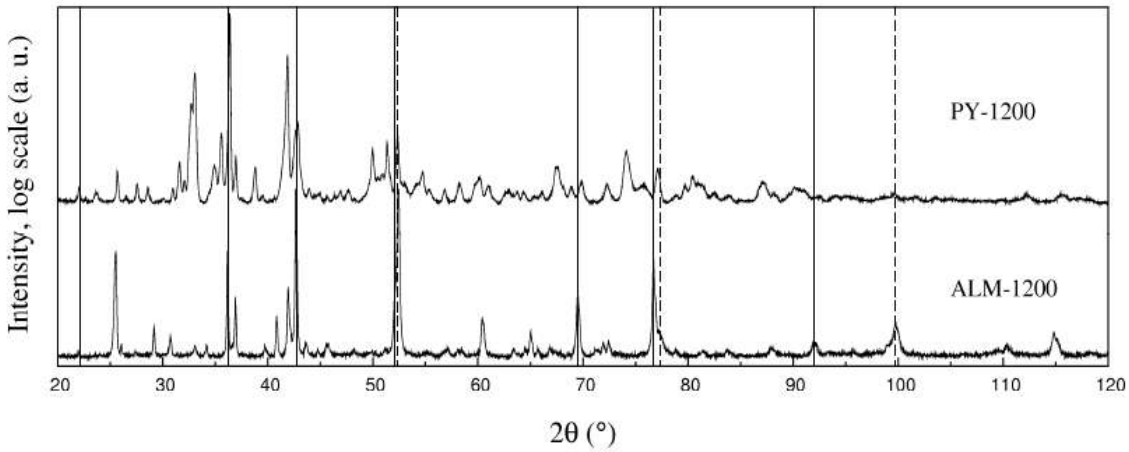

FIGURE 2. XRD powder patterns of ALM-1200 and PY-1200 samples, comparing their common phases: α-Fe (– – –) and spinel (——).

The decomposition of both pyrope and almandine starts above 1000 °C. However, the products of decomposition significantly differ for both garnets; therefore, the results will be presented and discussed separately for respective samples. Diffractograms of ALM-1070 and ALM-1200 samples represent the fully decomposed garnet and the newly formed phases were identified as alpha-iron (bcc structure), hercynite (ideally $FeAl_2O_4$), fayalite (ideally Fe_2SiO_4), cristobalite (SiO_2), and Fe-cordierite (ideally $(Fe^{2+},Mg)_2Al_4Si_5O_{18}$). Alpha-iron originates partially from ilmenite decomposition, but its contribution to the total α-Fe is less than 7 %. The variation in the amount of decomposition products in the ALM-1070 and ALM-1200 samples, according to the results of the Rietveld refinement and relative areas of Fe-bearing phases in MS, indicates consecutive reactions of primary products of decomposition as soon as they were formed. One example documenting this process can be seen in the increasing content of fayalite (+ 13.4 %) phase at the expense of alpha iron (– 5.0 %) and cristobalite (– 10.0 %) phases, as confirmed by the Rietveld refinements of the ALM-1070 and ALM-1200 samples. Similarly, iron and hercynite react together towards a formation of Fe-cordierite.

The decomposition of pyrope started at around 1105 °C (based on TGA); however, diffractions of pyrope were identified also in the PY-1125 sample where enstatite (ideally $(Mg,Fe)SiO_3$), spinel phase ($(Mg,Fe^{2+})(Al,Cr,Fe^{3+})_2O_4$), and anorthite ($CaAl_2Si_2O_8$) were also observed. At 1200 °C, pyrope is completely decomposed and

the primary products are represented by α-iron, ferroan enstatite (clino and ortho polymorphs), spinel phase, γ-iron (fcc structure) and anorthite according to XRD. The formation of anorthite was enabled due to Ca content in pyrope. At temperatures of 1100 °C and 1125 °C, neither α- nor γ-Fe were identified.

Decomposition mechanisms of both garnets lead, in common, to the formation of alpha-iron and spinel phase. The spinel is obviously not identical from the chemical point of view as the iron-to-magnesium ratio significantly differs in both samples of garnet. The different nature of spinel is reflected by a slight shift of respective diffractions to smaller d-values in the case of the PY-1200 sample (Mg-rich spinel) compared to the ALM-1200 sample containing obviously more iron atoms in the spinel (see Fig. 2) following, thus, the Vegard's law. Hercynite formed from almandine seems to contain some magnesium in the tetrahedral site according to stoichiometric calculations and also because it is the only primary phase which can bear Mg in its structure. Moreover, in the case of pyrope decomposition, the spinel acts as a sink for Cr.

The Fe-bearing phases in both series (ALM and PY) were characterized by means of Mössbauer spectroscopy (see Fig. 3). In the ALM-1070 sample, the almandine is totally decomposed and alpha-iron (50.2 % of the spectral area) constitutes the dominant phase in the Mössbauer spectrum. The progressive reaction of alpha-iron with cristobalite and water vapor leading to formation of fayalite [17] caused a decrease of α-Fe spectral area to 35.4 % (ALM-1200) and an increase of fayalite spectral area from 13.8 % (ALM-1070) to 27.6 % (ALM-1200). In the Mössbauer spectra of the ALM-1070 and ALM-1200 samples, we also confirmed other Fe-bearing phases (all present as paramagnetic doublets), previously identified by XRD: Fe-cordierite (5.0 and 5.4 % for the ALM-1070 and ALM-1200 samples, respectively), and hercynite (31.0 and 31.6 % for the ALM-1070 and ALM-1200 samples, respectively). More details concerning the reductive decomposition of almandine will be given in the paper of Aparicio et al. [18].

According to Mössbauer spectroscopy, the pyrope decomposition starts between 1000 and 1100 °C (see Fig. 3) where an enstatite formation was observed (confirmed by XRD). Nevertheless, the pronounced decomposition of pyrope starts at or slightly below 1125 °C, where the spectral component attributed to enstatite significantly increases. Together with enstatite formation there is a distinct sextet of alpha-iron in the PY-1125 (5.8 %; IS = – 0.02 mm/s, QS = 0.00 mm/s and B = 32.9 T) and PY-1200 samples (11.2 %; IS = – 0.02 mm/s, QS = 0.00 mm/s and B = 33.1 T). With respect to the obvious doublet overlap in 0 mm/s and 2.2 mm/s region, the fitting of two enstatite doublets is not sufficient to obtain a reasonable fit. Therefore, the doublet corresponding to the spinel phase could also be included, demonstrating thereby, that it is a Fe-bearing member of spinel group minerals which was not evident from XRD. In addition to the spinel, one singlet (IS ~ – 0.09 mm/s) present in spectra of the PY-1125 and PY-1200 samples could be related to magnetically non-split form of metallic iron (γ-Fe). Ordinarily, the bcc structure of the metallic iron changes to the fcc structure at a high temperature (~ 912 °C) and upon cooling, the metallic iron retains again the bcc structure. Therefore, the unusual presence of γ-Fe occurring together with α-Fe could easily be explained either by possible substitution of some elements into the structure of metallic iron or by epitaxial growth of γ-Fe on a suitable fcc

lattice. Nevertheless, the most probable explanation – with respect to the generally low iron content in pyrope – is that γ-Fe forms in the form of small and well separated particles blocking the transition into the bcc structure during cooling [19]. A similar case has been reported for iron nanoparticles (isomer shift of – 0.09 mm/s) enclosed inside the carbon nanotubes [20] and it also accords with the results of oxidative decomposition of pyrope where nanoparticles of hematite (with sizes of 15–20 nm) were observed [2].

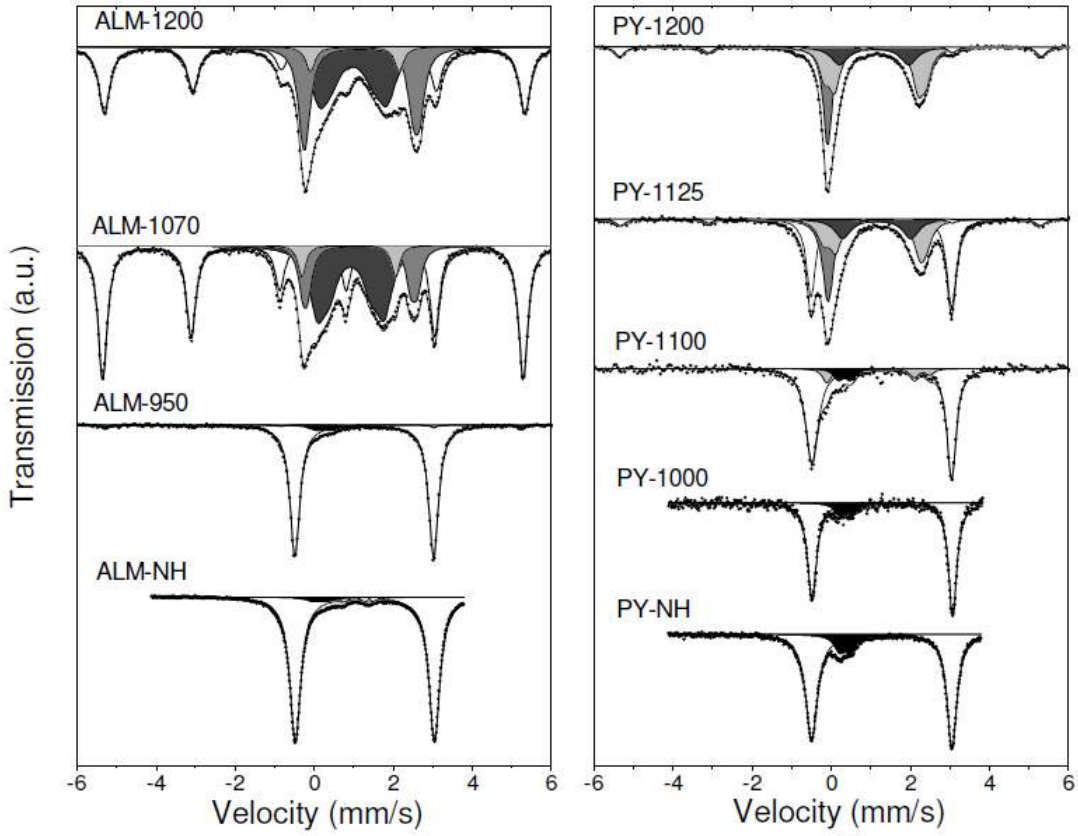

FIGURE 3. Room-temperature Mössbauer spectra for both series of almandine (left) and pyrope (right) samples showing the different phase composition. White doublet – Fe^{2+} in garnet, white sextet – α-Fe, black – Fe^{3+} in garnet, dark gray – spinel, medium gray – fayalite (ALM) or γ-Fe (PY), light gray – Fe-cordierite (ALM) or enstatite (PY).

Similarities and Differences in Decomposition of Almandine and Pyrope

Almandine and pyrope, when thermally treated in the reducing conditions, differ in decomposition onset (above 1000 °C for both garnets). Pyrope turned out to be more stable at high temperatures than almandine, remaining partially even at 1125 °C. Although both almandine and pyrope have the same crystal-structure, the phases resulting from their decomposition significantly differ. The main reason could be seen

in occupation of dodecahedral sites with different cations, influencing – among other things – the strength of inter-atomic bonds and, consequently, also the thermal stability of the structure. The formation of metallic iron (bcc) upon reduction of Fe in hydrogen atmosphere is confirmed to be a common feature of the decomposition of both garnets. Other primary products of almandine decomposition include cristobalite and hercynite. Fayalite represents the secondary product formed by the reaction of cristobalite, iron, and water vapor whereas Fe-cordierite is the secondary product formed in the case of the reaction of α-Fe with hercynite. In pyrope, on the contrary, enstatite is produced prior to the formation of α-Fe and γ-Fe, spinel and anorthite.

ACKNOWLEDGMENTS

We are indebted to Jana Ševčíková for Mössbauer spectroscopy data collection, Martin Heřmánek for thermal analysis, Radek Škoda for electron microprobe analysis and Oldřich Schneeweiss for constructive comments to the manuscript. Samples for this study we kindly provided by the Moravian Museum in Brno, Czech Republic. This work has been supported by research projects of the Ministry of Education of the Czech Republic (grant number MSM6198959218), Academy of Sciences of the Czech Republic (grant number KAN115600801) and the Grant Agency of the Czech Republic (grant number 205/08/0869).

REFERENCES

1. G. A. Novak and G. V. Gibbs, *Am. Mineral.* **56**, 791-825 (1971).
2. R. Zboril et al., *Phys. Chem. Miner.* **30**, 620-627 (2003).
3. R. Zboril et al., *Hyperfine Interact.* **156/157**, 403-410 (2004).
4. L. M. Anovitz et al., *Geochim. Cosmochim. Acta* **57**, 4191-4204 (1993).
5. L. Thiéblot, J. Roux, and P. Richet, *Eur. J. Mineral.* **10**, 7-15 (1998).
6. M. Mašláň et al., *Czech. J. Phys.* **47**, 571-574 (1997).
7. K. Barcova, M. Mashlan, and R. Zboril, *Czech. J. Phys.* **51**, 749-754 (2001).
8. M. Mashlan et al., "Mössbauer spectroscopy in studying the thermally induced oxidation of Fe^{2+} cations in iron-bearing silicate minerals" in *Material Research in Atomic Scale by Mössbauer Spectroscopy*, edited by M. Mashlan et al., NATO series II, Vol. 94, Kluwer Academic Publishers, Netherlands, 2003, pp. 271-284.
9. D. E. Harlov, *Am. Mineral.* **77**, 558-564 (1992).
10. R. Zboril et al., *Hyperfine Interact.* **139/140**, 597-606 (2002).
11. T. Žák and Y. Jirásková, *Surf. Interface Anal.* **38**, 710-714 (2006).
12. M. Chmielová, P. Martinec and Z. Weiss, *Eur J Mineral* **9**, 403-409 (1997).
13. G. Amthauer, H. Annersten and S. S. Hafner, *Z. Kristallogr.* **143**, 14-55 (1976).
14. C. A. Geiger, M. Grodzicki and G. Amthauer, *Phys. Chem. Miner.* **30**, 280-292 (2003).
15. K. Černá, M. Mášláň and P. Martinec, *Mater. Struct.* **7**, 6-9 (2000).
16. Y. Zhao and F. Shadman, *Ind. Eng. Chem. Res.* **30**, 2080-2087 (1991).
17. S. Hirano, Y. Iwai, and S. Somiya, "Morphology of hydrothermally grown fayalite crystal" in *Morphology and Growth Unit of Crystals*, edited by I. Sunagawa, Terra Scientific Publishing Company, Tokio, 1989, pp. 543-553.
18. C. Aparicio et al. (in preparation).
19. K. Haneda, Z. X. Zhou and A. H. Morrish, *Phys. Rev. B* **46**, 13832-13837 (1992).
20. I. S. Lybutin et al., *J. Exp. Theor. Phys.* **109**, 302-310 (2009).

Annex 2

Thermal behavior of almandine at temperatures up to 1,200 °C in hydrogen

C. Aparicio, J. Filip, H. Skogby, Z. Marusak, M. Mashlan & R. Zboril

Physics and Chemistry of Minerals **39**(4), 311–318 (2012)

Phys Chem Minerals (2012) 39:311–318
DOI 10.1007/s00269-012-0488-x

ORIGINAL PAPER

Thermal behavior of almandine at temperatures up to 1,200°C in hydrogen

Claudia Aparicio · Jan Filip · Henrik Skogby · Zdenek Marusak · Miroslav Mashlan · Radek Zboril

Received: 14 March 2011 / Accepted: 29 January 2012 / Published online: 15 February 2012

Abstract The thermally induced reductive decomposition of a natural near end-member almandine [$^{VIII}(Fe_{2.85}Mg_{0.11}Ca_{0.05}Mn_{0.02})^{VI}(Al_{1.99})^{IV}(Si_{2.99})O_{12}$] and possible hydrogen diffusion into its structure have been carried out at temperatures up to 1,200°C, monitored by simultaneous thermogravimetric analysis and differential scanning calorimetry (DSC), infrared and ^{57}Fe Mössbauer spectroscopy and X-ray powder diffraction. Below 1,000°C, evidence for hydrogen diffusion into almandine structure was not observed. At temperatures above 1,000°C, reductive decomposition sets in, as displayed by a sharp endothermic peak at 1,055°C on the DSC curve accompanied by a total mass loss of 3.51%. We observe the following decomposition mechanism: almandine + hydrogen → α-Fe + cristobalite + hercynite + water. At higher temperatures, fayalite and sekaninaite are formed by consecutive reaction of α-Fe with cristobalite and water, and cristobalite with hercynite, respectively. The metallic α-Fe phase forms spherical and isolated particles (~1 μm).

Electronic supplementary material The online version of this article (doi:10.1007/s00269-012-0488-x) contains supplementary material, which is available to authorized users.

C. Aparicio · J. Filip (✉) · Z. Marusak · M. Mashlan · R. Zboril
Regional Centre of Advanced Technologies and Materials, Departments of Experimental Physics and Physical Chemistry, Faculty of Science, Palacký University, Šlechtitelů 11, 783 71 Olomouc, Czech Republic
e-mail: jan.filip@upol.cz

H. Skogby
Department of Mineralogy, Swedish Museum of Natural History, Box 50007, 10405 Stockholm, Sweden

Keywords Fe-bearing garnet · Almandine · Thermal treatment · Hydrogen diffusion · Reductive decomposition · Iron particles

Introduction

Garnets of almandine composition have been intensively studied in the past few decades because of their widespread occurrence and significant role in the Earth's crust and upper mantel as accessory to major rock-forming silicates, and their phase equilibria are frequently used to interpret the genesis of igneous and metamorphic rocks (Deer et al. 1997; Geiger 2004 and references therein). Moreover, almandine is often used for industrial purposes as an abrasive material for grinding and blast cleaning, water-jet cutting or optical glass polishing, and as a high-density medium in water filtration (Chang 2002).

Garnet-group minerals may be exposed to very high temperatures (above 1,000°C) at low pressure during pyrometamorphism of silicate rocks resulting from igneous activity, as well as during spontaneous combustion of coal and coal-waste piles where reducing conditions may prevail (Grapes 2011). Synthetic (Fe, Al, Y)-garnets are also exposed to very high temperatures (usually in a mixture of Ar + H_2 gases) in plasma spraying technologies (Ravi et al. 2007). Therefore, the exact knowledge of the reductive decomposition of garnets might be of significant importance not only for construction of petrological models (e.g., Frost and McCammon 2008), but also for industrial applications of garnet.

The thermal decomposition of pyrope-almandine garnets has previously been studied in oxidizing (Thiéblot et al. 1998; Mašláň et al. 1997; Barcova et al. 2001; Zboril et al. 2003, 2004) and inert atmospheres (Schairer and Yagi 1952)

and also under non-ambient pressure (Anovitz et al. 1993). The decomposition occurs between 750 and 1,200°C, resulting in the formation of hematite, sillimanite and cristobalite (Anovitz et al. 1993; Thiéblot et al. 1998), where hematite (α-Fe_2O_3) might be formed by sequential polymorph transformation of maghemite (γ-Fe_2O_3) and ε-Fe_2O_3 at temperatures above 750°C (Zboril et al. 2002). At 1,200°C, cordierite, anorthite and spinel or maghemite have been identified as decomposition products of almandine-pyrope garnets (Zboril et al. 2004). In nitrogen atmosphere, almandine has been shown to decompose to hercynite, cordierite and fayalite after 2 weeks at 900°C (Schairer and Yagi 1952). Anovitz et al. (1993) investigated the oxidation mechanisms of almandine leading to formation of magnetite, quartz and sillimanite or hercynite, or to hercynite, fayalite and quartz or "Fe-cordierite" depending on the applied pressure. Moreover, almandine-rich garnet heated at 1,100°C for 10 h at a pressure of 1 kbar and an oxygen fugacity of 10^{-10} to 10^{-12} have been shown to decompose to aluminous orthopyroxene, cordierite and spinel (Zang et al. 1993). Natural examples of garnet decomposition include breakdown of almandine in xenoliths from the Eifel area, Germany (Grapes 2011), where garnet is replaced by fine-grained mixtures of pyroxenes (ortho- and clinopyroxene) and magnetite.

Under reducing conditions, however, different structural aspects and decomposition pathways might appear. Therefore, we have investigated the mechanisms of thermally induced reductive decomposition of almandine under hydrogen atmosphere. It is well known that thermally driven hydrogen diffusion into the structures of nominally anhydrous silicates like garnets might significantly change their physical and chemical properties, including stability (Rossman 1996). To exclude such effect, we initially studied the process of possible hydrogen diffusion into the almandine structure at temperatures up to 1,000°C.

The presented results are essential for understanding the mineral behavior during pyrometamorphism of silicate rocks as well as spontaneous combustion of natural/anthropogenic materials. At elevated pressures, comparable reactions might proceed also at lower temperatures (Keesmann et al. 1971), and thus, the presented reaction mechanisms become meaningful for petrologists and experimental geophysicists investigating the Earth's mantle where reducing conditions prevail (Frost and McCammon 2008). The understanding of reductive decomposition of iron-bearing silicates has also consequences in investigation of space weathering (e.g., Hapke 2001).

Sample description and experimental techniques

The investigated sample is a brownish-red near end-member almandine from the locality Zlatý Chlum near Jeseník, Czech Republic. Optically clear crystal fragments were hand-picked, washed in a cold diluted hydrochloric acid and finely ground in an agate mortar. For investigation of hydrogen diffusion into almandine structure, single-crystal slabs were prepared by parallel grinding and double-side polishing of impurity-free almandine fragments to a thickness of 380 μm.

The chemical composition of the untreated almandine was determined with a Cameca SX100 electron microprobe (EMP) operating in the wavelength dispersive mode with an accelerating voltage of 15 kV, a beam current of 20 nA and an analytical spot size of ~1 μm. The following standards and analytical spectral lines were used: K_α lines: sanidine (Si, Al, K), albite (Na), almandine (Fe), pyrope (Mg), andradite (Ca), rhodonite (Mn), TiO_2 (Ti), $ScVO_4$ (Sc, V); L_α lines: pollucite (Cs), Rb-leucite (Rb). The analytical data were corrected using the PAP correction procedure (Pouchou and Pichoir 1985) and normalized to 12 anions per formula unit.

The almandine single-crystal slabs were thermally treated for 1 and 2 h at 800°C in air using a conventional muffle furnace and, subsequently, for 1, 4, 12 and 24 h at 800, 900 and 1,000°C, and also for 93 h at 1,000°C under hydrogen in a horizontal glass-tube furnace. The experiments were started by placing the single-crystal slabs in the preheated furnace and terminated by rapid quenching prior to the FTIR spectroscopy measurements.

Unpolarized FTIR absorption spectra in the OH stretching frequency region of almandine single-crystal slabs were recorded from 3,000 to 4,000 cm^{-1} using a Bruker Equinox 55 spectrometer equipped with an NIR source, an LN_2 cooled InSb detector, a CaF_2 beam-splitter and circular sample apertures (100 μm in diameter). A total of 100 scans (resolution of 4 cm^{-1}) were performed in air for each sample and the respective background.

The thermal decomposition of almandine was in-situ monitored in a reducing hydrogen-containing atmosphere (10% of H_2 in N_2; atmospheric pressure) using a thermal analyzer (STA 449 C Jupiter, Netzsch) including both thermogravimetric analysis (TGA) and differential scanning calorimetry (DSC) coupled to a mass spectrometer (QMS 403 Aëolos, Netzch) for evolved gas analysis (EGA). In this case, powdered almandine samples were placed in an open alumina crucible, dynamically heated up to the chosen temperature (950, 1,070 and 1,200°C) with a heating rate of 10 K/min and then quickly cooled down. Phase analysis of untreated (labeled as ALM-NH) as well as thermally treated samples (labeled according to the final heating temperature; Fig. 1) was performed by X-ray powder diffraction (XRD) and ^{57}Fe Mössbauer spectroscopy at room temperature.

The XRD patterns were recorded with a PANalytical X'Pert PRO MPD diffractometer (CoK_α radiation) in the

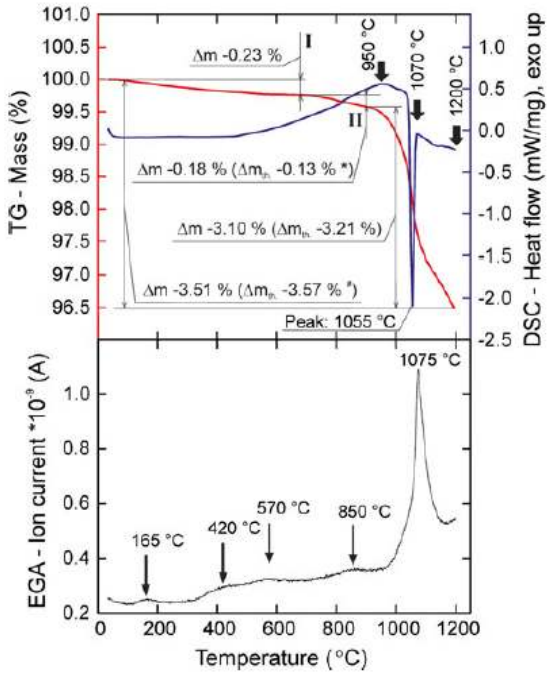

Fig. 1 *Upper part*: TGA (*red*) and DSC (*blue*) curves of almandine thermally treated in hydrogen (i.e., 10% of H_2 in N_2). *Thick arrows* indicate the temperatures of preparation of samples ALM-950, ALM-1070 and ALM-1200. *I*—temperature of 675°C; *II*—temperature of 900°C; Δm—experimentally observed mass difference; Δm_{th}—theoretical mass difference; *value considering 2 wt.% of ilmenite inclusions in ALM-NH sample; #value including Δm of −0.23% from fluid inclusions and considering 2 wt.% of ilmenite inclusions. *Lower part*: evolved gas analysis for a mass-to-charge ratio $m/z = 18$

Bragg-Brentano geometry, equipped with an X'Celerator detector and programmable divergence and diffracted beam anti-scatter slits. Samples were placed on a zero-background Si slide and scanned in a continuous mode (resolution of 0.017° 2 Theta, scan speed of 0.004° 2 Theta per second). Identification of crystalline phases and Rietveld refinements were obtained using the software High Score Plus (PANalytical) in conjunction with the PDF-4+ and ICSD databases. Peak shapes were modeled using the pseudo-Voigt function, separately refining the Caglioti parameters (u, v, w), unit cell parameters and scale factor for each phase.

Transmission ^{57}Fe Mössbauer spectroscopy on powdered samples was carried out in a constant acceleration mode using a ^{57}Co(Rh) source at room temperature. Spectra were folded and fitted by Lorentz functions, and the isomer shift values are expressed with respect to metallic α-iron. The recoil-free fractions of all phases were considered to be equal.

Results and discussion

Characterization of untreated almandine

The averaged results of the EMP analysis of the almandine sample (Table 1) lead to the crystal-chemical formula $^{VIII}(Fe_{2.85}Mg_{0.11}Ca_{0.05}Mn_{0.02})^{VI}(Al_{1.99})^{IV}(Si_{2.99})O_{12}$ (i.e., $Alm_{96}Py_4$, considering ideal almandine and pyrope end-members). Based on XRD analysis (not shown), the untreated sample is a nearly pure almandine with a cell parameter $a = 11.5341(2)$ Å, containing minor ilmenite inclusions that amount to less than 1 wt.% according to the Rietveld refinement. The ^{57}Fe Mössbauer spectrum (Fig. 2; Table 2) was fitted with three doublets. The dominant D1 doublet corresponds to Fe^{2+} in the dodecahedral 24*c* position (relative subspectrum area $A = 93$, or 97% excluding the ilmenite contribution), whereas the D2 doublet corresponds to Fe^{3+} in the octahedral 16*a* position ($A = 3\%$) in the almandine structure (cf., Geiger 2004). The hyperfine parameters of the D3 doublet ($A = 4\%$) are typical for Fe^{2+} in the ilmenite structure (cf., Stevens et al. 1998).

Dehydrogenation and hydrogen diffusion in almandine at temperatures below 1,000°C

The presence of OH stretching bands of low intensity in an unpolarized FTIR spectrum of untreated almandine sample indicates the existence of OH defects in the almandine

Table 1 Chemical composition of untreated almandine obtained by EMP

Oxide	TiO_2	Cr_2O_3	CaO	FeO	MnO	Na_2O	P_2O_5	SiO_2	Al_2O_3	MgO	Y_2O_3	Total
Wt.%	0.04	0.01	0.56	41.19	0.21	0.01	0.01	36.09	20.44	0.91	0.01	99.49
SD	0.02	0.01	0.11	0.15	0.06	0.02	0.01	0.22	0.14	0.05	0.01	0.35
Cation	Ti^{4+}	Cr^{3+}	Ca^{2+}	Fe^{2+}	Mn^{2+}	Na^{2+}	P^{5+}	Si^{4+}	Al^{3+}	Mg^{2+}	Y^{3+}	Total
Apfu	0.002	0.001	0.050	2.851	0.015	0.002	0.006	2.986	1.994	0.113	0.001	8.020
SD	0.001	0.000	0.010	0.011	0.005	0.003	0.005	0.007	0.007	0.006	0.001	0.006

Cations normalized to 12 oxygens

SD Standard deviation, *Wt.%* oxide weight percentage, *Apfu* Atoms per formula unit

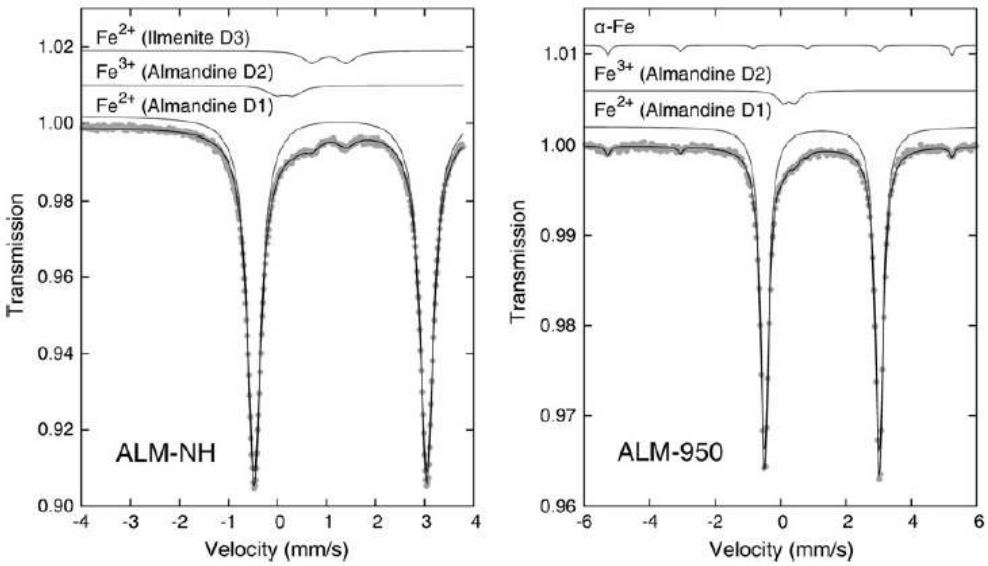

Fig. 2 Room-temperature ^{57}Fe Mössbauer spectra of samples ALM-NH and ALM-950. Note the different velocity scales

Table 2 Mössbauer parameters for samples ALM-NH and ALM-950

Component	Assignment	Parameter	ALM-NH	ALM-950
Almandine (D1)	$^{VIII}Fe^{2+}$	δ (mm/s)	1.29	1.27
		ΔE_Q (mm/s)	3.52	3.51
		Γ (mm/s)	0.34	0.30
		A (%)	93	93
Almandine (D2)	$^{VI}Fe^{3+}$	δ (mm/s)	0.15	0.25
		ΔE_Q (mm/s)	0.37	0.38
		Γ (mm/s)	0.45#	0.40#
		A (%)	3	4
Ilmenite (D3)	$^{VI}Fe^{2+}$	δ (mm/s)	1.05	–
		ΔE_Q (mm/s)	0.70	–
		Γ (mm/s)	0.42	–
		A (%)	4	–
α-iron	Fe^0	δ (mm/s)	–	0.00#
		ε_Q (mm/s)	–	0.00#
		B_{hf} (T)	–	32.7
		Γ (mm/s)	–	0.19
		A (%)	–	3

δ—isomer shift (±0.02), ΔE_Q—quadrupole splitting (±0.02), ε_Q—quadrupole shift (±0.02), Γ—experimental line width (±0.02), B_{hf}—hyperfine magnetic field (±0.2), A—relative area (±3), # fixed parameters. Roman numbers indicate the coordination number

structure (Fig. S1 in the supplementary material). The concentration, estimated according to Lambert–Beer's law, turned out to be approximately 2 ppm H_2O (using the calibration of Libowitzky and Rossman 1997). Such a low content of OH defects is typical for garnets of pyrope-almandine composition (Beran and Libowitzky 2006) and is several orders of magnitude lower than the values commonly reported for garnets of grossular-andradite or spessartine composition (cf., Johnson 2006). Upon heating in air (800°C, 1 and 2 h), the OH content drops to zero, demonstrating the complete dehydrogenation of the almandine structure (Fig. S1). Subsequent treatment at temperatures up to 900°C under hydrogen and a maximum of 24 h caused no observable hydrogen diffusion into the previously dehydrogenated almandine sample (Fig. S1). At 1,000°C and 1–110 h of treatment, almandine single-crystal slabs turned out to be less transparent for infrared radiation, and the resulting spectra were rough (i.e., clear indication of incipient decomposition of almandine; not shown) with no clear evidence for OH stretching bands. Interestingly, hydrogen diffusion into the structure of the studied metamorphic almandine is limited compared to other rock-forming silicates like pyroxenes (e.g., Sundvall et al. 2009). Thus, we can exclude the influence of hydrogen diffusion into the almandine structure in the subsequently discussed decomposition mechanisms of almandine under the strongly reducing hydrogen atmosphere.

Thermal behavior of almandine between 35 and 1,200°C in hydrogen: characterization of decomposition products

The TGA curve of the powdered almandine sample can be divided into three temperature intervals, which differ significantly in the respective mass loss behavior (Fig. 1). The

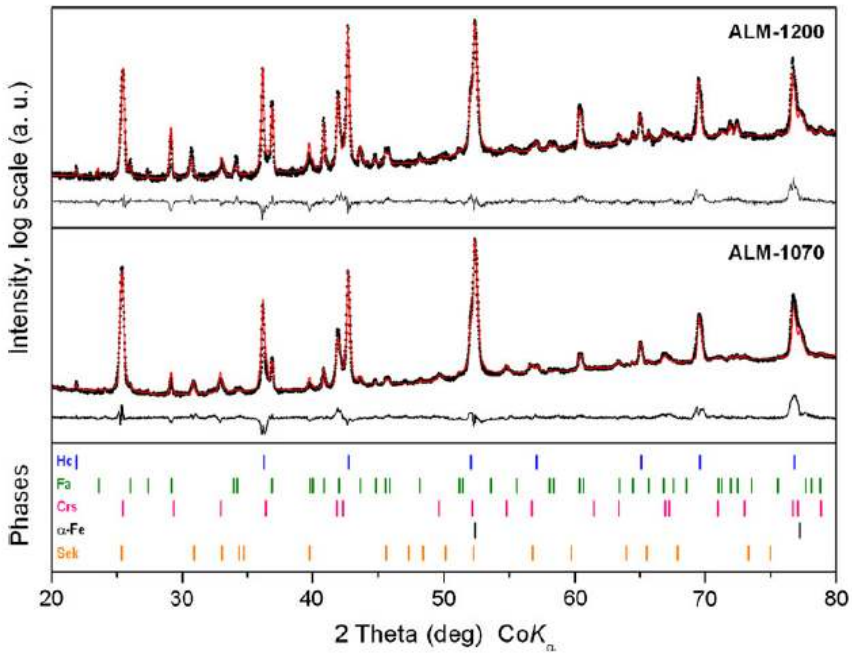

Fig. 3 XRD patterns of the thermally decomposed samples. The identified phases are hercynite (Hc; PDF No.: 00-034-0192), fayalite (Fa; PDF No.: 00-020-1139), bcc iron (α-Fe; PDF No.: 00-006-0696), cristobalite (Crs; PDF No.: 00-011-0695) and sekaninaite (Sek; PDF No.: 00-054-0679). *Black points* correspond to experimental data, *red solid line* show the Rietveld refinement of the data, and *black lines* under each of the XRD patterns represent the difference between the experimental and calculated intensities

steep fall in mass between 900 and 1,200°C correlates with a pronounced endothermic peak at 1,055°C on the DSC curve (Fig. 1).

The ^{57}Fe Mössbauer spectrum of ALM-950 sample (Fig. 2) is highly comparable to that of the untreated sample and was fitted by the D1 and D2 almandine doublets (Table 2) and an additional weak sextet corresponding to metallic iron (α-Fe). Metallic iron and rutile were confirmed by XRD (not shown), both being the products of reductive decomposition of ilmenite inclusions at temperatures lower than 950°C (cf., de Vries et al. 2007). The weight ratio of α-Fe and rutile derived from the Rietveld refinement implies that all α-Fe present in sample ALM-950 originates exclusively from ilmenite. The fraction of the ferric iron doublet can be considered equal for both the ALM-NH and ALM-950 samples (Table 2) as the difference is within the experimental error for Mössbauer spectroscopy. We can conclude that the almandine structure remains mostly unchanged up to 950°C and that no reduction of iron in almandine structure was observed.

The diffraction patterns of ALM-1070 and ALM-1200 samples (Fig. 3) represent the fully decomposed garnet sample, with the newly produced phases identified as α-Fe, hercynite, cristobalite, fayalite and sekaninaite (Table 3). The observed α-Fe arises partially from decomposition of ilmenite inclusions (as discussed above), but this contribution to the total α-Fe content is less than 5% relative. The variations in the phase composition of ALM-1070 and ALM-1200 samples (Table 3) indicate consecutive reactions of the primary almandine decomposition products as soon as they are formed: The fayalite content increases (+13.1 wt.%) at the expense of alpha-iron (−4.5 wt.%) and cristobalite (−11.5 wt.%). Moreover, the sekaninaite content increases (Table 3) at the higher temperature.

The ^{57}Fe Mössbauer spectra of the ALM-1070 and ALM-1200 samples were fitted by one sextet and five paramagnetic doublets (Fig. 4). The α-Fe sextet is dominant in the spectrum of the ALM-1070 sample, but weaker in sample ALM-1200 (Table 4). The contribution from fayalite was fitted with two paramagnetic doublets representing Fe^{2+} at M1 and M2 sites with their spectral area ratio (i.e., Fe atomic ratio) equal to 0.97 and 0.98 for the ALM-1070 and ALM-1200 samples, respectively, being close to the theoretical occupancy for iron in the olivine structure (Dyar et al. 2009). The spectral area for the fayalite doublet increases from 14% (ALM-1070) to 28% (ALM-1200), whereas the subspectrum doublet for sekaninaite has an equal area in the spectra of both samples (Table 4). The last two doublets are ascribed to ferrous iron in the tetrahedral T1 and T2 sites of hercynite (cf. Carbonin et al. 1996), with the inner doublet representing the more distorted tetrahedral site. The hercynite doublets have a summed area of 31 and 32% for the ALM-1070 and ALM-1200 samples, respectively. Octahedrally coordinated Fe^{3+} in hercynite was not confirmed.

The metallic α-Fe was further identified by scanning electron microscopy in the mixture of reaction products of sample ALM-1070. The metallic iron forms spherical and

Table 3 Results of quantitative phase analysis of all studied samples (from Rietveld refinement)

Phase	Chemical formula	Weight fractions (%)			
		ALM-NH	ALM-950	ALM-1070	ALM-1200
Almandine	$Fe_3Al_2Si_3O_{12}$	99.2(6)	98.8(7)	–	–
Ilmenite	$FeTiO_3$	0.8(1)	–	–	–
Rutile	TiO_2	–	0.5(2)	n.d.	n.d.
α-iron	Fe	–	0.7(1)	22.0(1)	17.5(1)
Hercynite	$(Fe,Mg)Al_2O_4$	–	–	44.9(2)	44.6(2)
Fayalite	Fe_2SiO_4	–	–	8.2(2)	21.3(1)
Cristobalite	SiO_2	–	–	23.6(2)	12.1(2)
Sekaninaite	$(Fe,Mg)_2Al_4Si_5O_{18}$	–	–	1.3(1)	4.5(1)

The numbers in parentheses indicate the estimated standard deviations. Cell parameters and ICSD collection codes of all refined phases are listed in Table S1 in the Supplementary material

n.d. not determined

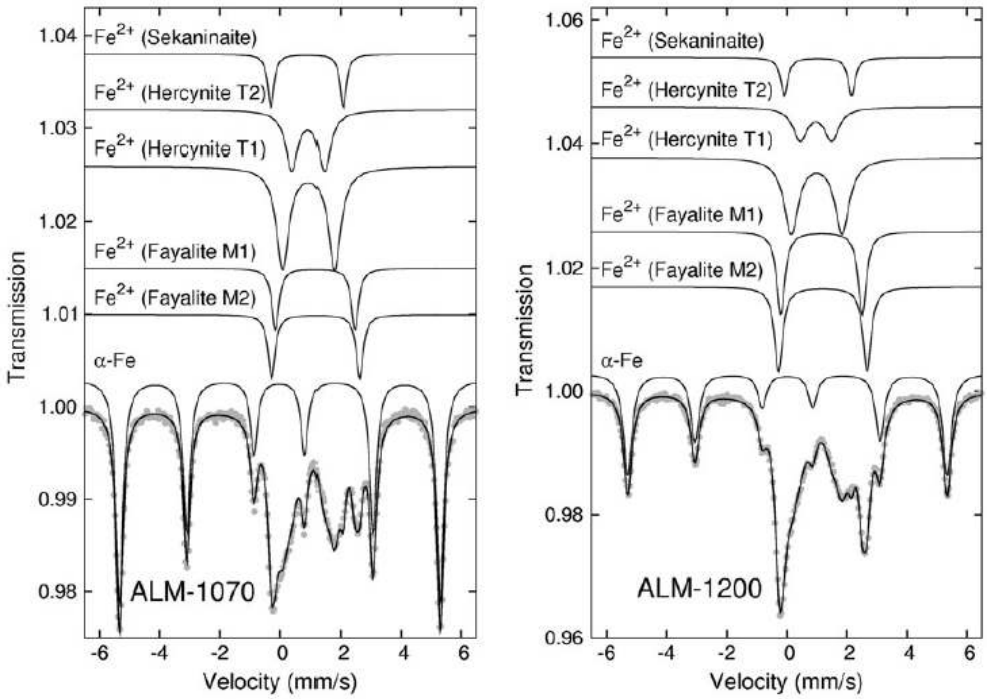

Fig. 4 Room-temperature ^{57}Fe Mössbauer spectra of samples ALM-1070 and ALM-1200

isolated particles with an average diameter of approximately 1 μm (Fig. S2 in the supplementary material).

Mechanisms of almandine thermal decomposition

In the temperature range from 35 to 675°C, the observed mass loss (Fig. 1) can be ascribed to release of water from fluid inclusions or fine cracks in the almandine sample (three very weak peaks in evolved gas analysis; Fig. 1). Between 675 and 900°C, mass loss and evident release of water (small peak at around 850°C) can be explained by decomposition of ilmenite inclusions and formation of both alpha-iron and rutile according to the reaction (cf., de Vries et al. 2007):

Table 4 Mössbauer parameters of samples ALM-1070 and ALM-1200

Component	Assignment	Parameter	ALM-1070	ALM-1200
α-iron	Fe^0	δ (mm/s)	−0.02	0.02
		ε_Q (mm/s)	0.00#	0.00#
		B_{hf} (T)	33.0	33.0
		Γ (mm/s)	0.28	0.34
		A (%)	50	35
Hercynite	$^{IV}Fe^{2+}$ T1	δ (mm/s)	0.94	1.00
		ΔE_Q (mm/s)	1.69	1.70
		Γ (mm/s)	0.50	0.58
		A (%)	20	22
Hercynite	$^{IV}Fe^{2+}$ T2	δ (mm/s)	0.93	0.97
		ΔE_Q (mm/s)	1.06	1.05
		Γ (mm/s)	0.49	0.58
		A (%)	11	10
Fayalite	$^{VI}Fe^{2+}$ M1	δ (mm/s)	1.17	1.20
		ΔE_Q (mm/s)	2.89	2.95
		Γ (mm/s)	0.28#	0.33#
		A (%)	7	14
Fayalite	$^{VI}Fe^{2+}$ M2	δ (mm/s)	1.16	1.16
		ΔE_Q (mm/s)	2.61	2.72
		Γ (mm/s)	0.28#	0.33#
		A (%)	7	14
Sekaninaite	$^{VI}Fe^{2+}$	δ (mm/s)	0.89	1.04
		ΔE_Q (mm/s)	2.37	2.25
		Γ (mm/s)	0.26	0.28
		A (%)	5	5

Symbols and abbreviations as in Table 2

$$FeTiO_3 + H_2(g) \rightarrow TiO_2 + \alpha\text{-}Fe + H_2O\ (g). \quad (1)$$

Finally, an observed mass loss between 950 and 1,200°C, a single pronounced endothermic peak at 1,055°C (DSC) and water vapor formation at 1,075°C (EGA; Fig. 1) demonstrate sudden and complete decomposition of almandine. The reaction of almandine with hydrogen leads to Eq. 2:

$$Fe_{3-x}Mg_xAl_2Si_3O_{12} + 2H_2(g) \rightarrow Fe_{1-x}Mg_xAl_2O_4 + 2\alpha\text{-}Fe + 3SiO_2 + 2H_2O(g) \quad (2)$$

($0 \leq x \leq 1$; $x = 0.15$ for the studied sample).

The presence of fayalite and sekaninaite in samples ALM-1070 and ALM-1200 suggests consecutive reactions of primary products with increasing temperatures. Moreover, the mass loss calculated for Eq. 2 is 6.42%, that is, far from the observed value of 3.10%. Therefore, the increase in fayalite content at temperatures from 1,070 to 1,200°C suggests the reaction of metallic iron with cristobalite and water vapor (cf., Ternes et al. 1991):

$$2\alpha\text{-}Fe + SiO_2 + 2H_2O(g) \rightarrow Fe_2SiO_4 + 2H_2(g). \quad (3)$$

Consumption of 1 molecule of H_2O from Eq. 2 by Eq. 3 would decrease the theoretical mass loss down to value of 3.21%, which is in very good agreement with the observed value of 3.10% (Fig. 1).

The formation of sekaninaite can be explained by reaction of hercynite and cristobalite (reaction without change in mass; Liu et al. 2009) according to:

$$2Fe_{1-x}Mg_xAl_2O_4 + 5SiO_2 \rightarrow (Fe_{1-x}Mg_x)_2Al_4Si_5O_{18}. \quad (4)$$

The predominant formation of fayalite relative to sekaninaite at temperatures up to 1,200°C (Table 3) might be caused by different reaction rates and higher stability of hercynite compared to α-Fe under the given conditions. Assuming that only 10% of hercynite reacts with cristobalite and 50% of α-Fe reacts with SiO_2 and water vapor, we get the overall reaction:

$$Fe_{3-x}Mg_xAl_2Si_3O_{12} + H_2(g) \rightarrow \alpha\text{-}Fe + 0.9Fe_{1-x}Mg_xAl_2O_4 + 2.25SiO_2 + 0.5Fe_2SiO_4 + 0.05(Fe_{1-x}Mg_x)_2Al_4Si_5O_{18} + H_2O(g) \quad (5)$$

Based on the acquired experimental data, we may propose a general mechanism of reductive decomposition of almandine in hydrogen (sekaninaite and fayalite are formed in amounts indicated as "a" and "b", respectively) as:

$$Fe_{3-x}Mg_xAl_2Si_3O_{12} + (2-b)H_2(g) \rightarrow (1-a)Fe_{1-x}Mg_xAl_2O_4 + (2-b)Fe + (b/2)Fe_2SiO_4 + (3-5a/2-b/2)SiO_2 + (a/2)(Fe_{1-x}Mg_x)_2Al_4Si_5O_{18} + (2-b)H_2O(g). \quad (6)$$

Assuming that all alpha-iron, cristobalite and water are consumed to form fayalite and sekaninaite in our model (i.e., $b = 2$ and $a = 4/5$ in Eq. 6), we obtain an equilibrium equation comparable to the one reported by Anovitz et al. (1993) for pure end-member almandine in the temperature range 650–850°C at pressures below 3.3 kbar. Evidently, the main difference between oxidative and reductive decomposition of almandine lies in the formation of iron oxides (Zboril et al. 2002) and metallic iron (this study), respectively, without valence changes of iron in the almandine structure up to the temperature of its reductive decomposition.

The presented mechanism including the formation of metallic iron particles from iron-bearing silicate might be correlated with processes in Earth's mantle where reducing conditions could prevail and cause metallic iron to be stable (Frost and McCammon 2008). Moreover, the presented formation of metallic iron particles has an analogy in space weathering where submicroscopic iron particles are formed by partial impact melting and reduction of

surfaces of Fe(II)-bearing minerals saturated with solar wind hydrogen (Hapke 2001).

Acknowledgments This work has been supported by research projects of the Academy of Sciences of the Czech Republic (grant no. KAN115600801) and the Ministry of Education, Youth and Sports of the Czech Republic (grant no. MSM6198959218; and the Operational Program Research and Development for Innovations—European Regional Development Fund, project no. CZ.1.05/2.1.00/03.0058). Part of this work has been done during a stay of JF at the Department of Mineralogy, Swedish Museum of Natural History, Stockholm (financed by the European Community—Research Infrastructure Action under the FP6 Program within SYNTHESYS; Project SE-TAF-4065). We wish to thank R. Škoda for EMPA measurements, M. Heřmánek, K Šafářová and J. Ševčíková for technical assistance and J. Tuček for language corrections. Samples for this study were kindly provided by the Moravian Museum in Brno, Czech Republic.

References

Anovitz L, Essene E, Metz G, Bohlen S, Westrum E, Hemingway B (1993) Heat capacity and phase equilibria of almandine, $Fe_3Al_2Si_3O_{12}$. Geochim Cosmochim Ac 57:4191–4204

Barcova K, Mashlan M, Zboril R, Martinec P, Kula P (2001) Thermal decomposition of almandine garnet: Mössbauer study. Czech J Phys 51:749–754

Beran A, Libowitzky E (2006) Water in natural mantle minerals II: olivine, garnet and accessory minerals. Rev Mineral Geochem 62:169–191

Carbonin S, Russo U, Della Giusta A (1996) Cation distribution in some natural spinels from X-ray diffraction and Mössbauer spectroscopy. Mineral Mag 60:355–368

Chang LLY (2002) Industrial mineralogy: materials, processes and uses, 1st edn. Prentice Hall, Upper Saddle River, New Jersey

de Vries M, Grey I, Fitz Gerald J (2007) Crystallographic control in ilmenite reduction. Metall Mater Trans B 38:267–277

Deer WA, Howie RA, Zussman J (1997) Rock-forming minerals, vol. 1A: orthosilicates, 2nd edn. Geological Society of London, London

Dyar M, Sklute E, Menzies O, Bland P, Lindsley D, Glotch T, Lane M, Schaffer M, Wopenka B, Klima R, Bishop J, Hiroi T, Pieters C, Sunshine J (2009) Spectroscopic characteristics of synthetic olivine: an integrated multi-wavelength and multi-technique approach. Am Mineral 94:883–898

Frost DJ, McCammon CA (2008) The redox state of Earth's mantle. Annu Rev Earth Pl Sc 36:389–420

Geiger CA (2004) Spectroscopic investigations relating to the structural, crystal-chemical and lattice-dynamic properties of $(Fe^{2+}, Mn^{2+}, Mg, Ca)_3Al_2Si_3O_{12}$ garnet: A review and analysis. In: Beran A, Libowitzky E (eds) EMU notes in mineralogy, vol 6. Eötvös University Press, Budapest, pp 589–645

Grapes R (2011) Pyrometamorphism, 2nd edn. Springer, Berlin

Hapke B (2001) Space weathering from Mercury to the asteroid belt. J Geophys Res 106:10039–10073

Johnson EA (2006) Water in nominally anhydrous crustal minerals: speciation, concentration, and geologic significance. Rev Mineral Geochem 62:117–154

Keesmann I, Matthes S, Schreyer W, Seifert F (1971) Stability of almandine in the system FeO–(Fe_2O_3)–Al_2O_3–SiO_2–(H_2O) at elevated pressures. Contrib Mineral Petr 31:132–144

Libowitzky E, Rossman GR (1997) An IR absorption calibration for water in minerals. Am Mineral 82:1111–1115

Liu S, Zeng Y, Jiang D (2009) Fabrication and characterization of cordierite-bonded porous SiC ceramics. Ceram Int 35:597–602

Mašláň M, Šindelář Z, Martinec P, Chmielová M, Kholmetskii A (1997) Mössbauer study of phase transition caused by oxidation in the temperature region from 20 to 1000°C in almandine garnets. Czech J Phys 47:571–574

Pouchou JL, Pichoir F (1985) "PAP" procedure for improved quantitative microanalysis. Microbeam Anal 20:104–106

Ravi BG, Guo XZ, Yan QY, Gambino RJ, Sampath S, Parise JB (2007) Phase evolution and magnetic properties of Al substituted yttrium iron garnet nanopowders and plasma-sprayed coatings. Surf Coat Tech 201:7597–7605

Rossman GR (1996) Studies of OH in nominally anhydrous minerals. Phys Chem Miner 23:299–304

Schairer JF, Yagi K (1952) The system FeO–Al_2O_3–SiO_2. Am J Sci Bowen 2:471–512

Stevens J, Khasanov A, Miller J, Pollak H, Li Z (eds) (1998) Mössbauer mineral handbook, Mössbauer Effect Data Centre (MEDC). Baltimore Press, Asheville

Sundvall R, Skogby H, Stalder R (2009) Dehydration-hydration mechanisms in synthetic Fe-poor diopside. Eur J Mineral 21:17–26

Ternes T, Meisel W, Griesbach P, Hanžel D, Gütlich P (1991) AES and CEMS analysis of the formation of layers on Si steel under thermal treatment in a flux of H_2/water vapor. Fresenius J Anal Chem 341:79–82

Thiéblot L, Roux J, Richet P (1998) High-temperature thermal expansion and decomposition of garnets. Eur J Mineral 10:7–15

Zang Q, Enami M, Suwa K (1993) Aluminium orthopyroxene in pyrometamorphosed garnet megacrysts from Liaoning and Shandong provinces, northeast China. Eur J Mineral 5:153–164

Zboril R, Mashlan M, Barcova K, Vujtek M (2002) Thermally induced solid-state syntheses of γ-Fe_2O_3 nanoparticles and their transformation to α-Fe_2O_3 via ε-Fe_2O_3. Hyperfine Interact 139(140):597–606

Zboril R, Mashlan M, Barcova K, Walla J, Ferrow E, Martinec P (2003) Thermal behavior of pyrope at 1000 and 1100°C: mechanism of Fe^{2+} oxidation and decomposition model. Phys Chem Miner 30:620–627

Zboril R, Mashlan M, Machala L, Walla J, Barcova K, Martinec P (2004) Characterization and thermal behavior of garnets from almandine-pyrope series at 1200°C. Hyperfine Interact 156(157): 403–410

Electronic Supplementary Material

Thermal behavior of almandine at temperatures up to 1,200 °C in hydrogen

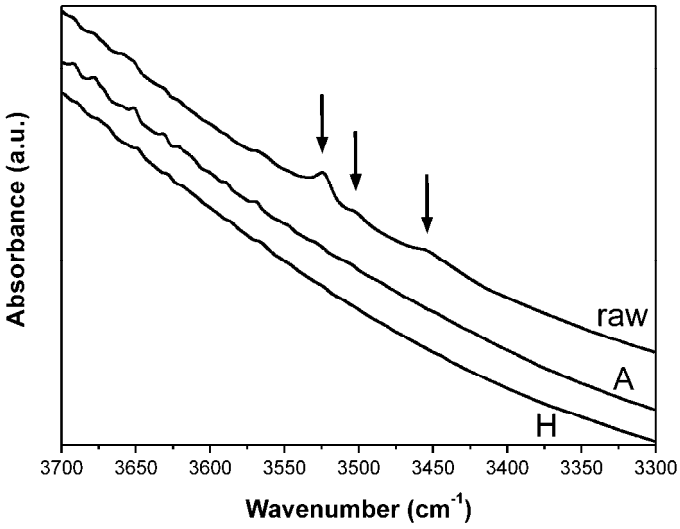

Fig. S1 Unpolarized FTIR absorption spectra in the OH stretching frequency region of untreated almandine (raw), after treatment for 2 hours at 800 °C in air (A) and after treatment for 24 hours at 900 °C in hydrogen (H). Arrows highlight the weak OH stretching bands.

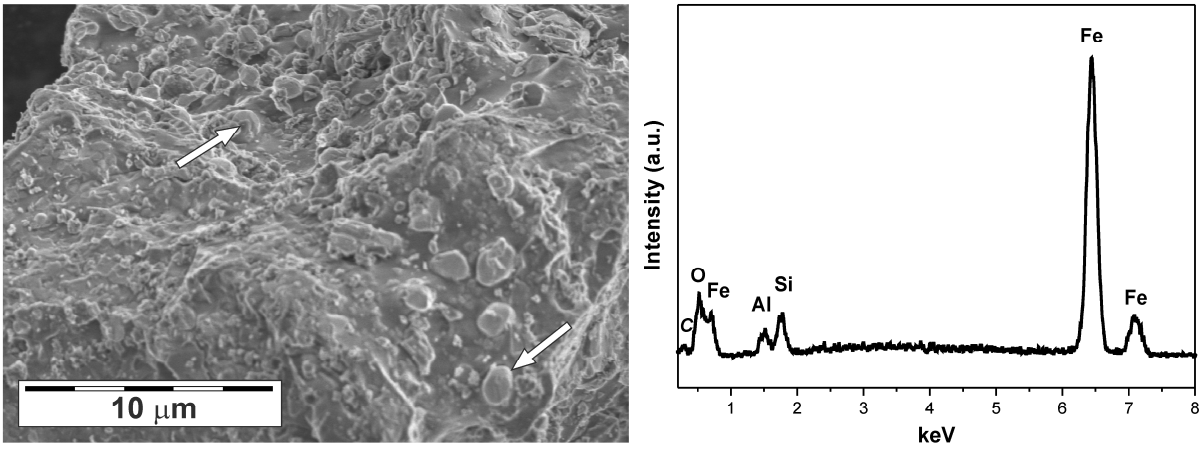

Fig. S2 Representative scanning-electron microscope image of decomposed almandine (sample ALM-1070) – arrows point to metallic iron particles on the surface of the decomposition products (left), and energy-dispersive X-ray (EDX) spectrum collected from a single metallic iron particle (right). Aluminum and silicon identified in EDX spectrum arise from reaction products beneath the iron particle. Data were collected on a field emission scanning electron microscope (Hitachi SU6600) with ultrahigh point-to-point resolution (1-2 nm).

Annex 3

Thermal decomposition of Prussian blue under inert atmosphere

C. Aparicio, L. Machala & Z. Marusak

Journal of Thermal Analysis and Calorimetry **110**(2), 661–669 (2012)

J Therm Anal Calorim (2012) 110:661–669
DOI 10.1007/s10973-011-1890-1

Thermal decomposition of Prussian blue under inert atmosphere

Claudia Aparicio · Libor Machala · Zdenek Marusak

Received: 21 June 2011 / Accepted: 25 August 2011 / Published online: 14 September 2011

Abstract The thermal decomposition of Prussian blue (iron(III) hexacyanoferrate) under inert atmosphere of argon was monitored by thermal analysis from room temperature up to 1000 °C. X-ray powder diffraction and ^{57}Fe Mössbauer spectroscopy were the techniques used for phase identification before and after sample heating. The decomposition reaction is based on a successive release of cyanide groups from the Prussian blue structure. Three principal stages were observed including dehydration, change of crystal structure of Prussian blue, and its decomposition. At 400 °C, a monoclinic Prussian blue analogue was identified, while at higher temperatures the formation of various polymorphs of iron carbides was observed, including an orthorhombic Fe_2C. Increase in the temperature above 700 °C induced decomposition of primarily formed Fe_7C_3 and Fe_2C iron carbides into cementite, metallic iron, and graphite. The overall decomposition reaction can be expressed as follows: $Fe_4[Fe(CN)_6]_3 \cdot 4H_2O \rightarrow 4Fe + Fe_3C + 7C + 5(CN)_2 + 4N_2 + 4H_2O$.

Keywords Insoluble Prussian blue · Iron carbide · XRD · Calcination

Electronic supplementary material The online version of this article (doi:10.1007/s10973-011-1890-1) contains supplementary material, which is available to authorized users.

C. Aparicio · L. Machala (✉) · Z. Marusak
Regional Centre of Advanced Technologies and Materials, Departments of Experimental Physics and Physical Chemistry, Faculty of Science, Palacky University, Slechtitelu 11, 783 71 Olomouc, Czech Republic
e-mail: libor.machala@upol.cz
URL: http://www.rcptm.com/

Introduction

The Prussian blue (PB) complex salt was unwittingly produced by a painter in the beginning of the eighteen century. From this day until now, PB has been employed in a wide range of applications in industry, pharmaceutics, and science. Prussian blue, "insoluble" PB, iron(III) hexacyanoferrate or ferric ferrocyanide are usually the names of this ferrocyanide compound. PB has an ideal chemical formula of $Fe_4^{III}[Fe^{II}(CN)_6]_3 \cdot xH_2O$ with the Fm-3m space group [1], where Fe^{2+} ions are found in a low-spin ($S = 0$) state and Fe^{3+} ions are found in a high-spin ($S = 5/2$) state. PB shows a ferromagnetic behavior below its Curie temperature $T_C = (5.5 \pm 0.5)$ K [2].

Physicochemical properties of PB have been investigated by several experimental techniques including infrared spectroscopy [3], X-ray diffraction [4], and Mössbauer spectroscopy (MS) [2, 6, 7]. These investigations were devoted to structural analysis [1, 8, 9], synthesis [10–12], magnetic properties [13], applications [14–16], PB-based analogs [17, 18], and some of them have been focused on behavior of PB at high temperatures [5, 6, 19].

In general, when hexacyanoferrate compounds containing crystalline water are heated, one endothermic effect (always below 200 °C) corresponds to a release of the water molecules. Afterward, the thermal decomposition occurs at higher temperatures depending on the composition of the starting compound [20]. According to De Marco [20–23], Brar [24], and Lehto [25] the decomposition of hexacyanoferrate compounds in air occurs with an exothermic effect and accompanied by a release of gaseous products ($(CN)_2$ or HCN). Finally, the oxidation of iron cations leads to the formation of iron oxides as common decomposition products [19, 24–27].

One of the oldest works on thermal decomposition of hexacyanoferrate in vacuum was reported by Gallagher and Prescott [28]. They studied thermal decomposition reactions of europium hexacyanoferrate(III) and ammonium europium hexacyanoferrate(II) compounds resulting to Eu hydroxide and $Fe(CN)_2$. Further decomposition of $Fe(CN)_2$ to Fe_3C and finally to metallic iron has been confirmed. Cosgrove et al. [18] studied thermal behavior of Prussian blue up to 530 °C in vacuum and in air using thermal analysis, X-ray diffraction, and MS. According to Mössbauer spectra, they identified the changes in iron sites with a temperature before and after cyanide release taking place around 290 °C. The reversibility of the process was proved only if the sample was heated at temperatures below 450 °C. Finally, the authors concluded that the structure of PB heated in vacuum up to 450 °C was partially destroyed and crystalline ferrous ferrocyanide with undetermined crystal structure was formed. On the other hand, when the PB sample was heated in air at 410 °C they obtained magnetite in addition to the above-mentioned phases.

Other study on PB thermal decomposition carried out in argon [5] described the simple mechanism toward Fe_3C, graphite and nitrogen as the final products. Years later, Inoue et al. [6] published the Mössbauer characterization of thermal decomposition products of PB in vacuum. In this paper, Inoue et al. explained the thermal behavior of the dried PB from 200 to 350 °C and assumed that changes in Mössbauer parameters above 250 °C corresponded to a flipping of cyanoligands or an existence of mixed-valence states. Therefore, it is clear that a full decomposition of PB has not been achieved at such low temperatures. Thus, one can see from the literature overview that the behavior of PB at high temperatures is not still completely understood. In order to fill this knowledge gap, this study is focused to describe the thermal behavior and elucidate the decomposition mechanism of PB at temperatures up to 1000 °C under an inert atmosphere.

Materials and methods

Starting material and sample preparation

The insoluble Prussian blue ($Fe_4[Fe(CN)_6]_3 \cdot xH_2O$) nanoparticles (60–80 nm) used in this study were manufactured by Sigma Aldrich. The Prussian blue nanopowder (PB) was heated up to different temperatures in argon atmosphere (gas flow of 30 mL/min, protective gas flow of 10 mL/min (Ar)), inside of an opened alumina crucible. The heating rate was 10 °C/min and the mean mass of the samples was 16 mg. The heat treatments of the samples were performed using a thermal analyzer (STA 449 C Jupiter, Netzsch) enabling simultaneous thermogravimetric analysis (TG) and differential scanning calorimetry (DSC). The analyzer is coupled to mass spectrometer (QMS 403 Aëolos, Netzsch) for the analysis of evolving gases (EGA) during the decomposition reaction. The PB was heated up to following temperatures: 400, 670, and 1000 °C. They were labeled as PB1, PB2, and PB3, respectively.

Samples characterization

All the samples were characterized by X-ray powder diffraction (XRD) and transmission ^{57}Fe MS. XRD patterns were recorded with a PANalytical X'Pert PRO MPD diffractometer (Co Kα radiation) in the Bragg–Brentano geometry, equipped with an X'Celerator detector and programmable divergence and diffracted beam anti-scatter slits. The samples were placed on a zero-background Si slide, gently pressed and scanned with a step size of 0.017°, and with angular range from 10° to 90°. The identification of crystalline phases in the recorded XRD patterns was performed using the High Score Plus software (PANalytical) in conjunction with PDF-4+ database.

Transmission ^{57}Fe MS (1024 channels) was carried out in a constant acceleration mode using a ^{57}Co gamma source in Rh matrix at room temperature (RT). The spectrometer was calibrated with a α-Fe foil, and the isomer shift (IS) values were expressed with respect to metallic α-iron at room temperature. The spectra were folded and fitted by Lorentz functions using the computer program CONFIT2000 [29]. Relative contents of iron-bearing phases are expressed through atomic percents given from a relative area of a given subspectrum.

Results and discussion

Characterization of PB samples

The PB sample was characterized by XRD and ^{57}Fe MS. Both techniques proved that the initial Prussian blue sample contained an admixture of a minor phase (~3%) identified as mineral jarosite ($(K,Na)Fe_3(SO_4)_2(OH)_6$). The Mössbauer spectrum was fitted with two doublets and one singlet (Fig. 1). The singlet and the major doublet correspond to low-spin (LS) ferrous ions octahedrally coordinated to six C atoms (IS = −0.14 mm/s, 50.6%) and high-spin (HS) ferric ions octahedrally coordinated to six N atoms (IS = 0.41 mm/s, QS = 0.17 mm/s, 47.0%) in Prussian blue, respectively. The minor doublet corresponds to ferric ions (IS = 0.32 mm/s, QS = 1.13 mm/s, 2.4%) in octahedral site of jarosite [30].

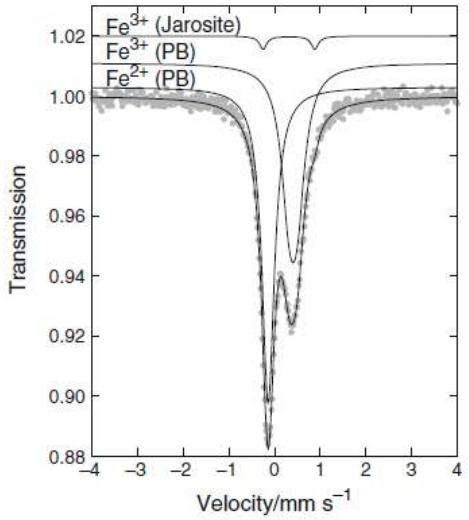

Fig. 1 RT Mössbauer spectrum of the PB sample. The subspectra are shifted along the vertical axis for clarity

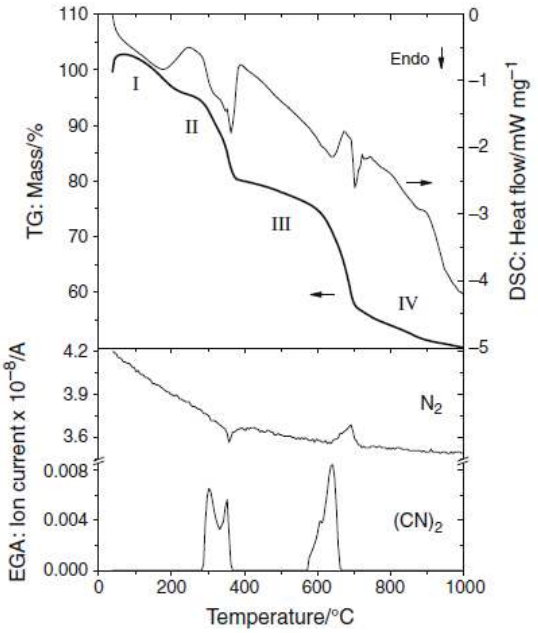

Fig. 2 TG (*thick black line*), DSC (*thin black line*), and EGA (*lower part*) of the PB sample carried out in argon atmosphere. *Roman numbers* indicate the stages of decomposition

Thermal behavior of PB

Simultaneous TG and DSC analyses under argon atmosphere up to 1000 °C (Fig. 2) showed four decomposition steps: I (67–262 °C), II (262–377 °C), III (377–707 °C), and IV (707–1000 °C). In step I, the mass decrease (7.62%) was assigned to water loss from the PB structure, accompanied by an endothermic peak at 178 °C in DSC graph and a wide peak with a centroid at 210 °C in the evolved gas analysis graph (not displayed). The number of water molecules per one molecule of PB was determined as four from TG. The mass losses detected within the steps II (14.75%) and III (23.02%) correspond mainly to a release of cyanide groups from the PB structure at average temperatures of 308, 352, 608, and 643 °C (Fig. 2), accompanied by endothermic reactions (I: 318 and 348 °C, II: 613 and 643 °C). In step III, in addition to $(CN)_2$ emission a release of nitrogen at 693 °C accompanied by an endothermic reaction has been detected. On the other hand, a consumption of nitrogen represented by a downward peak at 358 °C can not be related to the decomposition reaction but it only indicates the detection of other new formed gas by the mass spectrometer, which for a moment changes relative concentrations of the gases. Moreover, an irregular release of carbon dioxide, which was probably adsorbed from air by the surface of the PB sample before the measurement of thermal analysis, was detected by EGA (not displayed) within the measurement.

Sample heated up to 400 °C

The thermal analysis finished at 400 °C (sample PB1) shows that the original structure of PB released all of its structural water ($4H_2O$) and six $(CN)^-$ groups, i.e., $3(CN)_2$ in gaseous form (cyanogen). Temperature of crystal water release (210 °C) agrees well with other thermal studies of PB and PB analogs [5, 18].

The evident change in PB structure has been observed in both XRD pattern (Fig. 3) and Mössbauer spectrum (Fig. 4a) of PB2 ("as-prepared" sample), however, the spectral components of the original PB (~25%) are still present. Unfortunately, it was not possible to find any pattern in the PDF-4+ database, which matches the diffraction lines of the newly formed phase (Fig. 3). Given that some of these compounds are unstable, the same sample was characterized again after one and half year ("aged" sample) to verify its stability. This new XRD pattern is slightly different from the "as-prepared" PB2 sample. The cell group and cell parameters of those unknown phases were calculated with Fullprof 2000 software [31]. It was found that both phases show a monoclinic structure with space group P 2/m, nevertheless a difference in the cell parameters confirms the instability of the structure (see figures S1 and S2 on supporting information).

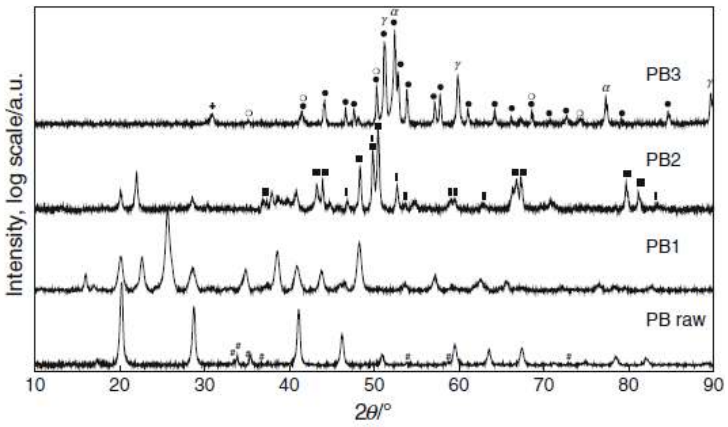

Fig. 3 XRD patterns of the PB samples before and after thermal analyses carried out in inert atmosphere. The *symbols* in the graphs represent the identified phases: Jarosite (#), Fe_2C (*filled square*), Fe_7C_3 (*vertical bar*), Fe_3C (*filled circle*), alpha iron (α), gamma iron (γ), magnetite (*open circle*), and graphite (*plus symbol*). Samples heated up to: 400 °C (PB1), 670 °C (PB2), and 1000 °C (PB3)

RT Mössbauer spectrum of PB2 consists of six spectral components (Fig. 4a), of which the singlet L1 and one doublet D1 belong to the starting PB (Table 1a). The increase in the quadrupole splitting (QS) value of D1 doublet agrees with the change in the environment of Fe^{3+} (HS) due to a dehydration process in Prussian blue [6]. D2 doublet has typical values for LS ferric iron octahedrally coordinated to six carbon atoms in $M_3[Fe(CN)_6]_2$ structures [32]. D3 doublet has the IS and QS values very close to those for Fe^{2+} HS in $K_2Fe[Fe(CN)_6]$ (IS = 1.09 mm/s, QS = 0.45 mm/s) [33]; a doublet with similar values of IS and QS were also obtained from pyrolyzed soluble Prussian blue ($FeK[Fe(CN)_6]\cdot xH_2O$), and aged Prussian brown ($Fe(H_3O)[Fe(CN)_6]\cdot xH_2O$). Mössbauer parameters of D4 and D5 doublets are comparable with those of ferrous trivalent hexacyanides ($Fe_3[M^{III}(CN)_6]_2\cdot xH_2O$), which have a cubic structure and two different iron environments [34].

The doublets D2 and D4 show hyperfine values corresponding to flipping of cyano ligands in PB structure as proposed by Inoue et al. [6]. In our case this indicates the change in the crystal structure of PB after the beginning of its decomposition. Our Mössbauer spectrum resembles the spectrum measured on a PB sample heated up to 460 °C in a vacuum by Cosgrove et al. [18]. They suggest the formation of ferrous ferricyanide after heating when PB has released cyanide groups. Ferrous ferricyanide is not a stable compound; therefore the newly formed compound may be a different one with no cubic structure. With respect to the IS values, the doublets D2 and D3 correspond to iron atoms octahedrally coordinated with six carbon and nitrogen atoms, respectively. From relative areas of subspectra, it is possible to determine the relation between ferric and ferrous ions as $Fe^{3+}/Fe^{2+} = 0.89$. Thus, a possible arrangement of iron atoms can be expressed as $Fe^{+2}_{1.2}Fe^{+2}_{1.8}[Fe^{+3}(CN)_6]_2$, where LS Fe^{3+} is identified by D2 component, and HS Fe^{2+} is identified by D3, D4, and D5 subspectra.

The Mössbauer measurement of the aged PB1 sample (Fig. 4b; Table 1b) also revealed that the structure did not remain stable. The change is reflected by an absence of D4 and D5 doublets, but a presence of a new doublet with the hyperfine parameters typical for a mixed-valence state and the second singlet with the IS peculiar to low-spin ferrous ions. The aging process is thus based on a slow oxidation of the sample.

Sample heated up to 670 °C

Three crystalline phases including Prussian blue, Eckström-Adcock carbide (Fe_7C_3, space group $P6_3mc$) and iron carbide (Fe_2C) have been identified by XRD (Fig. 3). The latter phase is predominant and the corresponding diffraction lines match for two patterns in the database, the first one is a pseudo-hexagonal ε'-Fe_2C and the second one is an orthorhombic Fe_2N. Nevertheless, there are still a few more diffraction lines in the diffractogram that could not be assigned to any pattern in the database.

The very complex RT Mössbauer spectrum of PB2 sample was fitted by five sextets, three doublets, and one singlet (Fig. 5, Table 2). S1, S2, and S3 sextets were ascribed to three non-equivalent positions of iron atoms in the hexagonal structure of Fe_7C_3 (sum of sub-spectral areas: 10.3%) [35]. Literature values for the hyperfine interactions of Fe_7C_3 were taken from Lodya's and Yamada's papers [36, 37]. L1 singlet and D3 doublet show the hyperfine parameters typical for anhydrous Prussian blue. Relatively low areas of L1 and D3 subspectra (together 11.6%) point out that decomposition of the Prussian blue is almost completed at this temperature (670 °C).

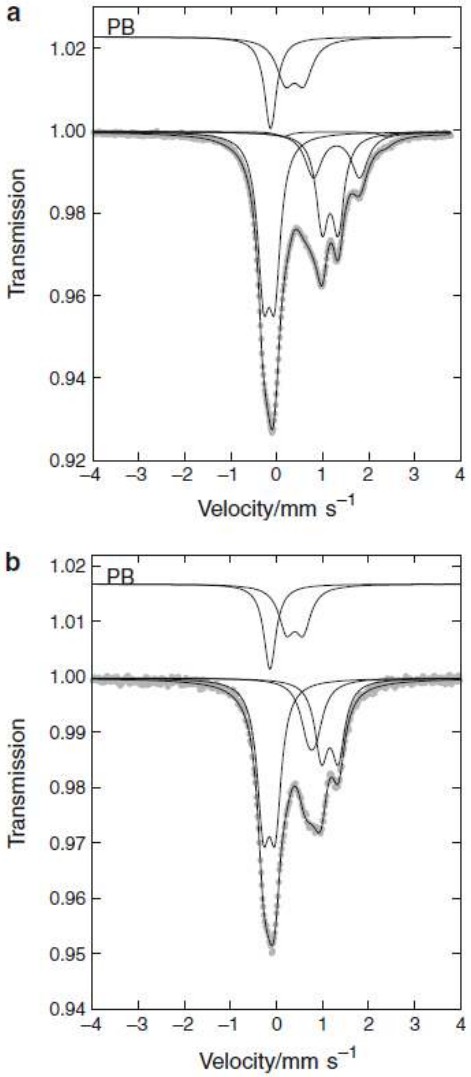

Fig. 4 RT Mössbauer spectra of PB1 (400 °C): **a** "as-prepared" and **b** aged. The subspectra are shifted along the vertical axis for clarity

Table 1 Mössbauer parameters of the PB1 sample (400 °C): a) "as-prepared" and b) aged

	Iron state	IS[a]/mm s^{-1}	QS/mm s^{-1}	W/mm s^{-1}	Area/%
(a)					
D1	Fe^{3+} HS	0.38	0.40	0.47	14.7
D2	Fe^{3+} LS	−0.17	0.24	0.32	34.6
D3	Fe^{2+} HS	1.16	0.35	0.32	22.4
D4	Fe^{2+} HS	1.30	1.00	0.44	15.3
D5	Fe^{2+} HS	1.26	2.24	0.37	1.4
L1	Fe^{2+} LS	−0.14	–	0.32	11.6
(b)					
D1	Fe^{3+} HS	0.40	0.36	0.41	14.9
D2	Fe^{3+} LS	−0.16	0.26	0.32	36.4
D3	Fe^{2+} HS	1.16	0.36	0.35	22.0
D4	$Fe^{2+/3+}$ HS	0.77	0.16	0.42	14.9
L1	Fe^{2+} LS	−0.14	–	0.32	11.8

IS isomer shift (±0.01), *QS* quadrupole splitting (±0.01), *W* experimental line width (±0.01), Area (±0.5), *D* doublet, *L* singlet, *HS* high spin, *LS* low spin

[a] Relative to metallic iron (α-Fe)

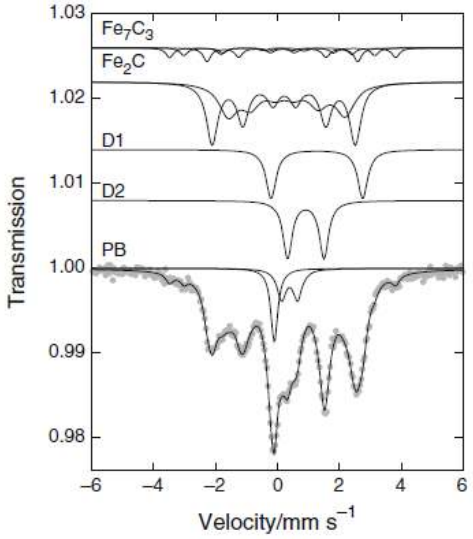

Fig. 5 RT Mössbauer spectrum of sample PB2 (670 °C). The subspectra are shifted along the vertical axis for clarity

Sextets S4 and S5 (Fig. 5; Table 2) can be attributed to a major Fe_2C compound, which could have pseudo-hexagonal or orthorhombic structure (sum of sub-spectral areas: 56%). Although it is known that hexagonal iron carbides and iron-nitrides are isostructural [38], the orthorhombic ζ-Fe_2C (Pbcn space group) is almost unknown being in many cases incorrectly identified as pseudo-hexagonal ε′ phase [39–42]. Comparing the hyperfine parameters with those reported for Fe_2C, we can find a slight disagreement in the values of the hyperfine magnetic field. The values obtained in our work (14.4 and 11.7 T) are smaller than those usually measured for hexagonal ε-carbides (between 17 and 24 T). The lowest hyperfine magnetic field of 17 T has been obtained by Niemantsverdriet et al. [40] and Amelse et al. [41]. The reason for a smaller hyperfine field given by Le Caër et al. [42] is an alternative ordering of iron and carbon atoms in the structure or a different crystalline symmetry. Niemantsverdriet et al. [40] also measured the XRD pattern of this carbide, and they obtained

Table 2 Mössbauer parameters of sample PB2 (670 °C)

	Phase	IS[a]/mm s^{-1}	QS/mm s^{-1}	W/mm s^{-1}	B/T	Area/%
S1	Fe_7C_3	0.23	−0.13	0.30[b]	22.7	3.2
S2	Fe_7C_3	0.04	0.04	0.30[b]	19.2	2.6
S3	Fe_7C_3	0.16	0.00	0.30[b]	15.1	4.5
S4	Fe_2C	0.21	-0.02	0.45	14.4	30.5
S5	Fe_2C	0.26	0.08	0.73	11.7	25.5
D1	Fe^{2+}	1.27	2.96	0.39	–	10.7
D2	Fe^{2+}	0.91	1.18	0.36	–	11.4
D3	PB	0.39	0.52	0.36	–	5.9
L1	PB	−0.10	–	0.27	–	5.7

IS isomer shift (±0.01), *QS* quadrupole splitting (±0.01), *W* experimental line width (±0.01), *B* hyperfine magnetic field (±0.1), Area (±0.5), *S* sextet, *D* doublet, *L* singlet

[a] Relative to metallic iron (α-Fe)

[b] Fixed value

practically the same diffractogram as described by Barton and Gale [39], and which is also shown in our work (Fig. 3, sample PB2). Thus, both S4 and S5 sextets can be ascribed to an orthorhombic ζ-Fe_2C. The broader lines and smaller hyperfine field of these sextets indicate some kind of a size distribution of the iron carbide particles.

The doublets D1 and D2 could not be directly assigned to any phase. They might be a result of the formation of other phases, or they could belong to a cyanide compound of the type $Fe^{II}_3[M^{III}(CN)_6]_2$.

Sample heated up to 1000 °C

Metallic iron with bcc and fcc lattice (α and γ, respectively), cementite θ-Fe_3C (orthorhombic, Pnma space group), graphite (hexagonal, $P6_3mc$ space group) and a small amount of magnetite Fe_3O_4 (~4 wt%), were the phases identified by XRD on sample PB3. The quantitative results obtained by Rietveld refinement of the respective XRD pattern are shown in Table 3. The aforementioned phases, except carbon, were also identified by MS; furthermore it was possible to reveal by MS that the gamma iron phase is not pure metallic iron, but fcc iron with carbon structural inclusions, i.e., austenite phase, as has been clearly indicated by the presence of a doublet subspectrum with IS close to zero (Fig. 6; Table 4). The estimation of a content of carbon atoms in the structure (0.93 wt%) was calculated according to the relationship given by Ron [43]. Magnetite identified by XRD and MS appears owing to an oxidation of metallic iron.

Table 3 Results of Rietveld refinement for the PB3 sample (1000 °C)

Phase	Weight percentage/%
α-Fe	22.8 (1)
γ-Fe	26.3 (1)
Fe_3C	38.3 (2)
Fe_3O_4	3.9 (1)
C	8.7 (3)

The number in parentheses denotes the uncertainty of the last digit ($\chi^2 = 2.52$)

Overall mechanism of thermal decomposition

Within the first step, four water molecules are released from the crystal structure of PB:

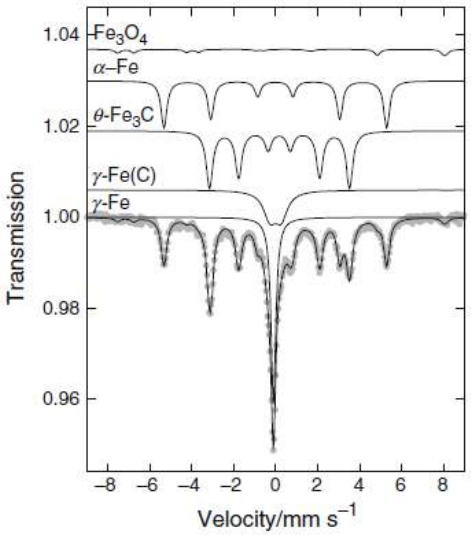

Fig. 6 RT Mössbauer spectrum of sample PB3 (1000 °C). The subspectra are shifted along the vertical axis for clarity

Table 4 Mössbauer parameters of the PB3 sample (1000 °C)

Component	IS[a]/mm s^{-1}	QS/mm s^{-1}	W/mm s^{-1}	B/T	Area/%
α-Fe	−0.02	0.00	0.34	33.0	26.3
θ-Fe_3C	0.17	0.02	0.37	20.7	35.2
Fe_3O_4 (tet)	0.29	0.01[b]	0.32[b]	48.7	1.9
Fe_3O_4 (oct)	0.61	0.02[b]	0.31[b]	45.9	1.8
γ-Fe(C)	−0.01	0.54	0.73	–	14.8
γ-Fe	−0.11	–	0.28	–	19.9

IS isomer shift (±0.01), *QS* quadrupole splitting (±0.01), *W* experimental line width (±0.01), *B* hyperfine magnetic field (±0.1), Area (±0.5)

[a] Relative to metallic iron (α-Fe)

[b] Fixed value

$$67-262\,^{\circ}\mathrm{C}:\ Fe_4[Fe(CN)_6]_3\cdot 4H_2O \rightarrow Fe_4[Fe(CN)_6]_3 + 4H_2O \quad (1)$$

The second decomposition step is accompanied by a formation of a ferricyanide phase, which could not be found in the PDF database. According to the model constructed from the analysis of the Mössbauer spectrum of the PB1 sample, it is possible to suggest the following equation:

$$67-377\,^{\circ}\mathrm{C}:Fe_4[Fe(CN)_6]_3\cdot 4H_2O \rightarrow 0.26Fe_4[Fe(CN)_6]_3 + 0.74(7/5\ Fe_3^{II}[Fe^{III}(CN)_6]_2 + 3/5\ (CN)_2) + 4H_2O \quad (2)$$

This equation, expecting the formation of the ferricyanide compound with three structural positions of high-spin ferrous ions, however, does not satisfy the mass loss determined from TG and emission of three moles of $(CN)_2$ as determined from EGA. In fact, the mass loss calculated from this reaction is only 9.1%.

In accordance with the overall mass loss of 45.39% determined from TG during the steps I, II, and III (from 67 to 707 °C), a release of 4 mol of H_2O, 4 mol of N_2, and 5 mol of $(CN)_2$ by the decomposition of 1 mol of PB can be considered (see Eq. 3). The theoretical mass loss is then $\Delta m_{th} = 47.7\%$. Importantly, while the emission of 3 mol of $(CN)_2$ during the step II results only to the structural change of the PB compound, the release of next 2 mol of $(CN)_2$ during the step III is accompanied by a total decomposition of PB toward iron carbides and graphite. Taking into account the Mössbauer spectral areas of Fe_7C_3 and Fe_2C (Table 2), we can calculate corresponding coefficients for solid decomposition products in Eq. 3.

$$67-707\,^{\circ}\mathrm{C}:\ Fe_4[Fe(CN)_6]_3\cdot 4H_2O \rightarrow 3Fe_2C + 1/7\ Fe_7C_3 + 32/7\ C + 5(CN)_2 + 4N_2 + 4H_2O \quad (3)$$

Within the step IV (from 707 to 1000 °C), the solid-state decompositions of Eckström-Adcock carbide (Fe_7C_3) as well as Fe_2C carbide to Fe_3C carbide (cementite) and graphite take place (Eckstrom and Adcock [44], Cohn and Hofer [45]):

$$3Fe_7C_3 \rightarrow 7Fe_3C + 2C \quad (4)$$

$$3Fe_2C \rightarrow 2Fe_3C + C \quad (5)$$

The cementite is further decomposed into metallic iron and graphite. The quantitative analysis of the XRD pattern (Table 3) and relative areas of the Mössbauer spectrum (Table 4) of the PB3 sample (the minor admixture of magnetite has been neglected) then gives an overall equation for the carbides decomposition:

$$3Fe_2C + 1/7Fe_7C_3 + 32/7C \rightarrow Fe_3C + 4(\alpha,\gamma) - Fe + 7C \quad (6)$$

Conclusions

Thermally induced decomposition of an insoluble Prussian blue ($Fe_4[Fe(CN)_6]_3\cdot 4H_2O$) under inert atmosphere consists of three main steps. After the dehydration, a restructuration of the original crystal lattice accompanied by the changes in valence and spin states of iron atoms and release of cyanogen—$(CN)_2$ take place. Above 400 °C, the decomposition of PB is finished resulting to iron carbides and graphite. The increase of temperature up to 1000 °C induces the formation of metallic iron, cementite and graphite. The overall decomposition reaction can be expressed by the following equation:

$$1000\,^{\circ}\mathrm{C}:\ Fe_4[Fe(CN)_6]_3\cdot 4H_2O \rightarrow 4(\alpha,\gamma) - Fe + Fe_3C + 7C + 5(CN)_2 + 4N_2 + 4H_2O \quad (7)$$

More detailed characterization of the ferrocyanide intermediate, which was found to be unstable in an opened air, is a subject of future investigations.

Acknowledgements This study has been supported by the Operational Program Research and Development for Innovations—European Regional Development Fund (CZ.1.05/2.1.00/03.0058), the internal IGA grants of Palacky University (PrF_2010_010, PrF_2011_013), the projects of the Ministry of Education of the Czech Republic (1M6198959201 and MSM6198959218), and the project of the Academy of Sciences of the Czech Republic (KAN115600801). The authors would like to thank to Jan Filip for XRD measurements, Martin Heřmánek for TG measurements, Jana Ševčíkova for Mössbauer measurements, Oldřich Schneeweiss for his comments on carbide phases, and Jiří Tuček for language corrections.

References

1. Buser HJ, Schwarzenbach D, Petter W, Ludi A. The crystal structure of Prussian blue: $Fe_4[Fe(CN)_6]_3 \cdot xH_2O$. Inorg Chem. 1977;163:2704–9.
2. Ito A, Suenaga M, Ono K. Mössbauer study of soluble Prussian blue, insoluble Prussian blue, and Turnbull's blue. J Chem Phys. 1968;48:3597–9.
3. Wilde RE, Ghosh SN, Marshall BJ. The Prussian blues. Inorg Chem. 1970;9:2512–6.
4. Weiser HB, Milligan WO, Bates JB. X-ray diffraction studies on heavy-metal iron-cyanides. J Phys Chem. 1942;46:99–111.
5. Allen JF, Bonnette AK. Thermal decomposition of Prussian blue: isotopic labeling with Mössbauer-inactive Fe-56. J Inorg Nucl Chem. 1974;36:1011–6.
6. Inoue H, Nakazawa T, Mitsuhashi T, Shirai T, Fluck E. Characterization of Prussian blue and its thermal decomposition products. Hyperfine Interact. 1989;46:725–31.
7. Ludi A, Güdel HU. Structural chemistry of polynuclear transition metal cyanides. Struct Bond. 1973;14:1–21.
8. Herren F, Fischer P, Ludi A, Hälg W. Neutron diffraction study of Prussian blue, $Fe_4[Fe(CN)_6]_3 \cdot xH_2O$. Location of water molecules and long-range magnetic order. Inorg Chem. 1980;19:956–9.
9. Vaucher S, Li M, Mann S. Synthesis of Prussian blue nanoparticles and nanocrystal superlattices in reverse microemulsions. Angew Chem Int Ed. 2000;39:1793–6.
10. Fiorito PA, Gonçales VR, Ponzio EA, Córdoba de Torresi SI. Synthesis, characterization and immobilization of Prussian blue nanoparticles. A potential tool for biosensing devices. Chem Commun. 2005;3:366–8.
11. Shen X, Wu S, Liu Y, Wang K, Xu Z, Lu W. Morphology synthesis and properties of well-defined Prussian blue nanocrystals by a facile solution approach. J Colloid Interface Sci. 2009;329:188–95.
12. Zhou PH, Xue DS. Finite-size effect on magnetic properties in Prussian blue nanowire arrays. J Appl Phys. 2004;96:610–4.
13. Karyakin AA, Karyakina EE. Electroanalytical applications of Prussian blue and its analogs. Russ Chem Bull Int Ed. 2001;50:1811–7.
14. Koncki R. Chemical sensors and biosensors based on Prussian blues. Crit Rev Anal Chem. 2002;32:79–96.
15. Puganova EA, Karyakin AA. New materials based on nanostructured Prussian blue for development of hydrogen peroxide sensors. Sensor Actuator B. 2005;109:167–70.
16. Rasmussen PG, Meyers EA. An investigation of Prussian blue analogues by Mössbauer spectroscopy and magnetic susceptibility. Polyhedron. 1984;3:183–90.
17. Verdaguer M, Girolami G. Magnetic Prussian blue analogs. In: Miller JS, Drillon M, editors. Magnetism: molecules to materials V. Weinheim: Wiley-VCH Verlag GmbH & Co. KGaA; 2005. p. 283–346.
18. Cosgrove JG, Collins RL, Murty DS. Preparation of ferrous ferricyanide (not Turnbull's blue). J Am Chem Soc. 1973;95:1083–6.
19. Zboril R, Machala L, Mashlan M, Sharma V. Iron(III) oxide nanoparticles in the thermally induced oxidative decomposition of Prussian blue, $Fe_4[Fe(CN)_6]_3$. Cryst Growth Des. 2004;4:1317–25.
20. De Marco D, Marchese A, Migliardo P, Bellomo A. Thermal analysis of some cyano compounds. J Therm Anal Calorim. 1987;32:927–37.
21. De Marco D. Thermal analysis of some cyano compounds. Part II. Thermal behaviour of mixed $KLnFe(CN)_6 \cdot 4H_2O$ (Ln = La(III), Ce(III), Nd(III)). Thermochim Acta. 1988;128:127–40.
22. De Marco D. Thermal analysis of some cyano compounds. Note III. The thermal behaviour of $Na_4Fe(CN)_6 \cdot 10H_2O$, $K_2Cu_3[Fe(CN)_6]_2 \cdot xH_2O$, $K_2Zn_3[Fe(CN)_6]_2 \cdot xH_2O$ and $Pb_2Fe(CN)_6$. J Therm Anal Calorim. 1989;35:2279–90.
23. De Marco D, Linert W. Thermal analysis of some cyano compounds. Part IV. The thermal behaviour of $LnFe^{3+}(CN)_6 \cdot nH_2O$ (La = La(III), Ce(III), Pr(III), Nd(III)). Thermochim Acta. 1991;175:249–61.
24. Brar AS, Sandhu HS, Sandhu SS. Thermal decomposition of hexahydrato thorium(IV) ferrocyanide. Thermochim Acta. 1980;41:253–6.
25. Lehto J, Haukka S, Koskinen P, Blomberg M. Thermal decomposition of potassium cobalt hexacyanoferrates(II). Thermochim Acta. 1990;160:343–7.
26. Navarro MC, Lagarrigue MC, De Paoli JM, Carbonio RE, Gómez MI. A new method of synthesis of BiFeO3 prepared by thermal decomposition of $Bi[Fe(CN)_6] \cdot 4H_2O$. J Therm Anal Calorim. 2010;102:655–60.
27. Gil DM, Navarro MC, Lagarrigue MC, Guimpel J, Carbonio RE, Gómez MI. Synthesis and structural characterization of perovskite YFeO3 by thermal decomposition of a cyano complex precursor, $Y[Fe(CN)_6] \cdot 4H_2O$. J Therm Anal Calorim. 2011;103:889–96.
28. Gallagher PK, Prescott B. Further studies of the thermal decomposition of europium hexacyanoferrate(III) and ammonium europium hexacyanoferrate(II). Inorg Chem. 1970;9:2510–2.
29. Žák T, Jirásková Y. CONFIT: Mössbauer spectra fitting program. Surf Interface Anal. 2006;38:710–4.
30. Nomura K, Takeda M, Iiyama T, Sakai H. Mössbauer studies of jarosite, mikasaite and Yapavaiite, and implication to their Martian counterparts. Hyperfine Interact. 2005;166:657–64.
31. Rodriguez-Carvajal J. An introduction to the program Fullprof 2000 (version July 2001). http://www.ill.eu/sites/fullprof/index.html.
32. Reguera E, Fernández-Bertrán J. Effect of the water of crystallization on the Mössbauer spectra of hexacyanoferrates (II and III). Hyperfine Interact. 1994;88:49–58.
33. Reguera E, Fernández-Bertrán J, Balmaseda J. The existence of ferrous ferricyanide. Transit Metal Chem. 1999;24:648–54.
34. Reguera E, Yee-Madeira H, Fernández-Bertran J, Nuñez L. Mössbauer spectra of ferrous salts of transition metal cyano complexes. A survey. Transit Metal Chem. 1999;24:163–7.
35. Herbstein FH, Snyman JA. Identification of Eckstrom-Adcock iron carbide as Fe_7C_3. Inorg Chem. 1964;3:894–6.
36. Lodya JAL, Gericke H, Ngubane J, Dlamini TH. Synthesis of Fe-carbides species by reactive milling. Hyperfine Interact. 2009;190:37–42.
37. Yamada Y, Yoshida H, Kouno K, Kobayashi Y. Iron carbide films produced by laser deposition. J Phys Conf Ser. 2010;217:012096.
38. Fang CM, van Huis MA, Zandbergen HW. Structure and stability of Fe_2C phases from density-functional theory calculations. Scr Mater. 2010;63:418–21.
39. Barton GH, Gale B. The Structure of a pseudo-hexagonal iron carbide. Acta Crystallogr. 1964;17:1460–2.

40. Niemantsverdriet JW, van der Kraan AM, van Dijk WL, van der Baan HS. Behavior of metallic iron catalysis during Fischer-Tropsch synthesis studied with Mössbauer spectroscopy, X-ray diffraction, carbon content determination, and reaction kinetic measurements. J Phys Chem. 1980;84:3363–70.
41. Amelse JA, Grynkewich G, Butt JB, Schwartz LH. Mössbauer spectroscopic study of passivated small particles of iron and iron carbide. J Phys Chem. 1981;85:2484–8.
42. Le Caër G, Dubois JM, Pijolar M, Perrichon V, Busslère P. Characterization by Mössbauer spectroscopy of iron carbides formed by Fischer-Tropsch synthesis. J Phys Chem. 1982;86:4799–808.
43. Ron M. Iron-carbon and iron-nitrogen systems. In: Cohen RL, editor. Applications of Mössbauer spectroscopy, vol II. New York: Academic Press; 1980. p. 329–92.
44. Eckstrom HC, Adcock WC. A new iron carbide in hydrocarbon synthesis catalysis. J Am Chem Soc. 1950;72:1042–3.
45. Cohn EM, Hofer LJE. Mode of transition from Hägg iron carbide to cementite. J Am Chem Soc. 1950;72:4662–4.

Electronic Supplementary Material

Thermal decomposition of Prussian blue under inert atmosphere

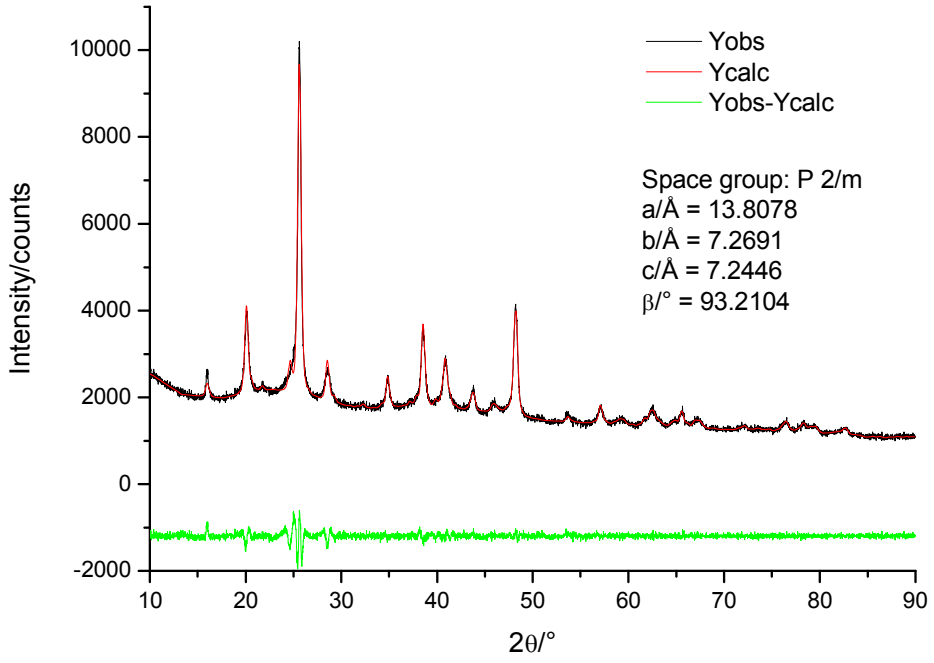

Fig. S1 Full profile fitting and cell refinement of sample PB2 “as prepared”.

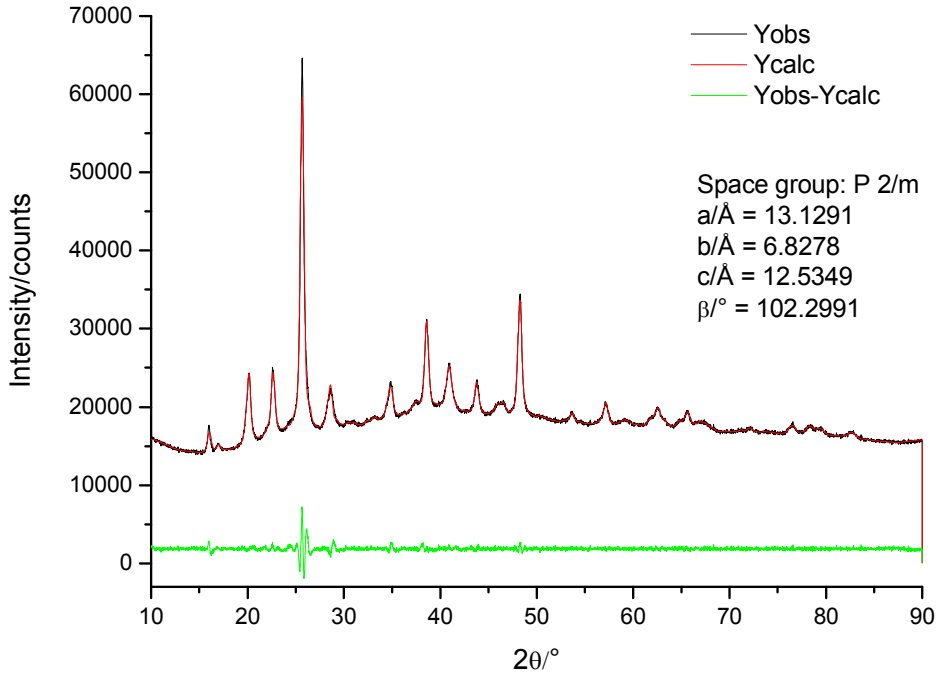

Fig. S2 Full profile fitting and cell refinement of sample PB2 “aged”.